

Brazilian
Journal Of Geophysics

Revista Brasileira de Geofísica

v. 37, n. 2

2019

PUBLICADA PELA SOCIEDADE BRASILEIRA DE GEOFÍSICA

ATTENUATION OF MULTIPLE REFLECTIONS ASSOCIATED WITH DIABASE SILLS FROM SOLIMÕES BASIN, BRAZIL, THROUGH THE PARABOLIC RADON TRANSFORM AND MULTICHANNEL PREDICTIVE DECONVOLUTION

Misael Possidonio de Souza¹, Michelangelo Gomes da Silva¹ and Milton J. Porsani^{1,2}

ABSTRACT. The Solimões Basin, Brazil, will be the subject of many discussions in the future due to the success of oil exploration in the 1970s with the discovery of oil and gas fields. The geology of this basin is characterized by significant thick igneous rocks layers, the diabase sills, which can be seen in any stacked section as reflectors with strong amplitude but low frequency. The high contrast of seismic impedance between the sedimentary rock layers and the diabase sills generate multiple reflection and reverberations that can lead to wrong seismic interpretation of stacked sections. In this work, to improve the quality of the stacked sections, we propose a seismic process flow that includes multiple filtering steps in land data, throughout the Multichannel Predictive Deconvolution and the Parabolic Radon Transform. This study was first performed on synthetic data to test the methodology, and then in real data provided by Agência Nacional do Petróleo, Gás Natural e Biocombustíveis (ANP). The conventional processing flowchart was applied using commercial processing software such as SeisSpace/ProMAX, and Fortran 90 codes available in the Centro de Pesquisa em Geofísica e Geologia, Universidade Federal da Bahia (CPGG/UFBA). The results obtained were satisfactory with the methodology used, besides visible improvements in the quality of the stacked seismic sections after attenuation of unwanted noises.

Keywords: multiple attenuation, seismic processing, seismic reflection.

RESUMO. A Bacia do Solimões será ainda tema de muitas discussões no futuro, devido ao sucesso da exploração de petróleo nas décadas de 1970 com a descoberta de campos de óleo e gás. A geologia desta bacia é caracterizada por espessas camadas de rochas ígneas, as soleiras de diabásio, que podem ser vistas em toda seção empilhada como refletores com forte amplitude e baixa frequência. O alto contraste de impedância sísmica entre as rochas sedimentares e as soleiras de diabásio gera reflexões múltiplas e reverberações que podem levar a uma interpretação sísmica errada das seções empilhadas. Neste trabalho, para melhorar a qualidade das seções empilhadas, propomos um fluxograma de processamento que adicione etapas de filtragem de múltiplas, através da Deconvolução Preditiva Multicanal e da Transformada Radon Parabólica. Este estudo foi realizado primeiramente em dados sintéticos para testar a metodologia, e depois em dados reais cedidos pela Agência Nacional do Petróleo, Gás Natural e Biocombustíveis (ANP). O fluxograma de processamento convencional foi aplicado utilizando *software* comercial de processamento, como o SeisSpace/ProMAX, códigos implementados em Fortran 90 disponíveis no Centro de Pesquisa em Geofísica e Geologia, Universidade Federal da Bahia (CPGG/UFBA). Os resultados obtidos foram satisfatórios com a metodologia utilizada, além de visíveis melhorias na qualidade das seções sísmicas empilhadas após atenuação dos ruídos indesejados.

Palavras-chave: atenuação de múltiplas, processamento sísmico, sísmica de reflexão.

¹Universidade Federal da Bahia, Centro de Pesquisa em Geofísica e Geologia, Instituto de Geociências, Campus Universitário da Federação, Salvador, BA, Brazil – E-mails: misael.geof@gmail.com; mykael_ba@yahoo.com.br; porsani@ufba.br

²National Institute of Science and Technology of Petroleum Geophysics (INCT/CNPq/MCTI).

INTRODUCTION

The Amazon region has always attracted interest from major oil companies, despite the current scenario of oil and gas exploration in onshore basins. In the 1978s, there was an intense exploration in the Amazon region including the Solimões Basin (Eiras, 1998), where gas wells were drilled in Urucu province. This basin presents high velocities contrasts between its sedimentation and diabase sills that generate multiple reflections observed in seismic data, making processing and interpretation more difficult. This can also be observed in synthetic data modeled by finite differences method (Silva Neto, 2004).

It is also known that land seismic data have low signal-to-noise ratio (Yilmaz, 2001), due to several factors, such as environmental noise, reverberations, aerial and refracted waves, ground roll (Silva, 2004), and therefore multiple identification and filtering is not an easy task (Alá'i & Verschuur, 2006). Most of these noises can be removed during conventional processing, throughout the NMO correction and stacking and $f-k$ filtering for linear or coherent noises. For multiple attenuation, there are several techniques already known in the industry for filtering, but for marine data. Some good techniques are Mono and Multichannel Predictive Deconvolution (Lima, 1999), Parabolic Radon Transform (Berkhout, 2006) and SRME method, the most robust so far (Verschuur et al., 1992).

Deconvolution aims the convolution of the seismic trace with its inverse filter in order to obtain the impulsive response of the Earth (Oliveira et al., 2014). For multiple filtering, a prediction distance is added inside the filter, which convolves only with the noise samples, preserving the signal, which is called by Predictive Deconvolution. It performs a statistical estimation of the inverse filter, throughout the Wiener-Levinson recursion, with a single trace. However, we can reinforce the inverse filter estimation using the ambiguity of seismic information, by adding more traces, which is then called Multichannel Predictive Deconvolution, a much more robust method than the previous one (Lima & Porsani, 2001). These techniques can be applied in Common Depth Points (CDP) and OFFSET domains, being more efficient in OFFSET domain (Oliveira et al., 2014).

On the other hand, the Radon Filtering is a method based on the difference of velocities between primary and multiple reflections, and it has been widely used in large companies such as Petrobras (Fernandes, 2014). It changes the domain from CDP in time $t-x$ to the Radon domain, where we can separate primary and multiple reflections, eliminating the noise and returning to the original domain throughout the Radon

Inverse Transform (Hampson, 1986). For multiple reflections attenuation, the Parabolic Radon Transform has proven itself to be more suitable and effective for seismic data filtering (Abbad et al., 2011). This technique acts similarly to $f-k$ filtering, but it is more efficient for short offsets failing in areas where geology is very complex.

To date, there are interesting works about attenuation of multiple reflections associated with diabase in synthetic data only, with some filtering techniques that are commonly used in seismic marine data. We hereby show interesting and new results of seismic processing and multiple filtering obtained in real land data from Solimões Basin provided by the ANP (Agência Nacional do Petróleo, Gás Natural e Biocombustíveis). We present a methodology to identify multiple reflections associated with diabase sills, assuming that there is periodicity, and applying Predictive Deconvolution and Parabolic Radon.

METHODOLOGY

Multichannel Predictive Deconvolution

Predictive Deconvolution is a statistical method of multiple filtering that is based on the periodicity of the primary and multiple energy. It aims to estimate an inverse filter that operates after a predictive distance, wisely chosen, to convolve with the noise leading us to a trace with primary reflections only. It is believed to be effective for long-period multiples in the marine case. Multichannel deconvolution mathematical formulation is similar to the single channel deconvolution, both use the Wiener-Levinson (WL) recursion to estimate the inverse filter.

In the following procedure, we describe how to obtain multichannel WL filters using 3 channels and number of filter coefficients per channel equal to 3. Let w , the desired data, x , y and z , the three strokes, then the calculated data w , can be represented by the

$$w(t) = h(t) * x(t) + f(t) * y(t) + g(t) * z(t) \quad (1)$$

where $h(t)$, $f(t)$ and $g(t)$ are operators acting respectively on the traits x , y and z . For operators with three coefficients in each signal, the above expression can be rewritten to,

$$w_t = \sum_{k=1}^3 x_{t-k+1} h_k + \sum_{k=1}^3 y_{t-k+1} f_k + \sum_{k=1}^3 z_{t-k+1} g_k \quad (2)$$

using matrix notation, we have:

$$\mathbf{W} = \begin{bmatrix} x_0 & 0 & 0 & y_0 & 0 & 0 & z_0 & 0 & 0 \\ x_1 & x_0 & 0 & y_1 & y_0 & 0 & z_1 & z_0 & 0 \\ \vdots & x_1 & x_0 & \vdots & y_1 & y_0 & \vdots & z_1 & z_0 \\ x_M & \vdots & x_1 & y_M & \vdots & y_1 & z_M & \vdots & z_1 \\ 0 & x_M & \vdots & 0 & y_M & \vdots & 0 & z_M & \vdots \\ 0 & 0 & x_M & 0 & 0 & y_M & 0 & 0 & z_M \end{bmatrix} \quad (3)$$

where \mathbf{W} is a block Toeplitz matrix from the traces x_t , y_t and z_t with M samples. We can then define \mathbf{a}^T by:

$$\mathbf{a}^T = [\mathbf{h}^T \quad \mathbf{f}^T \quad \mathbf{g}^T] \quad (4)$$

where the vectors \mathbf{h} , \mathbf{f} and \mathbf{g} are formed by the operators h_t , f_t and g_t . For a random vector \mathbf{a} , we can relate the predicted error vector by:

$$\mathbf{e} = \mathbf{W} - \mathbf{W}\mathbf{a} \quad (5)$$

minimizing the quadratic error, we find:

$$\mathcal{Q}(\mathbf{a}) = \mathbf{e}^T \mathbf{e} \quad (6)$$

and obtaining the Normal Equations, whose solution provides WL multichannel predictive filter. It is possible to estimate a filter with more than 3 channels, as long as your seismic data supports. Therefore, it is expected that the output of multichannel deconvolution shows an improvement in multiple filtering when compared with single channel deconvolution.

The Parabolic Radon Transform

The Parabolic Radon Transform maps parabolic events with different apertures where the amplitudes are summed along these parabolas, resulting in points or regions of coherence in the $\tau - q$ domain, with the different parabolas being concentrated in different regions. Hampson was the first to introduce its applications in seismic data. Basically, the data are organized into CDP families, and the NMO correction is done. An approximation of the travel time in the parabolic form is expressed in the equation below as:

$$t = \tau + qx^2 \quad (7)$$

where τ represents the intercept time or zero-offset time and q , the curvature of this parabola. Thus, the seismic data, $D(x_n, t)$ in the $x - t$ (CDP-OFFSET) domain, can be represented by the Direct Radon Transform $M(q_j, \tau)$ in the $\tau - q$ domain, given by:

$$D(x_n, t) = \sum_{j=1}^{N_q} M(q_j, \tau = t - q_j x_n^2), \quad (8)$$

where N_q is the number of q parameters. However, the Inverse Radon Transform is not fully reversible, which is a problem related to the discretization of the data and various limitations associated with the acquisition. We calculate the Fourier Transform of $D(x_n, t)$, that is $d(x_n, f)$, leading us to:

$$d(x_n, f) = \sum_{j=1}^{N_q} m(q_j, f) e^{i2\pi f q_j x_n^2}, \quad (9)$$

and using a matrix notation we have:

$$\mathbf{d}(\mathbf{f}) = \mathbf{L}(\mathbf{f})\mathbf{m}(\mathbf{f}) \quad (10)$$

where the operator \mathbf{L} is given by:

$$\mathbf{L} = \begin{bmatrix} e^{-i2\pi f q_1 x_1^2} & e^{-i2\pi f q_2 x_1^2} & e^{-i2\pi f q_3 x_1^2} & \dots & e^{-i2\pi f q_j x_1^2} \\ e^{-i2\pi f q_1 x_2^2} & e^{-i2\pi f q_2 x_2^2} & e^{-i2\pi f q_3 x_2^2} & \dots & e^{-i2\pi f q_j x_2^2} \\ \vdots & \vdots & \vdots & \vdots & \vdots \\ e^{-i2\pi f q_1 x_k^2} & e^{-i2\pi f q_2 x_k^2} & e^{-i2\pi f q_3 x_k^2} & \dots & e^{-i2\pi f q_j x_k^2} \end{bmatrix} \quad (11)$$

Therefore, the Direct Radon Transform (DRT) can be calculate by:

$$\mathbf{m} = \mathbf{L}^H \mathbf{d} \quad (12)$$

and the Inverse Radon Transform (IRT) can be estimated by least squares method, leading us to the expression:

$$\mathbf{d} = (\mathbf{L}\mathbf{L}^H)^{-1} \mathbf{L}\mathbf{m} \quad (13)$$

where \mathbf{L} and \mathbf{L}^H are an adjoint par of operators.

The Parameter q

In industry, Radon domain is not defined by the curvature of the parabola. We see the Radon domain as time of intersection τ versus against move-out (q) in time, instead. Most authors prefer to use Radon Filtering this way because it is more suitable. The parameter q of a parabola (a CDP after NMO correction) with intercept time τ are related by the following equation (Fernandes, 2014):

$$\tau = t - q \frac{x^2}{x_{MAX}^2} \quad (14)$$

where x represents the OFFSET and x_{MAX} , the maximum OFFSET. From this equation, the parameter q becomes the move-out time (ms). We can see that in many seismic processing software, such as SeisSpace/ProMAX, the Radon domain comes with $\tau - p$, with p being the move-out of a parabola.

The Seismic Processing Workflow

The process is divided into the following steps:

- (i) Quality Control, Geometry and Mute/Editing;
- (ii) First break picking and Field Statics Corrections;
- (iii) Spike deconvolution and Ground Roll Filtering;
- (iv) First Velocity Analysis and Stack;
- (v) Multiple Reflection Identification and Filtering;
- (vi) Second Velocity Analysis, Residual Stack Correction and Seismic Migration.

In this work, processing started importing the SEG-Y field files into the SeisSpace/ProMAX for geometry assembly. The next step consists of editing and muting noisy traces and defective stations in land data. Next, first breaks picking is performed to be used in statics corrections, in order to eliminate the effects of the weathering layer and irregular topography. The next step is the ground roll filtering, using the available tools in SeisSpace/ProMAX.

To apply deconvolution, data were, at first, exported to Seismic Unix, where they were organized in the CDP gathers. We applied MMO (Multiple Moveout Correction), which is an NMO correction using the velocity of primary reflection. We applied Multichannel Predictive Deconvolution and its results were re-imported into SeisSpace/ProMAX in SEG-Y format, where amplitude gains and spherical divergence correction and NMO correction were applied before stacking.

On the other hand, to use Radon Parabolic Transform, we applied NMO correction in the data organized in CDP domain in order to separate the primary and multiple reflections by their different move-outs. Data were then passed to Radon domain where the primary reflections showed a negative move-out $-q$ and the multiples reflections and reverberations showed a positive move-out $+q$.

After selecting the primary reflection region by applying a simple mute, we turned back to time domain through Radon Parabolic Inverse Transform, generating a filtered CDP as an output. At the end, we applied MMO correction in these filtered CDP gathers by both methods in order to compare and visualize their effect on multiples.

Multiple Reflection Identification on Land Data

The reflections of the diabase sill are easily recognized in any seismic line from the Solimões Basin, which presents high

amplitude due to the strong contrast of seismic impedance. After identifying the diabase layer, in the stacked section, we also identified the multiple reflections in a similar way it is done in marine seismic data. For this, we organized the data in CDP and applied constant NMO correction only in the reflection corresponding to the diabase layer. After MMO correction, it is expected that all seismic events of same velocity will be flattened, and consequently, the multiple associated with the diabase will stand out in front of the other events.

This methodology is also similar to the Predictive Deconvolution for multiple reflection attenuation and it is proven to be reliable. For example, if we would choose any other strong reflection without any multiple reflections associated with it, we would not find anything. On the other hand, choosing the diabase sill reflector, and applying NMO correction in a CDP in order to make it flat (MMO correction), all the multiple reflections associated with the sill will be visible, and also become flat.

In future work, it is proposed to use the SRME method to automatically predict all multiple reflections on Solimões Basin data, instead of the methodology presented here, due to the amount of time the interpreter would take to identify the noises. SRME performs the auto-convolution with the seismic data with itself showing us where the multiple reflections are located and being faster than other methods to identify multiple reflections.

NUMERICAL RESULTS ON SYNTHETIC AND REAL DATA FROM SOLIMÕES BASIN

Aiming to test our methodology, synthetic data were generated by Finite Difference method based on a velocity field (Fig. 1), which was created following the main geological features of Solimões Basin. The geometry of seismic modeled data is also illustrated in Table 1.

Table 1 – Acquisition parameters of the synthetic data.

Number of shots and channels	100
Fold	50
Geometry	1000 m - 20 m - x - 20 m - 1000 m
Shot and receiver interval	20 m
Total time of record	5 s
Sampling interval	2 ms

We applied MMO correction with the velocity of 2000 m/s in the data, sorted by CDP and absolute offsets, and all multiple

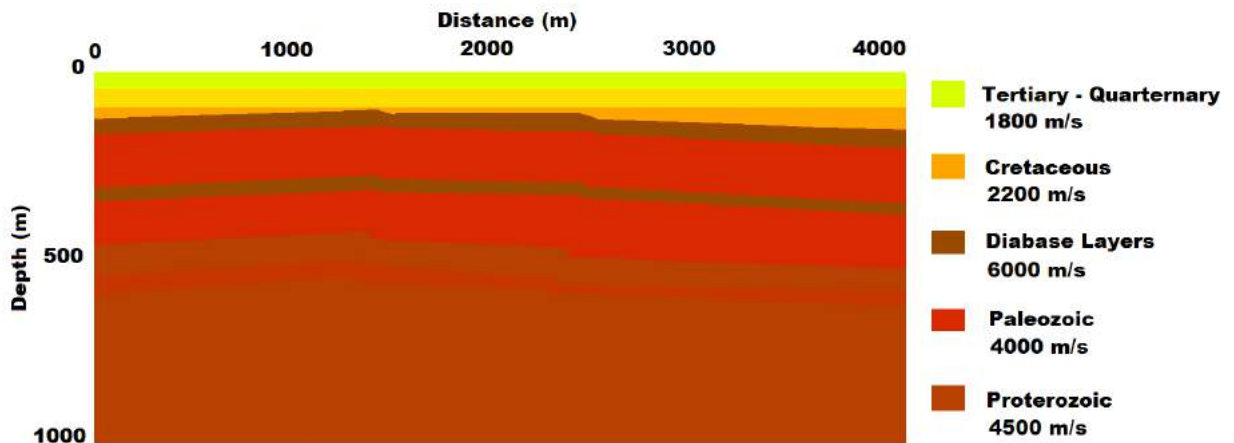


Figure 1 – Velocity field from Solimões Basin for seismic modeling.

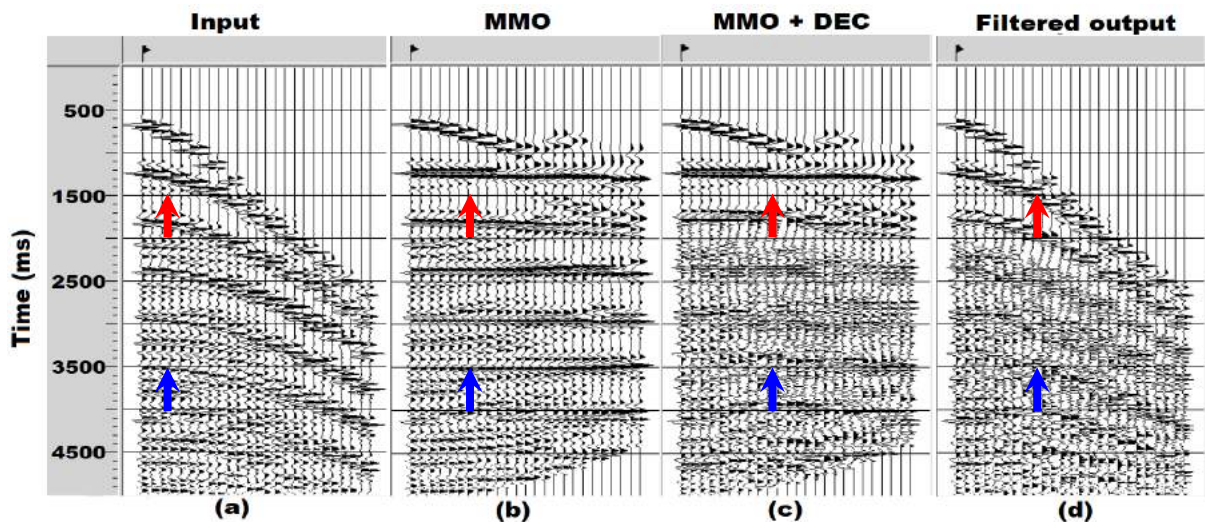


Figure 2 – Multichannel Predictive Deconvolution applied in a single modeled CDP. Main steps are shown from input (a), MMO correction (b), filtering (c) and inverse MMO correction (d). The red arrows indicate the primary reflection, the diabase sill, and the blue arrows indicate some of the multiple reflections.

reflections associated with this reflection became flat. So, we selected a single CDP (Fig. 2a) and the input of deconvolution has to be MMO corrected (Fig. 2b). The period between primary reflections and multiple has also to be known. Multichannel Predictive Deconvolution was then applied using 7 channels (Fig. 2c) and the results were very effective on modeled data after MMO inverse correction (Fig. 2d).

The results of a stacked section obtained from synthetic data before and after deconvolution are shown in Figure 3. It is hard to see underneath the diabase layer due to these noises and reverberations before filtering (Fig. 3a) and the output section

is closer to the original velocity field, which is more reliable (Fig. 3b).

The results of Parabolic Radon Filtering in synthetic data are shown with the same CDP chosen in previous figures (Fig. 4). The most important parameter is, in fact, the move-out difference between the signal and noise, which is determined by the velocity contrast. We applied an NMO correction with intermediate velocity before the Parabolic Radon Transform (Fig. 4a), leading us to a scenario where primaries reflections have negative move-out and multiples have positive move-out (Fig. 4b).

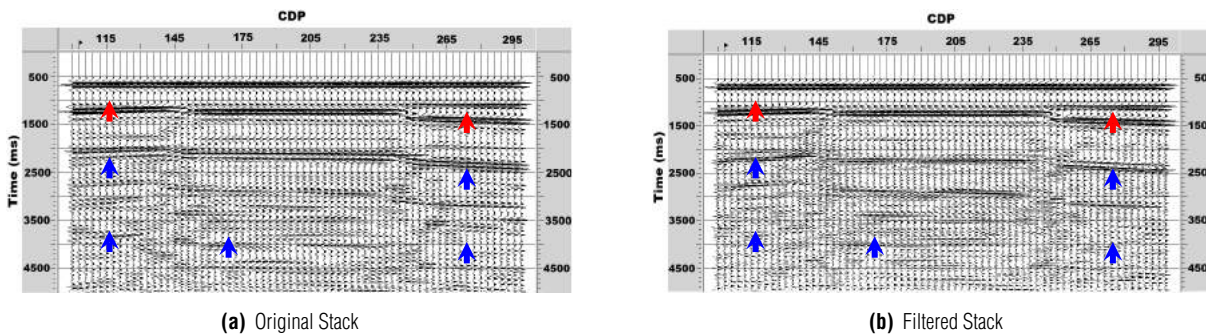


Figure 3 – Display of SeisSpace/ProMAX illustrating stacked sections from synthetic data, before deconvolution in (a), after deconvolution in (b).

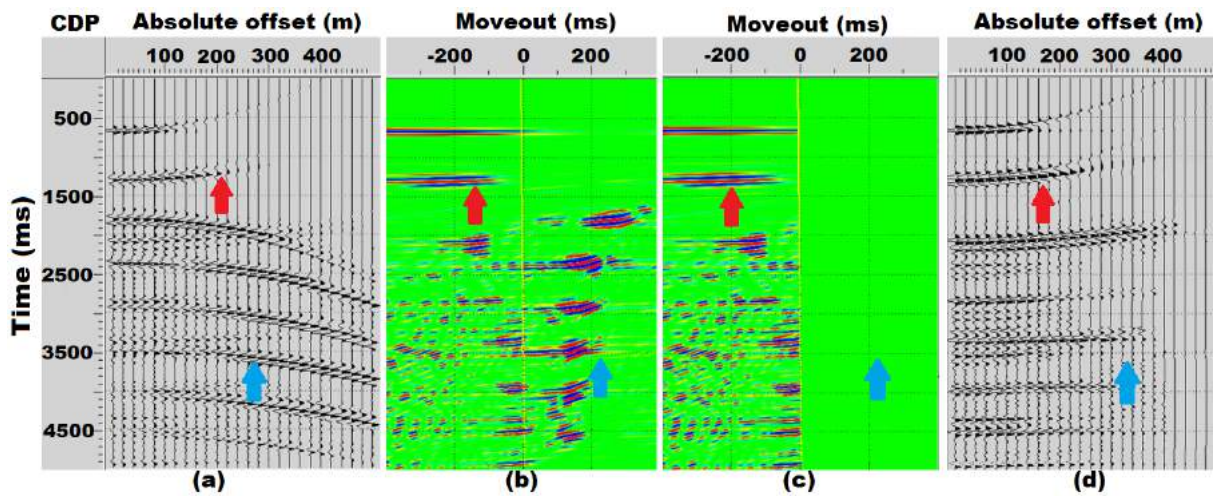


Figure 4 – Display of SeisSpace/ProMAX showing a CDP after NMO correction with RMS intermediate velocity (a), Parabolic Radon domain (b), mute in the multiple region (c) and the output after Inverse Transform (d). The red arrows indicate the primary reflection, the diabase sill, and the blue arrows indicate some of the multiple reflections.

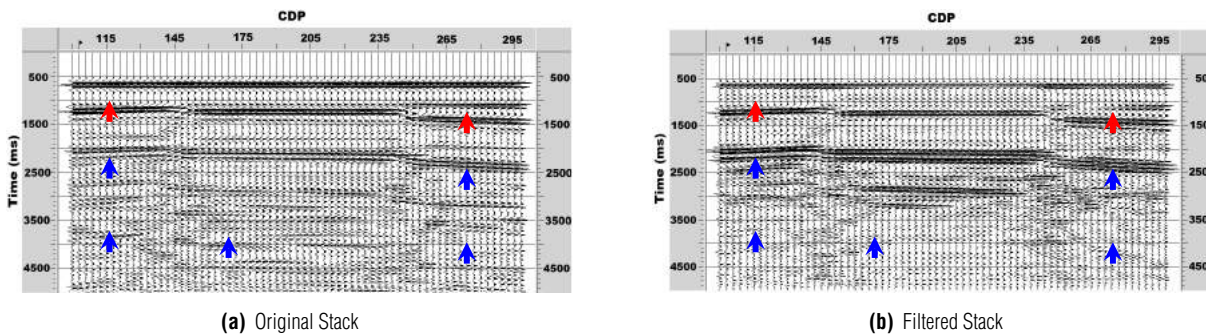


Figure 5 – Display of SeisSpace/ProMAX illustrating stacked sections from synthetic data, before Parabolic Radon Filtering (a) and after it (b).

We could mute the noisy area in the Radon domain (Fig. 4c) and then came back to time domain by applying Inverse Parabolic Radon Transform (Fig. 4d). We can see how effective this technique is by the quality of the filtered output. An inverse NMO correction with intermediate velocity is required before following the processing flow.

We show the results of a stacked section obtained from the synthetic data before (Fig. 5a) and after Radon Filtering (Fig. 5b). The quality is better when compared to the stacked section filtered by Deconvolution (Fig. 3b), which is closer to the original velocity field. In addition, Radon Filtering does not require any previous knowledge about how the multiple reflections were generated and does not assume periodicity in seismic data, becoming easier to perform than Deconvolution.

The real land seismic line from Solimões Basin was given by ANP as a research support. We followed the seismic

processing steps previous explained. The geometry of this seismic data is shown in Table 2.

Table 2 – Acquisition parameters of the seismic line 0254-0264 of the Solimões Basin.

Number of Shots	1225
Number of channels	240
Fold	120
Shot and receiver interval	25 m
Minimum OFFSET	50
Maximum OFFSET	3025
Total time of record	4 s
Sampling interval	2 ms

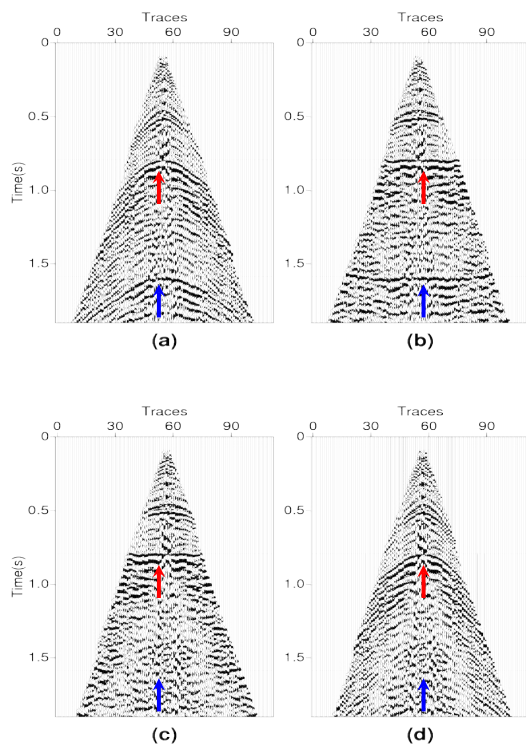


Figure 6 – Deconvolution steps for multiple attenuation in real data: a CDP gather in (a), after MMO correction on diabase layer in 0.8 s (b), after multichannel deconvolution with 5 traces (c) and after MMO inverse correction (d). The red arrows indicate the primary reflection, the diabase sill, and the blue arrows indicate the multiple reflections.

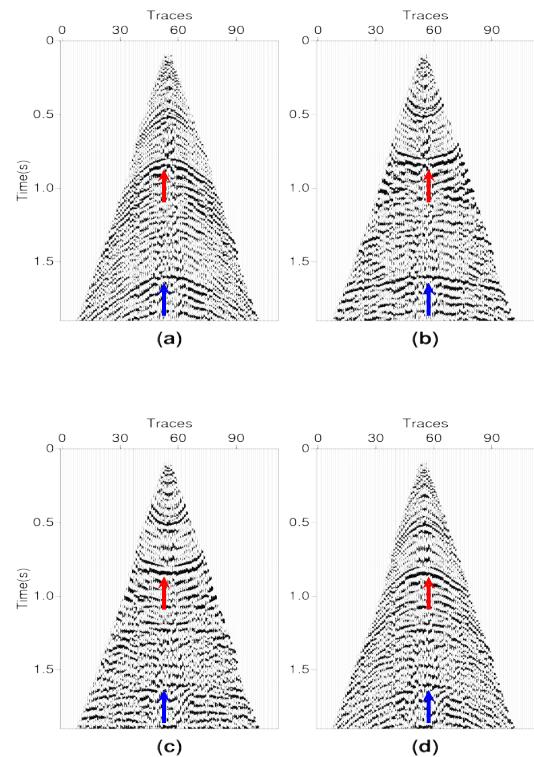
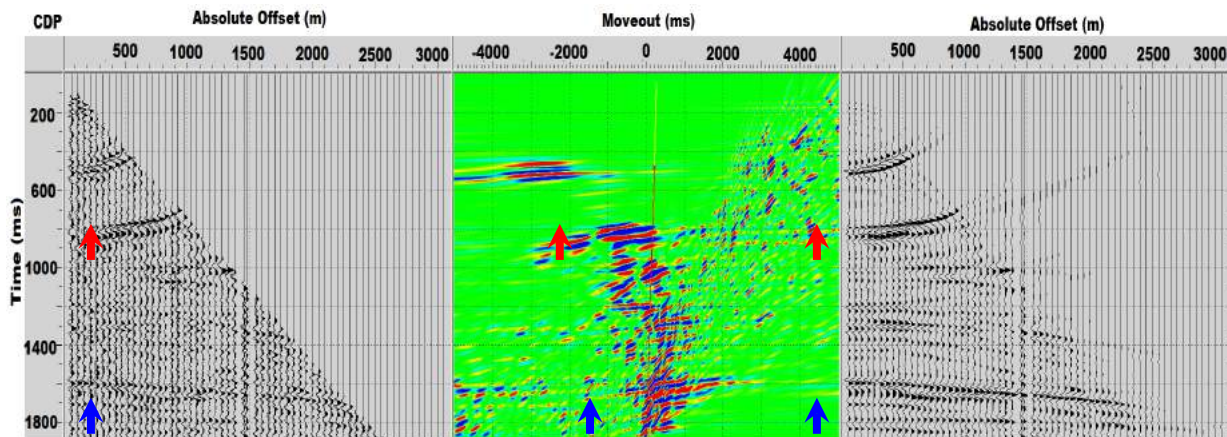
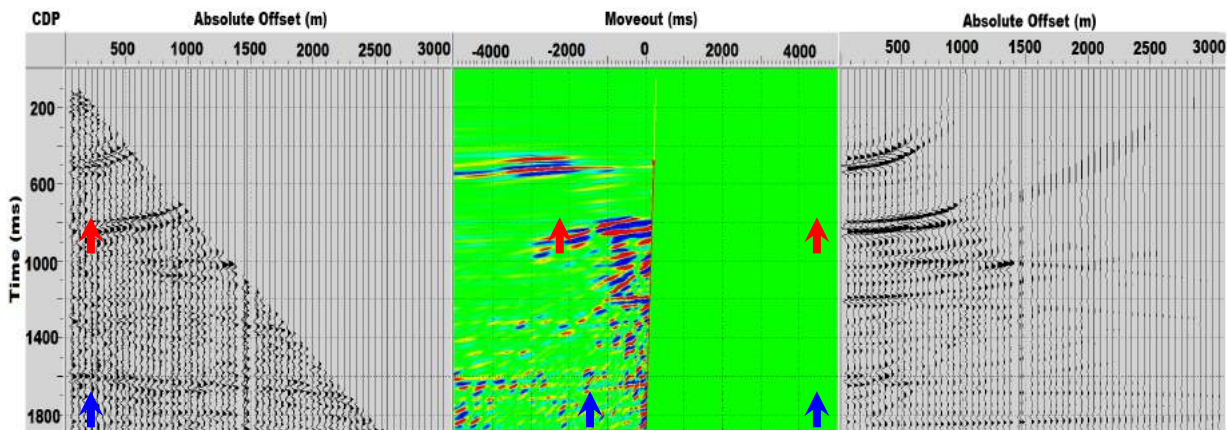


Figure 7 – Parabolic Radon Filtering steps for multiple attenuation in real data: a CDP gather (a), after NMO correction with intermediate velocity (b), after Radon Filtering (c) and after NMO inverse correction (d). The red arrows indicate the primary reflection, the diabase sill, and the blue arrows indicate the multiple reflections.



(a) CDP gather and its Radon domain before muting



(b) CDP gather and its Radon domain after muting

Figure 8 – Display of SeisSpace/ProMAX showing a real CDP gather after NMO correction with RMS intermediate velocity, its Parabolic Radon domain and its Inverse Transform (a); The same CDP here after a mute applied in the multiple reflections region and its Inverse Transform (b). The red arrows indicate the primary reflection, the diabase sill, and the blue arrows indicate the multiple reflections.

After applying the processing flow to improve the signal-to-noise ratio, a CDP gather was chosen to run Multichannel Predictive Deconvolution and Parabolic Radon tests. In this CDP gather (Fig. 6a) we see the diabase layer in 0.8s and its multiple associated in 1.6s, approximately. In order to perform Deconvolution, MMO correction was applied using a velocity of 2200 m/s on 0.8s (Fig. 6b). After that, the multiple reflection also showed a zero move-out. The Multichannel Predictive Deconvolution was applied (Fig. 6c) followed by an MMO inverse correction to generate the output filtered data (Fig. 6d).

A similar procedure was made for Radon Filtering. Firstly, the same CDP gather (Fig. 7a) was NMO corrected with an intermediate RMS velocity (Fig. 7b) in order to create a different move-out between primaries and multiples. After that, Radon Transform was applied, followed by a mute the noisy region, generating a filtered CDP without multiples (Fig. 6c). An NMO inverse correction was also required (Fig. 6d) to generate the output data. In the Radon domain, we can see the primaries and multiples of diabase layer are separated by its move-out (Fig. 8a). A mute function was designed and applied in order to eliminate those noises from seismic data before coming back

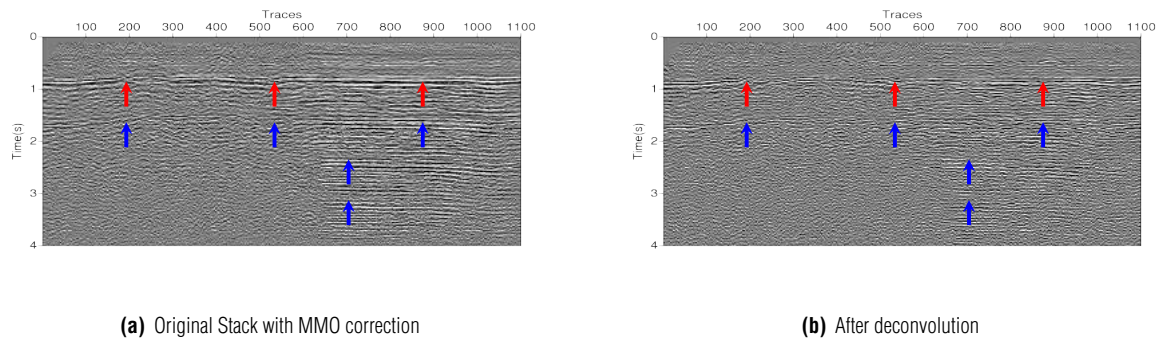


Figure 9 – Stacked sections from real data with MMO correction (a) and after deconvolution (b). The red arrows indicate the primary reflection, the diabase sill, and the blue arrows indicate the multiple reflections.

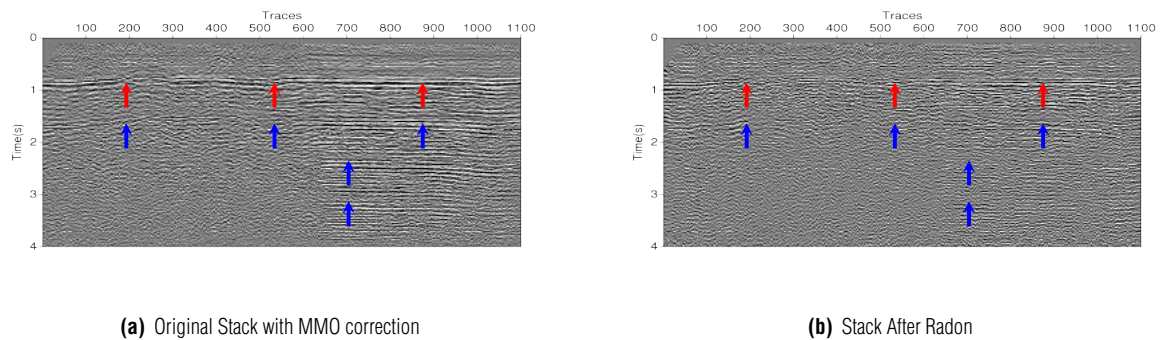


Figure 10 – Stacked sections from real data with MMO correction (a) and after Parabolic Radon Filtering (b). The red arrows indicate the primary reflection, the diabase sill, and the blue arrows indicate the multiple reflections.

to the CDP-OFFSET domain (Fig. 8b) throughout the Inverse Transform.

Despite the low signal-to-noise ratio, good results were observed using these techniques. Thus, for evaluation of the method, MMO correction was applied to all filtered CDPs and then stacked sections were generated, where only primary and multiple reflections would be present (Fig. 9) and (Fig. 10). The MMO stacked sections before deconvolution (Fig. 9a) shows many noises and reverberations that were eliminated (Fig. 9b) by multichannel deconvolution. On the other hand, MMO stacked section after Radon Filtering shows more improvement in quality (Fig. 10b) than the (Fig. 9b), which is more reliable for the geophysical interpretation of the whole data.

CONCLUSIONS

Solimões Basin, an intracratonic Paleozoic type, is located in Amazon State, north of Brazil. The seismogram is contaminated by multiple reflections associated to diabase sills, which has great amplitudes and low frequency. Multiple energy generated

by diabase sills can also be attenuated to improve seismic image quality.

Filtering techniques commonly applied in marine seismic data can be adapted for land data as we could see the results of Radon and Deconvolution, both were quite effective methods for attenuation of multiple associated to igneous rocks. Real and synthetic data were filtered effectively by the proposed methodology.

The problems with elevation and thickness of the weathering layer with low signal-to-noise ratio common in land data can be bypassed in order to guarantee the effectiveness of the Multichannel Predictive Deconvolution method. Radon Filtering showed more improvement in the seismic image than the Deconvolution. The choice of the number of channels for deconvolution interferes greatly in the obtained results: the filtering can be quite aggressive when worked with more than 7 channels.

Noise attenuation was satisfactory at the end of the stacked section, where the multiple reflections had a larger amplitude.

However, Parabolic Radon Transform is a high-intensity computer process depending on the sample rate of the seismic data and Deconvolution can be faster, being more computationally efficient in some cases, such as 3D seismic filtering. Finally, both methods could present satisfactory results and improve the velocity analysis of seismic data from Solimões Basin.

In future works, we propose a study with SRME method adapted for land seismic data in Solimões Basin and it is expected to show all kinds of noises associated with the diabase sills. A 3D seismic data processing and filtering is also a great subject to research in this time.

ACKNOWLEDGMENTS

The authors thank ANP for the data set from Solimões Basin and Landmark for the educational licenses granted to the Centro de Pesquisa em Geofísica e Geologia (CPGG-UFBA). This study was financed in part by the Coordenação de Aperfeiçoamento de Pessoal de Nível Superior – Brazil (CAPES) – Finance Code 001.

REFERENCES

- ABBAD B, URSIN B & PORSANI MJ. 2011. A fast, modified parabolic Radon transform. *Geophysics*, 76(1): V11-V24.
- ALÁ' R & VERSCHUUR E. 2006. Case study of surface-related and internal multiple elimination on land data. In: SEG/New Orleans 2006 Annual Meeting. 62: 2727- 2731.
- BERKHOUT AJ. 2006. Seismic processing in the inverse data space. *Geophysics*, 71(4): A29-A33.
- EIRAS JF. 1998. Tectônica, sedimentação e sistemas petrolíferos da Bacia do Solimões, estado do Amazonas. In: TAHA M. (Coord.). Searching for Oil and Gas in the land of giants: The Search Magazine. Special publication - Brazil. Argentina: Schlumberger.
- FERNANDES FV. 2014. Atenuação de reflexões múltiplas utilizando a Transformada Radon Parabólica. Master Dissertation on Geophysics - Centro de Graduação em Geofísica e Geologia, Universidade Federal da Bahia, Salvador, Brazil, 2014. 179 pp.
- HAMPSON D. 1986. Inverse velocity stacking for multiple elimination. *Journal of the Canadian Society of Exploration Geophysicists*, 22: 44-55.
- LIMA AP. 1999. Deconvolução de reflexões múltiplas nos domínios $t - x$ e $\tau - p$ com filtros multicanais. Master Dissertation on Geophysics - Centro de Graduação em Geofísica e Geologia, Universidade Federal da Bahia, Salvador, Brazil, 1999. 74 pp.
- LIMA AP & PORSANI MJ. 2001. Deconvolução preditiva de reflexões múltiplas e *peg-legs* utilizando filtragem Wiener-Levinson multicanal. *Brazilian Journal of Geophysics*, 19(3): 303-313.
- OLIVEIRA SLR, MACIEL RC, SILVA MG & PORSANI MJ. 2014. Attenuation of short-period multiples in seismic data processing of the Jequitinhonha Basin, Brazil. *Brazilian Journal of Geophysics*, 32(3): 395-403.
- SILVA NETO FA. 2004. Modelagem Acústica por diferenças finitas e elementos finitos em 2-D e 2,5-D. Master Dissertation on Geophysics. Centro de Geociências, Universidade Federal do Pará, Belém, Brazil, 2004. 103 pp.
- SILVA MG. 2004. Processamento de dados sísmicos da Bacia do Tacutu. Master Dissertation on Geophysics - Centro de Graduação em Geofísica e Geologia, Universidade Federal da Bahia, Salvador, Brazil, 2004. 143 pp.
- VERSCHUUR DJ, BERKHOUT AJ & WAPENAAR CPA. 1992. Adaptive surface-related multiple elimination. *Geophysics*, 57(9): 1166-1177.
- YILMAZ O. 2001. Seismic data analysis: processing, inversion and interpretation of seismic data. Tulsa, OK: SEG. 2027 pp.

Recebido em 13 de fevereiro de 2018 / Aceito em 24 de abril de 2019

Received on February 13, 2018 / Accepted on April 24, 2019

VISCO-ACOUSTIC MODELING IN THE FREQUENCY DOMAIN USING A MIXED-GRID FINITE-DIFFERENCE METHOD AND ATTENUATION-DISPERSION MODEL

Sheryl K. Avendaño^{1,2}, Juan Carlos Muñoz-Cuertas^{1,2}, Miguel A. Ospina² and Hebert Montegranario²

ABSTRACT. Seismic modeling is an important step in the process used for imaging Earth sub-surface. Current applications require accurate models associated with solutions of the equation of wave propagation in realistic medium. In this work, we propose a modeling for 2D wave propagation in a visco-acoustic medium with variable velocity and density, handled in the frequency domain under conditions that describe dissipation depending on the quality factor Q . We use mixed-grid finite-difference method and optimize it for the case of the visco-acoustic medium with the aim to minimize numerical dispersion. We present solutions for test cases in homogeneous media and compare the analytic solutions. Further, we compare the solution using conventional grid (5-point scheme) and our mixed-grid implementation (9-point scheme), finding a better response with the mixed-grid 9-point scheme. We also studied the characteristics of the numerical solution, wave fields for P-waves are discussed for different velocity profiles, damping functions and Q values finding that the method performs very well with potential in applications that require full knowledge of the wave field such as Full Waveform Inversion or Reverse Time Migration.

Keywords: seismic attenuation, wave propagation modeling, visco-acoustic medium, quality factor.

RESUMO. A modelagem sísmica é um passo importante no processo da construção de imagens da sub-superfície da Terra. Aplicações atuais exigem modelos de exatidão associados a soluções da equação de propagação de ondas em meio realista. Neste trabalho, nós propomos uma modelagem para propagação de ondas 2D em um meio visco-acústico com velocidade e densidade variáveis, manipuladas no domínio da frequência sob condições que descrevem a dissipação dependendo do fator de qualidade Q . Utilizamos o método de diferenças finitas em redes mistas e otimizamos para o caso do meio visco-acústico com o objetivo de minimizar a dispersão numérica. Apresentamos soluções para casos de teste em meios homogêneos e comparamos com as soluções analíticas. Além disso, comparamos a solução usando uma rede convencional (5-pontos) e nossa implementação de redes mistas (9-pontos), encontrando uma melhor resposta com o esquema de 9-pontos da rede mista. Também estudamos as características da solução numérica, campos de onda para ondas P são discutidos para diferentes perfis de velocidade, funções de amortecimento e valores de Q , descobrindo que o método funciona muito bem com potencial em aplicações que exigem conhecimento completo do campo de onda, como inversão de forma de onda completa ou Migração de Tempo Inverso.

Palavras-chave: atenuação sísmica, modelagem de propagação de onda, meio visco-acústico, fator de qualidade.

¹Universidad de Antioquia, Group of Computational Physics and Astrophysics, Instituto de Física, Medellín, Calle 67 No. 53-108, Colombia – E-mails: sheryl.avendano@udea.edu.co, juan.munozc@udea.edu.co

²Universidad de Antioquia, Group of Tomography and Seismics, Instituto de Matemáticas, Medellín, Calle 67 No. 53-108, Colombia – E-mails: maospina5@gmail.com, hebert.montegranario@udea.edu.co

INTRODUCTION

Realistic modeling of the propagation of waves in the continuous media is one of the most complex problems one faces in different scenarios of applied physics. Although this problem is complex, it is often a crucial step for the solution of many different situations, from the exploration of the inner structure of solids and medical imaging to seismic exploration. In the particular case of seismic exploration, modeling the wave propagation in the sub-surface is complex. In general, the physical conditions are non-ideal, therefore when one requires realistic, but still practical solutions to the problem, several simplifying approximations have to be made. For example, one usually ignores the effects of attenuation in wave propagation. However, Earth is not totally elastic neither totally viscous and a combination of both extreme behaviors should fit the properties of wave propagation.

The simplest approximation to wave propagation is the acoustic and isotropic case. However, when this approach is not enough to reproduce the observables, in order to get precise information about the physical properties of the sub-surface, it becomes necessary to consider a better model of the propagation of waves considering more realistic physical conditions such as viscosity, elasticity and anisotropy.

Viscosity and attenuation of mechanical waves are key physical phenomena and we shall focus our attention in this subject. The visco-acoustic media can be defined as a medium without cross propagation but exhibiting attenuation in the amplitude of the longitudinal wave. Considering viscosity in wave propagation introduces two phenomena not present in the acoustic case. First, dissipation produced by energy absorption such that the amplitude of the wave is reduced especially at high frequency. Second, dispersion by the change in the physical properties of the medium, where the wave velocity may depend on the frequency (Wang, 2009).

To describe the attenuation of energy of the seismic wavefront, Carcione et al. (2002) proposed a model based in linear solid material rheology and memory variables. They show in their work how the use of memory variables describes the propagation of waves in the medium and accounts for attenuation of the energy of the propagating waves at large distances from the source. Later, Dutta et al. (2013) used the same modeling approach, however, using only one relaxation mechanism, they show how the method works to compensate for attenuation in least-squares reverse time migration (LSRTM).

Wang et al. (2003) used a visco-acoustic wave equation to compensate for the energy decrease of wave propagation in

a realistic media using an extrapolator based in the propagator of the wave equation in the forward and backward direction. They show that using a Q -based attenuation model it is possible to fully describe the propagation of waves in the visco-acoustic media. Yang et al. (2014) present a detailed comparison of different visco-acoustic wave equations and studied their dissipation and dispersion properties, providing a rough idea about how the most commonly used visco-acoustic wave equations perform.

In particular, the realistic modeling of wave propagation is an important step in the process used for imaging Earth sub-surface. Currently, one of the most powerful techniques of seismic tomography that uses solutions of the equation of wave motion is the so-called Full Waveform Inversion (FWI) (Fichtner, 2011). FWI consists on obtaining the model parameters of the sub-surface through an inversion process that relates the comparison between models and observed data. To understand and emulate the complex wave phenomena in a realistic heterogeneous medium it is necessary to perform a seismic modeling where the result is a wavefield obtained through the numerical solution of the wave propagation.

This previous background shows that for different scenarios in seismic exploration it is still important to study the problem of wave propagation in visco-acoustic media. However, the numerical solution of the differential equation of wave propagation requires high accuracy, this translates in to a problem where large matrix operations are involved and this implies the demand of large computational resources. This consideration introduces expensive constraints from the technical point of view. The goal now then is to look for methods that provide high quality solutions that offer the opportunity to explore the computational power available to date.

We aim to provide a model for the propagation of waves in a general visco-acoustic media in the frequency domain optimized for applications in *FWI (Full Waveform Inversion)*, considering the effects of attenuation. It is one more solution to visco-acoustic wave equation but this time in frequency domain. There have been several proposals to include the effects of attenuation in the equations of wave motion (Yang et al., 2014). One possibility is to work in the frequency domain using a term known as complex bulk modulus, which is a method easy to implement and to relate to the quality factor Q (Carcione et al., 2002). Other works use Laplace transform for the model (Kamei & Pratt, 2013) and FWI (Shin & Ho Cha, 2008).

This work focuses on the propagation of mechanical waves in a medium with explicit attenuation modeled through the damping functions and quality factor Q . Frequency domain is adopted in this work since it allows the study of effects of the modeling (attenuation, dispersion) on individual wave frequencies. We pay especial attention to the quality of the solution and provide results of the implementation of optimal mixed-grid scheme looking for the minimization of the numerical dispersion in the implementation. Instead modeling explicitly the elastic and viscous excitation modes (Carcione et al., 2002), we model the dissipative effect of the medium explicitly through damping functions that attenuate the wave amplitude according to the quality factor of the media for different frequencies.

METHODOLOGY

Background and mathematical and physical formulation

Wave propagation rests on the basis of mechanics of the continuum medium. In order to formulate the problem we need to state a set of basic equations that describe the motion of the media and perturbations propagating inside it

$$\left(\frac{\partial}{\partial t} + \mathbf{v}(\mathbf{x}, t) \cdot \nabla\right) \rho(\mathbf{x}, t) + \rho(\mathbf{x}, t) \nabla \cdot \mathbf{v}(\mathbf{x}, t) = 0. \tag{1}$$

$$\rho(\mathbf{x}, t) \left(\frac{\partial}{\partial t} + \mathbf{v}(\mathbf{x}, t) \cdot \nabla\right) \mathbf{v}(\mathbf{x}, t) = \nabla \cdot \boldsymbol{\sigma}(\mathbf{x}, t) + \mathbf{f}(\mathbf{x}, t), \quad \int_V \boldsymbol{\varepsilon}_{ijk} \boldsymbol{\sigma}_{jk}(\mathbf{x}, t) dV = 0. \tag{2}$$

$$\boldsymbol{\sigma}_{ij} = \boldsymbol{\varepsilon}_{kl}(\mathbf{x}, t) \otimes \dot{\mathbf{C}}_{ijkl}(\mathbf{x}, t). \tag{3}$$

Equation (1) is the continuity equation, that is an statement of the conservation of mass, Equation (2) is an establishment of linear and angular momentum conservation, and Equation (3) is a governing equation. In these equations ρ is the density, \mathbf{v} represents the particle velocity, $\boldsymbol{\sigma}$ is the stress tensor, \mathbf{f} represents the body forces, $\boldsymbol{\varepsilon}$ is a Levi-Civita tensor, \mathbf{C} is the elastic tensor, $\boldsymbol{\varepsilon}$ is the strain tensor and \otimes is a convolution operator (Mase & Mase, 1999). Now, if we assume that the medium is visco-acoustic, irrotational and compressible but the flow is approximately constant and wave propagation is only longitudinal and there are no shear waves, we can reduce the governing equation, Equation (3) to

$$\boldsymbol{\sigma}_{ij}(\mathbf{x}, t) = -p(\mathbf{x}, t) \delta_{ij} = \nabla \cdot \mathbf{u}(\mathbf{x}, t) \otimes M(\mathbf{x}, t) \delta_{ij}, \tag{4}$$

where $p(\mathbf{x}, t)$ is a pressure wave, $\mathbf{u}(\mathbf{x}, t)$ is the particle displacement, δ_{ij} is a Kronecker delta and $M(\mathbf{x}, t)$ is the time derivative of the elastic tensor often named complex bulk modulus (Fichtner, 2011). $M(\mathbf{x}, t)$ accounts for the elastic and dissipative properties of the media. Using Equation (4) one can obtain Hooke's law and combining Eqs. (2) and (3) one can get Newton's law.

$$p(\mathbf{x}, t) = -\nabla \cdot \mathbf{u}(\mathbf{x}, t) \otimes M(\mathbf{x}, t). \tag{5}$$

$$\left(\frac{\partial}{\partial t} + \gamma(\mathbf{x})\right) \mathbf{v} = \frac{1}{\rho(\mathbf{x})} (\nabla \cdot \boldsymbol{\sigma} + \mathbf{f}), \tag{6}$$

where $\gamma(\mathbf{x})$ is called the rate deformation function, such that it represents the temporal variation of the stress tensor and is related to the viscosity of the medium. It is an important term in the relation of energy stored and energy lost per cycle (Wang, 2009). Applying a Fourier transform to Equations (5) and (6) we have

$$-i\omega P(\omega, \mathbf{x}) = M(\omega, \mathbf{x}) \nabla \cdot \mathbf{V}(\omega, \mathbf{x}). \tag{7}$$

$$-i\omega \mathbf{V}(\omega, \mathbf{x}) = -\frac{b(\mathbf{x})}{\xi(\omega, \mathbf{x})} \nabla P(\omega, \mathbf{x}) + \frac{b(\mathbf{x})}{\xi(\omega, \mathbf{x})} \mathbf{F}(\omega, \mathbf{x}), \tag{8}$$

where $\xi(\omega, \mathbf{x}) = 1 - i\frac{\gamma(\mathbf{x})}{\omega}$ and $b(\mathbf{x}) = \frac{1}{\rho(\mathbf{x})}$. The propagation of waves in a visco-acoustic media presents both dissipation and dispersion. These effects are modeled using the damping functions. The complex bulk modulus must be related to $\xi(\omega, \mathbf{x})$ subject to the constraint that when no dissipation $M(\omega, \mathbf{x}) \rightarrow K(\omega, \mathbf{x})$, where $K(\omega, \mathbf{x})$ is an acoustic bulk modulus. So we define

$$M(\omega, \mathbf{x}) = K(\mathbf{x}) \alpha(\omega, \mathbf{x}) = K(\mathbf{x}) \frac{1}{\xi(\omega, \mathbf{x})}, \tag{9}$$

where $\alpha(\omega, \mathbf{x})$ is complex. To establish a relation between α and ξ we combine the Equations (7) and (8) in the homogeneous case, with $\rho = cte$, $c = cte$ and $\gamma = cte$. If $\alpha = \xi$ this reduces to the acoustic wave equation in frequency domain, but since $\alpha = \frac{1}{\xi}$ then the equation is recast as

$$(\tilde{k}^2 + \nabla^2)P = \nabla \cdot \mathbf{F}. \tag{10}$$

Equation (10) is the Helmholtz equation with complex coefficients, where \tilde{k} is called complex wavenumber. The real part of \tilde{k} is $\frac{\omega}{c}$, the conventional wavenumber, and the imaginary part $\frac{\gamma}{c}$ is the pseudo-wavenumber. This concept is applied in attenuation-dispersion models related to the quality factor Q .

Equation of propagation in a visco-acoustic medium

Then, the equation for wave propagation in the visco-acoustic media can be obtained combining Equations (7), (8) and (9) as

$$\frac{\omega^2 P(\omega, \mathbf{x})}{K(\mathbf{x})} + \frac{1}{\xi(\omega, \mathbf{x})} \nabla \cdot \left(\frac{b(\mathbf{x})}{\xi(\omega, \mathbf{x})} \nabla P(\omega, \mathbf{x}) \right) = \frac{1}{\xi(\omega, \mathbf{x})} \nabla \cdot \left(\frac{b(\mathbf{x})}{\xi(\omega, \mathbf{x})} \mathbf{F}(\omega, \mathbf{x}) \right). \tag{11}$$

In this situation we have the freedom to choose the way we model the attenuation, and one can then, for instance, use analytic models for this function (e.g. Wang, 2009). Wang (2009) present different models where they define the wavenumber as $k(\omega) = \frac{\omega}{c(\omega)} = \frac{\omega}{v(\omega)} - i\kappa(\omega)$, where $c(\omega)$ is the complex velocity, $v(\omega)$ the phase velocity and $\kappa(\omega)$ the attenuation wavenumber, rewriting in terms of ξ , it can be shown like

$$\xi(\omega, \mathbf{x}) \cong \frac{c}{v(\omega)} - i \frac{\kappa(\omega)c}{\omega} \approx 1 - i \frac{\kappa(\omega)c}{\omega},$$

where $v(\omega) \sim c$. According to this, in this work we present results using the modified Kolsky's model for attenuation-dispersion (Kolsky, 2003)

$$\kappa(\omega, \mathbf{x}) = \frac{|\omega|}{2Q(\mathbf{x})c(\mathbf{x})}; \quad \frac{1}{v(\omega, \mathbf{x})} = \frac{1}{c(\mathbf{x})} \left(1 - \frac{1}{\pi Q(\mathbf{x})} \ln \left| \frac{\omega}{\omega_h} \right| \right), \tag{12}$$

where ω_h is the highest possible seismic frequency, about 1000π Hz. Substituting Equations 12 in the last relation for $\xi(\omega, \mathbf{x})$, and considering that for values of Q and ω in the range of interest ($Q \in [30, 650]$, $\omega \in [2\pi, 1000\pi]$) the term $\frac{1}{\pi Q} \ln \left| \frac{\omega}{\omega_h} \right|$ vanishes (Wang, 2009), then the damping function can be simplified to

$$\xi(\omega, \mathbf{x}) \approx 1 - i \frac{1}{2Q(\mathbf{x})}, \tag{13}$$

which leads to a very simple model of attenuation that is only dependent on the Q factor that can enter as a new parameter in the model.

Numerical solution technique

In general, obtaining a solution of Equation (11) is not possible for arbitrary medium properties and boundaries. A natural approach is then to look for numerical solutions using e.g. finite-differences. Assuming a 2D problem with coordinates (x, z) the problem can be re-written as

$$-i\omega P(\omega, \mathbf{x}) = K(\mathbf{x}) \frac{1}{\xi(\omega, \mathbf{x})} \left(\frac{\partial V_x(\omega, \mathbf{x})}{\partial x} + \frac{\partial V_z(\omega, \mathbf{x})}{\partial z} \right), \tag{14}$$

$$-i\omega V_x(\omega, \mathbf{x}) = -\frac{b(\mathbf{x})}{\xi(\omega, \mathbf{x})} \frac{\partial P(\omega, \mathbf{x})}{\partial x} + S_x(\omega, \mathbf{x}), \tag{15}$$

$$-i\omega V_z(\omega, \mathbf{x}) = -\frac{b(\mathbf{x})}{\xi(\omega, \mathbf{x})} \frac{\partial P(\omega, \mathbf{x})}{\partial z} + S_z(\omega, \mathbf{x}), \tag{16}$$

where $S_x(\omega, \mathbf{x}) = \nabla \cdot \left(\frac{b(\mathbf{x})}{\xi(\omega, \mathbf{x})} F_x(\omega, \mathbf{x}) \right)$ and $S_z(\omega, \mathbf{x}) = \nabla \cdot \left(\frac{b(\mathbf{x})}{\xi(\omega, \mathbf{x})} F_z(\omega, \mathbf{x}) \right)$. Although the finite-difference method is widely used for solving differential equations, it has very well known problems of numerical dispersion that are related to the discretization of the media. Jo (1996) propose a scheme of two overlapping grids to solve the PDE aimed to avoid these numerical dispersion problems. Although Jo (1996) presents its method for the solution of acoustic problems, we go a step further and implement the ideas for the solution of our problem of the visco-acoustic wave equation. In Jo (1996), one of the grids is a horizontally oriented cartesian grid, while the second one is a rotated cartesian grid (see Fig. 1). In this kind of setup, the solution is obtained evaluating the fields in a total of 9 grid points, thus reducing the numerical dispersion and trying to cover all directions of propagation.

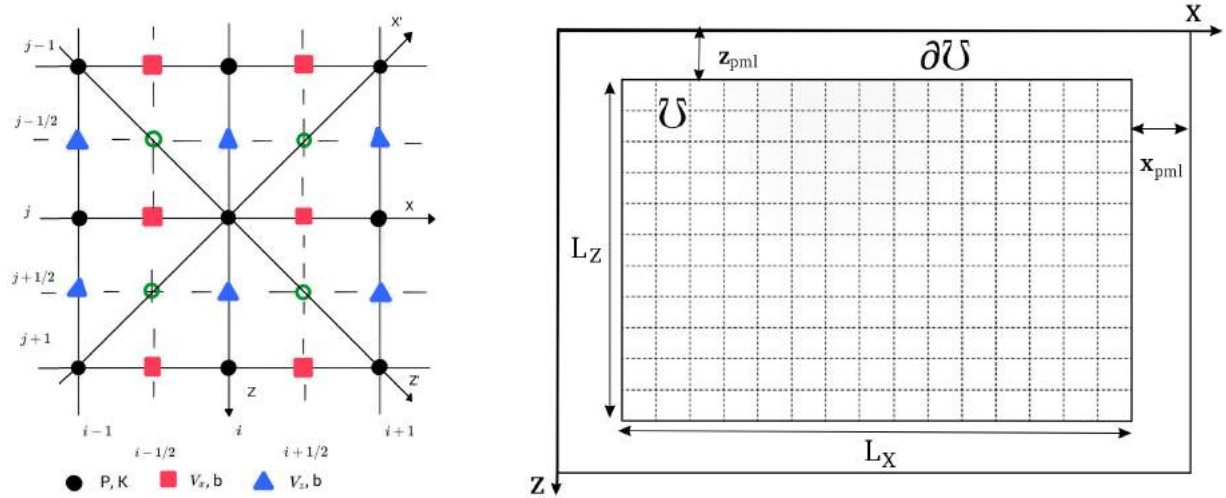


Figure 1 – (Left) Illustration of the mixed-grid used in the numerical solution. The black points represent the field pressure in the conventional grid, the triangular and square symbols represent the field particle velocity in the intercalated grid, the diagonals represent the axes for the rotated grid. The partial derivatives are computed for points in conventional grid and rotated grid, in total 9 points. (Right) Workspace \mathcal{U} and boundary workspace $\partial\mathcal{U}$ for the numerical solution.

Mixed-Grid and Lumped Mass strategy

Then, using centered finite-differences for partial derivatives, in the conventional grid, the derivatives of the function $\mathbf{V}(\mathbf{x}, \omega)$ and $P(\mathbf{x}, \omega)$ are expressed as

$$\frac{\partial V_x}{\partial x} \Big|_{(i,j)} \approx \frac{1}{\Delta} (V_{x(i+1/2,j)} - V_{x(i-1/2,j)}), \quad \frac{\partial V_z}{\partial z} \Big|_{(i,j)} \approx \frac{1}{\Delta} (V_{z(i,j+1/2)} - V_{z(i,j-1/2)}). \tag{17}$$

$$\frac{\partial P}{\partial x} \Big|_{(i\pm 1/2,j)} \approx \frac{1}{\Delta} (\pm P_{(i\pm 1,j)} \mp P_{(i,j)}), \quad \frac{\partial P}{\partial z} \Big|_{(i,j\pm 1/2)} \approx \frac{1}{\Delta} (\pm P_{(i,j\pm 1)} \mp P_{(i,j)}), \tag{18}$$

where Δ is the grid spacing. Now, for the rotated grid, using a rotation of 45° , we obtain the transformation rule for the derivatives in that system such that centered finite-differences of partial derivatives, in the rotated grid of $\mathbf{V}(\mathbf{x}, \omega)$ and $P(\mathbf{x}, \omega)$ are

$$\frac{\partial V_x}{\partial x'} \Big|_{(i,j)} \approx \frac{1}{\sqrt{2}\Delta} (V_{x(i+1/2,j-1/2)} - V_{x(i-1/2,j+1/2)}), \tag{19}$$

$$\frac{\partial V_z}{\partial z'} \Big|_{(i,j)} \approx \frac{1}{\sqrt{2}\Delta} (V_{z(i+1/2,j+1/2)} - V_{z(i-1/2,j-1/2)}). \tag{20}$$

$$\frac{\partial P}{\partial x'} \Big|_{(i\pm 1/2,j\mp 1/2)} \approx \frac{1}{\sqrt{2}\Delta} (\pm P_{(i\pm 1,j\mp 1)} \mp P_{(i,j)}), \tag{21}$$

$$\frac{\partial P}{\partial z'} \Big|_{(i\pm 1/2, j\pm 1/2)} \approx \frac{1}{\sqrt{2}\Delta} (\pm P_{(i\pm 1, j\pm 1)} \mp P_{(i, j)}). \tag{22}$$

To improve the accuracy of the mixed-grid stencil the pressure acceleration term $\frac{\omega^2 P(\omega, \mathbf{x})}{K(\mathbf{x})}$ may not be taken as a term implying only the collocation point (the so-called lumped approximation). The implementation of the mixed-grid aims to reduce the numerical dispersion taking 9 points to find the values of the derivatives, if the free term $\frac{\omega^2 P(\omega, \mathbf{x})}{K(\mathbf{x})}$ takes only the value at point (i, j) , $P_{i,j}$, the contribution of the rotated grid will not be considered and the homogeneity of the solution will be lost to some degree (Operto & Virieux, 2006) and the effort of using a rotated grid may be wasted.

In order to solve this issue we may approximate this term by using a weighted average over the mixed operator stencil nodes, in a similar way as it is done in finite-element modeling (see e.g. Marfurt, 1984 or Strikwerda, 2007). Then in this situation the lumped mass term shall take the form

$$\frac{\omega^2 P(\omega, \mathbf{x})}{K(\mathbf{x})} \Big|_{(i, j)} = \frac{\omega^2}{K_{(i, j)}} \left(m_2 \Sigma_{1(i, j)} P + \frac{m_4}{4} \Sigma_{2(i, j)} P \right), \tag{23}$$

with $\Sigma_{1(i, j)} P = \frac{1}{4}(P_{i+1, j} + P_{i-1, j} + P_{i, j+1} + P_{i, j-1})$, $\Sigma_{2(i, j)} P = \frac{1}{4}(P_{i+1, j-1} + P_{i-1, j-1} + P_{i-1, j+1} + P_{i+1, j+1})$ and $m_4 = 1 - m_2 + 4m_3$, where m_2 and m_3 are coefficients regulating the relation between the contribution of the terms by the conventional and rotated grid in the lumped mass term. The other terms in the conventional grid and in the rotated grid are given by

$$\frac{1}{\xi(\omega, \mathbf{x})} \nabla \cdot \left(\frac{b(\mathbf{x})}{\xi(\omega, \mathbf{x})} \nabla P(\omega, \mathbf{x}) \right) \Big|_{(i, j)} = \Gamma_{(i, j)} P, \quad \frac{1}{\xi(\omega, \mathbf{x})} \nabla' \cdot \left(\frac{b(\mathbf{x})}{\xi(\omega, \mathbf{x})} \nabla' P(\omega, \mathbf{x}) \right) \Big|_{(i, j)} = \Theta_{(i, j)} P, \tag{24}$$

where the notation ∇' stands for derivatives in the rotated system. Then, the final version of the discretization of Equation (12) is

$$m_1 \Gamma_{(i, j)} P + (1 - m_1) \Theta_{(i, j)} P + \frac{\omega^2}{K_{(i, j)}} \left(m_2 \Sigma_{1(i, j)} P + \frac{m_4}{4} \Sigma_{2(i, j)} P \right) = S(\omega, \mathbf{x}) \Big|_{(i, j)}, \tag{25}$$

where m_1 is a coefficient regulating the relation between the contribution of the terms by the conventional and rotated grid but in the remaining divergence terms in Equation (11).

As it is well known, one of the advantages of the solution of the problem of wave propagation in frequency domain is that at the end, the problem can be formulated as a linear problem for each single frequency ω . In our case, that linear problem shall have the form $\mathbf{A} \mathbf{p} = \mathbf{s}$, where the matrix \mathbf{A} is given by

$$\begin{aligned} A_{(m, n)} = & D_{(m)} \delta_{m, n} + D1_{(m)} \delta_{m, n+N_z} + D2_{(m)} \delta_{m, n-N_z} + D3_{(m)} \delta_{m, n+1} \\ & + D4_{(m)} \delta_{m, n-1} + D5_{(m)} \delta_{m, n+N_z-1} + D6_{(m)} \delta_{m, n-N_z+1} + D7_{(m)} \delta_{m, n+N_z+1} \\ & + D8_{(m)} \delta_{m, n-N_z-1}, \end{aligned} \tag{26}$$

with the coefficients $Dl_{(i, j)}$, for $l = 0, 1, 2, \dots, 8$, $m = iN_z + j$, $i = 0, 1, 2, \dots, N_x - 1$ and $j = 0, 1, 2, \dots, N_z - 1$ given by

$$\begin{aligned} Dl_{(i, j)} = & \frac{\omega^2}{K_{i, j}} A_l(m_2, m_3, m_4) + B_l(\eta_{x(i, j)}^\pm, \eta_{z(i, j)}^\pm) m_1 \\ & + C_l(\eta_{x1(i, j)}^\pm, \eta_{x2(i, j)}^\pm, \eta_{z1(i, j)}^\pm, \eta_{z2(i, j)}^\pm) (1 - m_1), \end{aligned} \tag{27}$$

where the functions A_l , B_l and C_l can be seen explicitly in Avendaño (2017) and terms η have the form

$$\eta_{x(i, j)}^\pm = \frac{1}{\xi_{(i, j)}} \frac{1}{\Delta^2} \frac{b_{(i\pm 1/2, j)}}{\xi_{(i\pm 1/2, j)}}, \quad \eta_{z(i, j)}^\pm = \frac{1}{\xi_{(i, j)}} \frac{1}{\Delta^2} \frac{b_{(i, j\pm 1/2)}}{\xi_{(i, j\pm 1/2)}}, \tag{28}$$

$$\eta_{x1(i, j)}^\pm = \frac{1}{\xi_{(i, j)}} \frac{1}{4\Delta^2} \frac{b_{(i\pm 1/2, j\mp 1/2)}}{\xi_{(i\pm 1/2, j)}}; \quad \eta_{z1(i, j)}^\pm = \frac{1}{\xi_{(i, j)}} \frac{1}{4\Delta^2} \frac{b_{(i\pm 1/2, j\mp 1/2)}}{\xi_{(i, j\mp 1/2)}}, \tag{29}$$

$$\eta_{x2(i, j)}^\pm = \frac{1}{\xi_{(i, j)}} \frac{1}{4\Delta^2} \frac{b_{(i\pm 1/2, j\pm 1/2)}}{\xi_{(i\pm 1/2, j)}}; \quad \eta_{z2(i, j)}^\pm = \frac{1}{\xi_{(i, j)}} \frac{1}{4\Delta^2} \frac{b_{(i\pm 1/2, j\pm 1/2)}}{\xi_{(i, j\pm 1/2)}}. \tag{30}$$

This matrix is sparse, indefinite, complex and square. The vector s in this linear problem is the source vector discretized around the coordinates (x_s, z_s) . For cases when the velocity, density and attenuation are not constant we propose that the source should have the form

$$S_{(i,j)} = \frac{b_{(i,j)}}{\xi_{(i,j)}^2} R_0 \frac{2}{\sqrt{\pi}} \frac{f^2}{f_s^3} e^{-\frac{f^2}{f_s^2}} \delta_{i,i_s} \delta_{j,j_s}, \quad (31)$$

where R_0 is the maximum amplitude of the Ricker wavelet, f_s the source frequency, (i_s, j_s) is a point in the grid where the source is placed and $\delta_{i,i_s} \delta_{j,j_s}$ can be approximated as

$$\delta_{i,i_s} \delta_{j,j_s} \approx \frac{1}{\pi \sigma_x \sigma_z} e^{-\left(\frac{x_i - x_s}{\sigma_x}\right)^2} e^{-\left(\frac{z_j - z_s}{\sigma_z}\right)^2}. \quad (32)$$

This definition comes from the Dirac delta function as the limit of the sequence of zero-centered normal distributions $\delta_\sigma(x) = \frac{1}{\sqrt{\pi}\sigma} \exp\left(-\frac{x^2}{\sigma^2}\right)$ as $\sigma \rightarrow 0$. The factor σ must have a relationship with the grid spacing Δ , i.e. $\sigma_x = \sigma_z = s\Delta$, where $s \in [0.75, 1.0]$ (see Avendaño, 2017). Finding \mathbf{p} as the solution to the problem stated in equation $\mathbf{A}\mathbf{p} = \mathbf{s}$ is equivalent to solve the system of Equations (11).

Dispersion Analysis

As it is clear from the use of finite-differences, the numerical solution requires a discretization to represent the physical domain that in our case is implemented in a regular mesh which has both a finite physical extent and finite number of mesh points. However, the number of points per unit wavelength that the approximate field encounters is not the same in every direction, and this artificial artifact due to the discreteness adds to the numerical dispersion of the solution. Clearly, this is not a problem that can be ignored. Since the solution is not exact, there is already an error on the approach, if we add this harmful effect to the solution, we will have, specially at long wavelengths, an inappropriate estimate of the solution due to the undersampling where long wavelengths are not sampled at high enough spatial frequencies to provide a trustable solution at those wavelengths (Deraemaeker & Bouillard, 1999; Ospina, 2016).

In this part we will make use of the know behavior of the problem of wave propagation in a homogeneous media (Eq. 10). In this case for constant velocity, density and attenuation in a media without source we have that the wave equation (Eq. 10) may be written as

$$(\nabla^2 + \tilde{k}^2)P(x_i, z_j) \approx m_1 \Gamma_{(i,j)} P + (1 - m_1) \Theta_{(i,j)} P + \Phi(m_2, m_3)_{(i,j)} P = 0, \quad (33)$$

where m_1, m_2, m_3 are parameters that can be found by minimizing the dispersion of the solution. To do so, remember that in this case ρ and c have a constant value, then the problem has an analytic solution given by $P(\mathbf{r}) = P_0 e^{-i(\tilde{\mathbf{k}} \cdot \mathbf{r})}$. Where $\tilde{\mathbf{k}}$ is a complex wave vector and \mathbf{r} is the position vector. Now, If we introduce the solution into the numerical scheme in Equation (33), we see that the numeric complex wavenumber can be written as the ratio of two functions A and B depending on the number of points per wavelength, G_r , and wave propagation angle θ (see Jo, 1996; Ospina, 2016) as

$$\tilde{k}^2 = \frac{1}{\Delta^2} \frac{A(\tau_r, \tau_i, \theta)}{B(\tau_r, \tau_i, \theta)}, \quad (34)$$

where $\tau_r = \frac{1}{G_r}$ is the number of wavelengths per grid point. The same relation holds for the pseudo grid number for pseudo wavelength G_i and $\tau_i = \frac{1}{G_i}$. With this notation, the relation between the complex wavenumber, complex wavelength and complex grid number is $\tilde{k} = \frac{\omega}{c} + i\frac{\gamma}{c}$; $\tilde{\lambda} = \Delta G_r + i\Delta G_i$; $\tilde{k} = \frac{2\pi}{\Delta G_r} + i\frac{2\pi}{\Delta G_i}$.

Taking the square root of Equation (34), dividing by the theoretical estimate of \tilde{k} , \tilde{k}^T and separating in to real and imaginary parts one gets

$$N(\tau_r, \tau_i, \theta) = \frac{k_r^N}{k_r^T} = \frac{1}{2\pi\tau_r} \Re \left(\sqrt{\frac{A}{B}} \right); \quad M(\tau_r, \tau_i, \theta) = \frac{k_i^N}{k_i^T} = \frac{1}{2\pi\tau_i} \Im \left(\sqrt{\frac{A}{B}} \right). \quad (35)$$

Then, our objective function is

$$\chi(m_1, m_2, m_3) = \int \int \int [(1 - N(\tau_r, \tau_i, \theta))^2 + (1 - M(\tau_r, \tau_i, \theta))^2] d\theta d\tau_r d\tau_i, \quad (36)$$

which we try to minimize in the range of values $\theta \in [0, \pi/2]$ and $\tau_r, \tau_i \in [0.001, 0.15]$ for the parameters m_1, m_2 and m_3 (Chen, 2004). The values of the parameters that minimize the dispersion are then $m_1 = 0.6667, m_2 = 0.6556, m_3 = 0.0889$. It is important to mention that when there is no attenuation, we get the same result presented in other works $m_1 = 0.5461, m_2 = 0.6248, m_3 = 0.09381$ (Jo, 1996). Also using the values $m_1 = 1.0, m_2 = 1.0, m_3 = 0.0$ we can recover the usual 5-point scheme.

To study the difference between the numerical dispersion produced by the scheme of 9-point and the scheme of 5-point, we plot in Figures 2 and 3 the relation between the theoretical and numeric wavenumbers for the real and imaginary parts, k_r^N/k_r^T and k_i^N/k_i^T . We use the optimum values found in the minimization, and plot the behavior for different propagation angles, $\theta = 0, \frac{\pi}{12}, \frac{\pi}{6}, \frac{\pi}{4}$ in the Equation (35). We calculate $M(\tau_r, \tau_i, \theta)$ for $\tau_r = 0.142857$, and $\tau_i \in [0.001, 0.15]$, and calculate $N(\tau_r, \tau_i, \theta)$ for $\tau_i = 0.020$ and $\tau_r \in [0.001, 0.15]$.

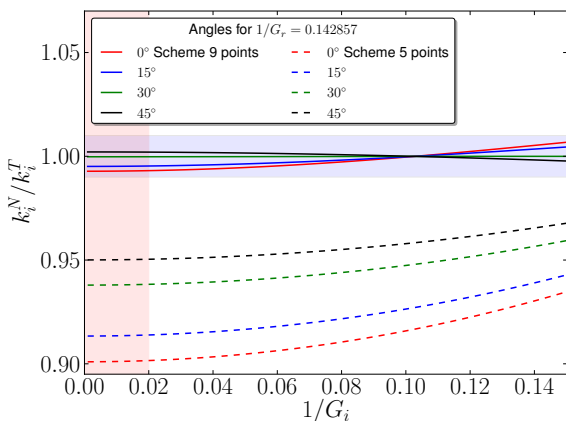


Figure 2 – Ratio between the imaginary part of theoretical and numerical wavenumber for $1/G_r = 0.142857$.

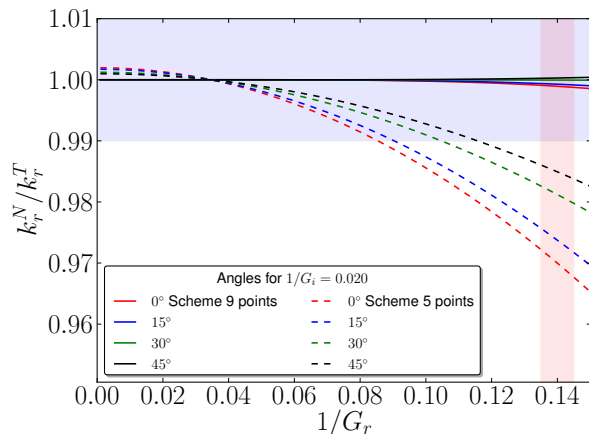


Figure 3 – Ratio between the real part of theoretical and numerical wavenumber for $1/G_i = 0.020$.

To understand this figure, remember that the closer these ratios are to 1, the lower the numerical dispersion is and better the quality of the solution. The solid lines show the ratio computed for the scheme of 9-point while dashed lines show the ratio estimated for the 5-point scheme. The different lines for each scheme (different color lines) show the result for different propagation angles θ .

Now, looking at the attenuation model discussed in Equation (13) one can show that for the value of the parameters used in this work and the physical conditions we explore, it will always be the case that $\lambda_i > \lambda_r$, then we always choose the approach to make Δ as a function of the wavelength and not of pseudo wavelength.

If $\tau_r = 1/7$ (see Fig. 2), for any value of τ_i , the dispersion is smaller for the 9-point scheme as the blue/horizontal highlighted region shows. Of course, if we choose the same Δ the expected values for τ_r are in the range $[0, 0.02]$ when the dispersion is smaller as the red/vertical highlighted region shows. If $\tau_i = 0.02$ (see Fig.3), for any value of τ_r , the dispersion is smaller for the 9-point scheme as the blue/horizontal highlighted region shows, especially in the region $\tau_r \in [0.135, 0.145]$ (red/vertical highlighted region). Now, according to the above, we define the cell size $\Delta = \frac{\lambda}{G_r} = \frac{c_{min}}{fG_r}$. Where $G_r = 7, c_{min}$ is the lower wave velocity and f is the frequency.

Perfectly-matched layer (PML) absorbing boundary conditions

An important ingredient of the numerical solution are the boundary conditions. Since numerical solutions are constrained to a finite computational area (2D problem), border effects may introduce artificial boundaries or reflectors that are not real physical objects in the field. In order to account for these effects, the propagation of waves leaving the computational domain (the workspace) have to be considered with special care. Let us name our workspace as the region \mathcal{U} such that $\mathcal{U} = \{(x, z) \in \mathfrak{R}^2 : x \in [x_{pml}, L_x + x_{pml}] \wedge z \in [z_{pml}, L_z + z_{pml}]\}$. \mathcal{U} represents the region of the space where we are interested in to study the propagation of waves. And we extend the workspace with $\partial\mathcal{U} = \{(x, z) \in \mathfrak{R}^2 : x \in [0, L_x + 2x_{pml}] \wedge z \in [0, L_z + 2z_{pml}] \wedge (x, z) \notin \mathcal{U}\}$ and use Perfectly-Matched-Absorbing layer (PML) boundary conditions (Berenger, 1994) (see Fig. 1) to solve for the propagation of waves in this extended region. This boundary conditions in frequency domain uses two damping functions ξ_x and ξ_z which are related to ξ .

In the expanded region, the damping functions have the form Operto & Virieux (2006)

$$\xi_x(\omega, \mathbf{x}) = \begin{cases} 1 + i \left[\frac{m_0 \gamma_{pml}}{\omega} \right] & \text{if } x < x_{pml} \quad \text{or} \quad x > x_{pml} + L_x \\ \xi(\omega, \mathbf{x}) & \text{if } x_{pml} < x < L_x + x_{pml} \end{cases}, \quad (37)$$

$$\gamma_{x_{pml}}(\omega, \mathbf{x}) = \begin{cases} \cos\left(\frac{x}{x_{pml}} \frac{\pi}{2}\right) + \gamma(\omega, x_{pml}, z) & \text{if } x < x_{pml} \\ 1 - \cos\left(\frac{x - L_x - x_{pml}}{x_{pml}} \frac{\pi}{2}\right) + \gamma(\omega, L_x, z) & \text{if } x > x_{pml} + L_x \end{cases}, \quad (38)$$

where m_0 is a parameter that changes with frequency and takes a value that makes the amplitude of the wave at the boundary of the domain to fall below a given threshold (Avendaño, 2017). The PML for z is defined in a similar way.

RESULTS

Once defined the optimal parameters for the discretization, we can model the propagation a P-wave in media with different velocity profiles and verify the performance of the numerical approach we propose. As a first test we model a Ricker pulse propagating in a medium with constant velocity, density and attenuation. The goal of this test is to compare with the solution of the Helmholtz equation with source that for this special case can be obtained analytically. Then we did several tests with different velocity profiles, the density in these cases, was calculated following the relation (Mavko et al., 2009)

$$\rho(\mathbf{x}) = \begin{cases} \sum_{i=1}^5 a_i c(\mathbf{x})^i \text{ Kg/m}^3 & \text{if } c(\mathbf{x}) > 1480 \text{m/s} \\ 1050 \text{ Kg/m}^3 & \text{if } c(\mathbf{x}) < 1480 \text{m/s} \end{cases} \quad (39)$$

where the constant parameters are $a_1 = 1.1 \times 10^{-16}$, $a_2 = -4.3 \times 10^{-12}$, $a_3 = 6.7 \times 10^{-8}$, $a_4 = -4.7 \times 10^{-4}$ and $a_5 = 1.66$. Besides this, the values for the quality factor associated with the different values of the velocity in the multiple layer media are modeled according to Lavergne (1986)

Constant density, velocity, and attenuation

In frequency domain, the Helmholtz equation with sources (Eq. 10) has an analytic solution given by Chen (2004)

$$P(\omega, \mathbf{x}, \gamma) = i\pi H_0^{(2)} \left(\frac{\omega - i\gamma}{c} r \right) S(\omega, \gamma), \quad (40)$$

where $S(\omega, \gamma)$ is a source, r accounts for the distance between the source and any point with coordinates (x, z) and is given by $r^2 = (x - x_s)^2 + (z - z_s)^2$. With x_s and z_s the position of source.

In order to compare the results of this analytic solution with results obtained with the 9-point and 5-point schemes, we compute the value of the P-wave amplitude in an area of $2\text{km} \times 2\text{km}$ by placing a line of receivers at 100 m depth and a second line of receivers and 1100 m depth, finding the waveform response in those points. For this experiment the constant velocity of the media is 2100 m/s, the Ricker frequency is 30 Hz, the constant quality factor is $Q = 50$ using the damping function shown in Equation (13), the cell size Ω is λ/G_r , where $G_r = 7$. The position of the source is $x_0 = 1\text{km}$ and $z_0 = 1\text{km}$.

In Figures 4 and 5 we show the normalized amplitude of the P-wave (real part) as a function of the offset for shots in the receivers at 1100 m depth and receivers at 100 m depth, respectively. They also show the difference between P-wave found by the analytic solution and 9-point scheme and 5-point scheme, at three different frequencies. Amplitudes are normalized dividing by its maximum value. In these figures the solid line is the analytic solution, the dashed line is the solution for the 5-point scheme and the dotted line is the solution for 9-point scheme. It is worth to note that for all frequencies the solution obtained by the 9-point scheme is the closest to the analytic solution.

One can also see the strong disagreement of the solution obtained with the 5-point scheme compared to the analytic one, this can be seen especially at P-waves away from the source. This is due mainly to numerical dispersion and grid point number, for 5-point scheme (see Fig. 1) for $\tau_r = 0.142857$ the relation between k_r^N/k_r^T is about 0.95 and k_i^N/k_i^T is about 0.98, when the optimal value is close to 1.0. The dispersion for P-waves away from the source is more noticeable because the effect of pollution propagates with distance from the source, the numerical dispersion makes the P-wave to be out of phase.

In order to avoid such dispersion in the solution for the 5-point scheme, we would have to use a larger amount of points (Jo, 1996) and that would mean a larger computational cost. In that sense we can conclude that the scheme of 9-point provides an appropriate solution at an acceptable computational cost.

Media with three layers velocity profile

The next test is performed with a different velocity profile and is performed in order to study the behavior of the solution in media with interfaces. In this experiment the P-wave field is computed in a media configured as the superposition of three parallel layers and all solutions are shown for the 9-point scheme.

In Figure 6 we show the real, imaginary parts and modulus of the P-wave field for frequency 5 Hz. At that low frequency regime, the reflectors are not well defined due to the fact that the wavelength is too big compared with the features and the scale of the discretization, and one can not define the exact position of the reflectors or anomalies at scales smaller than the wavelength of the perturbation, however the oscillation is uniform.

In Figures 7 and 8, we show the same for frequencies of 25 Hz and 50 Hz respectively. Note that increasing the frequency the reflectors become more evident, but given that the gradient of the velocity is smooth there is continuity in the propagation of waves, as expected if we had relatively continuous profiles.

Media with variable velocity, density and attenuation

For this final test we decided to use a complex velocity profile. As it can be seen in Figure 9, in this case we have several wedge and important discontinuities with velocity contrast ranging from 1.0 to 3.0. For this setup the source is close to the surface at 15 m depth and again only the solutions with the 9-point scheme are shown.

In Figures 10, 11 and 12, we show the real and imaginary parts and modulus of the P-wave field for frequencies of 5, 25 and 50 Hz. The result is less uniform than in the previous figures, revealing a natural response to the anisotropy of the velocity field. One can see how the features of the velocity field can distort the wavefront, even at large distances. Numerical dispersion have been minimized, so most of what can be seen is real response of the wave propagating inside the complex media.

DISCUSSION AND CONCLUSIONS

In this work we have studied the propagation of waves in a visco-acoustic medium through explicit modeling of the attenuation making use of damping functions that allow for dispersion that depends on the quality factor Q . We have implemented a finite-difference

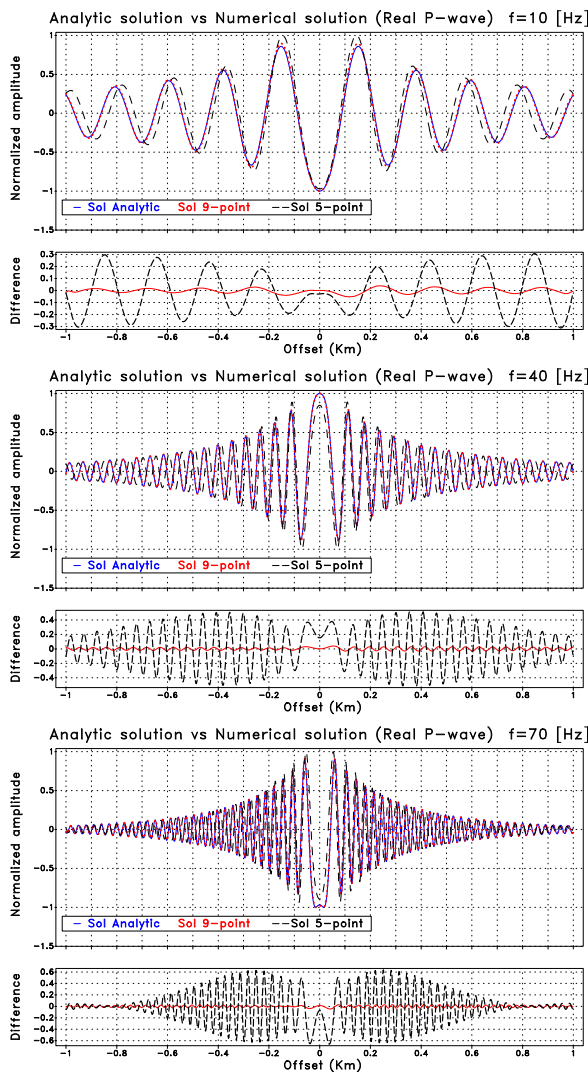


Figure 4 – Shots (real part) propagating in medium with constant velocity, density and attenuation for $f = 10, 40, 70$ Hz and receivers in $z = 1100$ m depth (close to the source in $z = 1000$ m). The bottom panels show the difference of the 9-point (red) and 5-point (black) schemes against the exact solution.

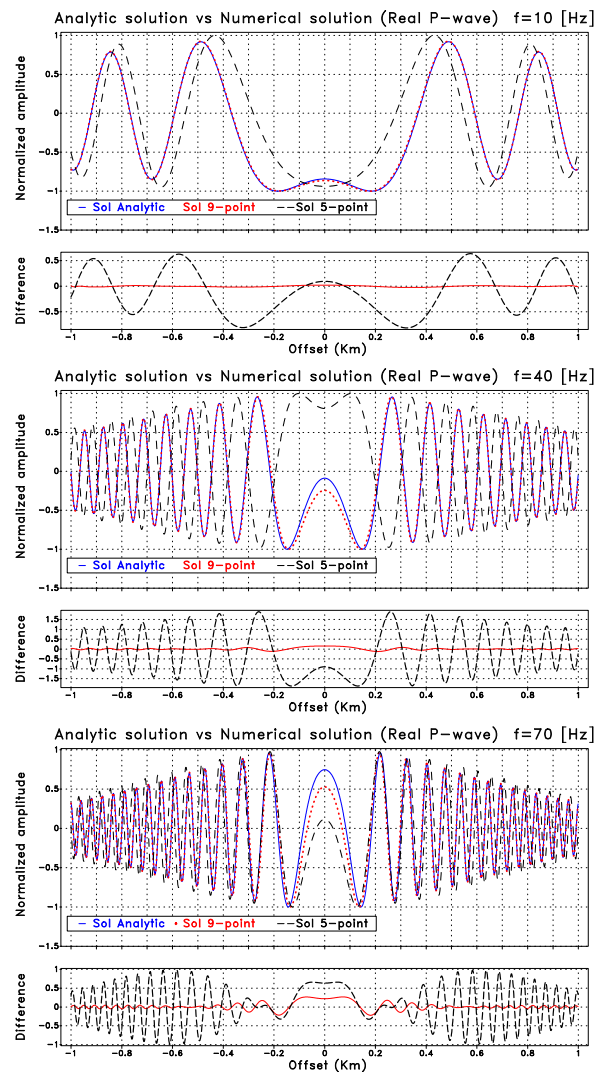


Figure 5 – Shots (real part) propagating in medium with constant velocity, density and attenuation for $f = 10, 40, 70$ Hz and receivers in $z = 100$ m depth (away from the source in $z = 1000$ m). The bottom panels show the difference of the 9-point (red) and 5-point (black) schemes against the exact solution.

scheme to solve the problem in frequency domain. Special care have been taken on the harmful numerical dispersion issues of the modeling, for which we have used a mixed-grid technique and optimal setup of the intercalated grids to minimize numeric dispersion.

We have shown the ability of the optimization scheme to minimize the numerical dispersion for the visco-acoustic case, and show that indeed the mixed-grid scheme (9-point) with the optimization scheme provides solutions that are very much close to the real solution than the solutions obtained for the classic 5-point scheme. Comparison of the numeric scheme with the analytic solution obtained for the case of wave propagation in a homogeneous medium has shown the advantages of the optimized mixed-grid scheme. As it was shown in Figures 1 and 5, the optimized 9-point mixed-grid scheme provides solutions that are in general a few percent away from the analytic solution, while the standard 5-point scheme deviates notoriously from the analytic solution even for this simplistic case.

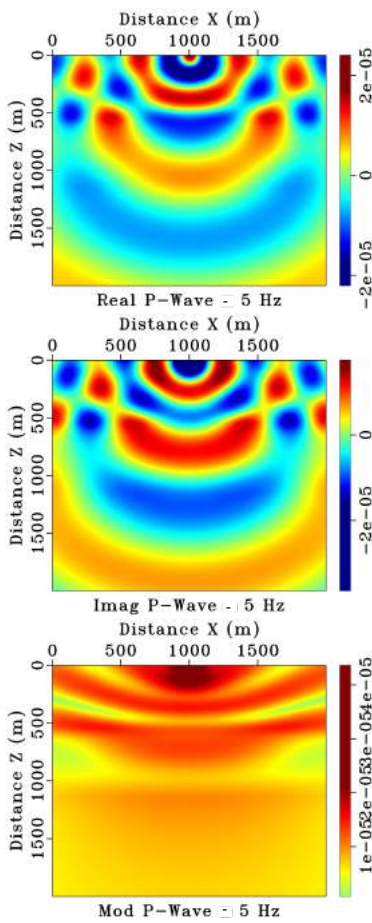


Figure 6 – Real, imaginary part and module at P-wave for 5 Hz with velocity field with three parallel layers ($v_1 = 2100$ in $[0, 0.6]$ km, $v_2 = 4300$ m/s in $(0.6, 1.2]$ km and $v_3 = 6500$ m/s in $(1.2, 2.0]$ km) The source is close to the surface at 15 m.

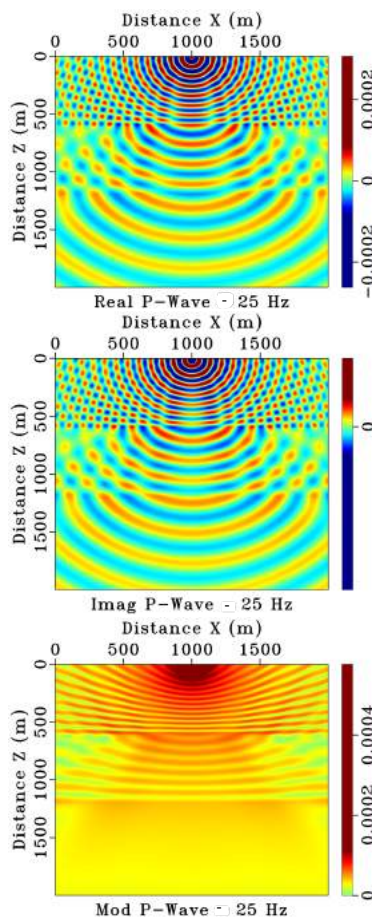


Figure 7 – Real, imaginary part and module at P-wave for 25 Hz with velocity field with three parallel layers ($v_1 = 2100$ in $[0, 0.6]$ km, $v_2 = 4300$ m/s in $(0.6, 1.2]$ km and $v_3 = 6500$ m/s in $(1.2, 2.0]$ km) The source is close to the surface at 15 m.

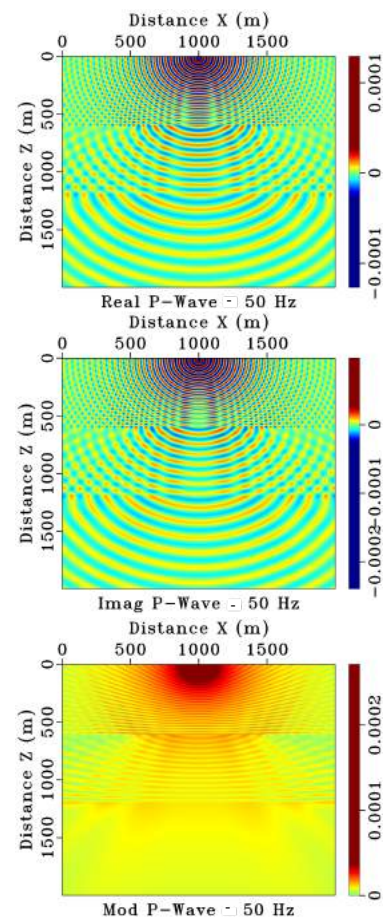


Figure 8 – Real, imaginary part and module at P-wave for 50 Hz with velocity field with three parallel layers ($v_1 = 2100$ in $[0, 0.6]$ km, $v_2 = 4300$ m/s in $(0.6, 1.2]$ km and $v_3 = 6500$ m/s in $(1.2, 2.0]$ km) The source is close to the surface at 15 m.

We have also shown that this modeling works quite well in models of high velocity/density contrast, commonly found in nature. We have shown that the explicit modeling of attenuation allows to model easily the superposition of complex velocity fields and to resolve properly the behavior of waves in such scenarios. Although in this work we have focused in the results of the application of Kolski’s model, we have verified the behavior of the method for other well known attenuation-dispersion models (Cole-Cole and general models; Wang, 2009), and in particular noticed the clear difference between the attenuation of the amplitude of the wavefront due to the distribution of energy in the expanding wavefront and the extra attenuation introduced by the damping functions.

This kind of behavior has a notorious importance for methods like FWI. In the case of seismic exploration, sub-surface information can be obtained through the use of Full Waveform Inversion. The quality of the information acquired through the inversion is of course dependent on the ability of the model to approach the physical properties of the medium. Visco-acoustic modeling represents a compromise between simplicity and realism that offers good results in the FWI technique, so, this kind of modeling has very promising impact in such procedures. In particular, given the iterative nature of FWI, the use of optimized mixed-grid technique ensures the quality of the solution at reasonable computational cost. Another potential use is that an appropriated modeling of the attenuation may lead to better compensation for correct processing in e.g. RTM migration.

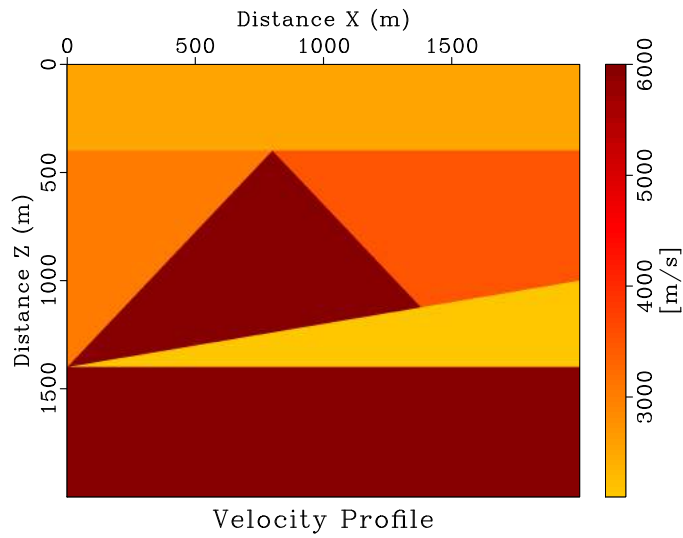


Figure 9 – Geometric configuration of the velocity profile.

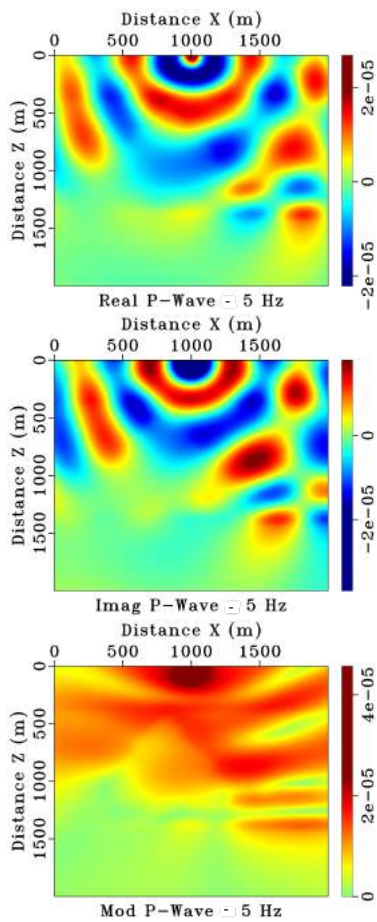


Figure 10 – Real, imaginary part and module at P-wave field for 5 Hz.

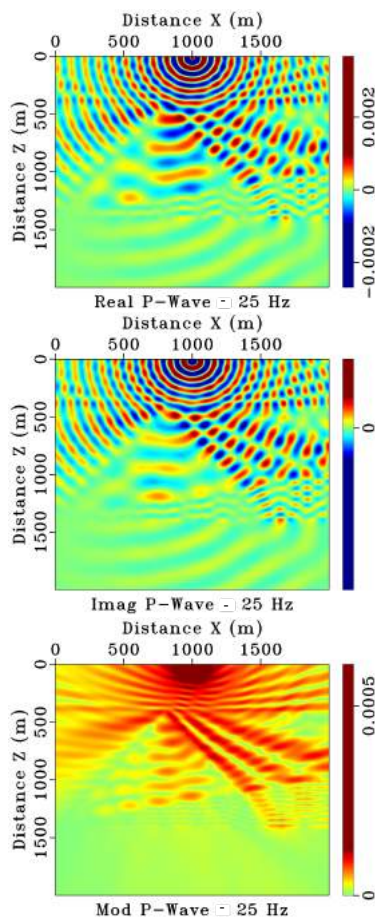


Figure 11 – Real, imaginary part and module at P-wave field for 25 Hz.

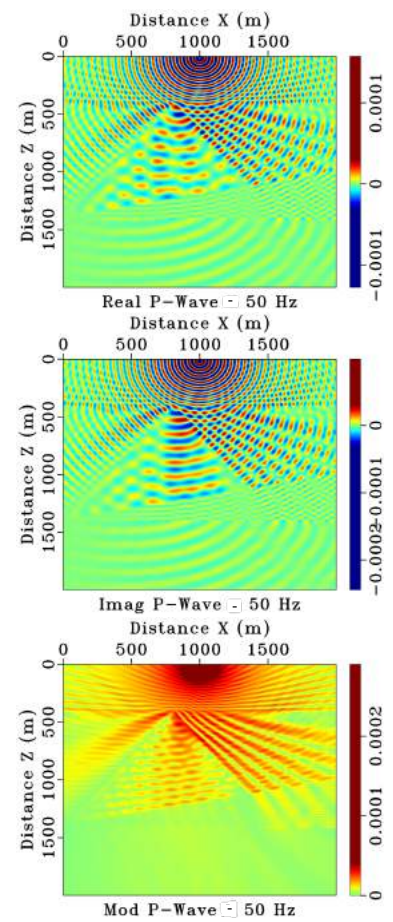


Figure 12 – Real, imaginary part and module at P-wave field for 50 Hz.

ACKNOWLEDGMENTS

This work is supported by Colombian Oil Company (ECOPETROL) and COLCIENCIAS as a part of the research project grant No. 0266-2013. JCMC wants to thank to “Estrategia de sostenibilidad, Universidad de Antioquia”. The authors want to acknowledge the anonymous referees for their observations to the document.

REFERENCES

- AVENDAÑO SK. 2017. Full Waveform Inversion (FWI) in frequency Domain for the wave propagation for Visco-acoustic medium applied in synthetic data. Master dissertation. Physics. Universidad de Antioquia. Available on: <http://www.udea.edu.co/wps/wcm/connect/udea/a429bbe8-369a-4b0c-8225-e29978fa195c/Informe_vsmall.pdf?MOD=AJPERES&CVID=mDQYHxx>. Access on: June, 2017, 129 pp.
- BERENGER JP. 1994. A perfectly matched layer for the absorption of electromagnetic waves. *Journal of Computational Physics*, 114: 185-200.
- CARCIONE JM, HERMAN GC & KROODE AT. 2002. Seismic modeling. *Geophysics*, 67: 1304-1325.
- CHEN JB. 2004. Laplace-Fourier-domain dispersion analysis of an average derivative optimal scheme for scalar-wave equation. *Geophys. J. Int.*, 197: 1681-1692.
- DERAEMAERKER A BABUSKA I & BOUILLARD P. 1999. Dispersion and pollution of the FEM solution for the Helmholtz equation in one, two and three dimensions. *International Journal for Numerical Methods in Engineering*, 46: 471-499.
- DUTTA G, LU K, WANG X & SCHUSTER G. 2013. Attenuation compensation in least-squares reverse time migration using the visco-acoustic wave equation. In: SEG Houston 2013 Annual Meeting. Volume 79, p. S251-S262. Houston, USA.
- FICHTNER A. 2011. Full Seismic Waveform Modelling and Inversion. Berlin: Springer. 343 pp.
- JO CH. 1996. An optimal 9-point, finite-difference, frequency-space, 2-D scalar wave extrapolator. *Geophysical Journal*, 61: 529-537.
- KAMEI R & PRATT RG. 2013. Inversion strategies for visco-acoustic waveform inversion. *Geophysical Journal International*, 194(2): 859-884. doi: 10.1093/gji/ggt109.
- KOLSKY H. 2003. *Stress Waves in Solids*. Dover Phoenix Editions. Dover Publications. 212 pp.
- LAVERGNE M. 1986. *Seismic Methods*. Editions Technip. 167 pp.
- MARFURT K. 1984. Accuracy of finite-difference and finite-element modelling of the scalar and elastic wave equations. *Geophysics*, 49: 553-559.
- MASE GT & MASE GE. 1999. *Continuum Mechanics for Engineers*. Boca Raton, Florida: CRC Press. 400 pp.
- MAVKO G, MUKERJI T & DVORKIN J. 2009. *The Rock Physics Handbook*. Volume II. California: Cambridge University Press. 329 pp.
- OPERTO S & VIRIEUX J. 2006. Practical aspects of Frequency-domain finite-difference modelling of Seismic wave propagation. *Ecole thématique SEISCOPE*. 87 pp.
- OSPINA MA. 2016. *Dispersión y Estabilidad en el procesos demodelado en Full Wave Inversion para un medio visco-acustico en el dominio de la frecuencia en dos dimensiones*. Master dissertation, Mathematics. Universidad de Antioquia, Colombia. Available on: <<http://www.udea.edu.co/wps/wcm/connect/udea/19f488d1-8b01-4b93-b4b2-06b506efa4e4/Tesis.pdf?MOD=AJPERES&CVID=mDVAVfz>>. Access on: March, 2016, 87 pp.
- SHIN C & HO CHA Y. 2008. Waveform inversion in the Laplace domain. *Geophys. J. Int.*, 173: 922-931.
- STRIKWERDA J. 2007. *Finite Difference Schemes and Partial Differential Equations*. Philadelphia: Society for Industrial and Applied Mathematics. 434 pp.
- WANG H, ZHANG L & MA Z. 2003. Seismic wave imaging in visco-acoustic media. *Science in China Series A: Mathematics*, 47: 146-154.
- WANG Y. 2009. *Seismic Inverse Q Filtering*. Wiley. 248 pp.
- YANG Z, LIU Y & REN Z. 2014. Comparisons of visco-acoustic wave equations. *Journal of Geophysics and Engineering*, 11: 025004.

Recebido em 16 de maio de 2018 / Aceito em 30 de janeiro de 2019

Received on May 16, 2018 / Accepted on January 30, 2019

IMPACTS OF HALOKINESIS IN SEISMIC INTERPRETATION AND GENERATION OF THE TOP SALT SURFACE IN A DISTAL PORTION OF THE SANTOS BASIN, BRAZIL

Wagner M. Lupinacci¹, Rafael P. C. Viana¹, Danilo J. A. Ferreira^{1,2}, Igor de A. Neves¹, João Paulo R. Zambrini¹, Maria O. Azul³, André L. Ferrari¹ and Luiz Antônio P. Gamboa¹

ABSTRACT. Studies on evaporitic rocks are of great importance for the oil and gas industry as they can create traps and seals for the hydrocarbon accumulations. Also, salt high ductility allows the formation of complex structures associated with halokinesis posing thus major challenges for imaging the rocks at their flanks and below the structures. This paper discusses the effects of salt tectonics on post-salt layers and the difficulties in interpreting the top salt surface in a particularly complex area of the Santos Basin. The available seismic and migration velocity model data are from an area located in the distal portion of the Santos Basin where the existing salt structures had a profound effect on the post-salt layers. Complex salt structures were formed in this area due to the intrinsic characteristics of salt rocks as it flew away from the terrigenous depocenters, pushed in the Atlantic Ocean realms. Structures such as overhangs are common and sometimes difficult to be mapped. Their geometry generates multiple points with the same latitude and longitude, but at different depths as they are interpreted and thus represent a challenge for current surface interpolation algorithms. A workflow is proposed to optimize multi-*z* surfaces generation from the top of the salt layer from the interpretation this surface in conjunction with the analysis of the migration velocity model. Finally, a zonation map of the salt walls, mini-basins, salt domes, overhang and salt window in the region is presented.

Keywords: halokinesis, seismic interpretation, salt structures zonation, top of the salt layer.

RESUMO. Estudos sobre rochas evaporíticas são de grande importância para a indústria de petróleo e gás, pois podem criar armadilhas e selos para o acúmulo de hidrocarbonetos. Além disso, a alta ductibilidade do sal permite a formação de estruturas complexas associadas à halocinese, representando assim grandes desafios para a visualização das rochas em seus flancos e abaixo das estruturas salinas. Este artigo discute os efeitos da tectônica de sal nas camadas do pós-sal e as dificuldades em interpretar a superfície do topo do sal em uma área particularmente complexa da Bacia de Santos. Os dados sísmicos e de poços utilizados são de uma área localizada na porção distal da Bacia de Santos, onde as estruturas de sal existentes tiveram um grande efeito nas camadas do pós-sal. Estruturas complexas de sal foram formadas nesta área devido às características intrínsecas das rochas salinas à medida que se distanciaram dos depocentros terrígenos, empurradas para o domínio do Oceano Atlântico. Estruturas como *overhangs* são comuns e às vezes difíceis de serem mapeadas. Sua geometria gera múltiplos pontos com a mesma latitude e longitude, mas em profundidades diferentes conforme são interpretadas e, portanto, representam um desafio para os algoritmos existentes de interpolação de superfície. Um fluxo de trabalho é proposto para otimizar a geração de superfícies multi-*z* do topo da camada de sal a partir da interpretação sísmica desta superfície em conjunto com a análise do modelo de velocidade de migração. Por fim, é apresentado um zoneamento das muralhas de sal, mini-bacias, domos de sal e janela de sal na área de estudo.

Palavras-chave: halocinese, interpretação sísmica, zoneamento das estruturas do sal, topo da camada do sal.

¹Universidade Federal Fluminense, Department Geology and Geophysics (GIECAR), Av. General Tavares de Souza, 24120-346, Niterói, RJ, Brazil – E-mails: wagnerlupinacci@id.uff.br, rafaelcherenev@gmail.com, dferreira8@slb.com, joaozambrini@id.uff.br

²Schlumberger, Software Integrated Solutions, Av. República do Chile 330, RJ, 20031-170, Brazil – E-mail: dferreira8@slb.com

³Petrogal Brasil S.A. Av. República do Chile, 330 - Centro, 20031-170, Rio de Janeiro, RJ, Brazil – E-mail: mariaolhoazul@petrogalbrasil.com

INTRODUCTION

The evaporites are rocks formed, generally, in environments with low terrigenous sedimentary input, submitted to dry climates and high evaporation rates. The rocks formed by salts are different from the most rocks, as they have both solid and liquid state characteristics. Evaporite rocks can be considered as mobile rocks because they move very easily, both chemically in aqueous solution and physically in solid flow (Mohriak et al., 2008).

Formation of evaporites can occur in both marine and continental environments. In marine marginal configuration, the evaporites are formed in sabkha and saline plains. In continental configuration, the saline lakes can precipitate thick layers of salts (da Silva et al., 2018).

In the Santos Basin, the evaporitic rocks were deposited in a transitional environment, during the Aptian and define the Ariri Formation. The Florianópolis High and the São Paulo Ridge acted as the barrier to oceanic water circulation and in addition to an arid climate created conditions for the deposition of a thick evaporite sequence (Karner & Gambôa, 2007). Its main lithological constituents are halite and anhydrite. However, thinner layers of more soluble salts, such as, tachyhydrite, carnallite and, locally, sylvite, also occur. Its lower limit is given by the contact with the carbonates from the Barra Velha Formation and its upper limit is given by the contact with open marine carbonates from the Guarujá Formation (Moreira et al., 2007).

Halokinesis, or salt tectonics, is produced by the movement of salt bodies caused through gravity action over evaporitic rocks, which are less resistant, presenting low viscosity. Salt deformation causes a series of structures related to its flow towards basin distal portions and in its ascension to lower lithostatic pressure levels (Jackson & Hudec, 2017).

Several studies in the Santos and Campos Basins and their African margin counterparts aimed to analyze the structures generated by the halokinesis and its role in gravitation tectonism during drift phase (Demercian et al., 1993; Modica & Brush, 2004; Gamboa et al., 2008; Mohriak et al., 2009; Davison et al., 2012; Guerra & Underhill, 2012; Dooley et al., 2015; Jackson et al., 2015; Alves et al., 2017). In general, the structures commonly found in dipping basinwards are, initially, pillows and anticlines, which gradate to locations with predominance of several forms of diapirism and, finally, in the more distal zones allochthonous salts occur.

Davison et al. (2012) proposed, based on observations of salt deformation in seismic lines along the Santos Basin, a zonation of evaporite layer rheological behavior where: in

the proximal portions of the basin, features associated with extensional tectonics predominate, with normal faulting presence and regularly experiencing a translational domain which changes to features linked to compression and, in the deeper regions, there is a zone where salt walls and allochthonous structures occur with the existence of prominent thrust faults.

In petroleum systems, evaporite rocks play a fundamental role, mainly associated with pre-salt and sub-salt reservoirs, where they can act as seals, preventing the migration of hydrocarbons and contributing to the formation of stratigraphic traps, because of their movement and deformation (Jackson, 1995; Warren, 2016; Jackson & Hudec, 2017). Another role that they can play is the creation of shallow areas as they move upward. Carbonate banks can develop on these areas (Vendeville & Jackson, 1992).

Kirkland & Evans (1981) and Schreiber (1988) observed that deposition of modern evaporites is associated with high levels of biological activity. They proposed that such levels of activity control, at least in part, the generation of hydrocarbons found in past analogues. The evaporite layer also plays another key factor in oil systems, which is directly associated with the success of exploration, because its thermal conductivity facilitates heat dissipation and allows organic matter to remain in the oil generation window for a longer time (Mello et al., 1995).

The evaporitic layers can represent a great challenge for hydrocarbons exploration. As the salts have capacity to deform significantly, which may allow them to flow into the well and replace the drilling mud, especially at high temperatures, putting the whole operation at risk (Perez et al., 2008). In many cases, a small deformation of the evaporitic layer may cause a decrease in well diameter or erroneous calibration, which leads to tube binding and to coating collapse (Barker et al., 1994).

The refractions and diffractions generated by the evaporitic layers can negatively affect seismic imaging. Studies focusing on solutions for this phenomenon have been of great importance for pre-salt imaging (Griffiths et al., 2011; Ji et al., 2011; Gobatto et al., 2016). Another challenge is the generation a top salt surface able to take into account the halokinesis-related deformations, which can have several points of the same latitude and longitude with multiple depth values, called multi-z points (Zlatanova & Prospero, 2005).

The aim of this paper is to present a workflow to solve the problems of generating a surface with multiple points in the z axis and the zoning of the main salt structures. For this, the top of the evaporitic layer was interpreted, and the main structures

generated by the halokinesis were identified as well as their influence in relation to the deformations in post-salt rocks and the seismic imaging in a distal area in the Santos Basin. For the generation of top salt surface, we used the integration of velocity model, as a guide, and the seismic interpretation, thus generating a more realistic surface that considers the salt structures such as mini-basins, overhangs and salt tongues.

IDENTIFICATION AND ANALYSIS OF THE MAIN SALT STRUCTURES IN THE STUDY AREA

The evaporitic layers constitute a group of unusual rocks, which contribute to the formation of structures with peculiar characteristics, that can intrude and deform adjacent and overlapping layers. In the study area, several features and structures of salt tectonics can be identified. Figure 1 shows a large diapir with four kilometers thick which, due to its movement towards the upper layers, has its top in discordant contact with the layers near the seafloor. In several locations a significant upwelling of salt structures occurs and the diapirs are almost in contact with the seafloor.

Salt wall features were also observed, as illustrates Figure 2, which are about thirty kilometers long and in some places

four kilometers thick. In Figure 3, it is possible to observe an example of a feature generated by the halokinesis, called salt tongue, having a length of approximately ten kilometers. It is typically formed by lateral salt movement towards regions of lower pressure, usually through thrust faulting. The seismic facies of this salt tongues are represented by an intense intercalation of high-amplitude reflectors, characterized as stratified evaporitic layer. Sub-salt sediments can be seen below this structure and, in some cases, it is not possible to observe the continuity of top salt reflector as well as lower layers reflectors.

Due to the strong halokinesis, features of more distal areas, large sediment tongues occur between two thick salt packages, generating even salt windows in these places (Fig. 4). With the salt intrusion and movement, post-salt layers may also be deformed, fractured and/or faulted. From the tensions generated by the halokinesis, complex structures are formed, such as: anticlines, synclines and rotated blocks (Fig. 5). In some areas close to the salt dome tops, due to the influence of the salt tectonics, the presence of chaotic seismic facies is observed, without correlation with the laterally associated sediments (Fig. 6). This fact is probably related to the local tension generated by salt movement, as well as the heating of these areas due to the "chimney effect" (Warren, 2016). Seismic imaging below these

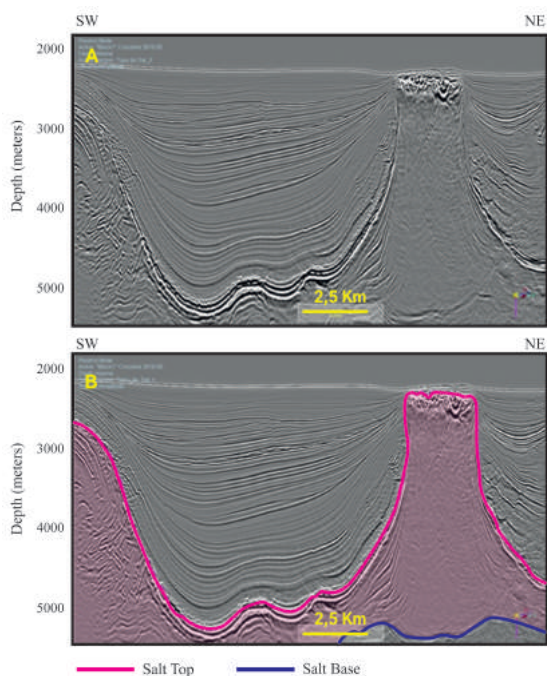


Figure 1 – Seismic section showing an example of a salt diapir: (A) uninterpreted section; and (B) interpreted section. Note the magnitude of the diapirs that can reach more than 3000 meters in height.

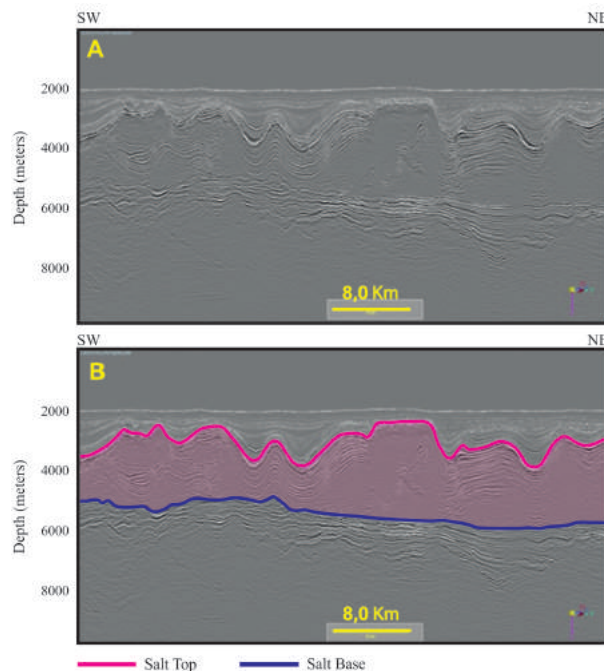


Figure 2 – Seismic section along the strike of the basin showing a gigantic salt wall: (A) uninterpreted section; and (B) interpreted section.

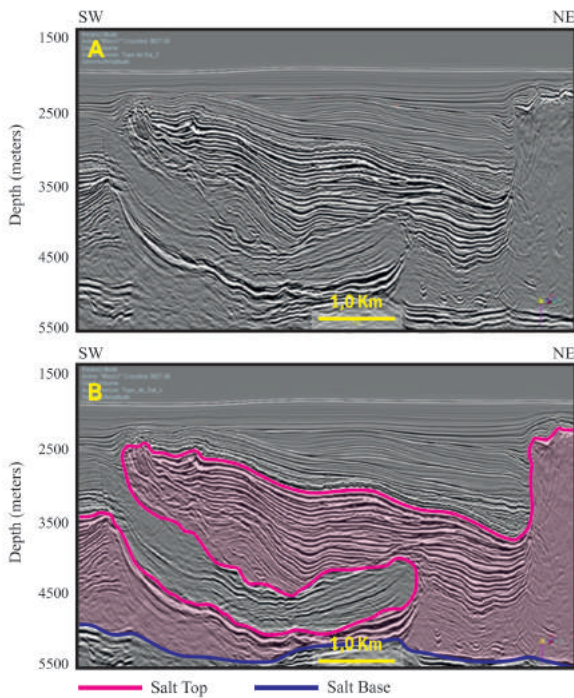


Figure 3 – Seismic section showing an example of a salt tongue: (A) uninterpreted section; and (B) interpreted section.

walls is impaired and, therefore, in many places it is not possible to clearly identify the reflector referring to the salt base.

Another structure interpreted in several regions of the study area was mini-basins. They are a confined space among the flanks of the diapirs formed by the deposition of sediments of greater density than the halite, being one of the causes of salt ascension and generation of accommodation space. Figure 7 shows an area with a mini-basin between two salt diapirs and inside salt strata it is also possible to observe stratification and even an angular unconformity within salt layers.

GENERATION OF THE TOP SALT SURFACE: DIFFICULTIES AND SOLUTIONS

Two interpretations of evaporite layer top were made: one simplified and one more detailed. In the simplified initial interpretation, complex salt overlapping and diapirism features were disregarded. This interpretation was performed to identify the main tendencies of top salt surface, thus ignoring the interpretation of points in depth with the same latitude and longitude (multi-z).

After the observation of the initial trends of the top of the evaporite layer, a more detailed analysis of the area was realized

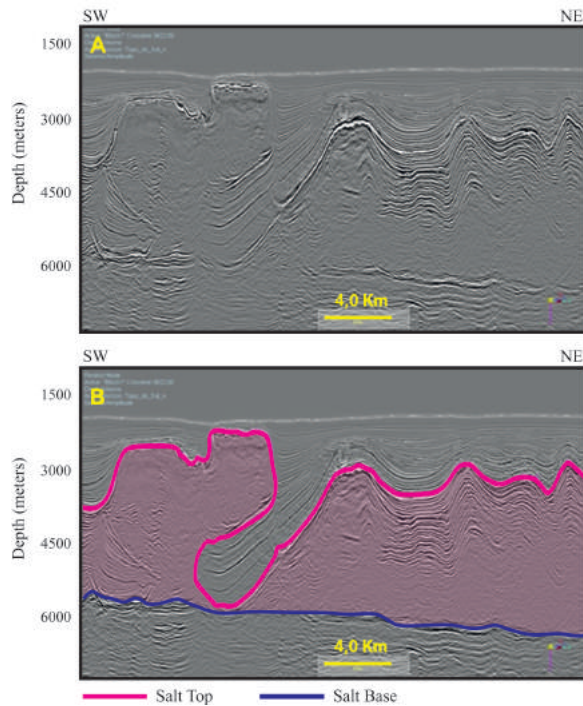


Figure 4 – Seismic section showing an example of overhang: (A) uninterpreted section; and (B) interpreted section.

and the influence of the halokinesis in the generation of complex structural features of the evaporite layer was considered in order to perform a more coherent and trustworthy interpretation. In this interpretation, the velocity model used in seismic migration aided the identification of salt structures (Fig. 8). In detailed analyses, the interpreted points have multiple values in depth with the same latitude and longitude (multi-z), reflecting structures such as salt tongues and overhangs. Even though some software suites can interpolate multi-z interpretations converting them to grid surfaces, these resulting surfaces cannot be used as inputs for geological model grid construction due to the size of the generated file. In other words, they can only be used for visualization purposes.

The generation of the interpolated surfaces was done, in the case of simple interpretation, by minimum curvature gridding algorithm (Smith & Wessel, 1990) and, in the case of detailed interpretation, by the Delauney triangulation method (Viviani & Manzato, 2005). However, several attempts were made using different parameters for the interpolation of manually interpreted sections and in all these attempts, it was not possible to achieve any top salt surface consistent enough with the interpretation of the complex structures generated by the halokinesis, as can

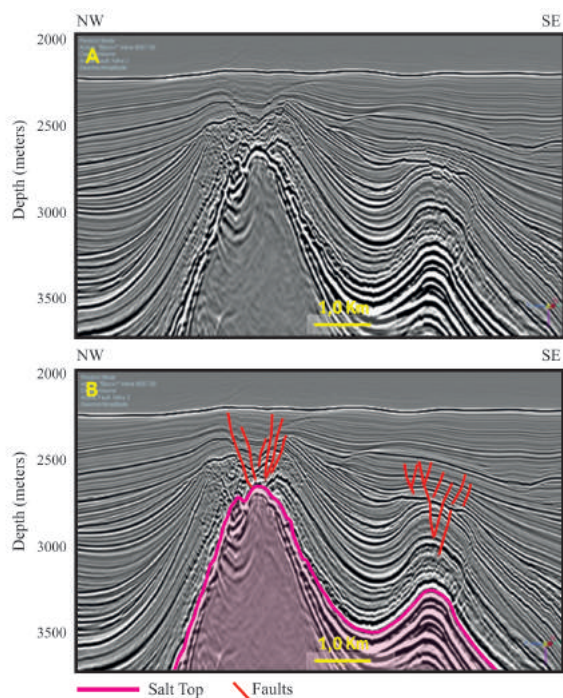


Figure 5 – Seismic section showing anticlinal and synclinal structures and many post-salt faults caused by halokinesis: (A) uninterpreted section; and (B) interpreted section.

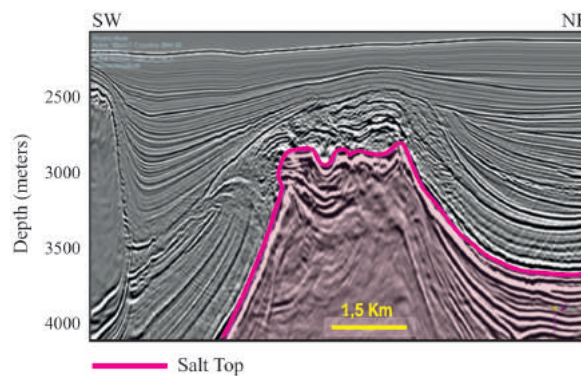


Figure 6 – Chaotic seismic facies above the top salt.

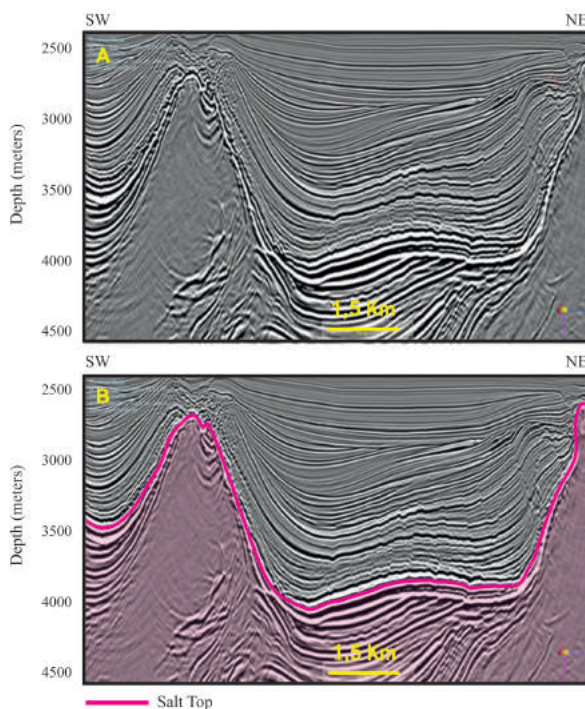


Figure 7 – Seismic section showing an example of mini-basins, salt stratification and angular unconformity among salt layers: (A) uninterpreted section; and (B) interpreted section.

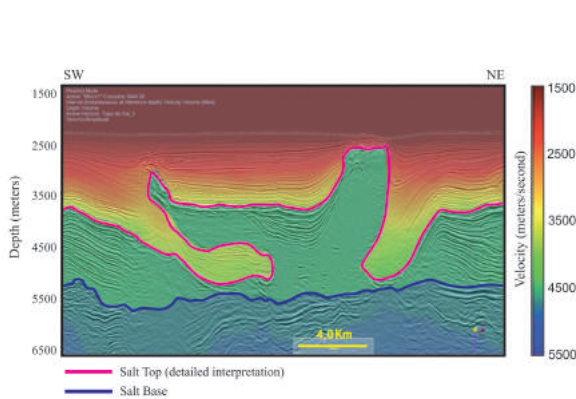


Figure 8 – The velocity model used in the seismic migration of the data with the detailed interpretation of the top salt.

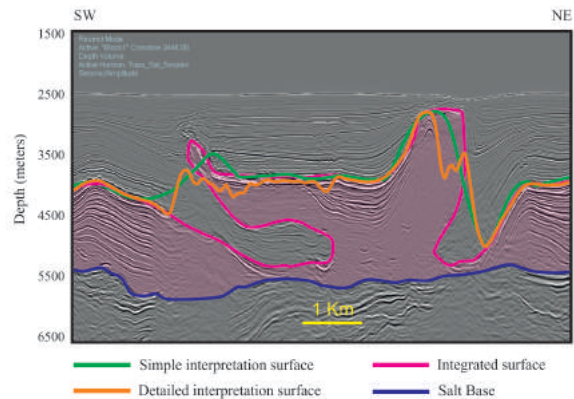


Figure 9 – Surfaces generated by the interpolation of simple interpretation (green), by the detailed interpretation (orange) and by the proposed method (purple).

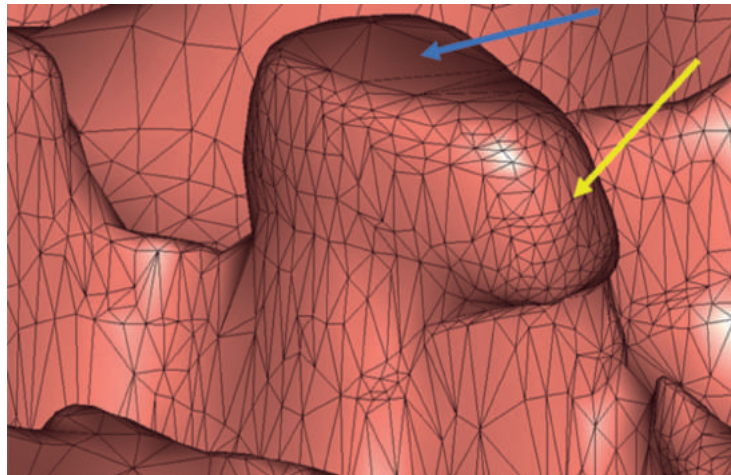


Figure 10 – Example of the triangulation procedure. Note that in the more complex areas require a greater amount of triangulation (yellow arrow), while in less complex areas there is no need for large amounts of triangulation (blue arrow).

be seen in Figure 9. The alternative solution was to generate a more reliable top salt surface to extract an iso-velocity curve of 4,500 m/s directly from the velocity model, this value corresponds to the average velocity of halite in the study area. This surface extracted from the velocity model was then refined using the detailed seismic interpretation. The refinement was done by modifying the iso-velocity surface points manually where the salt structures were not yet well represented. This method brought greater accuracy for the generated surface and agility to the process. In Figure 9, it is also possible to note how the integrated surface of the top salt is much more coherent with the complex features.

The surface generated through the integration of the velocity model and the interpretation resulted in a very extensive file to be used in geological modeling and in the illumination study. The alternative was to reduce the file size by diminishing the number of points in the less complex areas, that is, a greater number of vertices and points were used only in more complex areas, as shown in Figure 10.

Finally, Figure 11 highlights the difference, in map view, between the triangulated surface from the simple interpretation and the surface obtained from the proposed method. In these maps, it is possible to perceive that the surface generated using

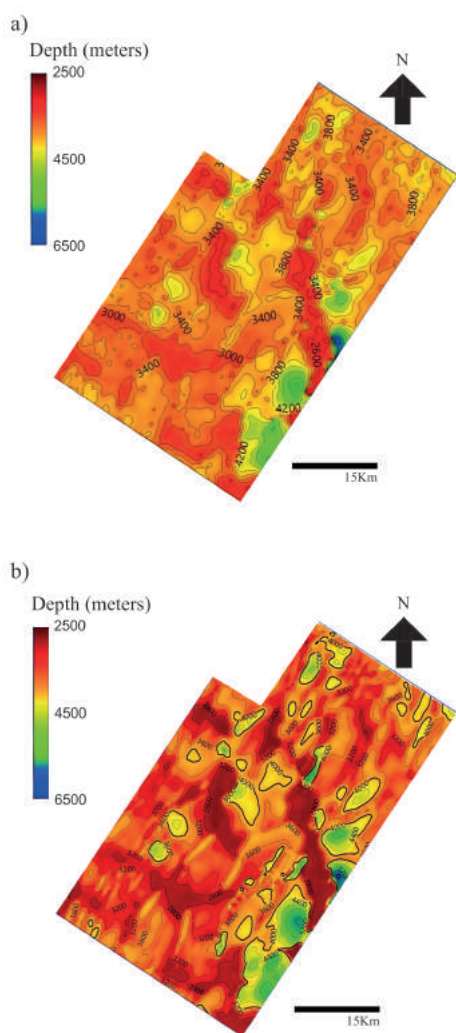


Figure 11 – a) Surface generated by the interpolation of the simple interpretation; b) Surface generated by the integrated method.

the proposed workflow has a much higher level of detail to represent complex salt features.

ZONING OF STRUCTURES GENERATED BY HALOKINESIS

Figure 12a shows the evaporite layer difference map in the study area generated from the top and base surfaces of the salt. It is important to note that it is not a thickness map since, especially in salt tongues, overhangs areas and salt windows below those structures, salt thickness is overestimated. However, the map still allows us to qualitatively infer about salt structures. It is possible to find regions of salt windows and areas with evaporitic layer

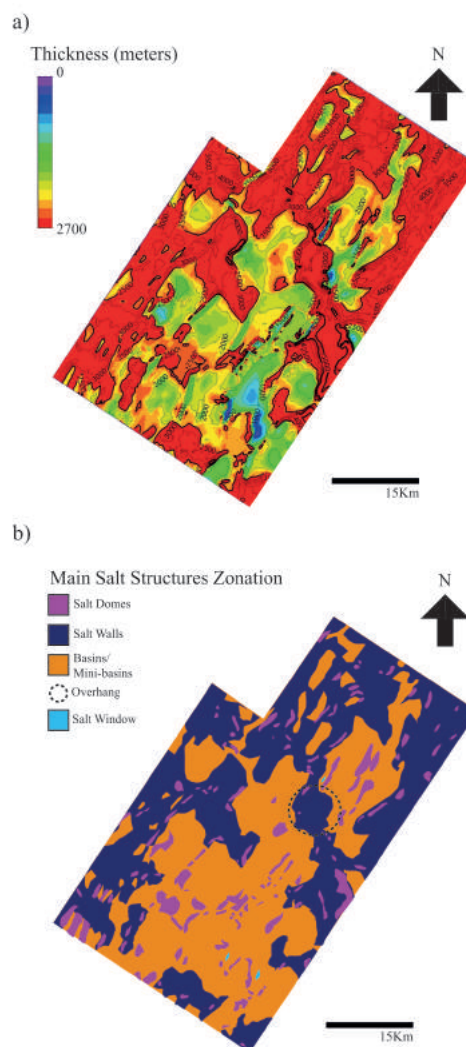


Figure 12 – a) Isopach map of the evaporites (the color palette was restricted at its maximum in 2700 meters for better visualization of salt features); b) Zonation map of structures formed by the halokinesis in the study region.

thicknesses that reach up to more than 4 kilometers. Figure 12b presents the result of zonation of the areas where each of the features generated by the effects of the halokinesis exists. Due to occurrence of structures of salt tongues and walls, it is possible to infer that the study area is in a region of salt tectonic compressive regimen under main gravitational tectonics.

CONCLUSION

We identified the influences of the salt tectonics on post-salt formations, which can generate discordant layers of saline body structures, anticlines and synclines above the domes and several faults and fractures. Due to the complexity of the horizon

interpreted from the top salt, a reliable interpolation becomes infeasible even with a dense mesh of manual interpretation. The proposed methodology using the velocity model as a guide and then manually refining with the detailed interpretation of salt structures was effective in creating a surface coherent with the actual salt forms in the study area. And finally, the zoning of the main structures generated by the halokinesis allowed the definition of the main domes, salt walls, mini-basins and overhangs generated by the salt movement and the existence of salt windows in the studied area.

ACKNOWLEDGEMENTS

The authors thank the Petrogal Brasil and Agência Nacional do Petróleo, Gás Natural e Biocombustíveis (ANP) for providing the field dataset and financial support for this research.

REFERENCES

- ALVES TM, FETTER M, LIMA C, CARTWRIGHT JA, COSGROVE J, GANGÁ A, QUEIROZ CL & STRUGALE M. 2017. An incomplete correlation between pre-salt topography, top reservoir erosion, and salt deformation in deep-water Santos Basin (SE Brazil). *Marine and Petroleum Geology*, 79: 300–320.
- BARKER JW, FELAND K & TSAO YH. 1994. Drilling long salt sections along the US Gulf Coast. *SPE Drilling & Completion*, 9(03): 185–188.
- DA SILVA MA, SCHREIBER BC & DOS SANTOS CL. 2018. Evaporitos como recursos minerais. *Revista Brasileira de Geofísica*, 18(3): 337–350.
- DAVISON I, ANDERSON L & NUTTALL P. 2012. Salt deposition, loading and gravity drainage in the Campos and Santos salt basins. Geological Society, London, Special Publications, 363(1): 159–174.
- DEMERCIAN S, SZATMARI P & COBBOLD P. 1993. Style and pattern of salt diapirs due to thin-skinned gravitational gliding, Campos and Santos basins, offshore Brazil. *Tectonophysics*, 228(3-4): 393–433.
- DOOLEY TP, JACKSON MP, JACKSON CAL, HUDEC MR & RODRIGUEZ CR. 2015. Enigmatic structures within salt walls of the Santos Basin—Part 2: Mechanical explanation from physical modelling. *Journal of Structural Geology*, 75: 163–187.
- GAMBOA L, MACHADO MP, DA SILVEIRA D, DE FREITAS J, DA SILVA S, MOHRIAK W, SZATMARI P & ANJOS S. 2008. Evaporitos estratificados no Atlântico Sul: interpretação sísmica e controle tectono-estratigráfico na Bacia de Santos. In: MOHRIAK W, SZATMARI P & ANJOS SMC (Org.). *Sal: Geologia e Tectônica, Exemplos nas Bacias Brasileiras*, São Paulo, Brazil: Editora Beca. p. 340–359.
- GOBATO F, MAUL A, TEIXEIRA L, GONZÁLEZ G, FALCÃO L, GONZÁLEZ M & BOECHAT JT. 2016. Refining velocity model within the salt section in Santos Basin: An innovative workflow to include the existing stratification and its considerations. In: SEG Technical Program Expanded Abstracts 2016. p. 5328–5333. Society of Exploration Geophysicists.
- GRIFFITHS M, HEMBD J & PRIGENT H. 2011. Applications of interbed multiple attenuation. *The Leading Edge*, 30(8): 906–912.
- GUERRA MC & UNDERHILL JR. 2012. Role of halokinesis in controlling structural styles and sediment dispersal in the Santos Basin, offshore Brazil. Geological Society, London, Special Publications, 363(1): 175–206.
- JACKSON CAL, JACKSON MPA, HUDEC MR & RODRIGUEZ CR. 2015. Enigmatic structures within salt walls of the Santos Basin—Part 1: Geometry and kinematics from 3D seismic reflection and well data. *Journal of Structural Geology*, 75: 135–162.
- JACKSON MPA. 1995. Retrospective salt tectonics. AAPG Special Volumes. 454 pp.
- JACKSON MPA & HUDEC MR. 2017. Salt tectonics: Principles and practice. Cambridge University Press. 494 pp.
- JI S, HUANG T, FU K & LI Z. 2011. Dirty salt velocity inversion: The road to a clearer subsalt image. *Geophysics*, 76(5): WB169–WB174.
- KARNER G & GAMBÔA L. 2007. Timing and origin of the South Atlantic pre-salt sag basins and their capping evaporites. Geological Society, London, Special Publications, 285(1): 15–35.
- KIRKLAND DW & EVANS R. 1981. Source-rock potential of evaporitic environment. *AAPG Bulletin*, 65(2): 181–190.
- MELLO UT, KARNER GD & ANDERSON RN. 1995. Role of salt in restraining the maturation of subsalt source rocks. *Marine and Petroleum Geology*, 12(7): 697–716.
- MODICA CJ & BRUSH ER. 2004. Postrift sequence stratigraphy, paleogeography, and fill history of the deep-water Santos Basin, offshore southeast Brazil. *AAPG Bulletin*, 88(7): 923–945.
- MOHRIAK W, NEMC OK M & ENCISO G. 2008. South Atlantic divergent margin evolution: rift-border uplift and salt tectonics in the basins of SE Brazil. Geological Society, London, Special Publications, 294(1): 365–398.
- MOHRIAK W, SZATMARI P & ANJOS SMC. 2009. Sal: Geologia e Tectônica; Exemplos nas Bacias Brasileiras. *Terrae Didática*, 4(1): 90–91.
- MOREIRA JLP, MADEIRA CV, GIL JA & MACHADO MAP. 2007. Bacia de Santos. *Boletim de Geociências da Petrobras*, 15(2): 531–549.
- PEREZ MA, CLYDE R, D'AMBROSIO P, ISRAEL R, LEAVITT T, NUTT L, JOHNSON C & WILLIAMSON D. 2008. Meeting the subsalt challenge. *Oilfield Review*, 20(3): 32–45.
- SCHREIBER BC. 1988. Evaporites and hydrocarbons. Volume 488. Columbia University Press, New York. 475 pp.

- SMITH W & WESSEL P. 1990. Gridding with continuous curvature splines in tension. *Geophysics*, 55(3): 293–305.
- VENDEVILLE BC & JACKSON MP. 1992. The rise of diapirs during thin-skinned extension. *Marine and Petroleum Geology*, 9(4): 331–354.
- VIVIANI E & MANZATO GG. 2005. Geração de modelos digitais de superfície por meio de plataformas computacionais com estrutura vetorial e raster. *Ciencia y Engenharia/Science and Engineering Journal*, 14(2): 27–33.
- WARREN JK. 2016. *Evaporites: A Geological Compendium*. Switzerland: Springer. 1813 pp.
- ZLATANOVA S & PROSPERI D. 2005. *Large-scale 3D data integration: challenges and opportunities*. Boca Raton: CRC Press. 240 pp.

Recebido em 18 de novembro de 2018 / Aceito em 15 de maio de 2019

Received on November 18, 2018 / Accepted on May 15, 2019

L2- AND L1-NORM APPLIED TO INVERSION OF NONHYPERBOLIC TRAVEL-TIME

Nelson Ricardo Coelho Flores Zuniga¹, Fernando Brenha Ribeiro¹ and Viacheslav Ivanovich Priimenko²

ABSTRACT. Several nonhyperbolic multiparametric travel-time approximations were tested to perform the velocity analysis in the last decade. The previous works studied not only the accuracy but also the complexity concerning the topology of the objective function and the statistical distribution. However, the variation of the norm was poorly studied. As some approximations presented very good results, it is important to understand the behavior of the application of the L1-norm rather than the L2-norm. Therefore, it was selected an approximation which showed the best set of results so far. Thus, this approximation was compared to the L2- and L1-norm aiming to observe its behavior for a PP and a PS reflection event. With this set of information, it is possible to evaluate what kind of improvement the L1-norm can bring for this kind of analysis.

Keywords: objective function, nonhyperbolic, probability distribution.

RESUMO. Diversas aproximações não-hiperbólicas multiparamétricas de tempos de trânsito foram testadas para realizar a análise de velocidades na última década. Trabalhos anteriores estudaram não apenas a precisão, mas também a complexidade de topologia da função objetivo e a distribuição estatística destas aproximações. Entretanto, a variação de norma foi pouco estudada. Como algumas aproximações apresentaram resultados muito bons, é importante entender o comportamento da aplicação da norma L1 ao invés da L2. Portanto, foi selecionada uma aproximação que apresentou o melhor conjunto de resultados até o momento. Dessa forma, esta aproximação foi comparada com as normas L2 e L1, visando observar seu comportamento para eventos de reflexão PP e PS. Com esse conjunto de informações, é possível avaliar que tipo de melhoria a aplicação da norma L1 pode trazer para este tipo de análise.

Palavras-chave: função objetivo, não-hiperbólica, distribuição probabilística.

¹Universidade de São Paulo, Instituto de Astronomia, Geofísica e Ciências Atmosféricas (IAG-USP), Departamento de Geofísica. Rua do Matão 1226 - Cidade Universitária - 05508-090, São Paulo, SP, Brazil. Phone: +55(11) 3091-4755 – E-mails: nelson.zuniga@iag.usp.br; fernando.brenha@iag.usp.br

²Universidade Estadual do Norte Fluminense (UENF), Laboratório de Engenharia e Exploração de Petróleo (LENEP), Avenida Brennand s/n – Imboacica – 27910-970, Macaé, RJ, Brazil. Phone: +55(22) 2765-6565 – E-mail: slava@lenep.uenf.br

INTRODUCTION

For several problems in signal processing the L2-norm is used, once the least squares error approximate solution is preferred for this kind of tasks. However, the L1-norm can be preferable in many situations, due to the fact that a complex topology of objective function with small distortions can be attenuated with the least absolute deviation (Khaleelulla, 1982; Bourbaki, 1987).

In seismic processing, some events can result in a very complex topology of the objective function, once the large offsets with layered media, the converted PS waves and the use of OBN (Ocean Bottom Nodes) data cause a strong nonhyperbolicity to the reflection event. The velocity analysis suffers significantly with this problem while the inversion procedure is being performed. Many approximations were developed in the last decades (e.g. Malovichko, 1978; Muir & Dellinger, 1985; Slotboom, 1990; Alkhalifah & Tsvanki, 1995; Li & Yuan, 2001; Ursin & Stovas, 2006; Blias, 2009) to deal with the different causes of the nonhyperbolicity with different parameters and different complexities.

Recent works (e.g. Zuniga et al., 2015, 2016a,b, 2017; Zuniga, 2017) showed not only the accuracy comparison among these nonhyperbolic approximations, but also the complexity analysis study concerning the objective function. This kind of test was important to understand the behavior of each approximation related to their statistical distributions. It was observed that some approximations showed always a multimodal behavior with a global and one or more local minimum regions (e.g. Muir & Dellinger, 1985; Li & Yuan, 2001), some always presented a unimodal behavior with only the global minimum region (e.g. Malovichko, 1978; Slotboom, 1990; Alkhalifah & Tsvanki, 1995), and others both behavior varying with the model (e.g. Ursin & Stovas, 2006; Blias, 2009), as observed by Zuniga et al. (2018).

As the use of the L1-norm can attenuate and even suppress the local minimum regions or subtle features, it is important to understand what kind of improvement in can be obtained. As the approximation proposed by Li & Yuan (2001) showed the best results in recent works concerning the accuracy, it was selected to be tested to understand if even a nonhyperbolic approximation with a complex topology of the objective function can have its results significantly improved with the L1-norm.

It is possible to compute the relative errors between the calculated curves with the nonhyperbolic multiparametric approximation and the observed curve of the reflection events of the chosen Model. The RFM (Residual Function Maps) can be

used to study the structure of the objective function aiming to analyze the complexity of its topology. The accuracy analysis can be performed with the Li & Yuan (2001) approximation for the conventional wave reflection event (PP) and the converted wave event (PS) and for both L2- and L1-norm. Thus, it is possible to find whether the L1-norm can provide more reliable results during the travel-time curves inversion.

OFFSHORE MODEL STUDIED

In the Table 1, presents the parameters of the Model used for this study. This Model is an offshore layered model with a carbonate reservoir ($V_p = 4010$ m/s and $V_s = 2012$ m/s). It is sealed by a salt structure composed by the 3rd, 4th and 5th layers.

The salt structure can be more easily observed in Figure 1, where the variations of the physical properties are shown.

In Figure 2, it is possible to observe the ray tracing generated by a simulation with parameters of the Model. The travel-time curves of the PP reflection event and the PS reflection event were generated (Margrave, 2000, 2003; Thorbecke & Draganov, 2012).

Table 1 – The parameters of the Model: Layer thickness (Δz), P-wave velocity (V_p), S-wave velocity (V_s) and V_p/V_s ratio.

Layer	Δz (m)	V_p (m/s)	V_s (m/s)	V_p/V_s
Water	2157	1500	0	-
1	496	2875	1200	2.40
2	108	3505	1628	2.15
3	664	4030	2190	1.84
4	262	5005	2662	1.88
5	1485	4220	2210	1.91

NONHYPERBOLIC MULTIPARAMETRIC TRAVEL-TIME APPROXIMATION

The Equation 1, the approximation proposed by Li & Yuan (2001), has a nonhyperbolic parameter, the γ parameter, previously studied by Li & Yuan (1999), and based on the anisotropic parameters of Thomsen (1986). This approximation considers the CP (Conversion Point) aiming to control the effects of a

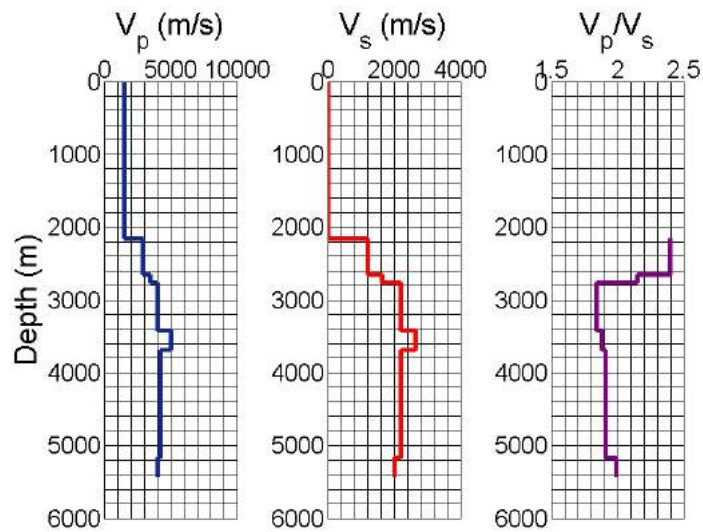


Figure 1 – P-wave velocity (V_p), S-wave velocity (V_s) and V_p/V_s ratio profiles of the Model.

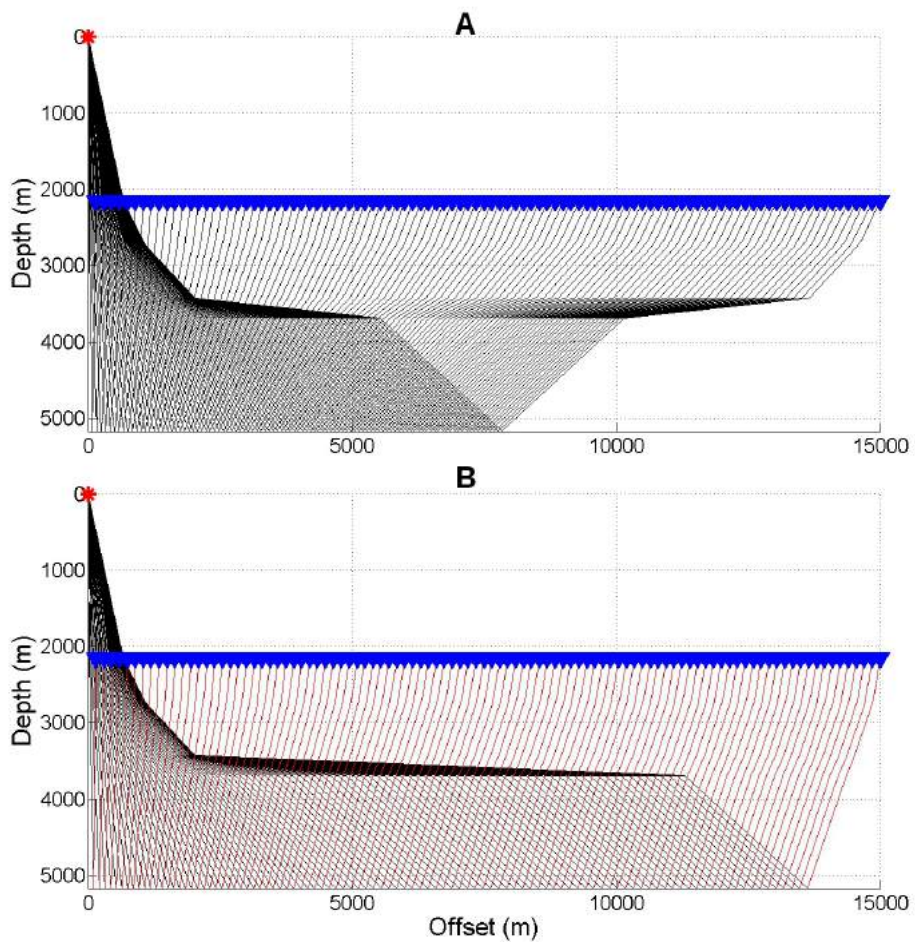


Figure 2 – Ray tracing of the (A) PP wave reflection event and (B) PS wave reflection event of the Model.

nonhyperbolicity associated to the wave conversion joint to large offsets for layered media.

$$t = \sqrt{t_0^2 + \frac{x^2}{v^2} - \frac{(\gamma-1)}{\gamma v^2} \frac{(\gamma-1)x^4}{4t_0^2 v^2 + (\gamma-1)x^2}} \quad (1)$$

Where γ is the ratio between the squared P-wave stacking velocity v_{P2} and the squared converted wave stacking velocity v_{C2} (Eq. 2).

$$\gamma = \frac{v_{P2}^2}{v_{C2}^2} = \frac{\gamma_{eff}(1 + \gamma_0)}{(1 + \gamma_{eff})} \quad (2)$$

The relation γ_{eff} is expressed by $\gamma_{eff} = \gamma_2^2/\gamma_0$, where γ_2 is the ratio between the P-wave and S-wave stacking velocities, and γ_0 is the ratio between P-wave velocity and S-wave velocity which travel along the normal component.

The approximation was lately studied concerning its parameter by Li (2003), and after compared with other approximations (Zuniga et al., 2015, 2016b, 2017; Zuniga, 2017). As the approximation showed to have a multimodal statistical distribution in previous works, it must be tested with the L1-norm rather than the L2-norm to observe if it could suppress the local minimum region, or at least makes a narrower global minimum region to increase the accuracy during the inversion.

COMPLEXITY ANALYSIS OF THE OBJECTIVE FUNCTION FOR L2- AND L1-NORM

The analysis of the objective function concerning its complexity can be performed by the use of residual function maps (RFM) aiming to study the complexity of the topology of an objective function (Larsen, 1999; Kurt, 2007).

In the case used here, the RFM represents the relation between the additional parameter and the RMS (root mean square) velocity of the event. The additional parameter is the γ nonhyperbolic parameter, used in the approximation proposed by Li & Yuan (2001). The third dimension of the hyperplane is the representation of the minimum values.

In mathematics, norm is the total length of a set of vectors in a vector space or the total size of a set of matrices in a matrix space. The norm is a function which assigns a strictly positive length of size to each vector in a vector space, being not valid to zero vector (and the same idea applied to matrices). The least squares method (L2-norm) is based on the sum of the square of the difference between the observed value and the estimated one. While the least absolute deviation (L1-norm), minimizes the sum of the absolute difference between the observed value and the estimated one.

In this work, the focus is to observe the variation of behavior between L2- and L1-norm for each reflection travel-time event (PP and PS) with the selected approximation.

In the Figure 3A, it is possible to observe a complex structure of the objective function, with the global minimum region and a local minimum one, with a significant variation between the maximum and the minimum regions. The variation of the structure alongside both axes is very similar, what shows a sensibility resembling between the velocity of the event and the nonhyperbolicity parameter. It is clearly observed that the γ parameter must be always higher than 0, and when this parameter is 1, there is an inconsistency in the topology, due to the fact that when $\gamma = 1$, the Li & Yuan (2001) becomes the hyperbola equation (Dix, 1955). Thus, it can be suggested that the local minimum region of this approximation is associated to the transition of the hyperbolic behavior.

In the Figure 3B, the application of the L1-norm brought a very similar structure of the objective function, with no variation concerning the statistical distribution. However, the global minimum region and the local minimum region are apparently more correlated, and the most interesting observation is the narrower global minimum region, with a more abrupt structure, fact that is important to perform a more accurate and faster inversion.

For the PS converted event (Fig. 4), it is possible to observe in Figure 4A, a structure similar to the Figure 3A, however with a displacement of the structure associated to the variation of the set of parameters, what was already observed in previous works. However, the characteristics of the structure are very similar to the PP reflection event.

Concerning the application of the L1-norm for this event (Fig. 4B), there is a more related local and global minimum region, but not so strong as the one showed by the conventional event. However, a more abrupt structure with a narrower global minimum region and a multimodal statistical distribution are observed, similarly to the conventional event.

ACCURACY ANALYSIS

To compare nonhyperbolic travel-time approximations was an important analysis to understand which approximation presents the best results and is the most reliable to perform a travel-time curve inversion procedure. This kind of comparison has been performed during the last decade (Aleixo & Schleicher, 2010; Golikov & Stovas, 2012; Zuniga et al., 2015, 2016a,b, 2017; Zuniga, 2017). As the recent works showed an extremely positive

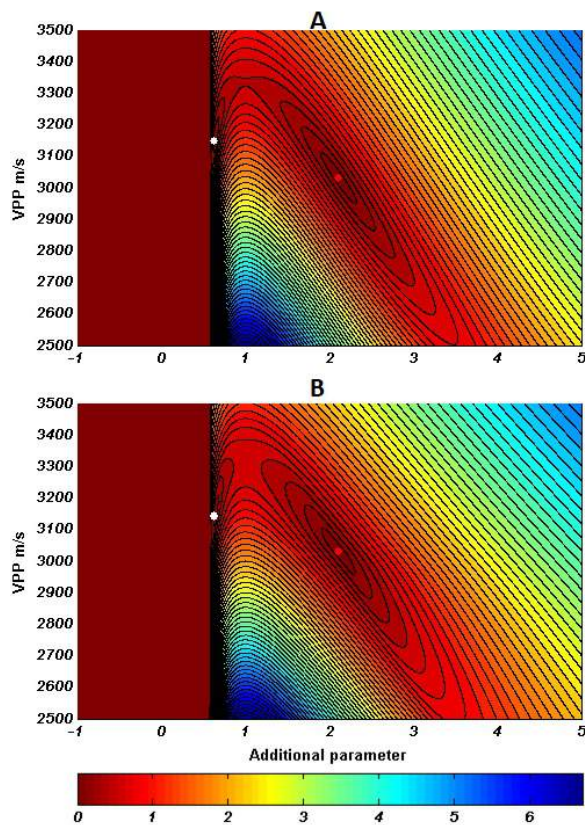


Figure 3 – Residual function maps to demonstrate the complexity of the approximation proposed by Li & Yuan (2001) for the PP wave reflection event with (A) L2-norm and (B) L1-norm. Red dispersions represent the global minimum region and the white dispersions represent the local minimum region.

results with the use of the approximation proposed by Li & Yuan (2001), the accuracy analysis of this equation is important to be performed concerning the L1-norm, once there is no previous works with this kind of tests.

After calculate the difference between the calculated curve with the selected approximation and the observed curve, the errors must be computed and compared for both reflection events and both norms.

For the PP wave reflection event, it is possible to observe that (as it was expected) the errors are significantly lower than the error for the converted wave reflection event (Fig. 5). However, the most important observation is concerning the comparison of the L2- and L1-norm, where it is possible to observe that for the PP reflection event, the L1-norm presents a lower error than the L2-norm. For the PS event, it is possible to observe the same behavior even with a more significantly lower error after the application of the L1-norm. Then, the L1-norm showed to be

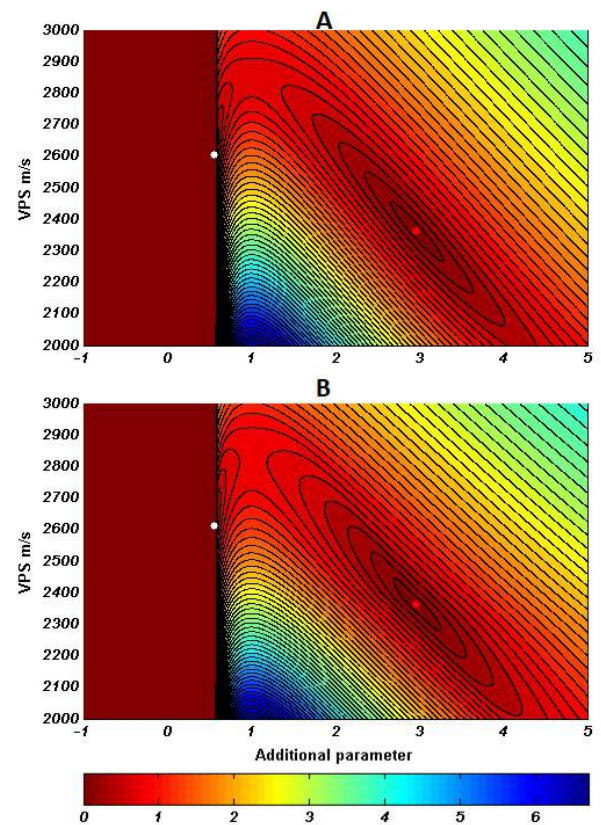


Figure 4 – Residual function maps to demonstrate the complexity of the approximation proposed by Li & Yuan (2001) for the PS wave reflection event with (A) L2-norm and (B) L1-norm. Red dispersions represent the global minimum region and the white dispersions represent the local minimum region.

more efficient than the L2-norm for this kind of problem with a processing time 16% lower for the PP event and 17% lower for the converted event.

CONCLUSIONS

The approximation proposed by Li & Yuan (2001) showed a better result after the application of the L1-norm for PP and the PS reflection events. The narrower global minimum region and the more abrupt structure of the objective function were the most important improvements of the L1-norm rather than the L2-norm.

There was a significant improvement for both reflection events concerning the accuracy, and even with no difference of statistical distribution, the results are clearly more precise with the L1-norm.

So, even for an always multimodal approximation, the application of the least absolute deviation rather than the least

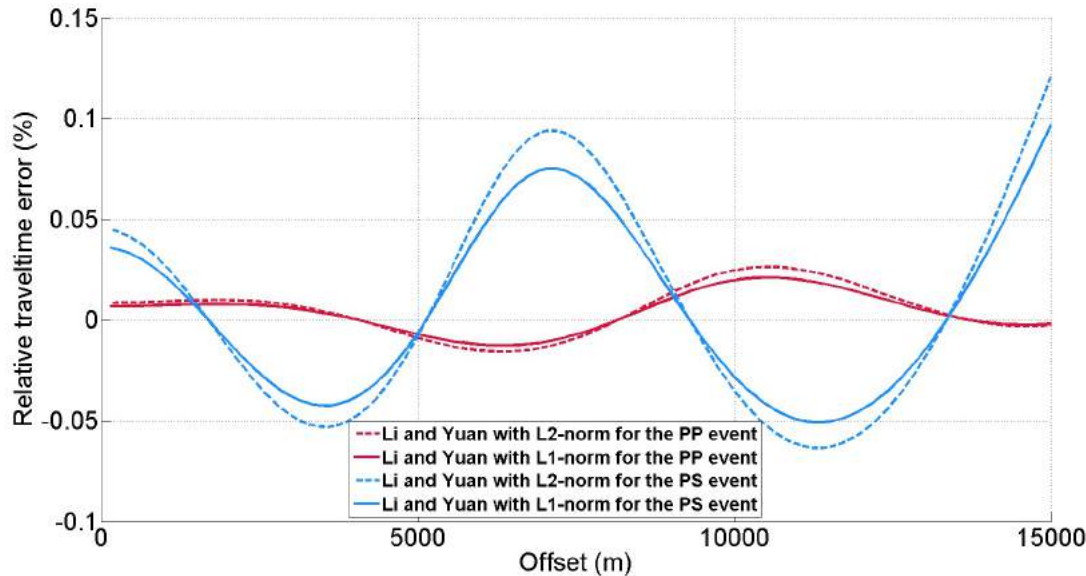


Figure 5 – Relative errors in travel-time between the observed curve and the calculated curve with the Li & Yuan (2001) approximation for each norm and for PP wave reflection event and PS wave reflection event.

squares presented a strong enhance in the quality of the parameters recovery, with more accurate results.

ACKNOWLEDGEMENTS

This study was financed in part by the Coordenação de Aperfeiçoamento de Pessoal de Nível Superior – Brazil (CAPES) – Finance Code 001. This study was financed in part by the Conselho Nacional de Desenvolvimento Científico e Tecnológico – Brazil (CNPq).

REFERENCES

- ALEIXO R & SCHLEICHER J. 2010. Traveltime approximations for q-P waves in vertical transversely isotropic media. *Geophysical Prospecting*, 58: 191-201.
- ALKHALIFAH T & TSVANKI I. 1995. Velocity analysis for transversely isotropic Media. *Geophysics*, 60: 1550-1566.
- BLIAS E. 2009. Long-offset NMO approximations for a layered VTI model: Model study. In: 79th Annual International Meeting. Expanded Abstract, p. 3745-3749. Houston, TX, USA: Society of Exploration Geophysicists.
- BOURBAKI N. 1987. *Topological vector spaces*. Springer-Verlag Berlin and Heidelberg. 362 pp.
- DIX C. 1955. Seismic velocities from surface measurements. *Geophysics*, 20: 68-86.
- GOLIKOV P & STOVAS A. 2012. Accuracy comparison of nonhyperbolic moveout approximations for qP-waves in VTI media. *Journal of Geophysics and Engineering*, 9: 428-432.
- KHALEELULLA S. 1982. *Counterexamples in topological vector spaces*. Berlin, Springer-Verlag Berlin and Heidelberg. 2nd ed., 184 pp.
- KURT H. 2007. Joint inversion of AVA data for elastic parameters by bootstrapping. *Computers & Geosciences*, 33(3): 367-382.
- LARSEN J. 1999. *AVO Inversion by Simultaneous P-P and P-S Inversion*. Master's dissertation. University of Calgary, Department of Geology and Geophysics. Calgary, Canada. 124 pp.
- LI X. 2003. Converted-wave moveout analysis revisited: The search for a standard approach. In: 73rd Annual International Meeting. Expanded Abstract, p. 805-808. Dallas, Texas, USA: Society of Exploration Geophysicists.
- LI X & YUAN J. 1999. Converted-wave moveout and parameter estimation for transverse isotropy. In: 61st EAGE Conference. Volume 1 Expanded Abstract, p. 4-35. Helsinki, Finland.
- LI X & YUAN J. 2001. Converted-wave imaging in inhomogeneous, anisotropic media: Part I – Parameter estimation. In: 63rd EAGE Conference. Volume 1 Expanded Abstract, p. 109. Amsterdam, Netherlands.
- MALOVICHKO A. 1978. A new representation of the travelttime curve of reflected waves in horizontally layered media. *Applied Geophysics*, 91(1): 47-53. [In Russian].

- MARGRAVE GF. 2000. New seismic modelling facilities in Matlab. CREWES Research Report. 12nd ed., 45 pp.
- MARGRAVE GF. 2003. Numerical Methods of Exploration Seismology with algorithms in MATLAB. Canada: The University of Calgary, Department of Geology and Geophysics. 225 pp.
- MUIR F & DELLINGER J. 1985. A practical anisotropic system. In: PROJECT SE (Ed.). SEP-44. p. 55-58.
- SLOTBOOM R. 1990. Converted wave (P-SV) moveout estimation. In: 60th Annual International Meeting. Expanded Abstract, p. 1104-1106. San Francisco, CA: Society of Exploration Geophysicists.
- THOMSEN L. 1986. Weak elastic anisotropy. *Geophysics*, 51: 1954-1966.
- THORBECKE J & DRAGANOV D. 2012. Finite-difference modeling experiment for seismic interferometry. *Geophysics*, 76: H1-H18.
- URSIN B & STOVAS A. 2006. Traveltime approximations for a layered transversely isotropic medium. *Geophysics*, 71: 23-33.
- ZUNIGA N. 2017. Análise comparativa de aproximações não-hiperbólicas dos tempos de trânsito de dados sísmicos multicomponente utilizando tecnologia OBN. Master's dissertation. Universidade de São Paulo. Brazil. 86 pp.
- ZUNIGA N, BOKHONOK O & DIOGO L. 2015. Comparison of nonhyperbolic travel-time approximations for multicomponent seismic data. In: 14th SBGf Congress. Expanded Abstract, p. 1176-1181. Rio de Janeiro, Brazil.
- ZUNIGA N, MOLINA E & PRADO R. 2016a. Inversion of multicomponent seismic data for VTI medium using the globalized Nelder-Mead optimization algorithm. In: 3rd EAGE/SBGf Workshop. Rio de Janeiro, Brazil. Expanded Abstract.
- ZUNIGA N, MOLINA E & PRADO R. 2016b. Inversion of multicomponent seismic data of the Santos Basin. In: Far East Hydrocarbons 2016. Expanded Abstract, Yuzhno-Sakhalinsk, Russia.
- ZUNIGA N, MOLINA E & PRADO R. 2017. Comparison of travel-time approximations for unconventional reservoirs from Santos Basin, Brazil. *Brazilian Journal of Geophysics*, 35(4): 273-286.
- ZUNIGA N, RIBEIRO F & PRIMENKO V. 2018. Relation between the model and the topography of the objective function in a velocity analysis using a nonhyperbolic multicomponent travel-time approximation. *Brazilian Journal of Geophysics*, 36(4): 375-384.

Recebido em 7 de março de 2019 / Aceito em 6 de maio de 2019

Received on March 7, 2019 / Accepted on May 6, 2019

RECOGNIZING LATE CRETACEOUS TO PALEOGENE CHANGES IN RELATIVE SEA LEVEL IN NORTHERN SANTOS BASIN, BRAZIL

Aurora M. Garcia¹, Cassio A. Pires¹, Daiane Münch¹, Iarema F.P. Carvalho¹, Luiza S. Freitas¹, Lucas A. Valore¹,
Carlos Eduardo Silva¹, Rosana N. Lima¹, Daniel F. Balensiefer¹ and Fernando F. Vesely²

ABSTRACT. The stratigraphy of the Santos Basin has become of great interest in the last decade because of the large oil accumulations in pre-salt (rift) and post-salt (drift) strata. Nevertheless, the most accepted stratigraphic models for the drift phase are only at a basin scale and can still be improved by more detailed work. In this paper we analyze an inline seismic section in the modern continental slope of the Santos Basin in order to describe the stratigraphy and to reconstruct relative-sea level (RSL) changes from the Campanian to the Eocene/Oligocene boundary. We mapped 40 seismic horizons, in which clinoform rollovers (former shelf margins) and stratal terminations were recognized. These data allowed for the construction of a chronostratigraphic chart and a RSL curve. The proposed stratigraphic chart displays three lower-order sequence sets comprising higher-order sequences including mostly alternating forced-regressive and normal-regressive system tracts, with the exception of three important transgressive episodes. Higher-order sequences above the intra-Maastrichtian unconformity exhibit low-angle ascending to descending shelf-margin trajectories and frequently truncated topsets, while aggradation was more important during Campanian to Maastrichtian. Expressive mass-transport deposits (chaotic seismic facies) at the bottomsets of some mapped horizons all match with forced-regressive episodes.

Keywords: seismic interpretation, sequence stratigraphy, shelf-margin clinoforms.

RESUMO. A Bacia de Santos tornou-se de grande interesse na última década devido às acumulações de petróleo no pré-sal (rifte) e pós-sal (deriva). No entanto, os modelos estratigráficos mais aceitos para a fase de deriva são em escala de bacia e podem ser incrementados por trabalhos de maior detalhe. Analisamos uma seção sísmica longitudinal no talude continental atual da bacia, a fim de descrever a estratigrafia e reconstruir mudanças do nível relativo do mar (NRM) do Campaniano ao limite Eoceno/Oligoceno. Quarenta horizontes sísmicos foram mapeados, nos quais margens da plataforma (*clinoform rollovers*) e terminações estratais foram reconhecidas. Esses dados permitiram a construção de um diagrama cronoestratigráfico e uma curva de variação do NRM. Identificou-se três conjuntos de sequências de menor ordem compreendendo sequências de ordem mais elevada, incluindo, na sua maioria, alternância entre regressão forçada e normal, com exceção de três importantes episódios transgressivos. As sequências de maior ordem acima da inconformidade intra-Maastrichtiano exibem trajetórias ascendentes de baixo ângulo a descendentes de margem de plataforma e *topsets* truncados, enquanto aggradação foi mais importante entre o Campaniano e o Maastrichtiano. Depósitos de transporte de massa (fácies sísmicas caóticas) nos *bottomsets* de alguns horizontes mapeados associam-se com episódios de regressão forçada.

Palavras-chave: interpretação sísmica, estratigrafia de sequências, clinofórmulas de margem de plataforma.

¹Universidade Federal do Paraná, Centro Politécnico, Programa de Pós-Graduação em Geologia, Jardim das Américas, Caixa Postal 19001, 81531-980, Curitiba, PR, Brazil – E-mails: auroramgarciaa@gmail.com, x_cassio@hotmail.com, daianemunch90@gmail.com, iaremaiaia@gmail.com, lufreitas145@gmail.com, lucasavalore@gmail.com, carloseduardo.oceano@gmail.com, natielilima21@gmail.com, danielbalen@yahoo.com.br

²Universidade Federal do Paraná, Centro Politécnico, Departamento de Geologia, Jardim das Américas, Caixa Postal 19001, 81531-980, Curitiba, PR, Brazil – E-mail: vesely@ufpr.br

INTRODUCTION

Seismic investigation of continental margins have improved our knowledge on the stratigraphic evolution of former shelf-margin systems by allowing estimating changes in relative sea level (RSL) and to assess its relationships with slope accretion and the transference of sediment to deep waters (e.g., Vail et al., 1977; Posamentier et al., 1988). More recently, the concept of shoreline and shelf-margin trajectory (e.g., Helland-Hansen & Hampson, 2009) as a tool for reconstructing RSL changes has been widely employed (e.g., Johannessen & Steel, 2005; Carvajal & Steel, 2006; Helland-Hansen & Hampson, 2009; Henriksen et al., 2009). This concept assumes that particular classes of trajectory (i.e., descending regressive, ascending regressive and transgressive) relate to depositional trends that, in turn, are a result of variations in accommodation and sedimentation rates at a given break in the depositional profile (shoreline or shelf-margin). Trajectory analysis can be performed with outcrop, well-log and seismic data. When dealing with seismic sections, shoreline breaks are usually undetected because of the low-resolution. In this case shelf-margin trajectory is often taken as a proxy for RLS change.

In the Santos Basin, offshore southeastern Brazil, seismic interpretations of shelf-margin clinoforms and the application of trajectory analysis allowed, for instance, to observe a direct relationship among RSL fall, slope failure events and the formation of mass-transport deposits during the Eocene (Berton & Vesely, 2016). However, the application of these results as a method for reviewing and refining the stratigraphic chart of the basin (e.g., Modica & Brush, 2004; Moreira et al., 2007; Assine et al., 2008) is still to be done. In this paper we analyze the Late Cretaceous to Eocene interval of northern Santos Basin by mapping the shelf-margin trajectory.

The main goal is to reconstruct RSL changes and to provide more detailed information on the sequence-stratigraphic framework of this basin. The Santos Basin has become the most prolific petroleum province in Brazil, with a total oil production that recently overcame that of the Campos Basin, the historical largest oil province in the country (Fernandez & Santos, 2017). Besides the enormous volumes of high-quality oil accumulations in pre-salt carbonates, post-salt turbidites and shallow marine sandstones hold significant amounts of oil and gas in the central and northern sectors of the Santos Basin (e.g., Sombra et al., 1990; Moreira et al., 2007; Assine et al., 2008; Chang et al., 2008).

GEOLOGICAL SETTING

The Santos Basin, offshore Brazil, is located between the Florianópolis lineament and the Cabo Frio high and is bounded landward by the Serra do Mar range, where Precambrian rocks are exposed (Macedo, 1989; Moreira et al., 2007). It is the largest basin of the Brazilian continental margin (Fig. 1) and formed as a result of Gondwana break-up and the opening of the South Atlantic Ocean. The sin-rift phase (Early Cretaceous) accumulated a thick succession of non-marine clastics and carbonates and corresponds to the time during which the most important oil-prone source rocks (lacustrine shale) and pre-salt reservoirs were deposited.

During the Aptian, a transitional or sag phase is associated with the deposition of extensive evaporitic beds in restricted and intermittent marine waters (Ariri Formation). This thick salt package is believed to have formed in clastic starved troughs that were periodically infilled by marine incursions and seepage waters (Karner & Gamboa, 2007). A submarine volcanic ridge parallel to the rift direction (Walvis – Rio Grande Ridge) played a key role in isolating the evaporitic basins from open waters (Karner & Gamboa, 2007; Mohriak, 2014; Buckley et al., 2015), which likely explains the absence of a salt sequence in the southernmost Pelotas Basin. The subsequent post-rift (drift) stage (Fig. 2) starts with the development of a prominent Albian carbonate platform recording the onset of a net-transgressive marine succession extending until the mid-Turonian (Itajaí-Açu Formation). This was followed by a major Late Cretaceous to Late Eocene regressive phase (Pereira & Macedo, 1990) referred to as the Jureia progradation, which has been associated with an increase in sediment supply due to uplifting and denudation in the Serra do Mar region (e.g., Zalán & Oliveira, 2005). The Eocene/Oligocene boundary records an expressive transgressive event that displaced the shelf-margin several tens of km landward. This transgression has been associated with a drastic reduction of clastic input into the Santos Basin because of the capture of the Paraíba do Sul river system (e.g., Zalán & Oliveira, 2005), one of the main sediment sources to the basin during the Jureia progradation. The post-rift evolution of the Santos Basin was highly influenced by salt tectonics. Subsurface displacement of Aptian evaporites controlled sedimentation by creating enhanced accommodation in salt-withdrawal (extensional) proximal regions and forming inter-dome mini-basins in more distal, compression-dominated areas (e.g., Assine et al., 2008; Quirk et al., 2012; Jackson et al., 2015). Among major salt-related structures, the Cabo Frio fault

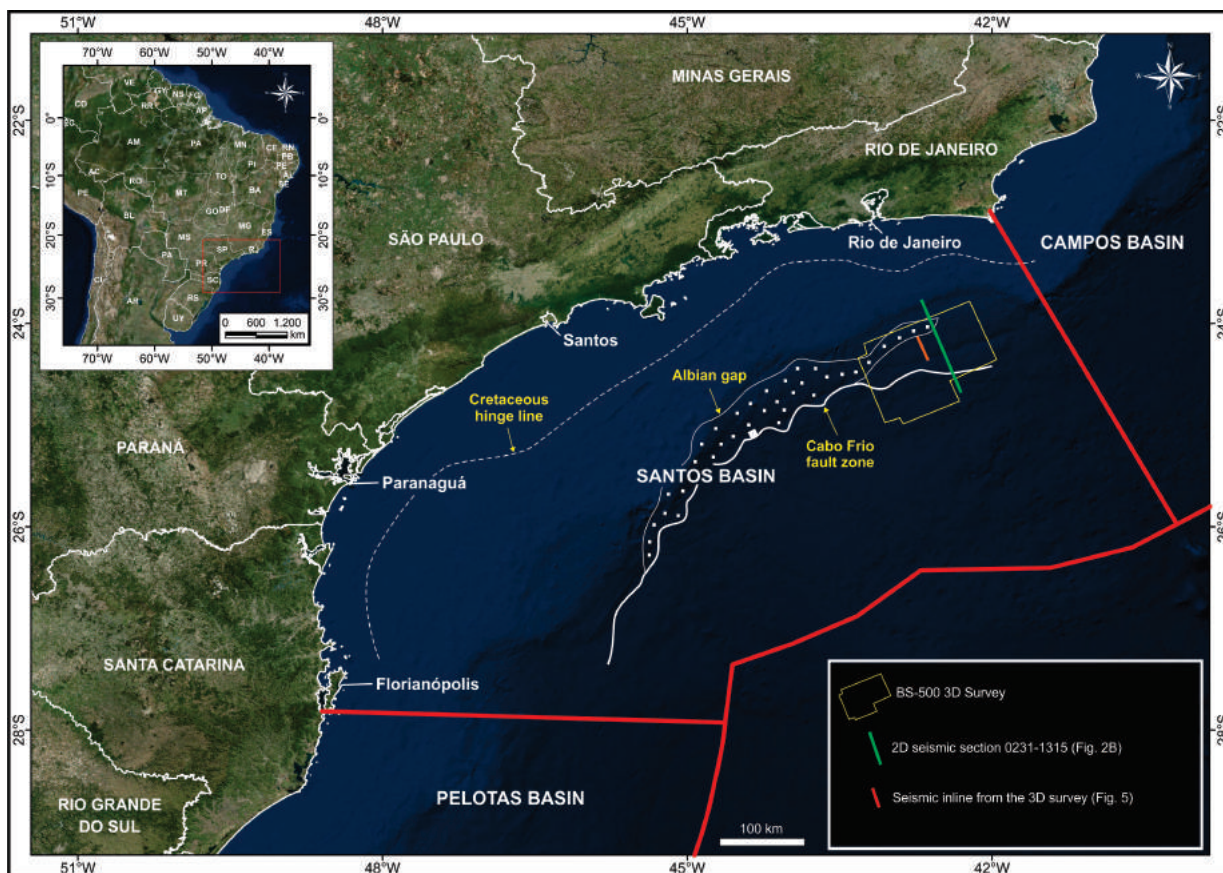


Figure 1 – Location of the study area in northern Santos Basin. Major structural features modified from Assine et al. (2008).

zone (Fig. 1) is a salt-attached, landward-dipping listric fault associated with rollover anticlines and thick growth strata mainly of Late Cretaceous age (e.g., Assine et al., 2008). The Albian gap (e.g., Mohriak et al., 1995; Jackson et al., 2015) is a structural feature related to rafting of Albian shelfal carbonates because of the basinward flow of underlying salt, which created a “gap” where the Albian succession is missing. The Albian gap and the Cabo Frio fault zone are genetically linked and the origin of both structures is due to a combination of gravity-driving salt withdrawal, carbonate rafting and growth faulting triggered by tilting and sediment overloading during the Jureia progradation (e.g., Jackson et al., 2015).

The interval examined in this paper (Fig. 2) corresponds to the upper part of the Jureia progradation (Late Campanian to Late Eocene). It has been previously studied mainly because of high-quality seismic data allowing the description of prograding clinoforms and thick chaotic units (mass-transport complexes) in greater detail. The stratigraphic architecture of the Eocene clinoforms has been analyzed (Moreira & Carminatti, 2004;

Berton & Vesely, 2016) as well as the external and internal framework of recurrent mass-transport complexes (Carlotto & Rodrigues, 2009; Jackson, 2011). Carlotto & Rodrigues (2009) did a detailed 3D characterization of a Maastrichtian mass-transport complex termed by them as the “Maricá slump”, which is located at the lower part of the examined succession.

METHODS AND KEY DEFINITIONS

This study is based on the stratigraphic analysis of a post-stack time migrated, dip-oriented (NW-SE) seismic inline of the BS500 3D seismic survey. A 2D seismic section (survey Santos 18A 0231) was also examined to place the results in a more regional context (Fig. 1). Data were provided by the Brazilian Agency of Petroleum, Gas and Biofuels (ANP). The inline is bounded by the UTM coordinates $X=730.082$; $Y=7.329.496$ (proximal edge) and $X=740.521$; $Y=7.303.325$ (distal edge), is 28 km long and is located on the modern continental slope of northern Santos Basin in water depths from 879 to 1485 m. The examined interval comprises about 1800 ms (TWT) and is limited at the top by

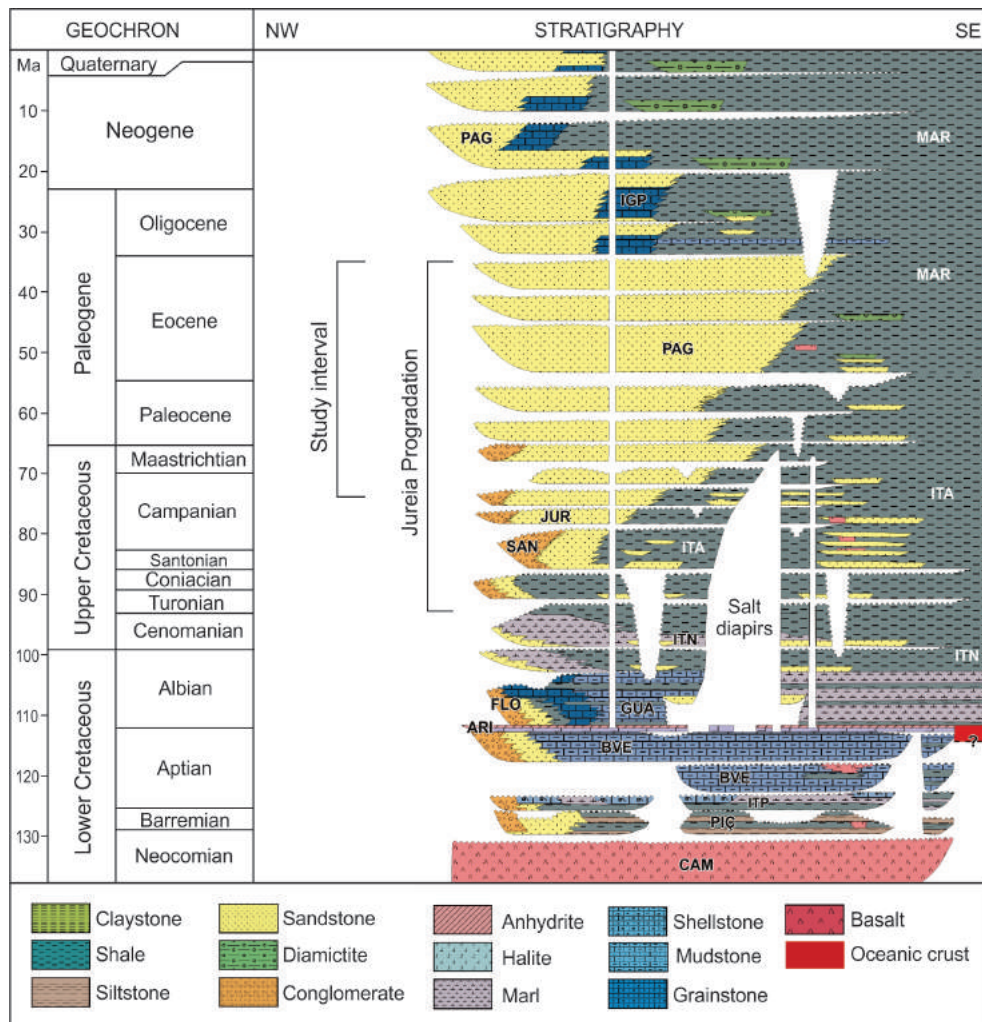


Figure 2 – Stratigraphic chart of the Santos Basin (adapted from Moreira et al., 2007) highlighting the study interval in the context of the Jureia Progradation. Key for lithostratigraphic names: CAM, Camboriú; PIÇ, Piçarras; ITP, Itapema; BVE, Barra Velha; ARI, Ariri; FLO, Florianópolis; GUA, Guarujá; ITN, Itanhaém; ITA, Itajaí-Açu; SAN, Santos; JUR, Jureia; PAG, Ponta Aguda; MAR, Marambaia; IGP, Iguape.

the Eocene/Oligocene maximum flooding surface and at the base by the oldest recognizable shelf-margin clinoform set of likely Campanian age (e.g., Moreira et al., 2007).

Seismic stratigraphy assumes that seismic reflections in sedimentary basins correspond to physical discontinuities related to former depositional surfaces (Vail et al., 1977), thus indicating paleo-sea floors morphology in marine basins. The geometric arrangement of seismic reflections can thus be analyzed based on types of terminations (e.g., onlap, downlap and truncation), providing a way to detect changes in depositional trends (progradation and retrogradation) and key stratigraphic surfaces such as depositional sequence boundaries (Posamentier

et al., 1988; Catuneanu, 2006; Catuneanu et al., 2011). If well-defined, shelf-slope profiles can be identified on reflectors, temporal changes in the position of former shelf margins (shelf-margin trajectory; Fig. 3) can be mapped and correlated to RSL changes (e.g., Helland-Hansen & Hampson, 2009; Henriksen et al., 2009).

RSL is defined as the sea level relative to a datum at the top of the basement and is controlled by global eustasy and vertical movements of the lithosphere (uplift and subsidence). The shoreline works as a proxy for RSL in such a way that with high-resolution datasets (outcrops and cores) changes in RSL can be recognized by tracing the shoreline trajectory. In this paper

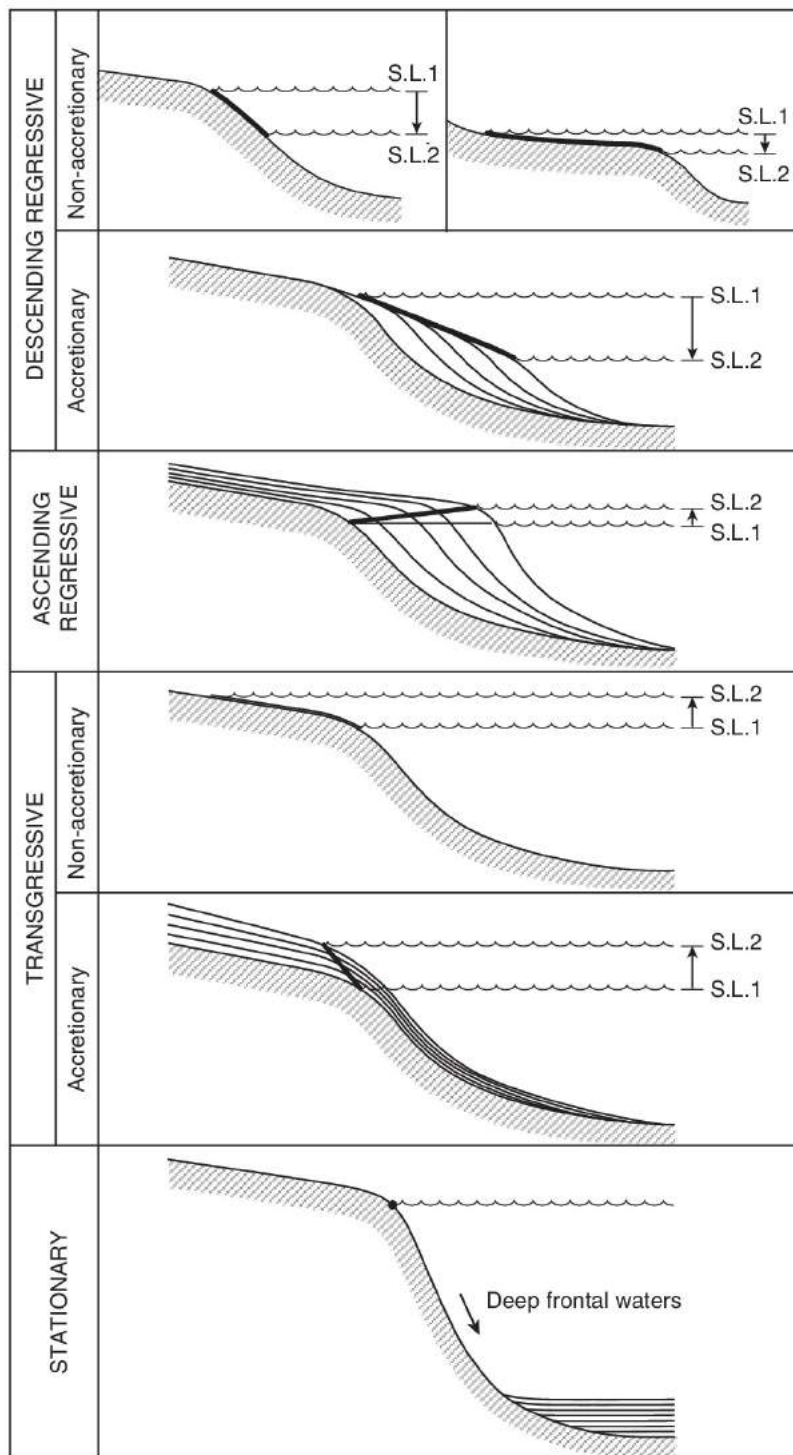


Figure 3 – The concept of trajectory according to Helland-Hansen & Hampson (2009).

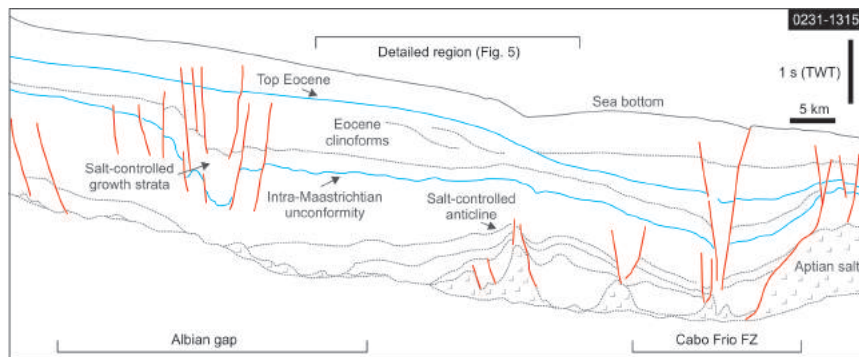


Figure 4 – Line drawing of a dip-oriented 2D seismic section highlighting the main post-rift structural features in the study area.

we adopt the premise that the shelf-margin adjusts to RSL, so the vertical component of shelf-margin trajectory at the seismic scale (low vertical resolution) approaches RSL fluctuations.

RESULTS

Figure 4 is a dip-oriented seismic interpretation of the post-rift interval in northern Santos Basin (see location in Fig. 1), in which the area examined herein can be tied to the overall geological context and the influence of salt tectonics be observed. The study area lies between the Albian gap and the Cabo Frio fault zone. In the more proximal domain, the interval of interest (roughly delimited by blue horizons; Fig. 4) is affected by an extensional fault zone that promotes stratal rollover, tilting and the development of growth strata. In the more distal segment, underlying beds are deformed by a gentle anticline floored by a set of salt domes. This anticline seems to be also controlled by stratal rollover associated with the Cabo Frio fault zone located few kilometers basinward.

The studied interval is dominated by sets of high- to moderate-relief (up to 400 m-thick) prograding clinoforms with a well-defined topset-foreset-bottomset morphology (Fig. 5-A). The overall framework observed in Figure 4 strongly suggests that stratal tilting related to extensional faulting was the mechanism that created the initial slope from which clinoforms prograded. The topset domain of the clinoforms may be aggradational or degradational, the latter being recorded as erosive unconformities that extend throughout the topset profile and truncate upper foreset strata. These unconformities are often associated with deep incisions with reliefs up to 150 m filled with high-amplitude and laterally discontinuous reflectors or transparent units. Aggradational topsets form parallel to divergent, high- to moderate-amplitude reflector packages.

The lower foreset and bottomset domain commonly display high-amplitude reflections and chaotic units that onlap the inclined foresets. The chaotic units are most typically 50 to 200 m thick, they have lenticular to sigmoidal geometry and exhibit internal deformation (faults, folds and tilted strata). In some stratigraphic levels these units are clearly associated upslope with steep scars that truncate the basinward segment of aggradational topset deposits. The prograding clinoforms can be interpreted as a product of shelf-margin accretion because of their relief of up to hundreds of meters (e.g., Helland-Hansen & Hampson, 2009). The bottomset high-amplitude and chaotic facies likely correspond to deepwater sands and mass-transport deposits respectively (e.g., Posamentier & Martinsen, 2011). A total of 40 seismic horizons were mapped (Fig. 5-B) and their correspondent stratal terminations (onlap, downlap and truncation) recognized. Clinoform rollovers (i.e., paleo-shelf margins) were picked for each horizon whenever possible and assumed as proxies for former positions of RSL. These data were used to build a trajectory diagram (Fig. 5-C) and a chronostratigraphic chart from which a RSL curve was interpreted (Fig. 6).

Relative ages for mapped key surfaces and stratigraphic intervals were determined by correlation with previous stratigraphic schemes (e.g., Modica & Brush, 2004; Moreira et al., 2007). Recognized shelf-margin trajectories include 1) flat to descending regressive (forced regression), 2) ascending regressive (normal-regressive) and 3) transgressive. Forced-regressive trends dominate the stratigraphy whereas transgressive trends are scarce. Ten main unconformities and their correlative conformities (sequence boundaries; SB01 to SB10) are recognized, corresponding to changes from forced- to normal-regressive or transgressive trends and limiting sequences lasting for approximately 3,5 My each. Two of these

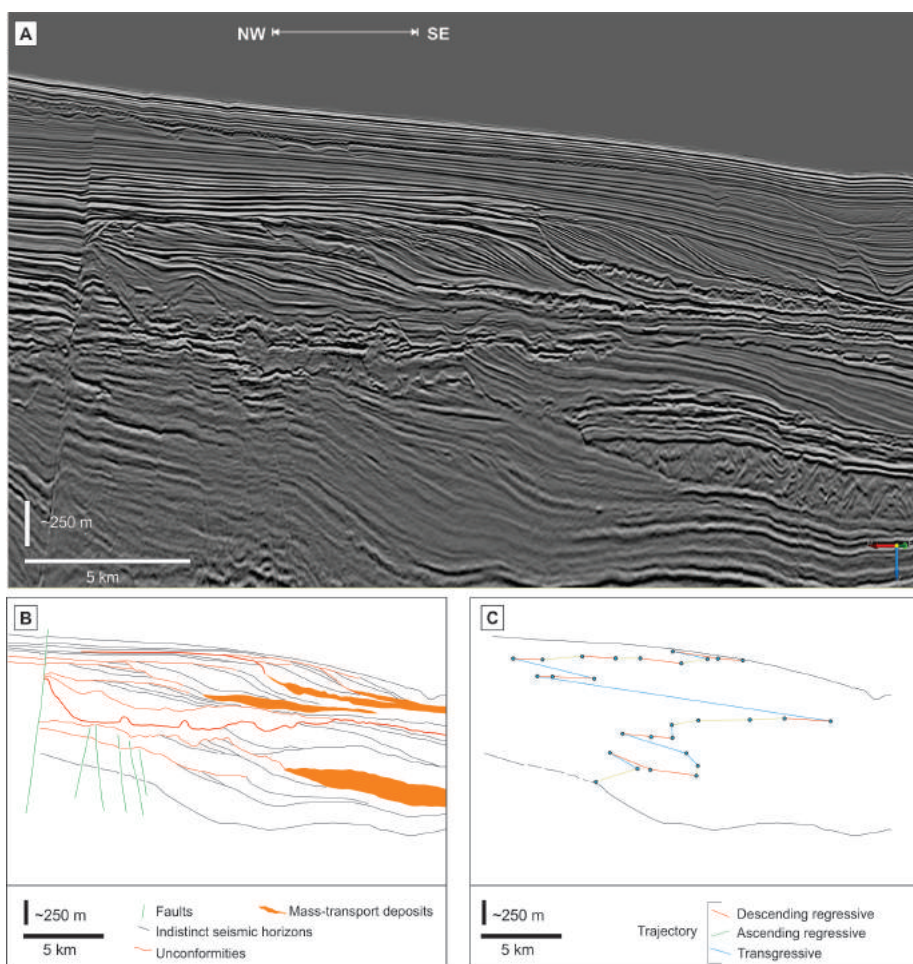


Figure 5 – Stratigraphic interpretations derived from the studied seismic section. A) Uninterpreted seismics. B) Line drawing showing the main mapped horizons and seismic facies. C) Shelf-margin trajectory diagram based on 28 recognized topset-foreset rollovers.

boundaries (SB03 and SB08) are remarkable for their larger time amplitude and because they record the most significant basinward shifts of onlapping surfaces. They are interpreted as lower order sequence boundaries and divide the stratigraphy into three sequence sets (SS01: Campanian-Maastrichtian; SS02: Paleocene; SS03: Eocene to earliest Oligocene) containing three to four higher-order sequences.

The Campanian-Maastrichtian sequence set has the largest amount of topset aggradation, materialized as a relatively high average angle of the shelf-margin trajectory and a low progradation/aggradation ratio ($P/A = 23$). In contrast, the overlying sequence sets present a more prominent progradational pattern (Paleocene $P/A = 65$; Eocene $P/A = 54$) and low-angle to descending regressive trajectories are more common (Fig. 5-C).

Three main transgressive episodes (T01 to T03) are identified, which were responsible for shifting the shelf-margin several km landwards. In the distal end of the section, significant non-depositional hiatuses appear associated with the downlap terminations of clinoform packages. The hiatuses with the largest temporal amplitude and farthest landward expression occur in SS02 (Paleocene) and are associated with the longest verified period of high RSL (Fig. 6). All the four main mass-transport deposits recognized (chaotic units) are related to forced-regressive trajectories, indicating emplacement during RSL falls (Fig. 6). Deepwater sands (high-amplitude bottomsets), on the other hand, seem to occur associated with both normal- and forced-regressive clinoform packages, indicating deposition during both falls and rises in RSL. The origin of these deepwater

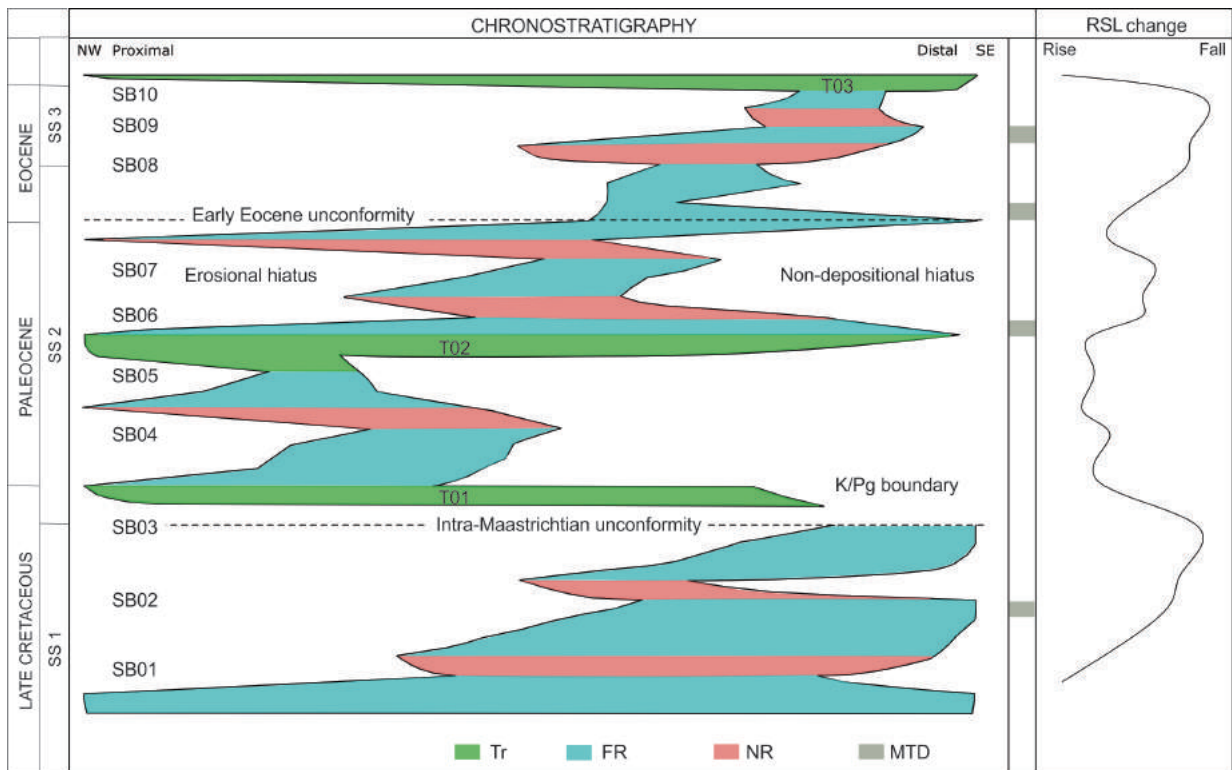


Figure 6 – Chronostratigraphic chart and RSL curve for the Late Cretaceous to Paleogene succession in northern Santos Basin. Tr, transgression; FR, forced regression; NR, normal regression; MTD, mass-transport deposit.

sands is uncertain because it was not possible to observe their geometry in map view in our dataset. However, based on previous work, they probably include an association of turbidite fans and bottom-current-related deposits (Moreira & Carminatti, 2004; Duarte & Viana, 2007; Berton & Vesely, 2016).

DISCUSSION

Recently, the overall sequence-stratigraphic framework of the Santos Basin was discussed in three main publications (Modica & Brush, 2004; Moreira et al., 2007; Assine et al., 2008). These authors subdivided the basin into a number of depositional sequences bounded by regional unconformities that reflect drops in base level or sediment starvation conditions. Our examination of the shelf-margin trajectory based on a local, but high-quality, seismic survey provides a more detailed understanding of the stratigraphic evolution for the Late Cretaceous to Paleogene interval of the basin. By comparison with those previous papers, the examined interval encompasses sequences 5 to 8 of Modica & Brush (2004), sequences K120, K130 and E10 to E60 of Moreira et al. (2007) and sequences H7-H7.1 to H8-H8.2 according to Assine et al. (2008).

The sequence SB03 defined in this work is equivalent to the “intra-Maastrichtian unconformity” (Moreira et al., 2007), “sequence boundary 6” (Modica & Brush, 2004) and horizon H7.1 (Assine et al., 2008). This unconformity, dated as 68,8 Ma, is the base of a sedimentary package recording the maximum seaward displacement of the shelf-margin during the Cretaceous (Moreira et al., 2007), which coincide with the interval showing the highest P/A rates in our study. According to the model of Modica & Brush (2004), SB03 does not have a good correlation with a major eustatic fall. RSL fall at that time was thus probably driven by uplifting at the Serra do Mar region during the Late Cretaceous (e.g., Zalán & Oliveira, 2005) or, alternatively, a result of local sin-depositional deformation related to halokinesis.

The prominent landward shift of the shelf-margin observed close to the K/Pg boundary (T01) matches with a transgressive event indicated by Moreira et al. (2007), but does not seem to be related to any important eustatic peak. As our study is based on one single section in the northern part of the basin, this event is probable related to local (e.g., lowering sediment supply, salt induced subsidence) instead of global drivers.

In contrast with the stratigraphic chart of Moreira et al. (2007), our chronostratigraphic diagram (Fig. 6) highlights the presence of important non-depositional hiatuses in the distal part of the basin. These times of very low sedimentation rates in the basin are more pronounced during SS02 (Paleocene), which correspond to a period of eustatic highstand (Modica & Brush, 2004) and encompasses two of the three transgressive episodes observed in the study area. The detection of these underreported time intervals of sediment starvation may have implications for the location of organic-rich layers (condensed sections) with petroleum source rock potential.

Concerning the occurrence of mass-transport deposits, our analysis corroborates the results obtained by Berton & Vesely (2016) in the Eocene, who linked submarine landslides to RSL falls. This correlation is also clear in the Late Cretaceous succession (SS01), in which a huge mass-transport deposit (Maricá slump; Carlotto & Rodrigues, 2009) is genetically linked to an irregular surface that deeply incises the outer shelf and upper slope (SB02 in the present paper). Concerning eustatic sea level, the whole studied interval is placed during a long-term sea level fall (Modica & Brush, 2004). This may explain why there is a general decrease in the amount of estimated topset aggradation (SS01 = 620 m; SS02 = 200 m; SS03 = 120 m), which is probable a result of progressively lower accommodation rates at the shelf from the Late Cretaceous to the Eocene. Higher-frequency cyclicity, however, does not fit well with eustatic sea level changes and seems to be related to local factors such as tectonics, changes in sediment supply and sedimentation rates and halokinesis.

Late Cretaceous to Eocene deepwater sands were previously indicated as important exploratory plays in northern Santos Basin (Chang et al., 2008). High-amplitude reflectors corresponding to these deposits occur at the bottomsets of clinoforms with both normal- and forced-regressive trajectories (see also Berton & Vesely, 2016) and seems to be unpredictable using sequence stratigraphy. However, those deepwater sands that are genetically related to base level drops are more often placed below and/or above mass-transport deposits. This may be prejudicial to seal effectiveness once these mass-transport deposits, which are chaotic, admixtures of fine and coarse-grained sediment (e.g., Carlotto & Rodrigues, 2009), tend to be less argillaceous than pelagic/hemipelagic muds.

CONCLUSIONS

From the interpretation of a high-quality dip-oriented seismic section, it was possible to expand the knowledge about the

stratigraphic framework of the post-rift succession in northern Santos Basin:

- The studied interval comprises Campanian-Maastrichtian, Paleocene and Eocene to earliest Oligocene sequence sets. Each of those contains three to four higher-order sequences lasting approximately 3.5 My. Most of these higher-order sequences include forced-regressive and normal-regressive shelf-margin trajectories associated with long-term RSL falls and relatively high sediment supply from the uplifted Serra do Mar region. Only three expressive transgressive episodes were identified, two of them during the Paleocene, which correlates to a period of higher eustatic sea level;
- The emplacement of voluminous mass-transport deposits triggered by clinoform instability in both the Cretaceous and Paleogene sequences can be associated with relative sea level falls observed as descending shelf-margin trajectories;
- Significant unreported non-depositional hiatuses were identified in the distal termination of shelf-margin clinoforms, which, because of sediment starvation conditions may be important to the generation of organic-rich layers with petroleum source rock potential. This is a major difference between our results and previous stratigraphic interpretations for the Santos Basin.

ACKNOWLEDGMENTS

This work was conducted during a sequence stratigraphy class of the Postgraduate Program in Geology at UFPR. The authors thank Agência Nacional do Petróleo, Gás Natural e Biocombustíveis (ANP) for seismic data. Coordenação de Aperfeiçoamento de Pessoal de Nível Superior (CAPES) is thanked for providing scholarships to A.M.G. and C.E.S. F.F.V. thanks Conselho Nacional de Desenvolvimento Científico e Tecnológico (CNPq) for financial support (grants 461650/2014-2 and 302842/2017-9). The authors also thank Webster Mohriak for helpful suggestions that improved the quality of the manuscript.

REFERENCES

ASSINE ML, CORRÊA FS & CHANG HK. 2008. Migração de depocentros na Bacia de Santos: importância na exploração de hidrocarbonetos. *Revista Brasileira de Geociências*, 38: 111–127. doi: 10.25249/0375-7536.2008382S111127.

- BERTON F & VESELY F. 2016. Stratigraphic evolution of Eocene clinoforms from northern Santos Basin, offshore Brazil: Evaluating controlling factors on shelf-margin growth and deep-water sedimentation. *Marine and Petroleum Geology*, 78: 356–372. doi: 10.1016/j.marpetgeo.2016.09.007.
- BUCKLEY JP, BOSENCE D & ELDERS C. 2015. Tectonic setting and stratigraphic architecture of an Early Cretaceous lacustrine carbonate platform, Sugar Loaf High, Santos Basin, Brazil. Geological Society, London, Special Publications, 418: 175–191. doi: 10.1144/SP418.13.
- CARLOTTO M & RODRIGUES L. 2009. The Maricá Slump - Anatomy of a Maastrichtian gravity mass flow deposit, Santos Basin. *Boletim de Geociências da Petrobras*, 18: 51–67.
- CARVAJAL CR & STEEL RJ. 2006. Thick turbidite successions from supply-dominated shelves during sea-level highstand. *Geology*, 34(8): 665–668. doi: 10.1130/G22505.1.
- CATUNEANU O. 2006. Principles of Sequence Stratigraphy. Boston: Elsevier. 375 pp.
- CATUNEANU O, GALLOWAY WE, KENDALL CGSC, MIALL AD, POSAMENTIER HW, STRASSER A & TUCKER ME. 2011. Sequence stratigraphy: methodology and nomenclature. *Newsletters on Stratigraphy*, 44(3): 173–245.
- CHANG HK, ASSINE ML, CORRÊA FS, TINEN JS, VIDAL AC & KOIKE L. 2008. Sistemas petrolíferos e modelos de acumulação de hidrocarbonetos na Bacia de Santos. *Revista Brasileira de Geociências*, 38(2 suppl): 29–46.
- DUARTE CSL & VIANA AR. 2007. Santos Drift System: stratigraphic organization and implications for late Cenozoic palaeocirculation in the Santos Basin, SW Atlantic Ocean. Geological Society, London, Special Publications, 276(1): 171–198.
- FERNANDEZ RO & SANTOS AJ. 2017. Bacia de Santos: Sumário Geológico e Setores em Oferta. Superintendência de Definição de Blocos. 14ª Rodada de Licitações da ANP, Brazil.
- HELLAND-HANSEN W & HAMPSON G. 2009. Trajectory analysis: concepts and applications. *Basin Research*, 21(5): 454–483.
- HENRIKSEN S, HAMPSON GJ, HELLAND-HANSEN W, JOHANNESSEN EP & STEEL RJ. 2009. Shelf edge and shoreline trajectories, a dynamic approach to stratigraphic analysis. *Basin Research*, 21(5): 445–453.
- JACKSON CAL. 2011. Three-dimensional seismic analysis of megaclastic deformation within a mass transport deposit; implications for debris flow kinematics. *Geology*, 39(3): 203–206.
- JACKSON CAL, JACKSON MPA & HUDEC MR. 2015. Understanding the kinematics of salt-bearing passive margins: A critical test of competing hypotheses for the origin of the Albian Gap, Santos Basin, offshore Brazil. *GSA Bulletin*, 127(11-12): 1730–1751.
- JOHANNESSEN EP & STEEL RJ. 2005. Shelf-margin clinoforms and prediction of deepwater sands. *Basin Research*, 17(4): 521–550.
- KARNER GD & GAMBOA LAP. 2007. Timing and origin of the South Atlantic pre-salt sag basins and their capping evaporites. Geological Society, London, Special Publications, 285(1): 15–35.
- MACEDO JM. 1989. Evolução tectônica da Bacia de Santos e áreas continentais adjacentes. *Boletim de Geociências da Petrobras*, 3: 159–173.
- MODICA CJ & BRUSH ER. 2004. Postrift sequence stratigraphy, paleogeography, and fill history of the deep-water Santos Basin, offshore southeast Brazil. *AAPG Bulletin*, 88(7): 923–945.
- MOHRIAK W. 2003. Bacias sedimentares da margem continental brasileira. In: BIZZI LA, SCHOBENHAUS C, VIDOTTI RM & GONÇALVES JH (Eds.). *Geologia, Tectônica e Recursos Minerais do Brasil*. CPRM, Brazil. p. 87–165.
- MOHRIAK W. 2014. Birth and development of continental margin basins: Analogies from the South Atlantic, North Atlantic, and the Red Sea. *AAPG Search and Discovery Article #41502*.
- MOHRIAK WU, MACEDO JM, CASTELLANI RT, RANGEL HD, BARROS AZN, LATGÉ MAL, RICCI JA, MIZUSAKI AMP, SZATMARI P, DEMERCIAN LS, RIZZO JG & AIRES JR. 1995. Salt tectonics and structural styles in the deep-water province of the Cabo Frio region, Rio de Janeiro, Brazil. *American Association of Petroleum Geologists Memoir*, 65: 273–304.
- MOREIRA J & CARMINATTI M. 2004. Eocene slope and basin depositional systems in the Santos Basin. *Boletim de Geociências da Petrobras*, 12: 73–87.
- MOREIRA J, CV M, GIL J & MACHADO M. 2007. Bacia de Santos. *Boletim de Geociências da Petrobras*, 15: 531–549.
- PEREIRA M, BARBOSA C, AGRA J, GOMES J, ARANHA L, SAITO M & BAGNI O. 1986. Estratigrafia da Bacia de Santos: análise das seqüências, sistemas deposicionais e revisão litoestratigráfica. In: 34 Congresso Brasileiro de Geologia. Anais, Goiânia, Brazil, p. 65–79.
- PEREIRA M & MACEDO J. 1990. A Bacia de Santos: perspectivas de uma nova província petrolífera na plataforma continental sudeste brasileira. *Boletim de Geociências da Petrobras*, 4: 3–11.
- PEREIRA MJ & FEIJÓ FJ. 1994. Bacia de Santos. *Boletim de Geociências da Petrobras*, 8: 219–234.
- POSAMENTIER HW, JERVEY MT & VAIL PR. 1988. Eustatic controls on clastic deposition I – conceptual framework. *SEPM Special Publication*, 42: 109–124. doi: 10.2110/pec.88.01.0109.
- POSAMENTIER HW & MARTINSEN OJ. 2011. The character and genesis of submarine mass-transport deposits: insights from outcrop and 3D seismic data. In: SHIPP RC, WEIMER P & POSAMENTIER HW (Eds.). *Mass-transport deposits in deepwater settings*. Volume 96, p. 7–38. Tulsa: SEPM Special Publication. doi: 10.2110/sepmsp.096.007.

- QUIRK DG, SCHØDT N, LASSEN B, INGS SJ, HSU D, HIRSCH KK & VON NICOLAI C. 2012. Salt tectonics on passive margins: examples from Santos, Campos and Kwanza basins. Geological Society, London, Special Publications, 363(1): 207–244.
- SOMBRA CL, ARIENTI LM, PEREIRA MJ & MACEDO JM. 1990. Parâmetros controladores da porosidade e da permeabilidade nos reservatórios clásticos profundos do Campo de Merluza, Bacia de Santos, Brasil. Boletim de Geociências da Petrobras, 4(4): 451–466.
- VAIL PR, MITCHUM Jr RM & THOMPSON S. 1977. Seismic stratigraphy and global changes of sea level: Part 3. Relative changes of sea level from Coastal Onlap: Section 2. Application of seismic reflection Configuration to Stratigraphic Interpretation. AAPG Special Volumes, 26: 63–81.
- ZALÁN PV & OLIVEIRA JAB. 2005. Origem e evolução estrutural do Sistema de Riftes Cenozóicos do Sudeste do Brasil. Boletim de Geociências da Petrobras, 13(2): 269–300.

Recebido em 30 novembro 2018 / Aceito em 6 maio 2019

Received on November 30, 2018 / Accepted on May 6, 2019

EVAPORITIC VELOCITY MODELING UNCERTAINTIES AND VARIABILITIES: IMPLICATIONS FOR PRE-SALT PROJECTS IN THE SANTOS BASIN, BRAZIL

Alexandre Rodrigo Maul^{1,2}, Marco Antonio Cetale Santos², Cleverson Guizan Silva²,
María de Los Ángeles González Farias³, Josué Sá da Fonseca¹,
Filipe Augusto de Souto Borges¹ and Carlos Eduardo Borges de Salles Abreu¹

ABSTRACT. Correct representation of the spatial distribution of physical and chemical properties of the evaporitic section is of great importance for development of pre-salt section reservoirs. In the offshore Santos Basin, SE Brazil, an increasing amount of high quality seismic, well-logs, and production data are available. The initial conceptual model of the evaporitic section, assuming inhomogeneous behaviors in terms of mineral composition, acoustic and elastic properties, had not been well documented yet. Therefore, this interval remains considered as mainly composed by halite, being slightly modified to include a few heterogeneities when needed. A simple way to represent those heterogeneities is by combining seismic attributes and well-log information, which are usually not available for the whole evaporitic section. To mitigate this problem, drill cuttings description can be used. In this paper, we describe some of the uncertainties related to the analysis of 1D information from wells, as well as a possible alternative to represent the data variability where information is missing. The proposed methodology includes generating a detailed evaporitic section model (3D), including properties and their related uncertainties. This model can be used to improve seismic imaging, depth positioning forecast and reservoir property values distribution.

Keywords: evaporitic section, data analysis, heterogeneities, property value, uncertainties.

RESUMO. Representar corretamente a distribuição espacial das propriedades físicas e químicas da seção evaporítica é muito importante no desenvolvimento dos reservatórios do pré-sal. Na Bacia *offshore* de Santos, região SE do Brasil, grande quantidade de dados sísmicos de alta qualidade, perfis de poço, dados de produção estão disponíveis. O modelo conceitual desta seção, assumindo o mesmo como não homogêneo, em termos de mineralogia e propriedades acústicas e elásticas, ainda não é bem documentado. Assim, este intervalo permanece sendo considerado como, principalmente, composto por halita e, localmente, modificado para incluir algumas heterogeneidades, quando necessário. Um caminho simples para representar estas heterogeneidades é combinar atributos sísmicos e informações dos perfis de poços que, usualmente, não estão disponíveis para toda a seção. Para mitigar este problema, descrição de amostras de calhas pode ser utilizada. Neste artigo, nós descreveremos algumas das incertezas relacionadas a esta análise 1D, oriundas das informações dos poços, assim como uma possível alternativa para representar as variabilidades destes dados inexistentes. A metodologia proposta inclui a geração de um modelo (3D) detalhado da seção evaporítica, incluindo suas propriedades e as incertezas relacionadas. Este modelo pode ser utilizado para melhorar as imagens sísmicas, com previsões de profundidade mais acuradas, e a distribuição de valores de propriedades de reservatórios.

Palavras-chave: seção evaporítica, análise de dados, heterogeneidades, valores de propriedades, incertezas.

¹Petrobras - Reservoir Geophysics, Av. República do Chile, 330, 9º andar, 20031-170 Rio de Janeiro, RJ, Brazil – E-mails: alexandre.maul@petrobras.com.br, josuefonseca@petrobras.com.br, filipeborges@petrobras.com.br, ceduardoabreu@petrobras.com.br

²Universidade Federal Fluminense – UFF, Geology and Geophysics, Av. Milton Tavares de Souza, s/nº - Gragoatá, 24210-340 Niterói, RJ, Brazil – E-mails: marcocetale@id.uff.br, cguizan@id.uff.br

³Emerson Automation Solutions, Av. Rio Branco, 138, sala 1702, 20040-002 Rio de Janeiro, RJ, Brazil – E-mail: maria.g.gonzalez@emerson.com

INTRODUCTION

Successful implementation of pre-salt projects in Brazilian ultra-deep waters, where huge capital investments are required, is highly dependent on the robustness and confidence of the available reservoir models. The first discovery of these large hydrocarbon reserves along the southeastern coast of Brazil happened in 2006, and represented a new chapter in global petroleum history. Since then, Petrobras has been facing major multidisciplinary technological challenges, sponsoring massive investments in research and development, working in collaboration with partners, suppliers, universities, and research centers, to economically explore these reserves in a sustainable way.

The construction of reliable velocity models, according to the known geology, enables the generation of seismic images that better represent the subsurface, both in terms of structural positioning and accurate seismic response. Jones & Davison (2014) report the challenge of seismic imaging close to (or inside) salt bodies, due to the high velocity contrasts observed in those areas. Operational safety and drilling hazards are other issues widely discussed in the literature of field development when salt bodies are present.

Most halokinetic models used to reconstruct the basin's structural styles consider the salt section as almost homogeneous, with predominance of halite (Demercian et al., 1993; Ings et al., 2004; Guerra & Szatmari, 2009; Guerra & Underhill, 2012). The concept of salt flooding is a common approach in seismic processing, and involves the assignment of a constant velocity to the evaporitic section prior to the tomographic inversion process to update it (Guo & Fagin, 2002; Zdraveva et al., 2011). Ji et al. (2011) defend the idea that heterogeneous salt velocity models improve the seismic imaging. Cornelius & Castagna (2018), using well-logs and drill cuttings, confirm that velocity variations exist, and that they must be incorporated into the models. The same concept for the evaporitic section has been widely mentioned in several salt stratifications studies (Maul et al., 2015; Amaral et al., 2015; Meneguim et al., 2015; Maul et al., 2018b, 2019; Teixeira & Lupinacci, 2019).

Regarding these heterogeneities, Schreiber et al. (2007) emphasize that evaporites precipitate due to brine evaporation, forming layers according to their solubility rates, with varying mineral compositions. These authors also mention that comprehension of the water supply to the brines, which breaks the expected salt precipitation order, represents the main difficulty when modeling this sort of mineral deposit. The mobility of

most evaporites also imposes difficulties to quantify the original mineral occurrence from present day information, either using wells or outcrop descriptions. Based on well data, Freitas (2006) identified more than a dozen evaporitic cycles in the Santos Basin, whereas Gamboa et al. (2009) mentioned the presence of 3 or 4 major evaporitic cycles when inspecting seismic data response.

The enigmatic structures presented in Jackson et al. (2015), which are nothing more than observations of folded strata within the evaporitic section, are clear evidences of a heterogeneous behavior. Costa & Poiate Jr (2009), inspecting outcrops and salt mines, confirmed that there are many different minerals inside the evaporitic sections: halite, anhydrite, gypsum, carnallite, tachyhydrite, and sylvite, just to name a few. Aiming at preventing drilling hazards, these authors recommended a detailed identification of the sequence, their mineral compositions, and their behavior under drilling. It is therefore reasonable to assume that the evaporitic section must be considered as heterogeneous instead of being represented by the halite behavior only.

Based on well information, the studies compilation presented by Maul et al. (2018b) proposed clustering the evaporitic minerals into three main groups, observing their compressional velocity. These groups are: (i) the Low Velocity Salts/Evaporites group (LVS), mainly composed by carnallite, tachyhydrite, sylvite and other mobile salts; which present compressional velocities lower than the represented by the halite mineral (4,500 m/s); (ii) the Halite group, usually abundant and considered as the background group; represented by the compressional velocity of about 4,500 m/s; and (iii) the High Velocity Salts/Evaporites group (HVS), basically composed by anhydrite and gypsum, having compressional velocities higher than 4,500 m/s. Intrusive rocks, when found, due to the same velocity behavior as HVS minerals, were also considered inside this group – an approach that has been adopted in many case studies (Meneguim et al., 2015; González et al., 2016; Gobatto et al., 2016; Falcão et al., 2016; Barros et al., 2017; Fonseca et al., 2017, 2018; Teixeira et al., 2018; Maul et al., 2018a,b, 2019; Dias et al., 2019). Fonseca et al. (2017) also observed carbonate and siliciclastic occurrences within the salt section, and suggested to group them within the Halite group, as their velocity behaviors are more similar to this background's group. These rocks, however, lack representativeness.

The workflow proposed by Maul et al. (2016) and presented in González et al. (2016) uses drill cuttings descriptions to fill in gaps observed in the well-logs in the evaporitic section, and

also to constrain the salt velocity modeling, as shown in Figure 1. Even in regions where well data are available, well-logs within the salt section are almost always incomplete, since evaporites are not the main target, and acquiring data in these sections is operationally challenging. To overcome this problem, Amaral et al. (2015) proposed to complete the well information with the described lithology from drill cuttings, a methodology that has been widely reproduced since then (Gobatto et al., 2016; Barros et al., 2017; González et al., 2018; Cornelius & Castagna, 2018; Fonseca et al., 2018; Teixeira et al., 2018; Maul et al., 2018a,b, 2019; Dias et al., 2019).

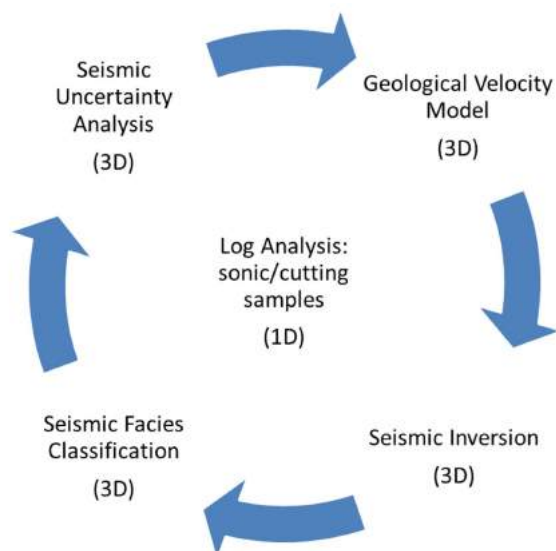


Figure 1 – Proposed workflow to generate a more realistic geological seismic velocity model (adapted from Maul et al., 2016 in González et al., 2016).

This methodology, albeit effective, should be considered as a semi-quantitative approach, mainly due to inexact sample positioning, potential rock collapse during drilling, and inaccuracies in sample descriptions. These factors impose ambiguities in the estimations of rock properties. The distinction between lack of data, inaccuracy in their measurements, uncertainty associated with interpretation, and data variability are in complete agreement with the classic article presented by Begg et al. (2014).

Maul et al. (2018b) demonstrated the wide applications of a reliable geological evaporitic section model, when simultaneously combining seismic attributes and well-logs, such as better seismic imaging, uncertainty analysis, seismic illumination for acquisition design, etc. The authors demonstrated, using several projects, that stratifications insertion inside the evaporitic section is a key aspect to consider for any

seismic purpose. Gobatto et al. (2016), Falcão (2017), Fonseca et al. (2018), Maul et al. (2018a), Dias et al. (2019) and Maul et al. (2019) compared the results obtained by using the proposed methodology for evaporitic velocity model building, in opposed to the ones from conventional velocity models, confirming the benefits of the stratification insertion for seismic imaging in several development and production pre-salt projects.

STUDY AREA AND AVAILABLE DATA

The study area is inserted in the pre-salt province in the Santos and Campos Basins (Fig. 2). A pre-stack depth-migrated (PSDM) volume covering an area of approximately 200 km² is available, together with 14 wells with a broad suite of logs. The Agência Nacional do Petróleo, Gás Natural e Biocombustíveis (ANP) has provided the data we used in this research. In this study, the wells were labeled with capital letters from A to N, and the official names can be found in Table 1. Maul et al. (2018a,c) showed, using almost 182 wells through 9 projects/fields in the Santos Basin, that the evaporitic section of these studied fields has many features in common, such as mineral percentages, mineral percentages x thickness, velocity ranges per mineral groups, etc.

Table 1 – Correspondence between the well designation used in this study and the official names from ANP.

This Study	ANP
A	3-BRSA-788-SPS
B	9-BRSA-1037-SPS
C	8-SPH-23-SPS
D	8-SPH-13-SPS
E	7-SPH-14D-SPS
F	7-SPH-8-SPS
G	7-SPH-4D-SPS
H	9-BRSA-928-SPS
I	7-SPH-5-SPS
J	9-BRSA-1043-SPS
K	1-BRSA-594-SPS
L	7-SPH-1-SPS
M	7-SPH-2D-SPS
N	3-BRSA-923A-SPS

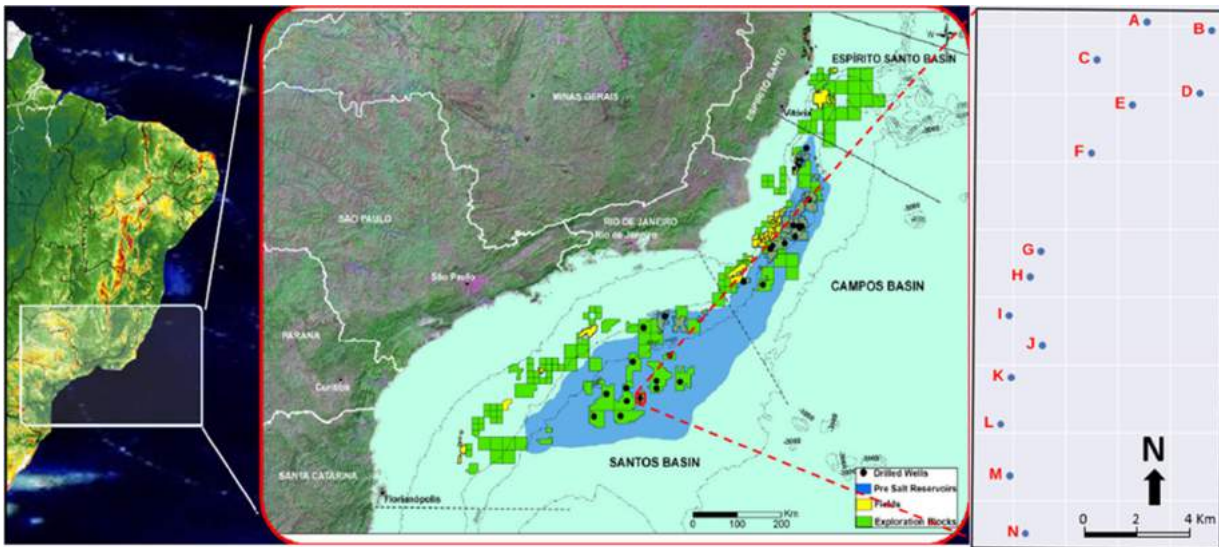


Figure 2 – Location of study area (regional) and details of the available data. Blue shading is the area with hydrocarbon occurrences in the pre-salt province in the Santos and Campos Basins, totaling an area of approximately 350,000 km². Water column ranges 2,000 to 3,000 m. Adapted from: <https://diariodopresal.files.wordpress.com/2010>.

PROPOSED METHODOLOGY

The main goals of this work are twofold: (1) identifying and characterizing the inherent uncertainties when dealing with the evaporitic section; and (2) assessing the property values from acquired logs, in order to build a 3D velocity model for the evaporitic interval.

Drill cuttings and well-logs were used to classify the entire evaporitic section into the three proposed groups: LVS, Halite and HVS. Almost every well which cross the evaporitic section presents a lack in the log-data. Each percentage per well is shown in Table 2.

Instead of using a simple standard velocity values, such as the halite velocity where the data were not acquired, the missing information (the rock/mineral/group) was established using the described lithologies from drilling cuttings, and a single velocity was imposed for each salt group, obtained from the variability/dispersion for each class and the velocity x salt thickness correlation. Therefore, the calculated velocity considering all of these assumptions seems to be more reliable.

RESULTS, ANALYSIS AND DISCUSSIONS

After combining well-logs and drill cuttings, we obtain a complete lithology log for the evaporitic section, for all 14 wells (Fig. 3, for wells I to N). Figure 4 and Table 3 show the percentage distribution for each mineral.

Table 2 – Percentage of registered log in the evaporitic section per well (14). Only a single well (K) has the entire evaporitic section logged.

WELL NAME	REGISTERED LOG (%)	MISSING LOG (%)
A	91.90	8.10
B	87.60	12.40
C	91.10	8.90
D	87.30	12.70
E	77.90	22.10
F	87.20	12.80
G	92.00	8.00
H	91.80	8.20
I	91.40	8.60
J	96.00	4.00
K	100.00	0.00
L	95.60	4.40
M	94.30	5.70
N	94.00	6.00
AVG	91.30	8.70

AVG = Average

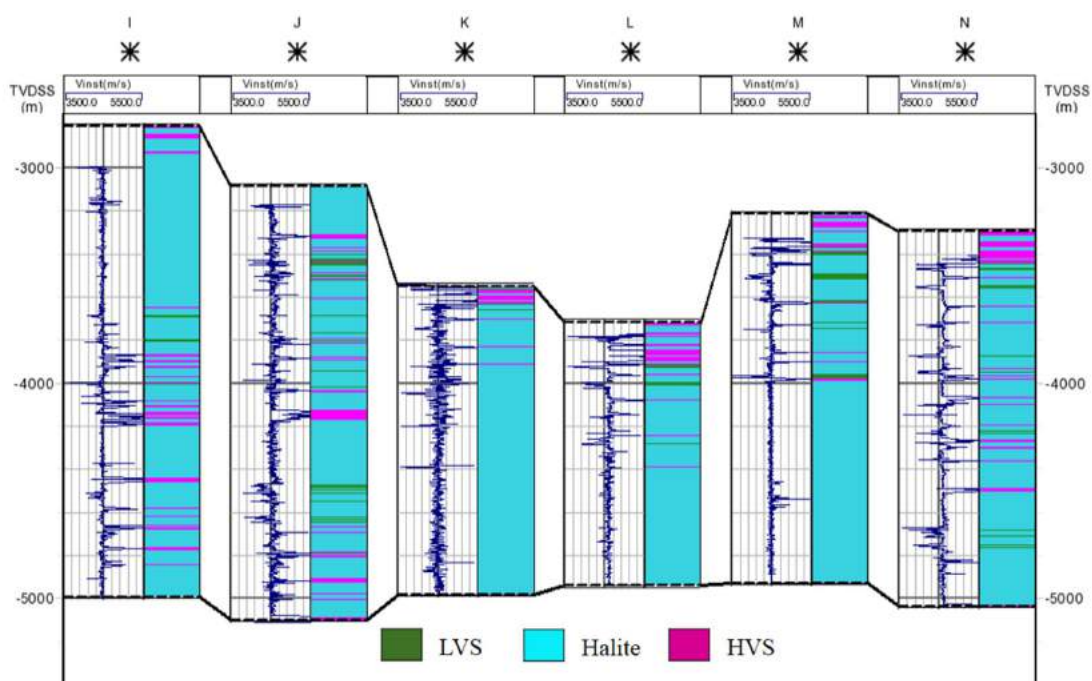


Figure 3 – A piece of a “N-S” stratigraphic cross-section crossing wells from I to N, showing sonic logs (blue lines – left tracks) and lithology group interpretation (right tracks) for the evaporitic section.

Table 3 – Fraction of mineral groups in the evaporitic section, considering registered logs and gap-filling from drill cuttings.

WELL NAME	LVS LOG LITHOTYPE (%)	HALITE LOG LITHOTYPE (%)	HVS LOG LITHOTYPE (%)
A	5.45	86.20	8.35
B	0.50	98.90	0.60
C	6.90	82.70	10.40
D	0.00	91.60	8.40
E	0.30	95.40	4.30
F	1.45	95.40	3.15
G	4.80	92.90	2.30
H	1.20	98.10	0.70
I	1.10	88.80	10.10
J	5.10	83.80	11.10
K	2.12	93.10	4.78
L	3.60	87.20	9.20
M	4.10	89.80	6.10
N	4.60	83.20	12.20
AVG	2.94	90.51	6.55

AVG = Average

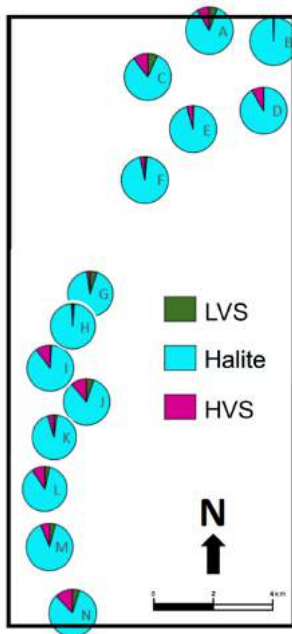


Figure 4 – Fraction of mineral groups in the evaporitic section, considering registered logs and gap-filling from drill cuttings, considering the mineral grouping suggested by Maul et al. (2018b): LVS, Halite and HVS.

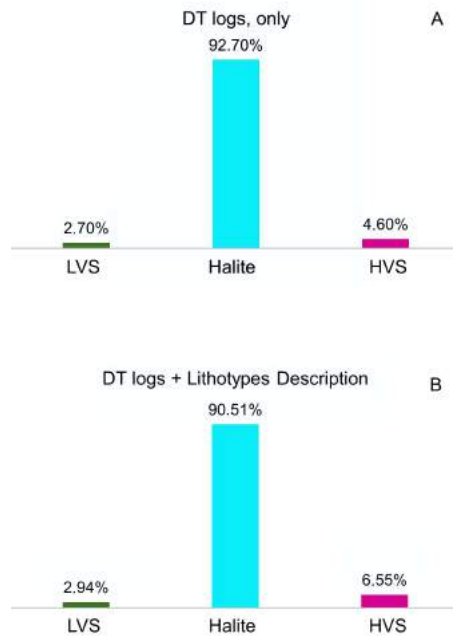


Figure 5 – Distribution of group mineral occurrences for all wells. 5A: Registered sonic logs only. 5B: After gap-filling with drill cuttings.

As expected, Halite is the dominant group in the evaporitic section, averaging over 90%, whereas HVS and LVS are much less frequent, with a higher content of HVS, as already described in literature (e.g., Jackson et al., 2015). We highlight that the HVS group percentage increases almost 50% when considering the gap-filled lithology (Fig. 5). This is the effect of a sampling bias: for safety reasons, changing of drill stages is preceded by placement of a casing shoe. This is commonly done on top and base of the evaporitic section, and blocks proper well-logging. As the top and base of the evaporitic section are classically characterized by anhydrite, this operational constraint leads to under sampling of anhydrite in the entire evaporitic layer.

Velocity distribution for each evaporitic group was also investigated. Figure 6A illustrates the distribution of velocity values for well L, which is the well in our sample that crosses the thinnest evaporitic section (1,280 m). Figure 6B shows the same, but for well B, which crossed the thickest evaporitic section (2,370 m) containing the three classes of salt grouping (LVS, Halite and HVS – the well D, which would be thickest well in this project, has no the LVS occurrence). Notice that well L presents a small dispersion of values, and Halite can be easily separated

from the LVS group. Well B shows a wider range of velocities for halite, which overlaps with the LVS group, rising ambiguous interpretations. The HVS group in well B has a significantly lower interval velocity, also overlapping with halite. Justen et al. (2013) mentioned that thicker evaporitic sections might have resulted from salt mobilization, which promotes mineral mixing. This is particularly stronger for the LVS.

Analysis of all wells together (Fig. 6C) shows a strong velocity overlap for all groups. This is why sometimes a single value is used to represent the whole section - which is clear inaccurate, as it does not capture heterogeneities.

Velocity variability with thickness is usually low for LVS and Halite groups, and higher for HVS (Fig. 7). This is in accordance with the statement presented by Maul et al. (2019). To better understand this variability, the wells are sorted from thinner (left) to thicker (right) evaporitic section. The anhydrite in the HVS group shows a more brittle behavior than Halite and LVS. Therefore, it is reasonable to infer that brittle high velocity evaporites, which are less mobile, better support the compaction effect in the same location, leading to an increase in velocity. The other groups are ductile/plastic and mobile, and

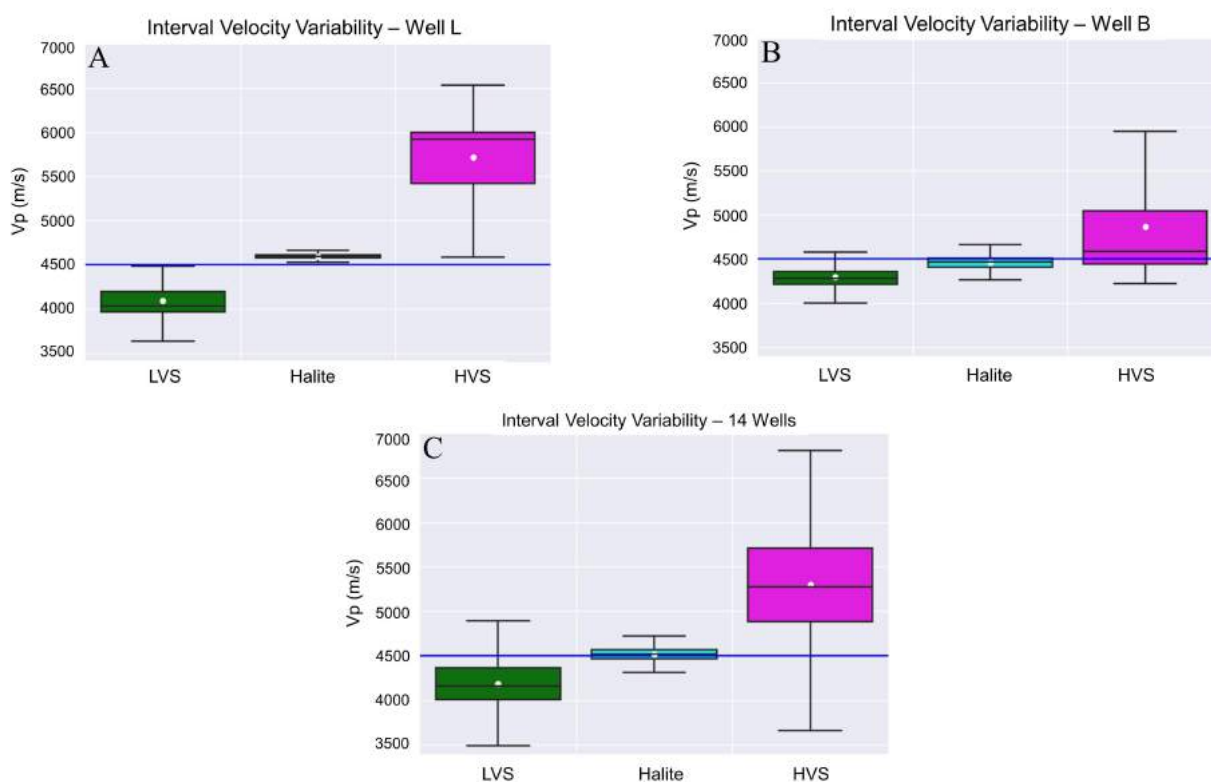


Figure 6 – Standard statistical box-plot representation of interval velocity variability, obtained from available sonic logs. 6A: Well L, where the evaporitic section thickness is around 1,280 m. 6B: Well B, where the evaporitic section thickness is over 2,370 m. 6C: All 14 wells, with an average evaporitic thickness of 1,900 m. Blue lines are the compressional velocity of reference (4,500 m/s), commonly used in the “salt flooding” for seismic migration purposes. White dots within the box-plots are the average value for the mineral group, and black lines are the median. Black bars spam \pm one standard deviation.

probably move under lithostatic pressure, suggesting that the compaction effect is weaker. The weight of the overburden (water + sediments above evaporites + evaporites) above the “salt” base was also considered but, due to its small variation (from 4,950m to 5,130m), it was assumed as negligible.

In order to avoid spurious values from well-log measurement, the lower and higher 5% values were excluded from the analysis. See Figure 7a, for example: a measurement in well C has Vp over 6,000 m/s, which would correspond to HVS and not to LVS values. The LVS velocity without those anomalous values is almost constant, even considering the evaporitic section thickness variation. This reinforces the hypothesis that this group does not suffer the compaction effect, as observed by the linear regression (thin green line). The Halite group (Fig. 7b) has the same behavior. On the other hand, HVS (Fig. 7c) shows greater variability, and an inverse correlation with evaporitic thickness. An explanation for this inverse correlation would be the compaction effect on anhydrites.

The compaction effects seem to be negligible for LVS and Halite, though noticeable for HVS. Our decision for this work was to consider the average values for gap-filling in each group. This is to be decided on a case-by-case basis, after investigation of a large number of wells and grouping them in representative classes, such as section thickness and burial depth. As shown in Table 2, about 8.70% of the well-logs are missing. Representing these missing values as constant artificially reduces the variability of our dataset, as we are replacing several values by a single one.

The next step is to estimate the velocity variations inside the evaporitic section. Lithology identification by itself is not enough; we need to populate a 3D model, segregated by facies, with the appropriate values. This is done with help of acoustic inversion. Discussions about the most suitable type of inversion for the evaporitic section are not the objective of this article, and the reader may refer to Barros et al. (2017), Fonseca et al. (2018), Teixeira et al. (2018) and Maul et al. (2018b) for further details on this particular subject.

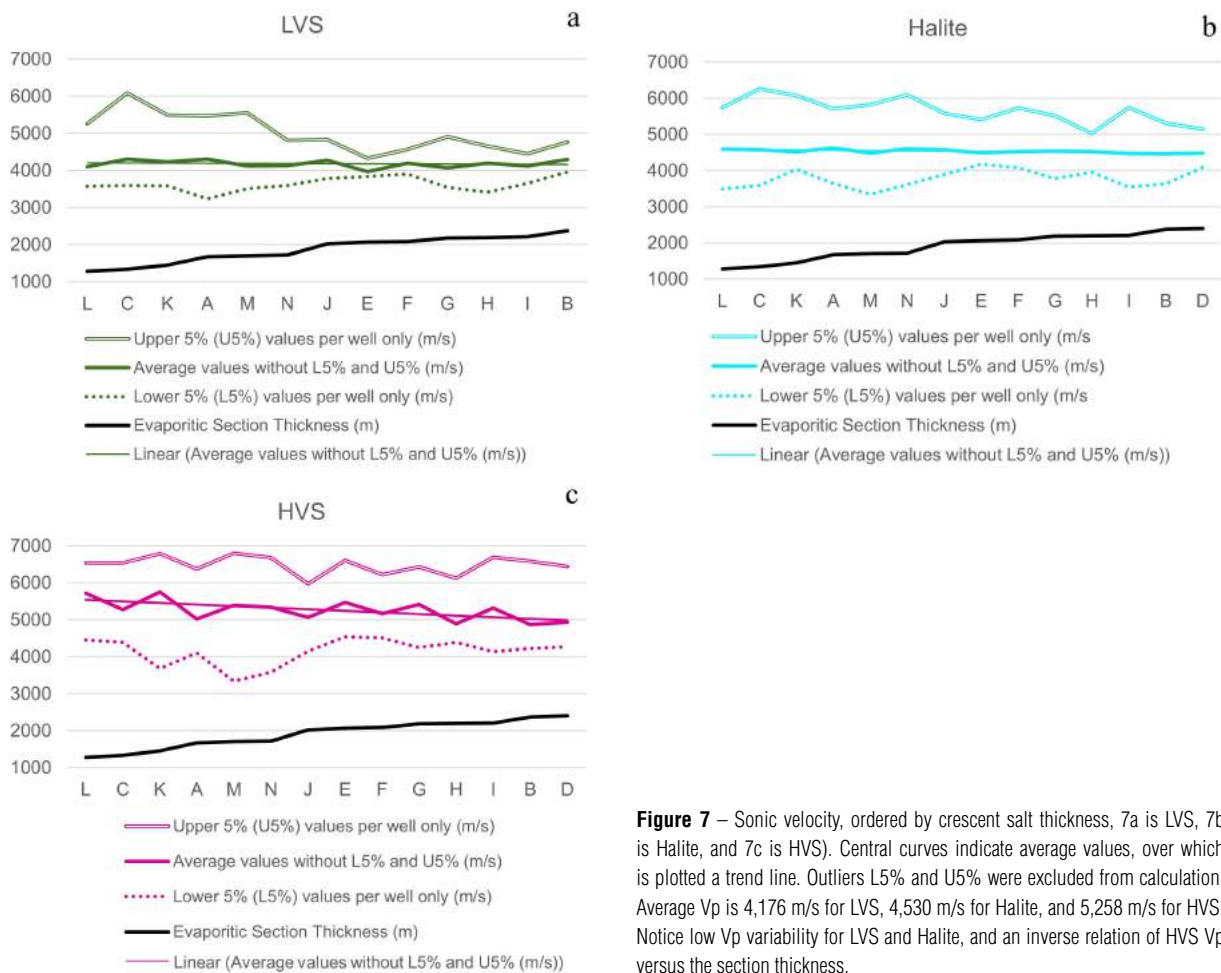


Figure 7 – Sonic velocity, ordered by crescent salt thickness, 7a is LVS, 7b is Halite, and 7c is HVS). Central curves indicate average values, over which is plotted a trend line. Outliers L5% and U5% were excluded from calculation. Average V_p is 4,176 m/s for LVS, 4,530 m/s for Halite, and 5,258 m/s for HVS. Notice low V_p variability for LVS and Halite, and an inverse relation of HVS V_p versus the section thickness.

The resulting acoustic impedance (I_p) from the acoustic inversion process is cross-plotted with the compressional wave velocity (V_p) and, from this cross-plot, a best-fit curve is calculated (Eq. 1). The resulting curve fit is applied to the whole 3D volume, generating a 3D velocity volume (Fig. 8). Curve-fitting choice is of course also another source of uncertainties.

$$V_p = ax^3 + bx^2 + cx + d \tag{1}$$

Where:

V_p = Compressional velocity; [V_p] = m/s

$x = I_p$; [I_p] = $\frac{g}{cm^2} * \frac{km}{s}$

I_p = Acoustic Impedance

$a = 1.426$; $b = -51.59$; $c = 753.4$; $d = 847$

A correlation between the evaporitic section thickness and the average V_p is also calculated (Fig. 9). Thinner salt sections show higher velocities, as expected by the Halite displacement mechanism. The displacement is attributed to the

vertical movement of halite and other mobile salts (LVS group), which is in accordance with the Rayleigh-Taylor instability: Halite and LVS present a plastic, fluid-like behavior, and do not resist the overburden stresses, being hence displaced and leaving behind thinner sections with a higher proportions of HSV (Lachmann, 1910; Arrhenius, 1913 both referred in Dooley et al., 2015). Evaporitic thickness and its average interval velocity are inversely proportional. This inverse correlation is in agreement with the ideas presented by Oliveira et al. (2015), who mentioned that, in their project, when the evaporitic section increases in thickness, the average velocity for the entire section decreases.

CONCLUSIONS

Modeling of heterogeneous evaporitic properties is a complex subject, and a clear understanding of the uncertainties and limitations of the available data is crucial to ensure a useful final product.

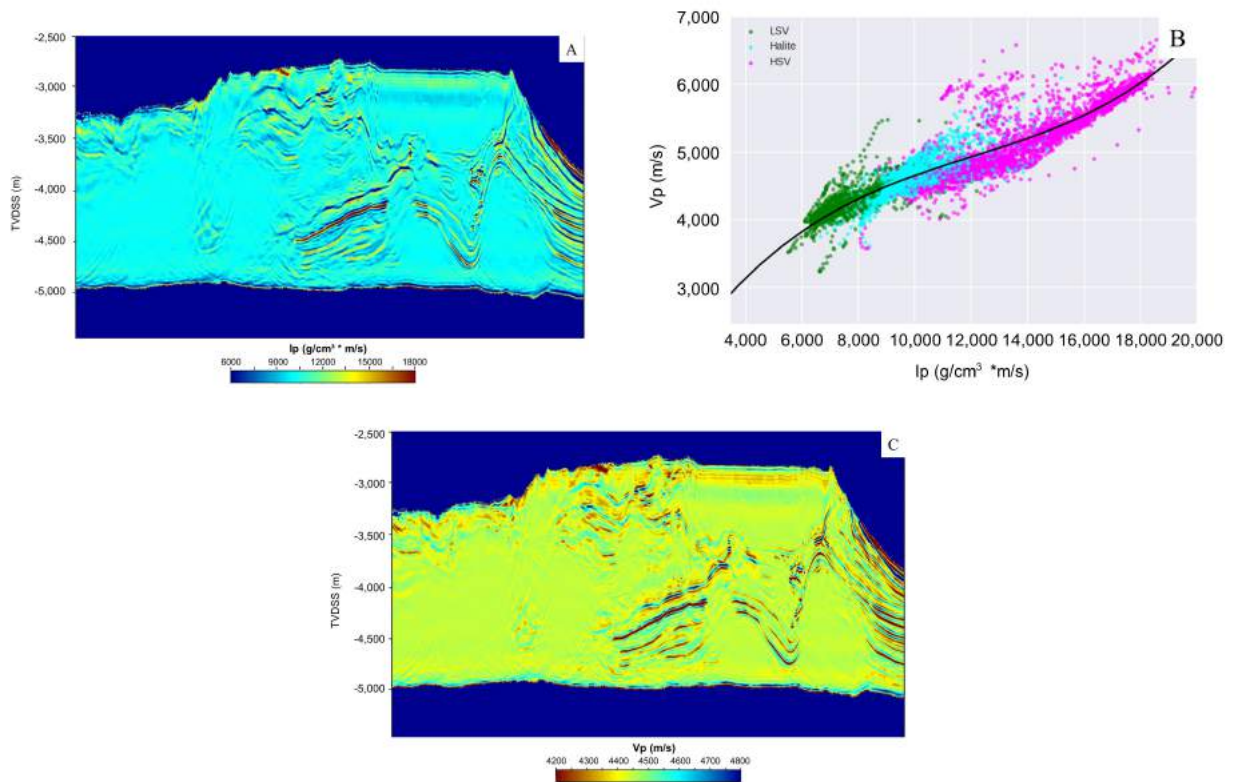


Figure 8 – Transformation from Acoustic Impedance (I_p) to Compressional Wave Velocity (V_p). 8A: Result of model-based acoustic inversion. 8B: Well-log cross-plot (V_p versus I_p). Colors are mineral groups (Green – LVS; Light Blue – Halite and Purple – HVS), as in Figure 7, and black line is the chosen polynomial fit in this work (Eq. 1). 8C: V_p calculated from impedance (i.e. the chosen polynomial fit (8B) applied on the acoustic inversion result (8A)).

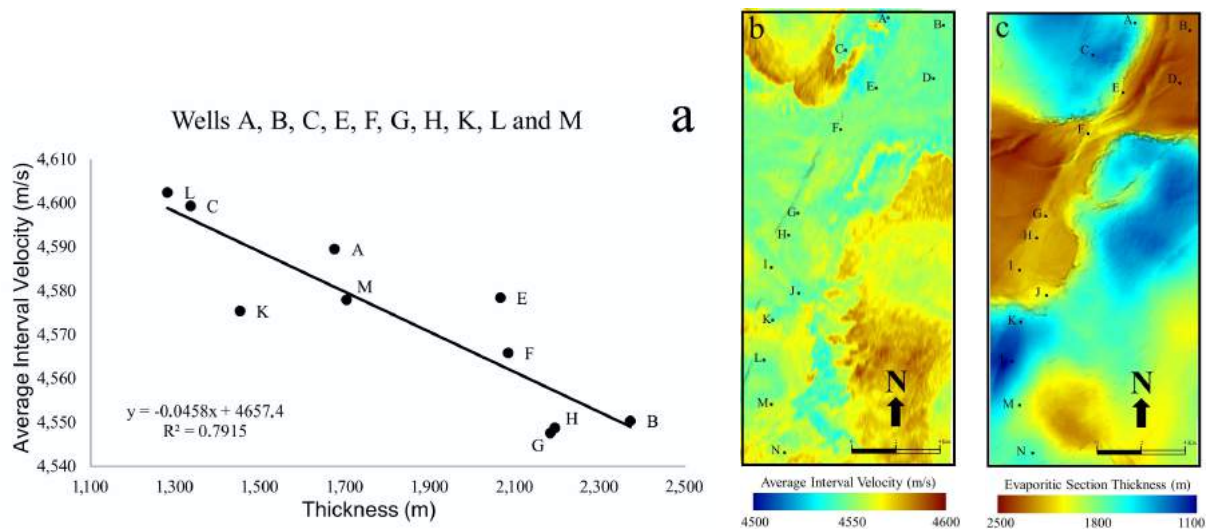


Figure 9 – Correlation between V_p and evaporitic section thickness. 9a: Inverse correlation between average interval velocity and evaporitic thickness. Each dot represents a well. 9b: Average V_p map for evaporitic section, calculated using Equation 1. 9c: Thickness map for evaporitic section.

In the Santos Basin, the evaporitic section is dominated by halite (about 80% in average – Maul et al. (2018a) – and 90% in the dataset used here). This can lead one to assume a homogeneous compressional velocity (V_p) of 4,500 m/s for the entire section – the high occurrence of halite dominates the cross-plot, dwindling the influence of other evaporitic minerals.

Velocity variability is nevertheless observed within the evaporitic section, especially in the HVS group, which could be related to the higher compaction effects in anhydrites. The variability is less pronounced in thicker evaporitic section. This behavior seems to be more related to the mixed mineralogy observed in these thicker sections, and less to the individual mineral variability by itself. We defend the idea that, in these thicker sections, mineral mixing leads us to analyze the halite influence (more stable) over other minerals.

The methodology presented in this work results in an improved initial velocity model for seismic tomography, lowering the computational efforts when compared to the conventional approach (“salt flooding” + inversion tomographic updates), as cited by Gobatto et al. (2016), Falcão (2017), Fonseca et al. (2018), Maul et al. (2018a), Dias et al. (2019) and Maul et al. (2019).

The workflow is easy to implement, and not costly. Besides, the improved velocity can be used to assist other reservoir characterization processes, such as properties distribution studies, depth positioning forecast, uncertainty estimation, geomechanical studies, and drilling in safer conditions.

The inverse relation between salt thicknesses and average interval velocities suggests that mobile salts (LVS and Halite) are expelled by the overburden weight, such as the carbonate rafts, leading to higher HVS fractions in thinner sections.

ACKNOWLEDGEMENTS

The authors would like to express their gratitude to the Agência Nacional do Petróleo, Gás Natural e Biocombustíveis (ANP) for authorization to use the data necessary for the development of this project, and for allowing the publication of the obtained results so far in the first author's doctoral research. The authors also thank Petrobras S.A. for all the financial support and availability of time and equipment, as well as the colleagues who have been collaborating with this research.

REFERENCES

AMARAL PJ, MAUL A, FALCÃO L, GONZÁLEZ M & GONZÁLEZ G. 2015. Estudo Estatístico da Velocidade dos Sais na Camada Evaporítica na Bacia de Santos. In: 14th International Congress of the Brazilian

Geophysical Society. Rio de Janeiro, RJ, Brazil. SBGf. doi: 10.1190/sbgf2015-131.

ARRHENIUS S. 1913. Zur Physik der Salzlagerstätten. *Medd. Vetenskapsakademiens Nobelinst*, 2(20): 1-25.

BARROS P, FONSECA J, TEIXEIRA L MAUL A, YAMAMOTO T, MENEGUIM T, QUEIROZ LE, TORÍBIO T, MARTINI A, GOBATTO F & GONZÁLEZ M. 2017. Salt Heterogeneities Characterization in Pre-Salt Santos Basin Fields. In: OTC Offshore Technology Conference. Rio de Janeiro, RJ, Brazil. IBP. doi: 10.4043/28147-MS.

BEGG SH, BRATVOLD RB & WELSH MB. 2014. Uncertainty vs Variability: What's the Difference and Why is it Important?. In: SPE Hydrocarbon Economics and Evaluation Symposium. Houston, TX, USA. doi: 10.2118/169850-MS.

CORNELIUS S & CASTAGNA JP. 2018. Variation in Salt-Body Interval Velocities in the Deepwater Gulf of Mexico: Keathley Canyon and Walker Ridge Areas. *Interpretation*, 6(1): T15-T27. doi: 10.1190/INT-2017-0069.1.

COSTA AM & POIATE Jr E. 2009. Rocha Salina na Indústria do Petróleo: Aspectos Relacionados à Reologia e à Perfuração de Rochas Salinas. In: MOHRIAK W, SZATMARI P & ANJOS SMC (Org.). *Sal. Geologia e Tectônica. Exemplos nas Bacias Brasileiras*. p. 362-385. São Paulo, SP, Brazil: Beca Edições LTDA.

DEMERCIAN S, SZATMARI P & COBBOLD P. 1993. Style and Pattern of Salt Diapirs due to Thin-Skinned Gravitational Gliding, Campos and Santos Basins, Offshore Brazil. *Tectonophysics*, 228(3-4): 393-433. doi: 10.1016/0040-1951(93)90351-J.

DIAS R, FONSECA J, BULCÃO A, DIAS B, TEIXEIRA LM, MAUL A & BORGES F. 2019. Salt Stratification and Least Square Migration to Improve Pre-Salt Images: Santos Basin, Brazilian Offshore Example. In: Second EAGE/PESGB Workshop on Velocities. London, United Kingdom. doi: 10.3997/2214-4609.201900051.

DOOLEY R, JACKSON M, JACKSON CAL, HUDEC MR & RODRIGUEZ CR. 2015. Enigmatic Structures within Salt Walls of Santos Basin – Part 2: Mechanical Explanation from Physical Modeling. *Journal of Structural Geology*, 75: 163-187. doi: 10.1016/j.jsg.2015.01.009.

FALCÃO LF. 2017. O Sal Estratificado e sua Importância na Modelagem de Velocidades para Fins de Migração Sísmica. *Dinâmica oceânica e costeira*. Universidade Federal Fluminense, UFF. Niterói, RJ, Brazil. 91 pp.

FALCÃO LF, MAUL AR, GOBATTO FO, GONZÁLEZ GAS & GONZÁLEZ MLAF. 2016. Results of incorporation Stratigraphy within the Evaporitic Sequence into the velocity Field for Reservoir Characterization. *Brazilian Journal of Geophysics*, 34(3): 341-349. doi: 10.22564/rbfg.v34i3.829.

FONSECA J, GOBATTO F, BOECHAT J, MAUL A, YAMAMOTO T, BORN E, TEIXEIRA L & GONZÁLEZ M. 2017. Dealing with Evaporitic Salts Section

- in Santos Basin during Geological Seismic Velocity Construction. In: 15th International Congress of the Brazilian Geophysical Society. Expanded Abstracts, Rio de Janeiro, RJ, Brazil, SBGf. doi: 10.1190/sbgf2017-350.
- FONSECA J, TEIXEIRA L, MAUL A, BARROS P, BOECHAT J & GONZÁLEZ M. 2018. Modelling Geological Layers into new Velocity Models for Seismic Migration Process: A Brazilian pre-Salt Case. In: First EAGE/PESGB Workshop on Velocities. London, United Kingdom. doi: 10.3997/2214-4609.201800010.
- FREITAS JTR. 2006. Ciclos Depositionais Evaporíticos da Bacia de Santos uma Análise Cicloestratigráfica a partir de Dados de 2 Poços e de Traços de Sísmica. Master's dissertation. Universidade Federal do Rio Grande do Sul, UFRGS. Porto Alegre, RS, Brazil. 160 pp.
- GAMBOA LAP, MACHADO MAP, DA SILVEIRA DP, DE FREITAS JTR, DA SILVA SRP, MOHRIAK W, SZATMARI P & ANJOS S. 2009. Evaporitos Estratificados no Atlântico Sul: Interpretação Sísmica e Controle Tectono-Estratigráfico na Bacia de Santos. In: MOHRIAK W, SZATMARI P & ANJOS SMC (Org.). *Sal. Geologia e Tectônica. Exemplos nas Bacias Brasileiras*. p. 340-359. São Paulo, SP, Brazil: Beca Edições LTDA.
- GOBATO F, MAUL A, TEIXEIRA L, GONZÁLEZ G, FALCÃO L, GONZÁLEZ M & BOECHAT JT. 2016. Refining Velocity Model within the Salt Section in Santos Basin: An Innovative Workflow to Include the Existing Stratification and its Considerations. In: 87th SEG Annual Meeting. p. 5328-5331. Dallas, TX, USA: Society of Exploration Geophysicist. doi: 10.1190/segam2016-13685489.1.
- GONZÁLEZ M, GOBATO F, MAUL A, FALCÃO L, GONZÁLEZ G, OLIVEIRA L, MENEGUIM T & AMARAL P. 2016. Proposed Workflow to Incorporate Stratification within Salt Section using Velocity and Seismic Attributes. In: Third EAGE/SBGf Workshop on Quantitative Seismic Interpretation of Lacustrine Carbonates. Expanded Abstracts, Rio de Janeiro, RJ, Brazil: EAGE/SBGf. doi: 10.3997/22144609.201600050.
- GONZÁLEZ G, MAUL A, JARDIM F, FALCÃO L, GOBATO F & GONZÁLEZ M. 2018. Estimando Incertidumbres sobre la Amplitud Sísmica para un Yacimiento del Presal a través de Mapas de Iluminación. *Geociencias Aplicadas Latinoamericanas*, 4(1): 3-9. doi: 10.3997/2352-8281.20180003.
- GUERRA MC & SZATMARI P. 2009. Modelagem Física de Processos Alogénicos. In: MOHRIAK W, SZATMARI P & ANJOS SMC (Org.). *Sal. Geologia e Tectônica. Exemplos nas Bacias Brasileiras*. p. 165-177. São Paulo, SP, Brazil: Beca Edições LTDA.
- GUERRA MC & UNDERHILL JR. 2012. Role of Halokinesis in Controlling Structural Styles and Sediment Dispersal in the Santos Basin, Offshore Brazil. In: ALSOP GI, ARCHER SG, HARTLEY AJ, GRANT NT & HODGKINSON R (Org.). *Salt Tectonics, Sediments and Prospectivity*. Volume 363. p. 175-206. Geological Society of London, Special Publications. doi: 10.1144/SP363.9.
- GUO N & FAGIN S. 2002. Becoming Effective Velocity-Model Builders and Depth Imagers, Part 2 – The Basics of Velocity-Model Building, Examples and Discussions. *The Leading Edge*, 21(12): 1210-1216.
- INGS S, BEAUMONT C & GEMMER L. 2004. Numerical Modeling of Salt Tectonics on Passive Continental Margins: Preliminary Assessment of the Effects of Sediment Loading, Buoyancy, Margin Tilt, and Isostasy. In: 24th Annual Research Conference. Expanded Abstracts, p. 36-68. Houston, TX, USA: Bob F. Perkins. GCSSEPM. CD-ROM.
- JACKSON CAL, JACKSON MPA, HUDEC M & RODRIGUEZ CR. 2015. Enigmatic Structures within Salt Walls of Santos Basin - Part 1: Geometry and Kinematics from 3D Seismic Reflection and Well Data. *Journal of Structural Geology*, 75: 135-162. doi: 10.1016/j.jsg.2015.01.010.
- JI S, HUANG T, FU K & LI Z. 2011. Dirty Salt Velocity Inversion: The Road to a Clearer Subsalt Image. *Geophysics*, 76(5): WB169-WB174. doi: 10.1190/GEO2010-0392.1.
- JONES IF & DAVISON I. 2014. Seismic Imaging in and around Salt Bodies. *Interpretation*, 2(4): SL1-SL20. doi: 10.1190/INT-2014-0033.1.
- JUSTEN JCR, VARGAS Jr EA, ALVES I & SOUZA ALS. 2013. Análise das Propriedades Elásticas de Rochas e Minerais Evaporíticos. In: 13th International Congress of the Brazilian Geophysical Society & EXPOGEF. p. 1154-1158. Rio de Janeiro, RJ, Brazil: SBGf. doi: 10.1190/sbgf2013-237.
- LACHMANN R. 1910. Über autoplaste (Nichttektonische) Formelemente im Bau der Salzlagerstätten Norddeutschlands. *Zeitschrift der Deutschen Geologischen Gesellschaft*, 62: 113-116.
- MAUL A, FALCÃO L, GOBATO F, NOVELLINO V, JARDIM F, OLIVEIRA L, MENEGUIM T, AMARAL P, BORGES F & TEIXEIRA L. 2016. Incorporação de Estratificações dentro da Seção Evaporítica utilizando Velocidades e Atributos Sísmicos. Technical Report 152. Informe Geofísico da Petrobras. 9 pp.
- MAUL A, JARDIM F, FALCÃO L & GONZÁLEZ G. 2015. Observing Amplitude Uncertainties for a Pre-Salt Reservoir using Illumination Study (Hit-Maps). In: 77th EAGE Conference & Exhibition. Madrid, Spain. doi: 10.3997/2214-4609.201412921.
- MAUL A, FONSECA J, TEIXEIRA L, BARROS P, BOECHAT JB, NUNES JP, YAMAMOTO T, GONZÁLEZ M & GONZÁLEZ G. 2018a. Modeling Intra-Salt Layers when Building Velocity Models for Depth Migration Examples of the Santos Basins, Brazilian Offshore. In: 88th SEG Annual Meeting. Anaheim, CA, USA: Society of Exploration Geophysicist. doi: 10.1190/segam2018-2996209.1.
- MAUL AR, SANTOS MAC & SILVA CG. 2018b. Few Considerations, Warnings and Benefits for the E&P Industry when Incorporating Stratifications inside Salt Sections. *Brazilian Journal of Geophysics*, 36(4): 461-477. doi: 10.22564/rbgf.v36i4.1981.

- MAUL AR, SANTOS MAC, SILVA CG, FONSECA JS, GONZÁLEZ MLAF, TEIXEIRA LMS, YAMAMOTO TM, BORGES FAS & PONTES RLB. 2018c. Evaporitic Section Characterization and its Impact over the Pre-Salt Reservoirs, Examples in Santos Basin, Offshore. In: Rio Oil & Gas Exposition and Conference. p. 55–68. Rio de Janeiro, RJ, Brazil: IBP.
- MAUL AR, SANTOS MAC, SILVA CG, FONSECA JS, GONZÁLEZ MLAF, TEIXEIRA LMS, YAMAMOTO TM, BORGES FAS & PONTES RLB. 2019. Geological Characterization of Evaporitic Sections and its Impacts on Seismic Images: Santos Basin, Offshore Brazil. *Brazilian Journal of Geophysics*, 37(1): 55–68. doi: 10.22564/rbgf.v37i1.1989.
- MENEGUIM T, MENDES S, MAUL A, FALCÃO A, GONZÁLEZ M & GONZÁLEZ G. 2015. Combining Seismic Facies Analysis and Well Information to Guide new Interval Velocity Models for a Pre-Salt Study, Santos Basin, Brazil. In: 14th International Congress of the Brazilian Geophysical Society. Rio de Janeiro, RJ, Brazil: SBGf. doi: 10.1190/sbgf2015-271.
- OLIVEIRA LC, FALCÃO LF, MAUL AR, ROSSETO JA, GONZÁLEZ M & GONZÁLEZ G. 2015. Geological Velocity Approach in order to obtain a detailed Velocity Model for the Evaporitic Section—Santos Basin. In: 14th International Congress of the Brazilian Geophysical Society & EXPOGEF. p. 1374-1377. Rio de Janeiro, RJ, Brazil: SBGf. doi: 10.1190/sbgf2015-273.
- SCHREIBER BC, BABEL M & LUGLI S. 2007. An Overview of Evaporite Puzzles. In: SCHREIBER B, LUGLI S & BABEL M (Eds.). *Evaporites through Space and Time*. Volume 285, p. 1-13. Geological Society, London, Special Publications.
- TEIXEIRA L & LUPINACCI W. 2019. Elastic Properties of Salt in the Santos Basin: Relations and Spatial Predictions. *Journal of Petroleum Science and Engineering*, 180: 215-230. doi: 10.1016/j.petrol.2019.05.024.
- TEIXEIRA L, NUNES JP, FONSECA J, MAUL A, BARROS P & BORGES F. 2018. Seismic-Based Salt Characterization for Geomechanical Modelling of a Pre-Salt Reservoir. In: 80th EAGE Conference & Exhibition. Copenhagen, Denmark. doi: 10.3997/2214-4609.201801331.
- ZDRAVEVA O, WOODWARD M, NICHOLS D & OSYPOV K. 2011. Building Anisotropic Models for Depth Imaging: comparing different approaches. In: 12th International Congress of the Brazilian Geophysical Society. Rio de Janeiro, RJ, Brazil: SBGf. doi: 10.4043/22827-MS.

Recebido em 22 abril, 2019 / Aceito em 11 junho, 2019

Received on April 22, 2019 / Accepted on June 11, 2019

NEW ITERATIVE AND MULTIFREQUENCY APPROACHES IN GEOPHYSICAL DIFFRACTION TOMOGRAPHY

Danilo Sande¹, Amin Bassrei² and Jerry Harris³

ABSTRACT. Seismic tomography is used in reservoir geophysics as an important method for high-resolution imaging. The classical Born approach, which is used in single-frequency diffraction tomography under the condition of weak scattering, is limited by the requirement to know the background velocity in advance. We propose tomographic inversion approaches within matrix formalism and the Born approximation conditions. These approaches are iterative (in the sense that the background velocity field is updated at each iteration) and do not require knowledge of the true background velocity. In the first approach, a single-frequency that is kept constant is used. In the second approach, several frequencies are also kept constant and are used simultaneously. In the third approach, in addition to the background velocity, the working frequency is also updated. Finally, in the last approach, the multiple frequencies used simultaneously are updated throughout the iteration. The proposed approaches were tested on a synthetic model containing a dipping layer and a paleochannel, with cross-well acquisition geometry, and the data were contaminated with Gaussian noise. When compared to the standard, single-frequency non-iterative approach, the iterative process with the use of multiple frequencies generated results with smaller RMS errors for model parameter, velocity and data.

Keywords: seismic inversion, seismic tomography, wave numerical modeling, reservoir characterization.

RESUMO. A tomografia sísmica é usada na geofísica de reservatórios como um método importante para obtenção de imagens de alta resolução. A abordagem clássica de Born, usada na tomografia de difração de única frequência sob a condição de espalhamento fraco, é limitada pela necessidade de se conhecer antecipadamente a velocidade do fundo homogêneo. Propomos abordagens iterativas de inversão tomográfica dentro do formalismo matricial e sob a condição da aproximação de Born. Essas abordagens têm uma natureza iterativa, onde o campo de velocidade de fundo é atualizado em cada iteração, sendo que o conhecimento da velocidade verdadeira do fundo homogêneo não é necessário. Na primeira abordagem é usada uma única frequência mantida constante. Na segunda abordagem são usadas simultaneamente várias frequências também mantidas constantes. Na terceira abordagem, além da velocidade do fundo homogêneo, a frequência de trabalho também é atualizada. Finalmente, na última abordagem, as múltiplas frequências usadas simultaneamente são atualizadas durante a iteração. As abordagens propostas foram testadas em um modelo sintético contendo uma camada inclinada e um paleocanal, com geometria de aquisição poço a poço, sendo os dados contaminados com ruído gaussiano. Quando comparado com a abordagem padrão não-iterativa de única frequência, o processo iterativo com o uso de múltiplas frequências gerou resultados com erros menores de RMS para o parâmetro de modelo, a velocidade e o vetor de dados.

Palavras-chave: inversão sísmica, tomografia sísmica, modelagem numérica de ondas, caracterização de reservatórios.

¹Universidade Federal da Bahia, Instituto de Geociências, Salvador, BA, Brazil – E-mail: danilosandesantos@gmail.com

²Universidade Federal da Bahia, Instituto de Geociências, Centro de Pesquisa em Geofísica e Geologia / INCT-GP. Rua Barão de Jeremoabo, s/n, Ondina, 40170-115, Salvador, BA, Brazil – E-mail: bassrei@ufba.br

³Stanford University, Department of Geophysics, California, USA – E-mail: jerry.harris@stanford.edu

INTRODUCTION

According to the wave equation, acoustic waves have scattering properties. When the wavelength is of the same order as the dimensions of the structure to be viewed, the energy is scattered, which implies the waveform can be used to infer the physical properties of the medium (Devaney, 1982); that is, the amplitude of the observed wave can be used to estimate the velocity contrast of the medium.

Diffraction tomography is an inversion technique that allows the estimation of the velocity distribution in the subsurface. Furthermore, this technique has applications in imaging problems in several fields, such as medicine and geophysics (Harris, 1987). The input data are the amplitudes of seismic signals recorded in the receivers. One of the pioneering works in diffraction tomography was published by Wolf (1969) and geophysical problem extensions were performed by Devaney (1982); Harris (1987); Wu & Toksöz (1987). These authors used the filtered retropropagation approach, while a more recent matrix approach was used by Lo & Inderwiesen (1994). The advantages of the use of multiple frequencies have been presented by several authors. For example, Harris & Yin (1994) used multifrequency diffraction tomography in a sequential scheme, and Rocha Filho et al. (1996) used it in a simultaneous scheme. Thompson et al. (1994) proposed a numerical solution for nonlinear diffraction tomography, avoiding the Born approximation, and Reiter & Rodi (1996) studied the nonlinear case in a cross-well problem. The question of the regularization of the inverse problem and the search for the optimal normalization parameter was studied by Santos & Bassrei (2007).

Diffraction tomography is a nonlinear, ill-posed, inverse problem that can be solved by several approaches. For example, the Born approximation considers the scattered field to be much smaller than the incident wavefield. This assumption linearizes the inverse problem, after which the velocity of the scattering medium can be obtained. The use of the Born approximation in diffraction tomography is a viable alternative with a low computational cost. However, it is a valid approximation only for low velocity contrasts or small-scale heterogeneity. The present work proposes some new extensions of the Born approximation, making use of multiple working frequencies, either iteratively or sequentially. The iterative aspect of the proposed approaches allows for inversion without the advanced knowledge of the medium background velocity. In addition, the multifrequency method generated better results than the conventional, single-frequency method.

INVERSE PROBLEMS AND REGULARIZATION

Inverse problems are usually ill-posed; that is, the solution may not exist, and if it exists, it may not be unique and/or stable. A linear, piecewise linear or linearized problem can be written as:

$$d = Gm, \tag{1}$$

where d is the data vector, m is the vector of model parameters and G is the $M \times N$ matrix that relates the M elements of the data parameter vector to the N elements of the model parameter vector. Many inverse problems in geophysics are ill-posed, and diffraction tomography is not an exception. Therefore, it is necessary to adopt a regularization procedure, such as regularization by derivative matrices, also called Tikhonov regularization. The idea behind this technique is presented as follows. Consider the objective function in the least squares sense:

$$\phi(m) = e^T e + \lambda L_n, \tag{2}$$

where $e = d - Gm$ and L_n represents the additional constraint, responsible for regularizing the solution, expressed as:

$$L_n = (D_n m)^T (D_n m), \tag{3}$$

where n is the order of the derivative matrix. Frequently, L_n represents either the flattening or the roughness of the model parameter when $n = 1$ and $n = 2$ respectively. The latter case is used in this work, and the operator $D_2 m$ can be expressed as:

$$\begin{pmatrix} 1 & -2 & 1 & 0 & \dots & 0 & 0 & 0 & 0 \\ 0 & 1 & -2 & 1 & \dots & 0 & 0 & 0 & 0 \\ \vdots & \vdots & \vdots & \vdots & \ddots & \vdots & \vdots & \vdots & \vdots \\ 0 & 0 & 0 & 0 & \dots & 0 & 1 & -2 & 1 \end{pmatrix} \begin{pmatrix} m_1 \\ m_2 \\ \vdots \\ m_N \end{pmatrix} = D_2 m. \tag{4}$$

λ is a positive constant known as the regularization parameter, and its choice is a problem in itself. Minimizing the objective function, we obtain the parameter vector of the estimated model:

$$m^{est} = (G^T G + \lambda D_n^T D_n)^{-1} G^T d. \tag{5}$$

The generalized cross-validation method (GCV) was proposed by Craven & Wahba (1979) as a tool for choosing the value of the optimal regularization parameter. The GCV estimate is an extension of ordinary cross-validation, which is based on the leaving-one-out concept. An element is removed from the data vector, and the regularized solution minimizing the objective function is calculated:

$$V_0(\lambda) = \frac{1}{M} \sum_{k=1}^M [d_k^{obs} - d_k(m_\lambda^k)]^2, \tag{6}$$

where the index k corresponds to the k -th element of the data parameter vector that was removed. If the value of λ is optimal, then the k -th element of the solution (vector of model parameters) will predict the failure, that is, \mathbf{m}_λ^k is the solution that minimizes the error. The GCV function presented by Craven & Wahba (1979) and Wahba (1990) is:

$$GCV(\lambda) = \frac{\|\mathbf{d}^{obs} - \mathbf{d}(\mathbf{m}_\lambda)\|}{\left[\frac{1}{M}Tr(\mathbf{I} - \mathbf{B}(\lambda))\right]^2}, \quad (7)$$

where $\mathbf{B}(\lambda)$ is defined as:

$$\mathbf{B}(\lambda) = \mathbf{G}(\mathbf{G}^T \mathbf{G} + \lambda \mathbf{D}_n^T \mathbf{D}_n)^{-1} \mathbf{G}^T. \quad (8)$$

Regin ska (1996) proposed another method of choosing a parameter related to the L-curve criterion. This method can be easily adapted to any situation in which the smoothing parameter is discrete. The method consists of finding the minimum of the functional:

$$\Psi_\mu(\lambda) = \|\mathbf{d}^{obs} - \mathbf{d}(\mathbf{m}_\lambda)\|^2 \|\mathbf{m}_\lambda\|^{2\mu}, \quad (9)$$

where $\mu > 0$ is the parameter to be defined. In this work, $\mu = 1$ was adopted for the numerical experiments.

SEISMIC DIFFRACTION TOMOGRAPHY

The propagation of a perturbation through a medium with a constant density and a variable velocity given by $c(\mathbf{r})$ can be modeled by the wave equation (Devaney, 1984; Harris, 1987; Wu & Toksöz, 1987):

$$\nabla^2 \Psi(\mathbf{r}, t) = \frac{1}{c^2(\mathbf{r})} \frac{\partial^2 \Psi(\mathbf{r}, t)}{\partial t^2}, \quad (10)$$

where $\Psi(\mathbf{r}, t)$ is the solution of the equation, usually displacement or pressure, \mathbf{r} is the position vector, t represents the time and ∇^2 is the Laplacian operator. Considering a harmonic variation in time, one can find the solution to the wave equation as follows (Lo & Inderwiesen, 1994):

$$\Psi(\mathbf{r}, t) = e^{-i\omega t} P(\mathbf{r}), \quad (11)$$

where $P(\mathbf{r})$ is the wave amplitude. From the wave equation, we obtain the Helmholtz equation:

$$\nabla^2 P(\mathbf{r}) + k^2(\mathbf{r})P(\mathbf{r}) = 0. \quad (12)$$

where $k(\mathbf{r})$ is the wavenumber expressed as $k(\mathbf{r}) = \omega/c(\mathbf{r})$. The scattering problem consists of an incident wave $P_I(\mathbf{r})$ propagating within a medium with a constant background

velocity, which is given by c_0 , as seen in Figure 1. The objective of the problem is to obtain an image of the 2-D medium with a velocity contrast $c(\mathbf{r})$. Any part of the medium where $c(\mathbf{r}) \neq c_0$ acts as a secondary source and scatters the incident wavefield. The total wavefield recorded at the receiver is $P_T(\mathbf{r})$, which is the sum of the incident and scattered wavefields:

$$P_T(\mathbf{r}) = P_I(\mathbf{r}) + P_S(\mathbf{r}). \quad (13)$$

For a constant density model, the Helmholtz equation describes the propagation of the total wavefield:

$$\nabla^2 P_T(\mathbf{r}) + k^2(\mathbf{r})P_T(\mathbf{r}) = 0. \quad (14)$$

The wavenumber associated with the constant background velocity medium is:

$$k_0 = \frac{\omega}{c_0}. \quad (15)$$

Therefore, we can define $k^2(\mathbf{r})$ as:

$$k^2(\mathbf{r}) = k_0^2 - k_0^2 M(\mathbf{r}). \quad (16)$$

In Equation (16), $M(\mathbf{r})$ is the object function, expressed as:

$$M(\mathbf{r}) = \left[1 - \frac{c_0^2}{c^2(\mathbf{r})}\right]. \quad (17)$$

From Equations (14) to (17), we obtain the Helmholtz equation for $P_S(\mathbf{r})$:

$$[\nabla^2 + k_0^2(\mathbf{r})] P_S(\mathbf{r}) = k_0^2 M(\mathbf{r}) [P_I(\mathbf{r}) + P_S(\mathbf{r})], \quad (18)$$

for which solution can be obtained using Green's functions (Lo & Inderwiesen, 1994) as follows:

$$P_S(\mathbf{r}) = -k_0^2 \int_A M(\mathbf{r}') G(\mathbf{r}|\mathbf{r}') [P_I(\mathbf{r}') + P_S(\mathbf{r}')] d\mathbf{r}', \quad (19)$$

where $G(\mathbf{r}|\mathbf{r}') = \frac{i}{4} H_0^{(1)}(k_0 |\mathbf{r} - \mathbf{r}'|)$ and $H_0^{(1)}(\blacksquare)$ is the Hankel function of first kind and zero order. This solution, based on Green's function, is known as the Lippmann-Schwinger integral equation. However, this equation has a nonlinear relationship because the scattered wavefield $P_S(\mathbf{r})$ is present within its integrand. The Born approximation, a way of linearizing the Lippmann-Schwinger integral equation, is based on the condition:

$$P_S(\mathbf{r}) \ll P_I(\mathbf{r}). \quad (20)$$

Consequently, an approximate Lippmann-Schwinger integral equation can be obtained:

$$P_S(\mathbf{r}) \approx -k_0^2 \int_A M(\mathbf{r}') G(\mathbf{r}'|\mathbf{r}) P_I(\mathbf{r}') d\mathbf{r}'. \quad (21)$$

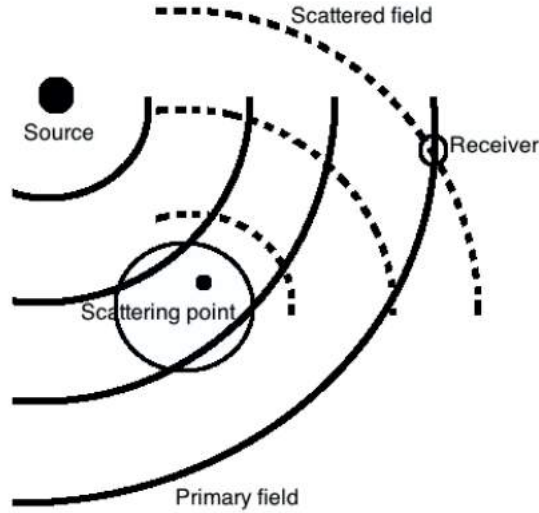


Figure 1 – Representation of the incident field and the scattered field in a medium with a scatterer point.

Since the primary source is a negative pulse located at \mathbf{r}_s , the incident wavefield can be written by using Green's function (Lo & Inderwiesen, 1994):

$$P_i(\mathbf{r}') = G(\mathbf{r}'|\mathbf{r}_s), \tag{22}$$

so that

$$P_s(\mathbf{r}_s, \mathbf{r}_r) \approx -k_0^2 \int_A M(\mathbf{r}') G(\mathbf{r}'|\mathbf{r}_s) G(\mathbf{r}_r|\mathbf{r}') d\mathbf{r}', \tag{23}$$

where $P_s(\mathbf{r}_s, \mathbf{r}_r)$ is the scattered wavefield recorded in \mathbf{r}_r . The above equation is the Lippmann-Schwinger integral equation linearized through the Born approximation. However, it requires weak scattering, which means small velocity contrasts through the medium.

MULTIFREQUENCY DIFFRACTION TOMOGRAPHY

The Born approximation provides a linear relationship between the scattered field $P_s(\mathbf{r}_s, \mathbf{r}_r)$ and the object function $M(\mathbf{r})$:

$$P_s(k, \mathbf{r}_s, \mathbf{r}_r) \approx \frac{k^2}{16} \int_A M(\mathbf{r}') H_0^{(1)}(k|\mathbf{r}' - \mathbf{r}_s|) H_0^{(1)}(k|\mathbf{r}' - \mathbf{r}_r|) d\mathbf{r}'. \tag{24}$$

For the matrix formulation, it is necessary to subdivide the integration area in a finite number of blocks, I (Rocha Filho et al.,

1996). As the acoustic velocity is constant within each block, the same will occur to the object function $M(\mathbf{r})$:

$$M(\mathbf{r}) = \sum_{i=1}^I m_i \phi_i(\mathbf{r}'), \tag{25}$$

where $\phi_i(\mathbf{r}')$ is a basis function, defined here as $\phi_i(\mathbf{r}') = 1$ when \mathbf{r}' is within the area i and as $\phi_i(\mathbf{r}') = 0$ when \mathbf{r}' is outside the area. Substituting the expression for $M(\mathbf{r})$ in the expression of the scattered field gives:

$$P_s(k, \mathbf{r}_s, \mathbf{r}_r) \approx \frac{k^2}{16} \int_A \sum_{i=1}^I m_i \phi_i(\mathbf{r}') H_0^{(1)}(k|\mathbf{r}' - \mathbf{r}_s|) H_0^{(1)}(k|\mathbf{r}' - \mathbf{r}_r|) d\mathbf{r}'. \tag{26}$$

Considering M sources located in $\mathbf{r}_{sm} (1 \leq m \leq M)$, N receivers located in $\mathbf{r}_{rn} (1 \leq n \leq N)$ and L wavenumbers $k_l (1 \leq l \leq L)$, the initial problem can be rewritten as the linear system $\mathbf{p} = \mathbf{W}\mathbf{m}$, which can be written in tensor form as:

$$p_{s,lmn} = \sum_{i=1}^I W_{lmmi} m_i, \tag{27}$$

where W_{lmmi} is defined as follows:

$$W_{lmmi} = \frac{k_l^2}{16} \sum_A \phi_i(x', z') H_0^{(1)}(k_l|(x', z') - (x_{sm}, z_{sm})|) H_0^{(1)}(k_l|(x_{rn}, z_{rn} - (x', z'))|) \Delta x \Delta z. \tag{28}$$

The matrix formulation allows the model retrieval by using several frequencies simultaneously during the inversion, which

increases the amount of information for the same number of source-receiver pairs. In addition, the matrix approach allows the arbitrary positioning of sources and receivers without the need for uniform spacing.

METHODOLOGY

Obtaining the estimated model requires an initial background velocity c_0 , which is not known in real cases. In this methodology, we propose that the background velocity of the zeroth iteration can be chosen arbitrarily, preferably using some a priori information. Based on the average velocity of the estimated model resulting from the initial background, a new background velocity can be defined for the next inversion (iteration 1). The process continues until the RMS relative deviation between consecutive iterations is less than a threshold, for example, 0.5%. For the zeroth iteration, the constant vector $c_0 = [c_0^{(0)}(1), c_0^{(0)}(2), \dots, c_0^{(0)}(N)]$ is used as background velocity in the forward modeling (Eqs. (17), (27) and (29)). Then with the inverse procedure, the estimated model $m^{est(0)}$ is obtained.

With the estimated model $m^{est(0)}$ we obtain the estimated velocity $c^{(0)}$ using the relation:

$$c_i^{(0)} = \sqrt{\frac{(c_0^{(0)})^2}{1 - m_i^{est(0)}}}, \quad i = 1, 2 \dots N. \tag{29}$$

The average value of the estimated velocity vector is calculated as $\overline{c^{(0)}} = \frac{1}{N} \sum_{i=1}^N c_i^{(0)}$ and becomes the new background velocity vector $c_0^{(1)}$; consequently, a new estimated model $m^{est(1)}$ is generated:

$$c_0^{(1)} = \frac{1}{N} \sum_{i=1}^N c_i^{(0)}, \tag{30}$$

Now using the vector $c_0^{(1)}$, the estimated model $m^{est(1)}$ is obtained. With the new estimated model $m^{est(1)}$, we obtain the velocity vector of the first iteration $c^{(1)}$ and calculate its average:

$$c_i^{(1)} = \sqrt{\frac{(c_0^{(1)})^2}{1 - m_i^{est(1)}}}, \quad i = 1, 2 \dots N. \tag{31}$$

and

$$\overline{c^{(1)}} = \frac{1}{N} \sum_{i=1}^N c_i^{(1)} \tag{32}$$

If the average $\overline{c^{(1)}}$ of the components of vector $c^{(1)}$ differs from the previous average $\overline{c^{(0)}}$ by less than a certain value, for example, 0.5%, the iterative process stops. Otherwise, the iteration continues:

$$\overline{c^{(1)}} = c^{(2)} \dots \tag{33}$$

If the initial choice $c_0^{(0)}$ is not too far from the true value, which may be reasonable with the use of some a priori information, the result of the estimated model will approximate the true model, thus reducing the associated errors.

The relative RMS error between the true and estimated model parameters ϵ_m , between the calculated data and the observed data ϵ_d and between the true and estimated velocities ϵ_v , were used to evaluate the quality of the inversion. The expressions are:

$$\epsilon_m = \sqrt{\frac{\sum_{i=1}^N (m_i^{true} - m_i^{est})^2}{\sum_{i=1}^N (m_i^{true})^2}} \times 100\%, \tag{34}$$

$$\epsilon_d = \sqrt{\frac{\sum_{i=1}^M (d_i^{obs} - d_i^{cal})^2}{\sum_{i=1}^M (d_i^{obs})^2}} \times 100\%, \tag{35}$$

$$\epsilon_v = \sqrt{\frac{\sum_{i=1}^N (v_i^{true} - v_i^{est})^2}{\sum_{i=1}^N (v_i^{true})^2}} \times 100\%, \tag{36}$$

where the subscript i refers to the i -th element of the vector, and the super-scripts *true*, *est*, *obs* and *cal*, refer to the true, estimated, observed and calculated values, respectively.

NUMERICAL SIMULATIONS

The above iterative procedure will be applied on a synthetic example with four extensions: (i) single-frequency; (ii) multifrequency; (iii) sequential single-frequency and (iv) sequential multifrequency. Each extension has some practical aspects in the implementation that will be detailed with the corresponding result.

The true model used in the simulations, which is presented in Figure 2, has a vertical variation of 250 m, a horizontal variation of 100 m and is composed of four layers of different velocities that increase with depth with three main features: a dipping layer, an approximately semicircular channel simulating a paleochannel and a flat layer of a higher velocity. The velocity variations are limited to 2%, allowing an adequate use of the Born approximation. Although this is a small velocity contrast, in several geological situations, such as reservoir characterization and monitoring, the region of interest is surrounded by layers with very similar velocities. The true model image presented in Figure 2 was discretized into 2.5 m \times 2.5 m cells for better visualization. However, all the inversions were performed by using a 5 m \times 5 m grid, to reduce the computational cost. In all inversions, Gaussian noise of approximately 1% was added to the data. The chosen frequencies varied according to the adopted approach, always considering the dimensions of the model. Twenty-five sources and 25 receivers were used in the well-to-well acquisition

geometry, resulting in a total of 1250 equations, as the real and the imaginary parts of the scattered field were separated. The medium was parametrized into $50 \times 20 = 1000$ blocks with distinct velocities, that is, 1000 unknowns, thus characterizing an overdetermined problem.

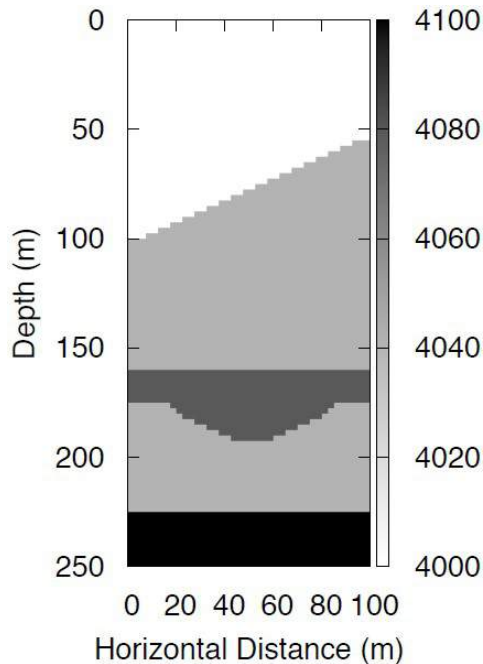


Figure 2 – True model used for the numerical simulations. The color bar represents the P-wave velocity in m/s.

ITERATIVE SINGLE-FREQUENCY

A single-frequency inversion with a central frequency of 500 Hz was performed and a good recovery of the true model was obtained at the end of 4 iterations, as seen in Figure 3. We have carried out several tests and concluded that velocity values ranging from 40% above to approximately 40% below the average velocity of the true model (≈ 4030 m/s) could be chosen for this noise level. We report the numerical results with an initial velocity of 2500 m/s, which is nearly 40% below the true average velocity. For higher levels of noise, the choice of the initial estimate becomes more sensitive. The reductions in the model and data RMS errors were considerable along the iterations, ending with a value of less than 6% for the model error in the fourth iteration. Figure 4 compares the evolution of the model and data errors using the GCV or Reginska method as the optimization parameter search method. For the iterative, single-frequency case in question, the GCV method presented better results and was used for the evolution of the iterations.

ITERATIVE MULTIFREQUENCY

To incorporate more data into the inversion process, several frequencies and different frequency steps (δf) were used for the model recovery. Using 3 frequencies, we obtained satisfactory results that were equivalent to those obtained with more frequencies. The maximum frequency offset (Δf) ranged from 0 to 30 Hz, as seen in Figure 5, which also shows that the inversion with the 500 ± 15 Hz range presented the best results with the noise level that was used. In general, the multifrequency was satisfactory in the inversion; however, when the maximum frequency offsets were wider than ± 30 Hz, the model error was higher than that of the single-frequency case. To define the best number of frequencies, the inversion was performed in the same range, that is, 500 ± 15 Hz, but with a higher number of frequencies. For example, for 5 frequencies, we simultaneously used 485, 492.5, 500, 507.5 and 515 Hz. The results are presented in Figure 6 and show that, when more than 3 frequencies were used simultaneously in the inversion, there was no significant reduction in the model error. Therefore, we adopted the use of 3 frequencies in the iterative multifrequency approach. The models recovered along the iterations using the iterative multifrequency approach are presented in Figure 7, which shows that the recovery of the model in the initial iterations was not superior to the inversion results in the iterative single-frequency case. However, the results were slightly better for the last iterations.

SEQUENTIAL ITERATIVE SINGLE-FREQUENCY

In this approach, only one frequency was used at each iteration, although the frequency value changed from iteration to iteration, maintaining a constant wavelength. The wavelength should be larger than the block size; in fact, a better result was observed using a wavelength between one and two times the block size ($\lambda \approx 7.8$ m). Thus, the choice of the inversion frequency was done based on its dependence on the recovered velocity, with the wavelength constant at each iteration. Figure 8 shows the images of the recovered model after 2 iterations using the sequential, iterative, single-frequency approach. The improvement in the image quality of the recovered model along the iterations is notable. In this approach, few iterations were necessary to reach a satisfactory result, and the relative RMS error in of the model the last iteration was less than 2.5%, a superior result to those of the previous approaches.

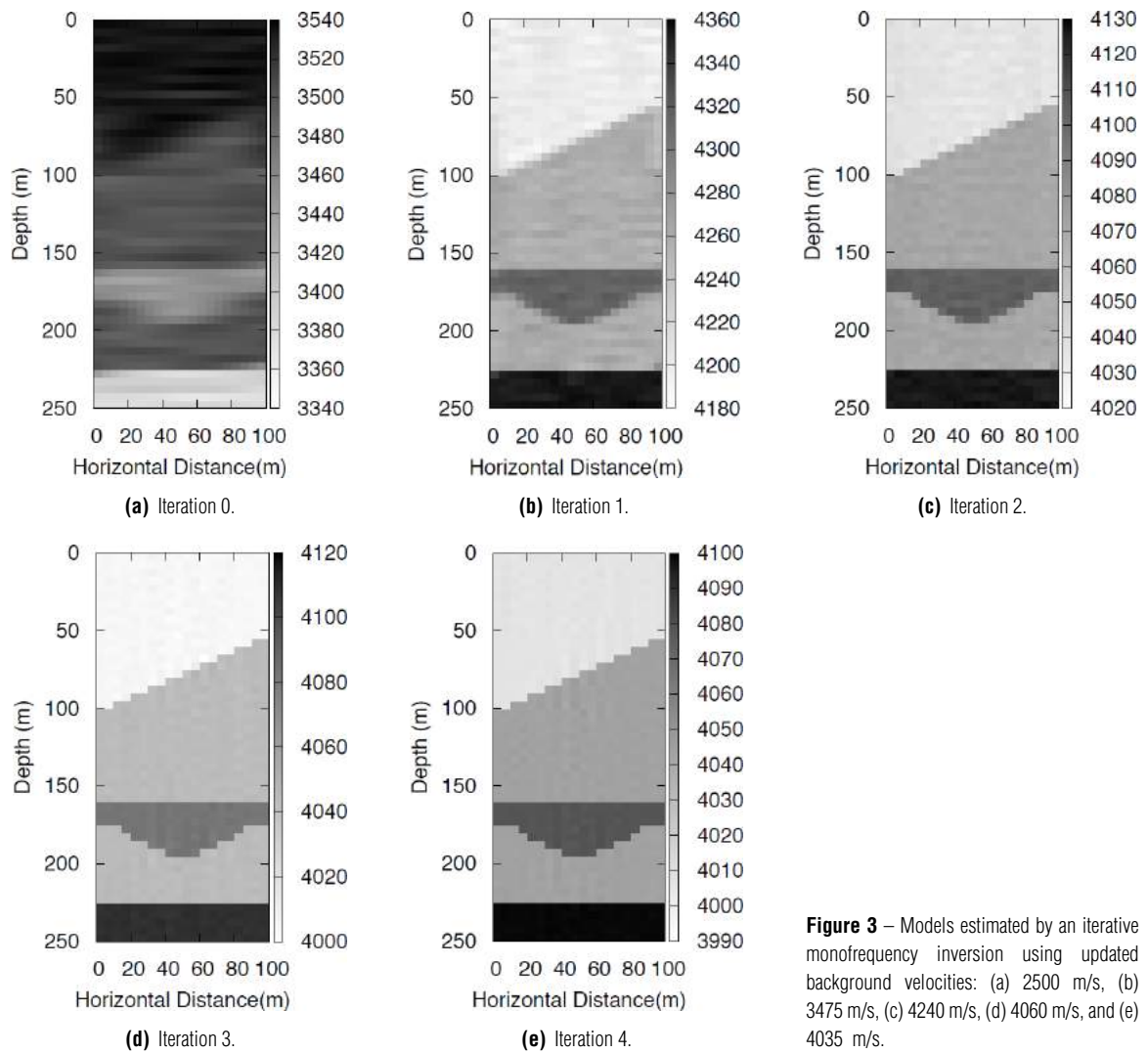


Figure 3 – Models estimated by an iterative monofrequency inversion using updated background velocities: (a) 2500 m/s, (b) 3475 m/s, (c) 4240 m/s, (d) 4060 m/s, and (e) 4035 m/s.

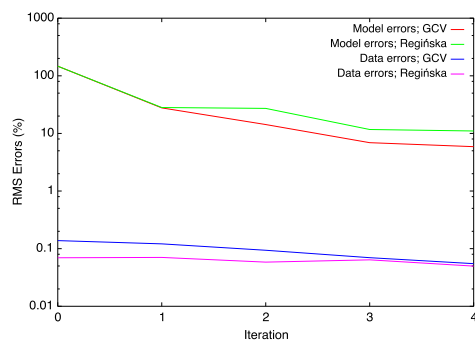


Figure 4 – Data and model relative RMS errors along the iterations using the Regińska and GCV methods to search for the optimization parameter.

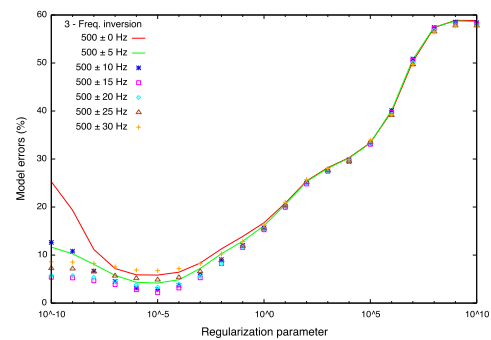


Figure 5 – Model relative RMS error for inversion with 3 frequencies, for different maximum frequency offsets, as a function of the parameter of regularization.

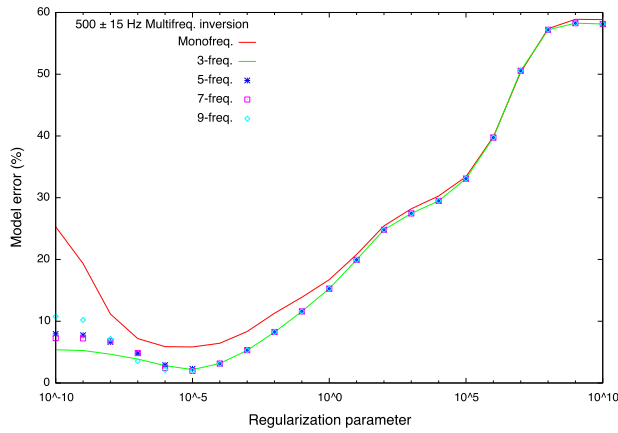


Figure 6 – Model relative RMS error of the multifrequency inversion, for a constant maximum frequency offset and different numbers of frequencies, as a function of the regularization parameter.

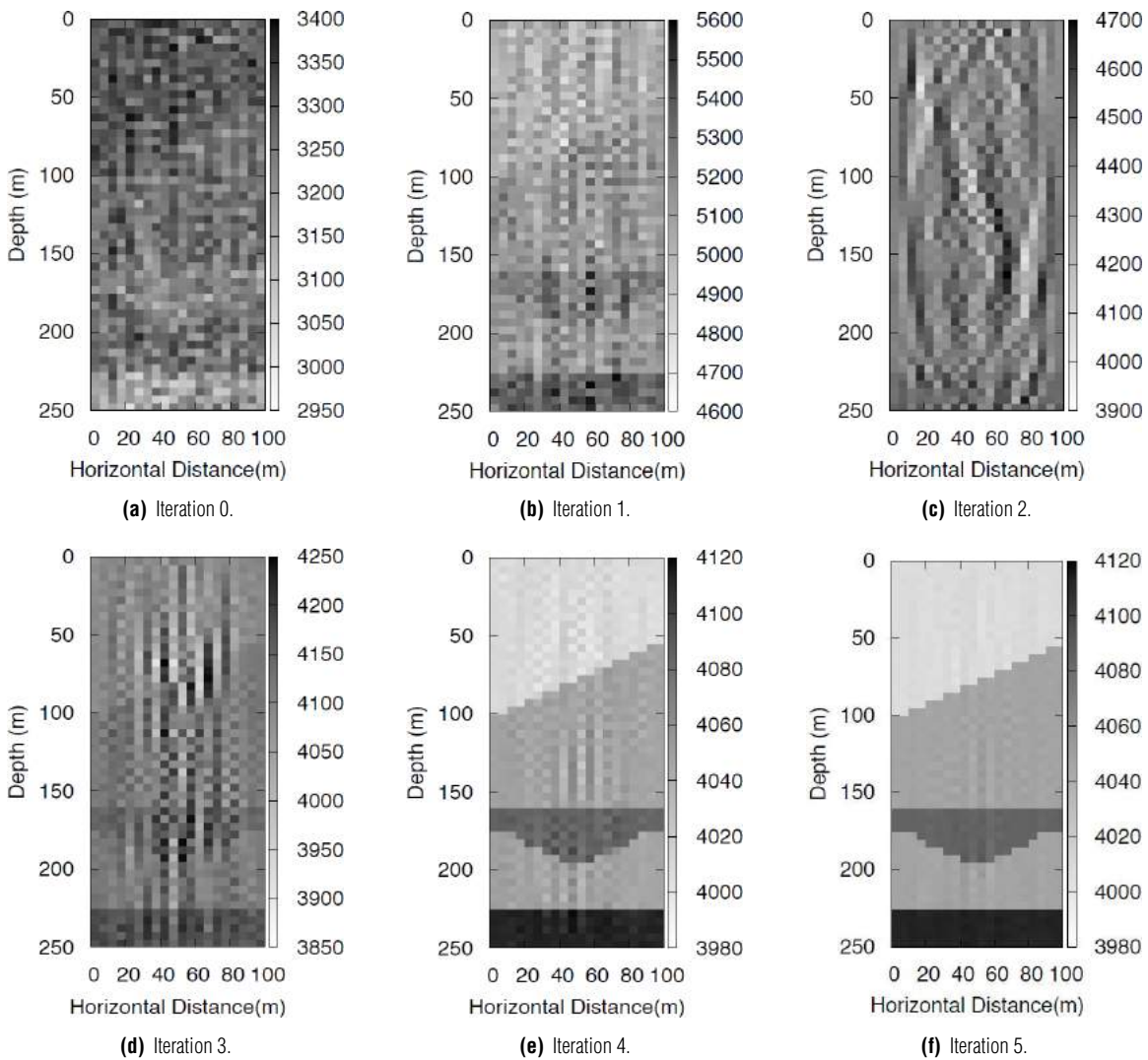


Figure 7 – Models estimated by an iterative multifrequency inversion using updated background velocities: (a) 2500 m/s, (b) 3200 m/s, (c) 5005 m/s, (d) 4305 m/s, (e) 4060 m/s and (f) 4030 m/s.

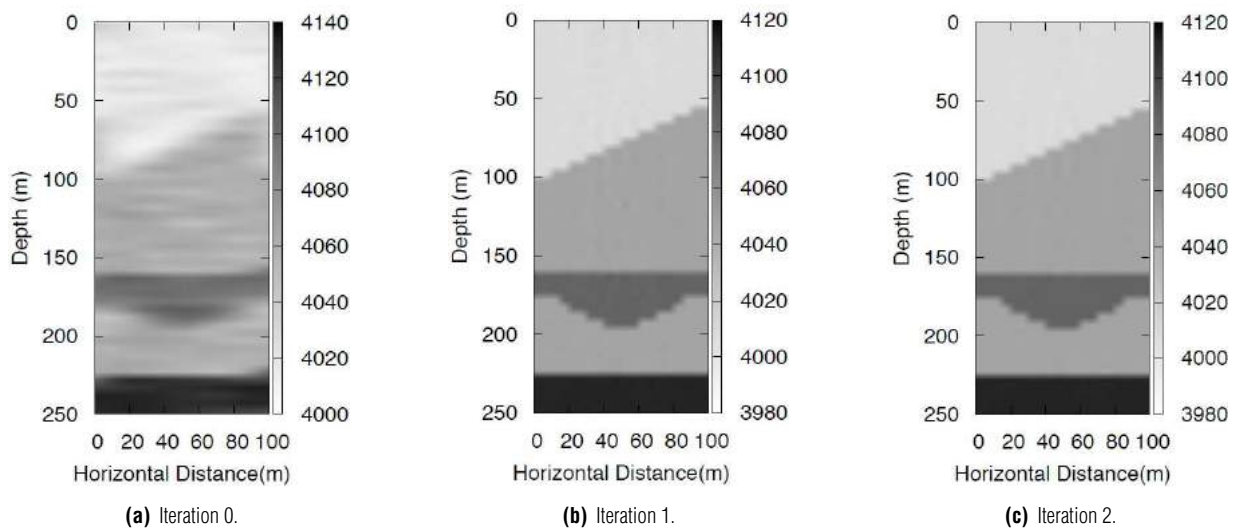


Figure 8 – Model estimated by a sequential iterative single-frequency inversion using background velocities and frequencies: (a) 2500 m/s and 319 Hz, (b) 4045 m/s and 516 Hz, and (c) 4030 m/s and 514 Hz.

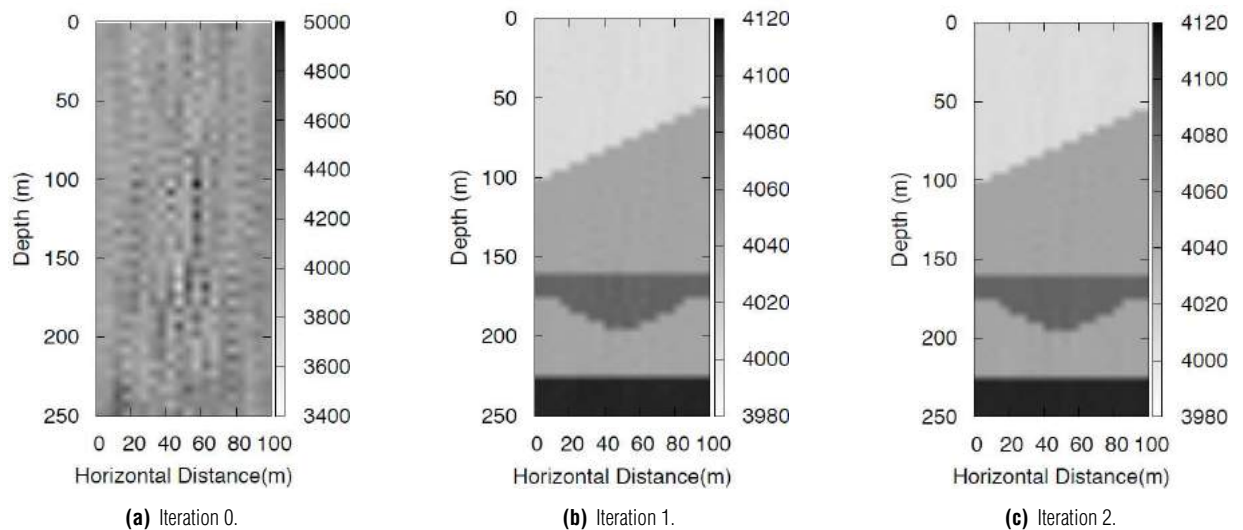


Figure 9 – Model estimated by a sequential iterative multifrequency inversion using updated background velocities and 3 frequencies: (a) 2500 m/s and 318.5 ± 0.5 Hz, (b) 4050 m/s and 516 ± 0.5 Hz, and (c) 4030 m/s and 513.5 ± 0.5 Hz.

SEQUENTIAL ITERATIVE MULTIFREQUENCY

In this approach, several frequencies were used simultaneously at each iteration, and these varied according to the background velocity, maintaining the wavelength range constant. Figure 9 shows the tomograms obtained with this approach, demonstrating that the results were also satisfactory with fewer iterations. However, the model RMS error did not improve significantly when compared to that of the previous, single-frequency case.

COMPARATIVE TABLE

Table 1 summarizes the results of the presented approaches, showing that the velocity error was similar among the four approaches. The average velocity of the recovered model converged to the average velocity of the true model at each iteration in all cases. This is the reason for the low velocity errors obtained at the end of the iterations. The data error presented a behavior similar to that of the velocity error, whose value was very close in the four approaches. On the other hand, the

Table 1 – A comparison of the velocity, object function and data relative RMS errors of the four presented approaches, referring to the last iteration and the number of iterations.

Approach	Features	ϵ_v	ϵ_m	ϵ_d	Iterations
Single	Constant frequency	0.041	5.487	0.038	4
Multi	Constant multifrequencies	0.028	3.877	0.032	5
Single Sequential	Variable frequency	0.016	2.146	0.036	2
Multi Sequential	Variable multifrequencies	0.024	3.345	0.032	2

model error had the greatest disparity among the four approaches. The sequential approaches proved to be more effective than the constant frequency approaches, both with respect to errors and the number of iterations required. This is because the chosen constant wavelength was the one that best “viewed” the medium, which was repeated in all iterations, different from the cases of the constant frequency approaches. In addition, we noticed that the use of multifrequency was more effective in the case of constant frequencies, and we do not recommend its use when the frequency varies at each iteration. When keeping the frequency or the frequencies constant, the use of the multiple frequencies improved the result. The additional information mitigated a little bit the system ill-conditioning. In other words, the addition of more frequencies implied in an information gain, and decreased both on the RMS error between the true object function and the estimated one (ϵ_m) and RMS error between the true velocities and the estimated velocities (ϵ_v).

CONCLUSIONS

In this work, we present several single and multifrequency tomographic inversion approaches, investigating the iterative aspect of the diffraction tomography method, as well as the sequential aspect of the use of frequencies. The results of the iterative, single-frequency method were satisfactory, especially via the use of the GCV method to choose the regularization parameter, which significantly reduced the RMS error of the recovered model and allowed the use of an arbitrary initial background velocity. To obtain a better model recovery, several frequencies were introduced in the inversion with different frequency steps. It was verified that the multifrequency inversion presented the smallest errors. Another important aspect of the approaches is the pitch of the frequency step, as it is unreasonable to use a very wide pitch, since the frequency is related to the wavelength, and in theory, only a certain wavelength range “sees”

the medium properly. This is based on the block dimensions with which the interest region is discretized. We also noticed that the use of variable frequencies, in both single and multifrequency inversions provided a better recovered model and reduced the number of iterations required. In summary, the approach with the iterative and sequential Born approximation was satisfactory, with a smaller model error than the conventional approach. These approaches also made the inversion possible without the knowledge of the true background velocity of the medium.

ACKNOWLEDGMENTS

The authors thank FINEP for the project Rede Cooperativa de Pesquisa em Geofísica de Exploração, and CNPq for the project Instituto Nacional de Ciência e Tecnologia de Geofísica do Petróleo. This study was financed in part by the Coordenação de Aperfeiçoamento de Pessoal de Nível Superior – Brazil (CAPES) – Finance Code 001. Amin Bassrei thanks CNPq, the Geophysics Department, and the Center for Latin American Studies for their support of his visiting professorship at Stanford University where this research was performed.

REFERENCES

- CRAVEN P & WAHBA G. 1979. Smoothing noisy data with spline functions: Estimating the correct degree of smoothing by the method of generalized cross-validation. *Numerische Mathematik*, 31: 377–403.
- DEVANEY AJ. 1982. A filtered backpropagation algorithm for diffraction tomography. *Ultrasonic Imaging*, 4(4): 336–350.
- DEVANEY AJ. 1984. Geophysical diffraction tomography. *IEEE Transactions on Geoscience and Remote Sensing*, 1: 3–13.
- HARRIS JM. 1987. Diffraction tomography with arrays of discrete sources and receivers. *IEEE Transactions on Geoscience and Remote Sensing*, 4: 448–455.

- HARRIS JM & YIN F. 1994. Nonlinear multifrequency wave equation inversion. In: SEG Technical Program Expanded Abstracts 1994. p. 988–991. Society of Exploration Geophysicists.
- LO T-W & INDERWIESEN PL. 1994. Fundamentals of seismic tomography. Tulsa, OK: Society of Exploration Geophysicists. 178 pp.
- REGIN SKA T. 1996. A regularization parameter in discrete ill-posed problems. *SIAM Journal on Scientific Computing*, 17(3): 740–749.
- REITER DT & RODI W. 1996. Nonlinear waveform tomography applied to crosshole seismic data. *Geophysics*, 61(3): 902–913.
- ROCHA FILHO AA, HARRIS JM & BASSREI A. 1996. A simple matrix formulation diffraction tomography algorithm. In: 39th Brazilian Congress of Geology. Salvador, Brazil. Volume 2, p. 312–315.
- SANTOS ETF & BASSREI A. 2007. L- and θ -curve approaches for the selection of regularization parameter in geophysical diffraction tomography. *Computers & Geosciences*, 33(5): 618–629.
- THOMPSON DR, RODI W & TOKSÓZ MN. 1994. Nonlinear seismic diffraction tomography using minimum structure constraints. *The Journal of the Acoustical Society of America*, 95(1): 324–330.
- WAHBA G. 1990. Spline models for observational data. Volume 59. Philadelphia: SIAM. 169 pp.
- WOLF E. 1969. Three-dimensional structure determination of semi-transparent objects from holographic data. *Optics Communications*, 1(4): 153–156.
- WU RS & TOKSÓZ MN. 1987. Diffraction tomography and multisource holography applied to seismic imaging. *Geophysics*, 52(1): 11–25.

Recebido em 18 janeiro, 2019 / Aceito em 21 junho 2019

Received on January 18, 2019 / Accepted on June 21, 2019

RESIDUAL GRAVITY ANOMALY OF BRAZILIAN MARAJÓ BASIN USING CRUSTAL MODELING: IDENTIFYING STRUCTURAL AND TECTONIC FEATURES

Gilberto Carneiro dos Santos-Junior, Cristiano Mendel Martins and Nelson Ribeiro-Filho

ABSTRACT. Dealing with gravity data at complex geological environments is a hard task because regional and residual anomalies are unknown. Due to the fact former techniques do not apply geologic information for separating gravity data, interpretation could lead to common mistakes. In order to allow a better interpretation at sedimentary basins, we applied a different approach for separating regional and residual anomalies for gravity data: the crustal modeling procedure. This approach consists on discretizing the Earth's crust in prismatic cells and calculating the predicted signal due to Earth's crust. We set horizontal dimensions of each prism, while the top and bottom are defined by Earth's topography and depth of crust-mantle boundary, usually called Moho. Additionally, when the predicted signal is calculated, the residual anomaly is obtained from simple subtraction. We applied our methodology at Marajó basin (North, Brazil), where previous geological studies identified a system of faults and grabens, also known as Marajó graben system. Moreover, our results are well compared with previous interpretation through the seismic method, exemplifying the approach's quality and efficiency. We believe, therefore, that the crustal modeling approach could be considered for studying any Brazilian sedimentary basin and other interesting areas.

Keywords: crustal modeling, residual gravity anomaly, Marajó basin, Marajó graben system.

RESUMO. Interpretar dados gravimétricos em ambientes geológicos de grande complexidade é uma tarefa difícil de ser realizada, visto que anomalias regionais e residuais são desconhecidas. Devido ao fato de que conhecidas técnicas de separação regional-residual não consideram informações geológicas, a interpretação final pode fornecer resultados equivocados. A fim de permitir uma melhor interpretação nas bacias sedimentares, aplicamos uma diferente abordagem para separação regional-residual: a modelagem crustal. Esta abordagem consiste em discretizar a crosta terrestre em células prismáticas e calcular o sinal regional predito. Definimos as dimensões horizontais de cada prisma, enquanto o topo e a base são definidos pela topografia e profundidade da interface crosta-manto, respectivamente. Após o cálculo do sinal predito, a anomalia residual é calculada via subtração. Aplicamos nossa metodologia na bacia do Marajó (região Norte, Brasil), onde estudos geológicos identificaram um sistema de falhas e grábens, definido por sistema de gráben do Marajó. Nossos resultados apresentam boa correspondência quando comparados com interpretações realizadas via método sísmico, o que exemplifica a qualidade e eficiência da nossa proposta. Acreditamos, portanto, que esta abordagem de modelagem crustal poderia ser considerada para o estudo de qualquer bacia sedimentar brasileira e de outras regiões de interesse.

Palavras-chave: modelagem crustal, anomalia gravimétrica residual, bacia do Marajó, sistema de gráben do Marajó.

INTRODUCTION

Geophysical methods can obtain information about internal structure of the Earth by measuring and analyzing the differences of each associated physical property Luiz & Silva (1995). The gravity method, precisely, provides a quite good information about deep structures and zones within crust and mantle and closeness. This method is widely used on identification of crustal features, due to the existing differences of density along lithosphere, with a fast acquisition and an efficient interpretation in the most of cases (Telford et al., 1990).

Studying sedimentary basins from gravity data is an application that becomes possible due to the fact that density of rocks varies while the depth increases. Additionally, the difficult lies on the changes of different sediment packs and composition of minerals. Moreover, the difference between densities of sedimentary package and the crustal basement is usually negative, despite changes on amplitude can occur easily. This shift befalls when deep-large structures are present, especially the crust-mantle interface: the Mohorovicic discontinuity (i.e. Moho). Once gravity signal is a result of all possible effects (Telford et al., 1990; Blakely, 1996), a very careful data processing is required. They include: (i) residual anomalies, usually the main goal in a study; (ii) longer-wavelength regional components from deep-large geological sources; and (iii) shorter-wavelength noise from errors and/or shallow sources (Robinson, 1988; Telford et al., 1990; Hinze et al., 2013). Therefore, the separation of regional and residual data becomes necessary.

The process of removing interfering regional and noise components in the anomaly field is the regional-residual problem, which is a critical step for interpretation (Al-Heety et al., 2017). This procedure can be done by many different approaches: (i) analyzing the anomaly spectrum in Fourier domain (Spector & Grant, 1970; Syberg, 1972), (ii) applying the wavelet transform to identify the depth of geological features (Fedi & Quarta, 1998) and/or (iii) fitting the regional field by low degrees polynomials (Agocs, 1951; Simpson Jr, 1954; Beltrão, 1989; Beltrão et al., 1991). The main limitation of those mentioned techniques is the absence of geological information. Then, most of the regional-residual separation techniques fails when the environment presents a quite complexity in its geology. Nevertheless, performing this separation of gravity data by means of the crustal modeling technique is also a possibility that is been used nowadays. In addition to, the residual signal is calculated by subtracting the observed gravity data and the regional signal, that is predicted by the modeled crust of the Earth.

The existence of a complex graben system in the Marajó basin (Azevedo, 1991; Zalán & Matsuda, 2007) can lead to a mistaken interpretation on using gravity data only. That reason enforces us to go forward on performing the regional-residual separation following a different path and provide an interpretation. In this research, the interest lies on selecting a residual anomaly for the Marajó basin, which is performed by applying the crustal modeling procedure. Moreover, an important research based on seismic data is used to stand the assumptions gravity results. Regional and residual signals present a decent correspondence with geological information and results of seismic data presented in Villegas (1994); Costa et al. (2002) as well. Therefore, we believe this new approach for separating gravity data should be use more often.

CRUSTAL MODELING APPROACH

The methodology of crustal modeling consists on using geometric models with the purpose of evaluate Earth's crust that normally require an extensive processing time. Suppose a topography model along with continental and oceanic crusts could be divided by a set of rectangular prisms, as illustrated in Figure 1. This interpretative model has a right-orientation Cartesian coordinated x and y axes, and z -axis being positive downward. To calculate a predicted gravity data and evaluate the interpretative model, only the number of prisms and its dimensions is necessary though.

Let \mathbf{g} be the gravitational vertical attraction of a rectangular prism with known dimensions in the horizontal and vertical directions. The thickness of each prism varies through the following condition: the top of each prism in the interpretative model represents the Earth's topography and each value for the bottom is consisted with the Moho surface. By setting a grid of observation points (x, y) and a level z , with a set of gravity observations \mathbf{g}_{obs} , the gravity vertical attraction of each M prism at the observation point (x_i, y_i, z_i) can be written as follow:

$$\mathbf{g}_i(x_i, y_i, z_i) = \sum_{j=1}^M \mathbf{f}_i(\mathbf{p}_j, \rho_i) \quad (1)$$

where \mathbf{f}_i is a non-linear function represented as $\mathbf{f}_i(\mathbf{p}_j, \rho_i) = \mathbf{f}_i(x_i, y_i, z_i)$, when i goes from 1 to M , representing the number of prisms.

The calculation of $\mathbf{f}_i(x_i, y_i, z_i)$ represents the vertical component of gravitational field, firstly described by Nagy (1966); Blakely (1996) as:

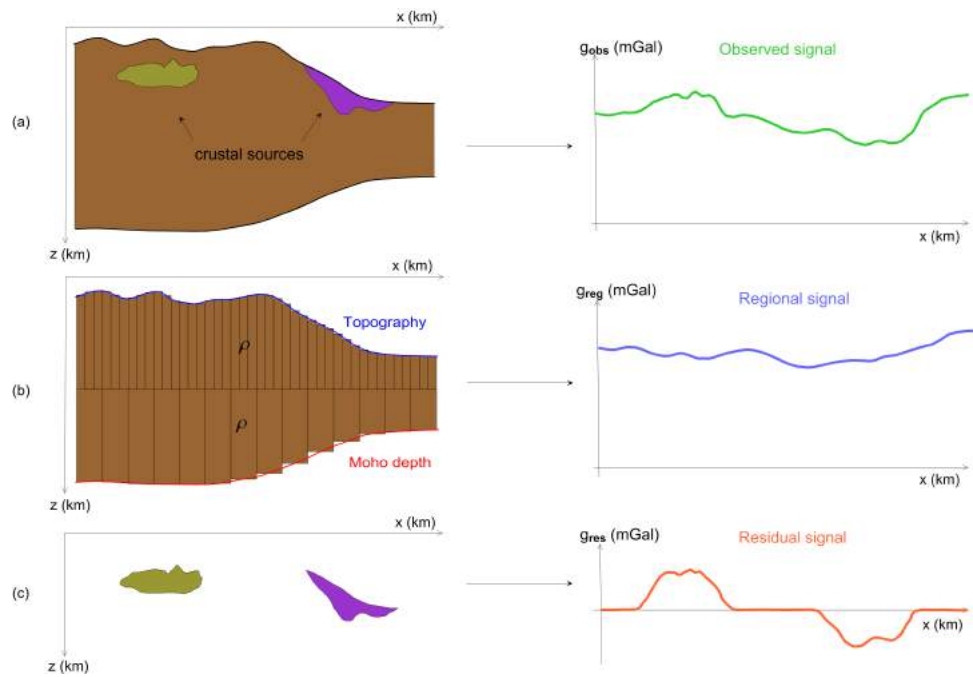


Figure 1 – Interpretative scheme for calculating the residual gravity anomaly. (a) Example of heterogeneous and (b) homogeneous crusts, (c) sketched model with existing crustal sources only and its corresponded signals.

$$f_i(x_i, y_i, z_i) = \gamma \rho \int_0^{p_j} \int_{y_a}^{y_b} \int_{x_a}^{x_b} \frac{(z_i - z'_j) dx'_j dy'_j dz'_j}{[(x_i - x'_j)^2 + (y_i - y'_j)^2 + (z_i - z'_j)^2]^{\frac{3}{2}}} \quad (2)$$

where γ is the universal gravitational constant (i.e. $6.673 \cdot 10^{-11} \text{ m}^3 \text{ kg}^{-1} \text{ s}^{-2}$); (x_i, y_i, z_i) are the observation point and (x_j, y_j, z_j) are the center of each j -th prism with volume $dv'_j = dx'_j dy'_j dz'_j$. The denominator in Equation 2 represents the distance between the i -th observation point and the j -th prism position for this specific case. In addition, the limits of integration can be written as $x_a = x_j - \frac{dx}{2}$, $x_b = x_j + \frac{dx}{2}$, $y_a = y_j - \frac{dy}{2}$, $y_b = y_j + \frac{dy}{2}$. Moreover, the numerical solution for Equation 2 was proposed by Plouff (1976):

$$f_i(x_i, y_i, z_i) = \gamma \rho \sum_{k=1}^2 \sum_{l=1}^2 \sum_{m=1}^2 \mu_{klm} \left[z_m \arctan \frac{x_k y_l}{z_m R_{klm}} - x_k \log(R_{klm} + y_l) - y_l \log(R_{klm} + x_k) \right] \quad (3)$$

where $R_{klm} = \sqrt{x_k^2 + y_l^2 + z_m^2}$; $\mu_{klm} = (-1)^k (-1)^l (-1)^m$.

The top z_t of each prism is set by topography of surface, which is obtained by using a digital elevation model. In the meanwhile, the bottom z_b represent the relief of Moho. Once the crust is modeled, the calculation of gravity anomaly due to the

set of prisms is calculated, representing the regional anomaly (i.e. $f_i(x_i, y_i, z_i) = g_{reg}$). Computing the difference between observed data and predicted data, the residual gravity anomaly, define here as g_{res} , illustrated in the Figure 1, can be encountered:

$$g_{res} = g_{obs} - g_{reg} \quad (4)$$

The residual anomaly showed in Equation 4 is responsible for characterizing the Earth's surface and its contents, such as geologic faults or lineaments, intrusion and sedimentary basins (Blakely, 1996; Al-Heety et al., 2017).

CHARACTERIZATION OF THE MARAJÓ BASIN

Marajó basin is located in the North of Brazil, state of Pará, containing a total sedimentary area close of 162 km² (see Fig. 2). Foz do Amazonas basin in the north-side, Gurupá and Tocantins arches are the limits of Marajó basin. In addition, Marajó basin was formed by an interconnected graben system, previously described in important geologic studies (Azevedo, 1991; Zalán & Matsuda, 2007).

Geological background

Marajó basin was formed during the Mesozoic as well as others sedimentary basins in the northern of Brazilian equatorial margin.



Figure 2 – Location map of northern Brazil. The dashed box indicates the study area. Red line represents the boundary of Marajó basin.

The presence of a large extensional rift system is associated with the opening of South Atlantic Ocean (Zalán & Matsuda, 2007; Soares Júnior et al., 2008, 2011). Additionally, the system was formerly aborted. The inside area is composed by four sub-basins, described by Costa et al. (2002); Soares Júnior et al. (2008) as Mexiana (north), Limoeira (center), Mocajuba (south) and Cameté (southeast). Moreover, those sub-basins were settled along zones of crustal weakness, such as the Araguaia and Gurupá orogenic belts (Costa et al., 2002; Zalán & Matsuda, 2007).

A complex architecture on Marajó basin is defined by normal faults NW-SE oriented. In addition, a NE-SW strike-slip faults system separates the mentioned sub-basins, controlling the existing geometry of Marajó basin (Villegas, 1994; Costa et al., 2002), as can be seen in Figure 3. The graben system on Marajó basin was formed by two main sedimentary sequences: rift phase and post-rift, that can be seen in the stratigraphic column in Figure 4.

The rift sequence is divided in two different stages (Avenius, 1988; Carvajal et al., 1989). The oldest was associated to

the opening of Central Atlantic Ocean. On the other hand, the nearest is more important, associated with the basin's enlargement. In addition to, this former event is dated as the Apatian-albian transition, formed by Breves, Jacarezinho and Anajás formations (Azevedo, 1991). In contrast, the post-rift sequence is divided in three sedimentary units: Limoeiro formation (Campanian) and Marajó and Tucunaré formations (Schaller et al., 1971). According to Villegas (1994), the post-rift base has a discontinuity, which is well defined. Therefore, the author described that the structure can be associated with erosion process or the non-deposition.

DATA SELECTION

As previously explained, on applying the crustal modeling approach for separating regional and residual of gravity data, a choice of top and bottom for each prismatic cell on the partitioned surface is necessary. To do so, top and bottom of each prism (i.e. z_t and z_b) was set by the Earth's topography and the Moho surface, respectively. ETOPO1 Amante & Eakins (2009) was used as topography and the Moho depth from Uieda & Barbosa (2016)

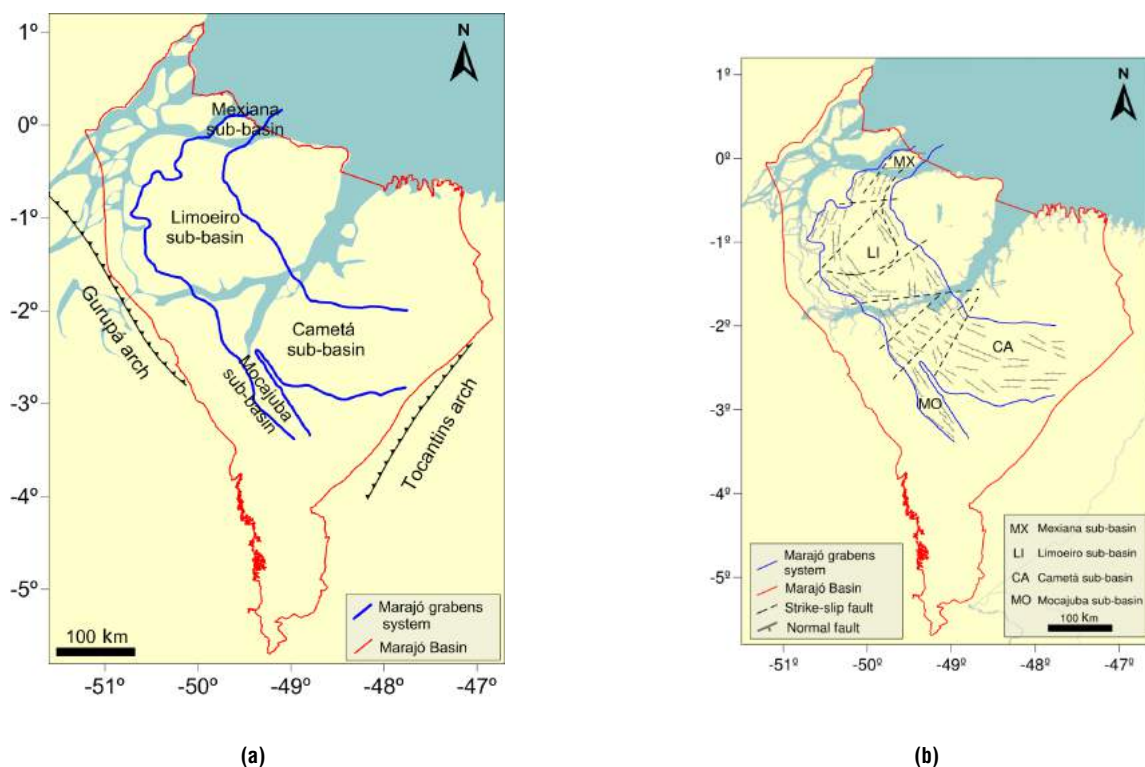


Figure 3 – Marajó basin map indicating (a) the graben system (i.e. blue lines) and Tocantins and Gurupá arches and (b) tectonic structures, black dashed lines are structural faults taken from Villegas (1994).

Age		Lithostratigraphy	
		Subsurface	
Quaternary		Tucunaré Formation	
Paleogene		Marajó Formation	
		Limoeiro Formation	
Cretaceous	Late	Maastrichtian	Anajás Formation
		Campanian	
		Santonian	
	Early	Caniancian	Breves Formation
		Turonian	
		Cenomanian	
	Albian	Jacarezinho Formation	
	Aptian		
	Barremian		

Figure 4 – Lithologic column of Marajó basin. The red dashed lines indicate the intervals of rift and post-rift sequences, taken from Rossetti (2010).

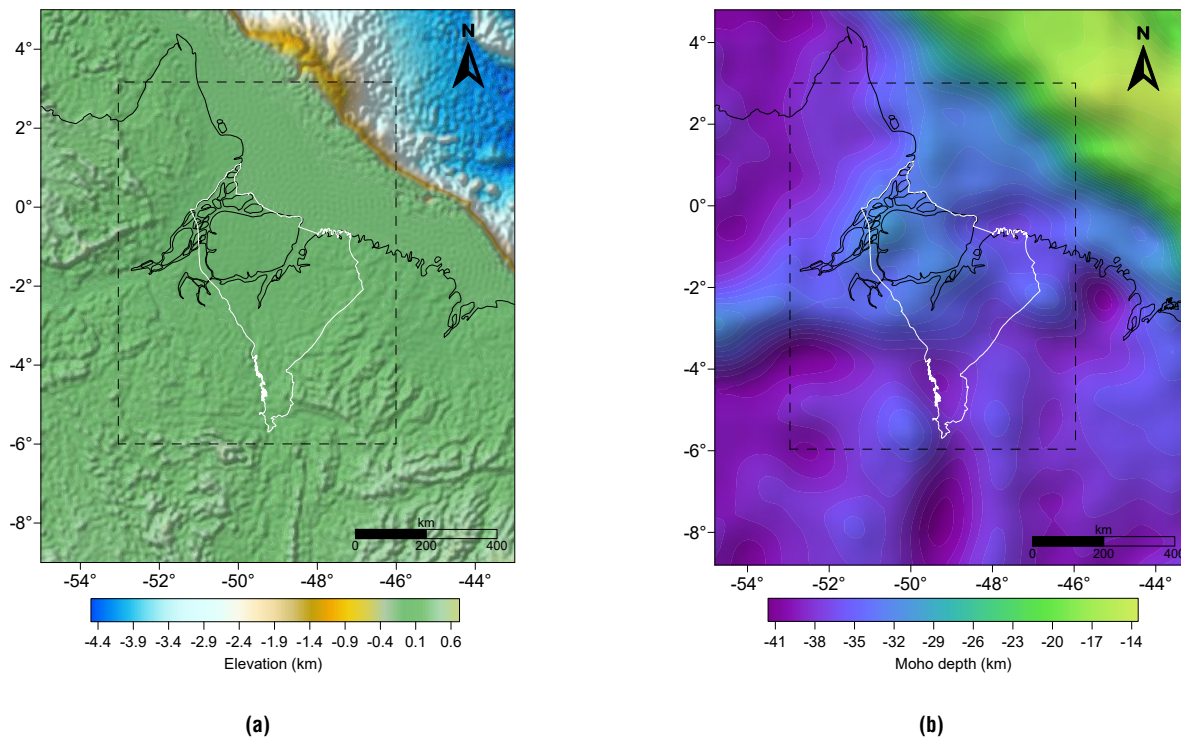


Figure 5 – (a) Topography from ETOPO1 (Amante & Eakins, 2009) and (b) Moho depth data from Uieda & Barbosa (2016). Black continuous line indicates the Brazilian coast line. The black dashed line shows our study area and white line represents the Marajó basin boundary.

was set for the prism's bottom. Maximum and minimum values for topography goes from ≈ 750 m on the continent and ≈ 4.5 km in the ocean. When Moho depth is analyzed, the variation goes from ≈ 13.5 km to ≈ 41.4 km. Figure 5 illustrates the topography and depth of Moho for the selected study area.

With purpose of avoiding edge effects and limitations in crustal modeling procedure, a larger area of gravity data was selected, as illustrated in Figures 5 and 6. Primary step of dealing with real data is converting coordinates, in this case geodetic (i.e. latitude and longitude) into metric (i.e. North and East), where the corresponding Universal Traverse Mercator (UTM) zone is 22.

We created two regular grids with different dimensions in order to define the position of top and bottom of each prism. Those prisms have x and y dimensions equal to $dx = 5.57$ and $dy = 5.58$ in the top of our model, respectively, while the bottom was discretized with $dx = 43.126$ and $dy = 44.625$, respectively, with both measurements in kilometers. Those choices were made considering the fact topography surface usually presents lower wavelength in gravity data, while relief of Moho is smoother than Earth's topography.

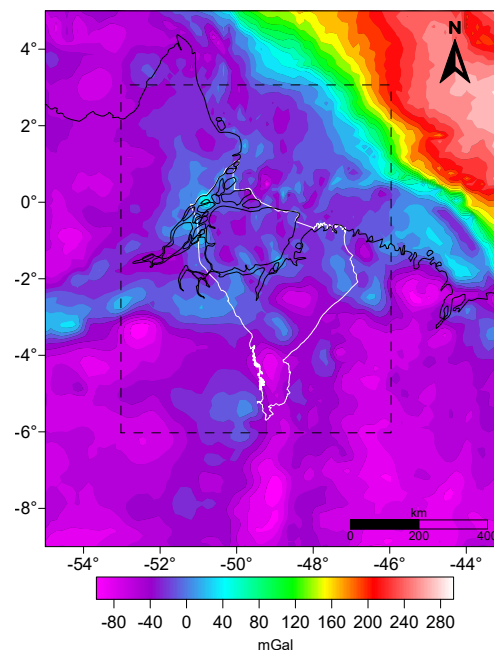


Figure 6 – Observed Bouguer anomaly at Marajó basin area. Black dashed line shows the study area while white line represents the Marajó basin's contour. The maximum and minimum value of Bouguer anomaly goes from -109 to 294 mGal.

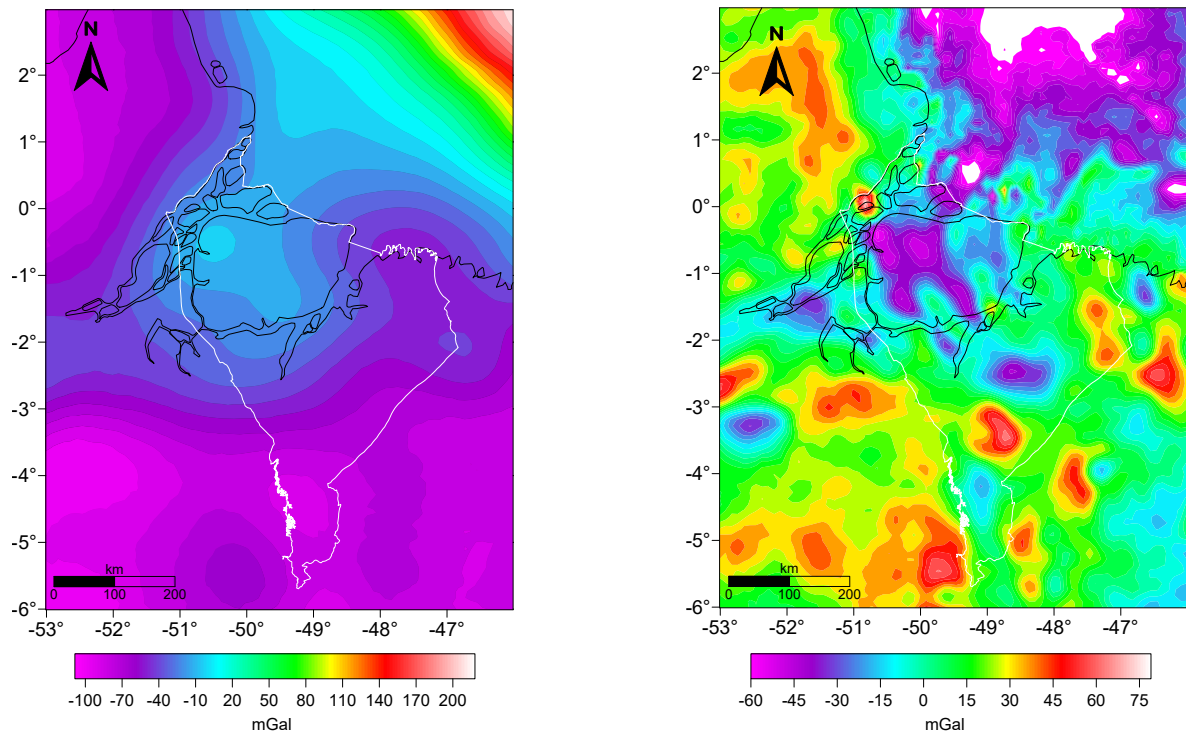


Figure 7 – (a) Regional and (b) residual anomalies that were obtained by means that crustal modeling and subtracting the observed data and the regional data, respectively. The amplitudes of the regional anomaly go from -109 to 217 mGal, while the residual anomaly has minimum equals to -60 and maximum of 80 mGal. Black and white lines represent the Brazilian coast line and the Marajó basin contour, respectively.

The choice for simple Bouguer anomaly (see Fig. 6) is a relevant topic to discuss. Although some researchers presented gravity disturbance should be more effective for modeling and inversion (Li & Götze, 2001; Hackney & Featherstone, 2003), the simple Bouguer anomaly without terrain correction is quite similar to gravity disturbance when topography is corrected. Moreover, due to the lack of elevated features or mountains at the area the terrain correction was not applied.

RESULTS AND DISCUSSION

Once Earth's crust is partitioned in prismatic cells and Equation 3 is applied on observation points, the predicted anomaly is calculated. Here we defined as regional anomaly (\mathbf{g}_{reg}), corresponding to contribution of long wavelength sources (i.e. Moho relief), as illustrated in Figure 7a. Residual data (\mathbf{g}_{res}) are finally calculated after the subtraction between observed \mathbf{g}_{obs} and regional \mathbf{g}_{reg} data are performed. Figure 7 depicts the obtained result of regional and residual data from applying crustal

modeling procedure. Furthermore, a better detailed interpretation is presented in the next subsection.

Geophysical interpretation from gravity data

An initial interpretation can be done by analyzing the residual gravity anomaly presented in Figure 7 only. Regional signal presents a smooth signal, with more positive values along the ocean. following a negative tendency in the continental part as expected. However, the residual signal shows a zone with a more negative signature, significant in this study. The behavior of \mathbf{g}_{res} inside Marajó basin could represent its shape and also the structure of Marajó graben system (see Figs. 3 and 4), which was previously sketched in the research of Villegas (1994).

When negative part of residual anomaly is considered only, it is possible shape of Marajó graben system and the corresponded signal are well-correlated. This assumption is completely understandable, once negative and inflections seem to be related to geological structures and faults. Moreover, it is

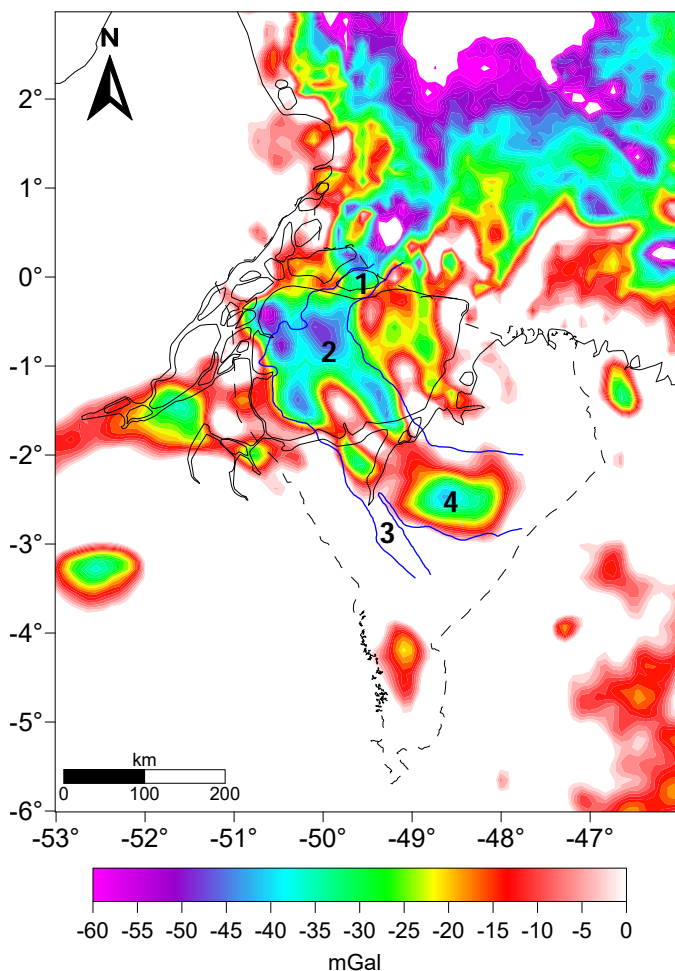


Figure 8—Negative part of residual anomaly. Black dashed line represents the Marajó basin's contour while blue lines indicate the Marajó graben system. The numbers are (1) Mexiana, (2) Limoeiro, (3) Mocajuba and (4) Cametá sub-basins.

notable that the graben system is larger in NW direction, as well as the main part of residual anomaly. Figure 8 illustrates the negative-residual anomaly, which follows a NW tendency inside the Marajó basin.

Correlation with seismic interpretation

The seismic sections were, in essence, presented in an interesting study of Villegas (1994); Costa et al. (2002). They analyzed seismic reflection data with the purpose of mapping Marajó graben system, obtaining excellent results. From this point of view, we believe gravity and seismic data could provide a better interpretation when compared simultaneously. To do so, three

profiles in residual gravity anomaly were analyzed, due to the location of seismic data, aiming for plausible correspondence. Profiles A—B and C—D are located northward of Limoeiro sub-basin, while E—F profiles is near to Mocajuba and Cametá sub-basins. Figure 9a exhibits the location of each seismic section inside the residual signal and the seismic interpretation is presented in Figure 9b.

Profile A—B intersects the boundary of Marajó graben system west and eastward. This intersection is clearly visible in the seismic section. Negative high values in the profile of residual gravity anomaly could indicate the presence of normal faults in the east part. A second plausible indication of geologic faults would

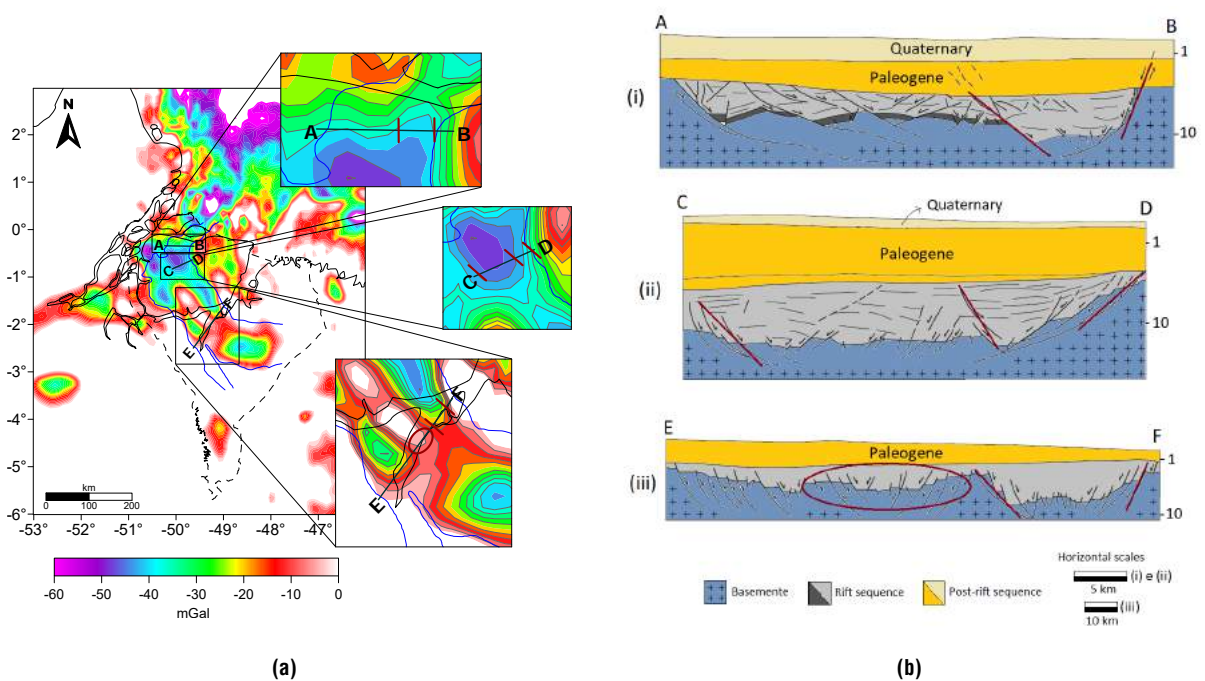


Figure 9 – (a) Highlight of three gravity profiles on residual anomaly map. (b) Seismic sections inside Marajó graben system area, previously presented in Costa et al. (2002).

be the tendency on residual signal, also sketched in seismic interpretation.

A second section C—D is located at east boundary of Marajó graben system. Similar to the A—B section, a negative high value is observed in residual anomaly. This low gravity zone can be associated to an existing sub-basin or geologic faults, once basin and faults normally show negative tendencies. Additionally, the uplift of igneous basement increases the value of gravity data, which is notable in the residual anomaly.

Profile E—F shows two significant faults and a possible formation of a horst-graben system, which in this case represent part of Marajó graben system. An interesting assumption is the depth of basement in seismic section, which decrease in SW-NE direction. Moreover, this tendency is clearly observed in the residual data, presenting a positive-negative trend.

CONCLUSIONS

Selecting the best gravity residual anomaly is a difficult task to perform when complex geological environments are present. With the purpose of improving regional-residual separation technique, we used a crustal modeling approach for separating regional and residual anomalies for gravity data. Our approach consists on

discretizing the Earth's crust in rectangular prisms. Geometric parameters are defined by user, while top and bottom are set by topography and Moho surface. Therefore, residual anomaly is obtained from subtracting observed and predicted data.

We applied the former procedure at Marajó basin. The main reason lies on the lack of geophysical studies. Moreover, the presence of a known graben system intrigued us to go forward on interpreting this area. Despite geologically complex, crustal modeling approach clearly illustrated the Marajó graben system, mapped in former studies. To support gravity interpretation, a comparison with seismic data was done. Then, Marajó graben system observed from gravity data corresponds well when compared to seismic data. Geologic faults in the seismic section are seen as negative values in the gravity anomaly, while the rise of basement appears as a positive value and high tendency in the residual.

We believe the crustal modeling procedure was very interesting on selecting the best residual anomaly, providing a quite good interpretation despite the complexity of Marajó basin. At those types of geological environments, common techniques of separating regional and residual data are not recommended. Therefore, we also believe the presented approach is easily

applicable and quite appropriated for any Brazilian sedimentary basin, once all data set used in this work are free.

ACKNOWLEDGEMENTS

The authors would like to thank to Faculdade de Geofísica (portuguese version of *Faculty of Geophysics*) and Centro de Pós-Graduação em Geofísica (portuguese version of *Geophysical Post-Graduate Center*) for providing computational and financial supports. Third author has a special thank to Programa de Pós-Graduação em Geofísica, Observatório Nacional (ON/MCTI). The authors also appreciate the efforts of Dr. Boris Chaves Freimann, for help on geologic details and maps. Finally, the authors would like to thank the reviewers, for the significant assessments and suggestions in order to make this research better as well.

REFERENCES

- AGOCS W. 1951. Least squares residual anomaly determination. *Geophysics*, 16(4): 686–696.
- AL-HEETY EMS, AL-MUFARJI MA & AL ESHO LH. 2017. Qualitative Interpretation of Gravity and Aeromagnetic Data in West of Tikrit City and Surroundings, Iraq. *International Journal of Geosciences*, 8(02): 151.
- AMANTE C & EAKINS B. 2009. ETOPO1 1 Arc-Minute Global Relief Model: procedures, data sources and analysis. National Environmental Satellite, Data, and Information Service, National Geophysical Data Center Marine Geology and Geophysics Division, 19 pp.
- AVENIUS CG. 1988. Cronostratigraphic study of the post-rift/sin-rift unconformity, Marajó Rift system. Belém, Brazil: Texaco/Canada Report.
- AZEVEDO RP. 1991. Tectonic evolution of Brazilian equatorial continental margin basins. Ph.D. thesis. Imperial College, University of London. 494 pp.
- BELTRÃO JF. 1989. Uma nova abordagem para interpretação de anomalias gravimétricas regionais e residuais aplicada ao estudo da organização crustal: exemplo da Região Norte do Piauí e Noroeste do Ceará. Ph.D. thesis. Centro de Geociências, Universidade Federal do Pará, Belém, PA-Brazil. 156 pp.
- BELTRÃO JF, SILVA JBC & COSTA JC. 1991. Robust polynomial fitting method for regional gravity estimation. *Geophysics*, 56(1): 80–89.
- BLAKELY RJ. 1996. Potential theory in gravity and magnetic applications. Cambridge University Press. 461 pp.
- CARVAJAL DA, DORMAN JT, KENCK AR, KEY CF, MILLER CJ & SPECHT TD. 1989. Final report of the third exploration phase, Marajó. Belém, Brazil: Texaco/Canada. Report.
- COSTA J, HASUI Y, BEMERGUY RL, SOARES-JÚNIOR AV & VILLEGAS J. 2002. Tectonics and paleogeography of the Marajó Basin, northern Brazil. *Anais da Academia Brasileira de Ciências*, 74(3): 519–531.
- FEDI M & QUARTA T. 1998. Wavelet analysis for the regional-residual and local separation of potential field anomalies. *Geophysical Prospecting*, 46(5): 507–525.
- HACKNEY R & FEATHERSTONE W. 2003. Geodetic versus geophysical perspectives of the 'gravity anomaly'. *Geophysical Journal International*, 154(1): 35–43.
- HINZE WJ, VON FRESE RR & SAAD AH. 2013. Gravity and magnetic exploration: Principles, practices, and applications. Cambridge University Press. 525 pp.
- LI X & GÖTZE HJ. 2001. Ellipsoid, geoid, gravity, geodesy, and geophysics. *Geophysics*, 66(6): 1660–1668.
- LUIZ JG & SILVA LMC. 1995. Geofísica de prospecção. Editora Universitária UFPA. Brazil. 335 pp.
- NAGY D. 1966. The gravitational attraction of a right rectangular prism. *Geophysics*, 31(2): 362–371.
- PLOUFF D. 1976. Gravity and magnetic fields of polygonal prisms and application to magnetic terrain corrections. *Geophysics*, 41(4): 727–741.
- ROBINSON ES. 1988. Basic exploration geophysics. Somerset, NJ (US); John Wiley and Sons, Inc. 576 pp.
- ROSSETTI DF. 2010. Tectonic control on the stratigraphic framework of Late Pleistocene and Holocene deposits in Marajó Island, State of Pará, eastern Amazonia. *Anais da Academia Brasileira de Ciências*, 82(2): 439–449.
- SCHALLER H, VASCONCELOS D & CASTRO J. 1971. Estratigrafia preliminar da bacia sedimentar da Foz do Amazonas. In: XXV Congresso Brasileiro de Geologia da SBG. São Paulo - SP, Brazil. Volume 3, p. 180–202.
- SIMPSON JR SM. 1954. Least squares polynomial fitting to gravitational data and density plotting by digital computers. *Geophysics*, 19(2): 255–269.
- SOARES JÚNIOR AV, COSTA JBS & HASUI Y. 2008. Evolução da margem Atlântica Equatorial do Brasil: Três fases distensivas. *Geociências (São Paulo)*, 27(4): 427–437.
- SOARES JÚNIOR AV, HASUI Y, COSTA JBS & MACHADO FB. 2011. Evolução do rifteamento e paleogeografia da margem Atlântica Equatorial do Brasil: Triássico ao Holoceno. *Geociências*, 30(4): 669–692.
- SPECTOR A & GRANT F. 1970. Statistical models for interpreting aeromagnetic data. *Geophysics*, 35(2): 293–302.
- SYBERG F. 1972. A Fourier method for the regional-residual problem of potential fields. *Geophysical Prospecting*, 20(1): 47–75.

TELFORD WM, TELFORD W, GELDART L & SHERIFF RE. 1990. Applied Geophysics. Cambridge University Press. 792 pp. Volume 2.

UIEDA L & BARBOSA VC. 2016. Fast nonlinear gravity inversion in spherical coordinates with application to the South American Moho. *Geophysical Journal International*, 208(1): 162–176.

VILLEGAS J. 1994. Geologia estrutural da Bacia do Marajó. Master's dissertation. Centro de Geociências, Universidade Federal do Pará, Belém, PA-Brazil. 119 pp.

ZALÁN PV & MATSUDA NS. 2007. Bacia do Marajó. *Boletim de Geociências da Petrobras*, 15(2): 311–319.

Recebido em 31 de janeiro de 2019 / Aceito em 28 de junho de 2019

Received on January 31, 2019 / Accepted on June 28, 2019

SEISMIC SIGNAL ANALYSIS USING MINIMUM PHASE AND SINGULAR VALUE DECOMPOSITION METHODS. APPLICATION TO GROUNDROLL ATTENUATION

Anderson Silva Santos and Milton José Porsani

ABSTRACT. A challenge in land seismic data processing is the coherent noise groundroll. This noise is related to the propagation of surface waves of the Rayleigh type, this undesired event has as characteristics: low frequencies, high amplitudes and strong dispersion, which masks the events of interest in the stacked seismic section. The seismic data from the Tacutu Basin, besides having a low signal-to-noise ratio, are also strongly contaminated by groundroll noise, which makes it a challenge to obtain stacked seismic section with high resolution of this sedimentary basin. The 1D and 2D frequency filters are widely used for groundroll attenuation, but these methods besides attenuating the noisy also eliminate part of the signal by rejecting part of the frequency band of the seismic signal. Therefore, we are introducing a new filter to groundroll attenuation that uses two powerful tools for decomposition of the seismic signal together, minimum phase decomposition and singular value decomposition. The proposed method aims to estimate the reflectivity function for each seismic trace and then perform a decomposition of this reflectivity function. Since the low frequency noise is confined in the first portion of the decomposed signal it is possible to make a separation between the noise and the signal. The filtering method was included in the 2D seismic processing flow chart of the Tacutu Basin. The results showed that the proposed method was able to attenuate the groundroll noise and generate at the end a stacked seismic section with a good resolution.

Keywords: minimum phase decomposition, singular value decomposition, groundroll attenuation.

RESUMO. Um desafio no processamento de dados sísmicos terrestres é o ruído coerente *groundroll*. Este ruído está relacionado à propagação de ondas de superfície do tipo Rayleigh, este evento indesejado tem como características: baixas frequências, altas amplitudes e forte dispersão, o que mascara os eventos de interesse na seção sísmica empilhada. Os dados sísmicos da Bacia do Tacutu, além de apresentar uma baixa relação sinal-ruído, também estão fortemente contaminados pelo ruído do solo, o que dificulta a obtenção de seções sísmicas empilhadas com alta resolução desta bacia sedimentar. Os filtros de frequência 1D e 2D são amplamente utilizados para a atenuação do *groundroll*, mas esses métodos além de atenuar o ruído também eliminam parte do sinal rejeitando parte da banda de frequência do sinal sísmico. Portanto, estamos introduzindo um novo filtro para a atenuação de *groundroll* que usa duas ferramentas poderosas para a decomposição do sinal sísmico, decomposição em fase mínima e decomposição em valor singular. O método proposto tem como objetivo estimar a função de refletividade para cada traço sísmico e então realizar a decomposição dessa função refletividade. Uma vez que o ruído de baixa frequência é confinado na primeira porção do sinal decomposto, é possível fazer uma separação entre o ruído e o sinal. O método de filtragem foi incluído no fluxograma de processamento sísmico 2D da Bacia do Tacutu. Os resultados mostraram que o método proposto foi capaz de atenuar o ruído *groundroll* e gerar ao final uma seção sísmica empilhada com boa resolução.

Palavras-chave: decomposição em fase mínima, decomposição em valores singulares, atenuação do *groundroll*.

INTRODUCTION

The filtering of seismic reflection data aims to attenuate all undesirable events present in the seismic data. If the filtration was good the result is an increase of the signal to noise ratio, providing a good stacked seismic section. There are many methods to filtering seismic data, but several require some knowledge about the noise and signal that we want, if we apply a filter without criterion it can prejudice the events of interest. For example, frequency filters, which are widely used to attenuation of high and low frequencies noises, create an undesirable effect, when we use these methods, we need cut the frequency band where the noise is located. If we do it, we can attenuate the noise but the interest signal in that region is lost (Santos, 2014).

The coherent noise groundroll is a problem when we need processing seismic land data. This noise is caused by propagation of surface waves called Rayleigh, this noise is characterized by: low frequencies, high amplitudes, low velocity and strong dispersion, which makes it very undesirable in the seismic section. This energetic event masks the reflections and it is a problem to seismic interpreter. The seismic data from Tacutu Basin located in Brazil that we choose to test the new filter has strongly concentration of the groundroll noise, which makes it more difficult to obtain seismic sections with high resolution in this sedimentary basin (Silva, 2004).

There are a lot of methods for groundroll attenuation. The frequency filters 1D and 2D ($f - k$ filter) are large used to attenuate this noise, but rejecting part of the frequency band where the noise is located, part of the signal of interest also is lost (Santos, 2014). Alves (2015) used the empirical mode decomposition (EMD) and singular value decomposition to attenuate the groundroll noise. Porsani et al. (2009) used the SVD method to groundroll attenuation and Melo et al. (2009) used a 2D time domain derivative filter for groundroll attenuation. Santos (2014) used a radial directional filtering in the time domain to attenuate this noise. Porsani et al. (2013b) used the minimum-delay decomposition method to get a dynamic reflectivity estimation. Using the minimum phase decomposition we can get a reflectivity estimation and using the SVD method we can get a seismic decomposition of reflectivity function.

In order to present a filter that provide an estimate of the reflectivity function as well as a decomposition of the reflectivity function in order to filter the influence of the low frequency noise, we present the filter MPD+SVD (Minimum Phase Decomposition plus Singular Value Decomposition). First we obtain an estimation of the minimum phase wavelets in a

seismic trace, after that we obtain a SVD decomposition of the matrix that contains in its columns all the estimated wavelets in the seismic trace, finally using the convolutional model of the seismic trace and inverting the system generated by this model we can obtain a decomposition of the reflectivity function. With the propose to do this new filter more efficient we implement it using the MPI paradigm (Message Passing Interface) in FORTRAN code. We did a 2D seismic processing of a Brazilian sedimentary basin, the Tacutu Basin, using the software Seismic Unix from CWP (Center for Wave Phenomena from Colorado School of Mines).

THEORY

Minimum Phase Decomposition

The minimum phase decomposition method (MPD) is based on the Wiener-Levinson deconvolution, where for each sliding window taken in the seismic trace, it is estimated minimum phase wavelets.

Take a seismic trace d_t with ns samples in time. If we take a window of length lw we get d_t^{lw} , where $lw \leq ns$. The auto-correlation function r_d from the window lw will be given by:

$$r_d = \sum_{k=1}^{lw} d_t d_{t+k} \tag{1}$$

Once the auto-correlation function has been calculated from inside the window within in the seismic trace, we get the normal equations in (2) which was used to get the Wiener-Levinson's filter coefficients.

$$\begin{bmatrix} r_0 & r_1 & \dots & r_n \\ r_1 & r_0 & \ddots & \vdots \\ \vdots & \ddots & \ddots & r_1 \\ r_n & \dots & r_1 & r_0 \end{bmatrix} \begin{bmatrix} 1 \\ g_1 \\ \vdots \\ g_n \end{bmatrix} = \begin{bmatrix} E_{g,n} \\ 0 \\ \vdots \\ 0 \end{bmatrix} \tag{2}$$

where \mathbf{g} is the unitary predict filter or Wiener-Levinson's filter and n is the number of filter coefficients. Taking into account that the auto-correlation matrix is a Toeplitz matrix, we can solve the system (2) efficiently use the Levinson's recursion (Porsani, 1986). After we calculated the coefficients of the vector \mathbf{g} , we can obtain the minimum phase wavelets \mathbf{w} by inversion of the following system of equations (Porsani et al., 2013a):

$$\mathbf{g}_n^{lw} * \mathbf{w}_n^{lw} = \delta_n^{lw}, \tag{3}$$

$$\text{where } \delta = \begin{cases} 1, & \text{if } t = 0 \\ 0, & \text{if } t \neq 0 \end{cases}$$

We can represent the seismic trace through the following matrix-vector notation

$$\begin{bmatrix} d_0 \\ d_1 \\ \vdots \\ \vdots \\ d_{ns} \end{bmatrix} = \begin{bmatrix} 1 & 0 & 0 & 0 & 0 \\ w_0(1) & 1 & 0 & 0 & 0 \\ \vdots & \ddots & \ddots & 0 & 0 \\ w_0(lw) & \ddots & \ddots & 1 & 0 \\ 0 & \ddots & \ddots & w_{ns-1}(1) & 1 \end{bmatrix} \begin{bmatrix} r_0 \\ r_1 \\ \vdots \\ \vdots \\ r_{ns} \end{bmatrix} \quad (4)$$

The equation above can be written as follows:

$$\mathbf{d} = \mathbf{W}\mathbf{r} \quad (5)$$

Where \mathbf{d} represents the seismic trace, the vector \mathbf{r} is the reflectivity function and matrix \mathbf{W} contains the minimum phase wavelets in their columns that were estimated within each time-sliding window in the seismic trace.

A next step is to get the singular value decomposition of the matrix \mathbf{W} and rewrite the Equation (5) in order to explore the advantages of the seismic trace decomposition using these two powerful tools for seismic signal analysis.

Singular Value Decomposition of matrix \mathbf{W}

The singular value decomposition (SVD) is an important theorem from algebra that was used to decompose the matrix containing the minimum phase wavelets \mathbf{W} of $ns \times ns$ into a sum of rank unitary matrices, where ns is the number of samples of the seismic trace. The theory of SVD theorem with applications in seismic data is well grounded in Freire (1986).

The SVD decomposition of the matrix $\mathbf{W}_{ns \times ns}$ into singular values can be written in the reduced form as follows:

$$\mathbf{W} = \mathbf{U}\mathbf{\Sigma}\mathbf{V}^T \quad (6)$$

where $\mathbf{\Sigma} = \text{diag}\{\sigma_1, \dots, \sigma_{ns}\}$ is a matrix that contains the singular values $\sigma_1 \geq \dots \geq \sigma_{ns} \geq 0$ on its main diagonal.

$\mathbf{U} = [\mathbf{u}_1, \dots, \mathbf{u}_{ns}]$ is an array of the eigenvectors of the covariance matrix $\mathbf{W}\mathbf{W}^T$ related with the time dimension.

$\mathbf{V} = [\mathbf{v}_1, \dots, \mathbf{v}_{ns}]$ is an array of the eigenvectors of the covariance matrix $\mathbf{W}^T\mathbf{W}$ related with the space dimension.

The matrices \mathbf{U} and \mathbf{V} are unitary and orthogonal. Another way to write the Equation (6) is:

$$\mathbf{W} = \sum_{k=1}^r \sigma_k \mathbf{u}_k \mathbf{v}_k^T = \sum_{k=1}^r \widetilde{\mathbf{W}}_k, \quad (7)$$

r is the matrix rank \mathbf{W} .

According to the Equation (7), the matrix \mathbf{W} can be seen as a sum of unitary rank matrices, weighted by their respective singular values (Freire, 1986). Each scalar product $\mathbf{u}_k \mathbf{v}_k^T$ set a unitary rank matrix, called by Andrews & Hunt (1977) as eigenimage of \mathbf{W} . So $\widetilde{\mathbf{W}}_k = \sigma_k \mathbf{u}_k \mathbf{v}_k^T$ represents the k -th eigenimage of the matrix \mathbf{W} .

The SVD decomposition is done adaptive where for each column of the matrix \mathbf{W} , a subset of N neighboring columns is collected, taking as reference the central column for which we wish to obtain the SVD decomposition. In this way we obtain a sliding window that travel the entire data matrix obtaining the SVD decomposition in the center of the sliding window (Fig. 1). This procedure preserves the amplitudes and highlight the continuity and coherence of reflection events (Silva, 2015). After that, the SVD decomposition of the matrix \mathbf{W} can be represent as follows:

$$\mathbf{W} = \widetilde{\mathbf{W}}_1 + \widetilde{\mathbf{W}}_2 + \dots + \widetilde{\mathbf{W}}_L = \sum_{i=1}^L \widetilde{\mathbf{W}}_i \quad (8)$$

$\widetilde{\mathbf{W}}_i$ is the i -th eigenimage of the matrix \mathbf{W} after SVD decomposition and L is the size of the sliding window (number of traces).

Now we can use the Equation (8) to rewrite the Equation (5) and we get:

$$\mathbf{d} = \mathbf{W}\mathbf{r} = \left(\sum_{i=1}^L \widetilde{\mathbf{W}}_i \right) \cdot \mathbf{r} \quad (9)$$

If we know \mathbf{r} (by solution of Eq. (5)) and $\widetilde{\mathbf{W}}_i$ we can decompose \mathbf{d} and we get:

$$\mathbf{d} = \widetilde{\mathbf{d}}_1 + \widetilde{\mathbf{d}}_2 + \dots + \widetilde{\mathbf{d}}_L = \widetilde{\mathbf{W}}_1 \mathbf{r} + \widetilde{\mathbf{W}}_2 \mathbf{r} + \dots + \widetilde{\mathbf{W}}_L \mathbf{r} = \sum_{i=1}^L \widetilde{\mathbf{d}}_i \quad (10)$$

This results in the following system of equations:

$$\widetilde{\mathbf{d}} = \widetilde{\mathbf{W}}\mathbf{r} \quad (11)$$

In the same way if we know $\widetilde{\mathbf{d}}$ and $\widetilde{\mathbf{W}}$ we can decompose \mathbf{r} .

Reflectivity function estimation

The system of Equations (11) allows us to obtain an estimate of the reflectivity function for each $\widetilde{\mathbf{d}}_i$. When we solve this system to find \mathbf{r} we find:

$$\widetilde{\mathbf{r}} = \widetilde{\mathbf{W}}^{-1} \widetilde{\mathbf{d}} \quad (12)$$

The matrix $\widetilde{\mathbf{W}}$ that has 1 on its main diagonal is lower triangular. This property allows us to solve the system quickly and

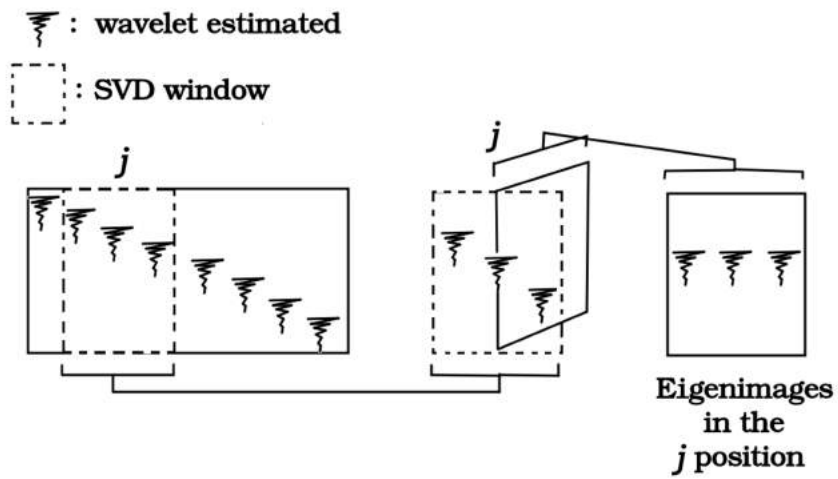


Figure 1 – Schematic diagram illustrating the SVD window application in a set of seismic trace to get the SVD decomposition on j position.

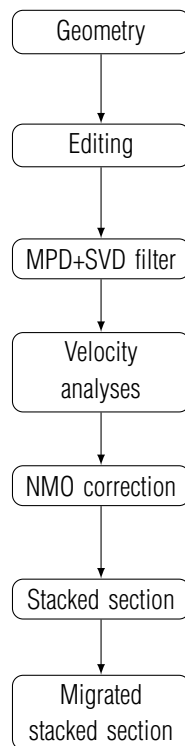


Figure 2 – Flowchart adopted to the 2D seismic processing from Tacutu Basin.

efficiently by back-substitution. The reflectivity function \mathbf{r} can be represented as:

$$\mathbf{r} = \tilde{\mathbf{r}}_1 + \tilde{\mathbf{r}}_2 + \dots + \tilde{\mathbf{r}}_L = \sum_{i=1}^L \tilde{\mathbf{r}}_i \quad (13)$$

As shown above, we can make use of these two powerful tools to decompose the seismic signal in order to obtain an estimate of the reflectivity function, a parameter of extreme importance for the seismic interpreter, since the reflectivity function is related to the behavior of the rocks in subsurface. Using the Equation (13) and knowing that the groundroll noise is located in the first eigenimage of the reflectivity function, we can attenuate it making new filtering method called MPD+SVD filter (Minimum Phase Decomposition plus Singular Value Decomposition filter).

MPD+SVD filter

We chose a sliding window containing 11 traces for the SVD decomposition of the matrix \mathbf{W} , which means that we generated 11 eigenimages of this matrix that contain the minimum phase wavelets in their columns. We performed the filtering using two interactions (i.e. the noise of the first filter stage was the input in the next step). This methodology is interesting since it avoids the non-criterion discarding of the first decomposition where the coherent noise is located, since that in this section also have a significant part of the interest signal. At the end of the process we add up all the portions of the signal and apply an AGC (Automatic Gain Control). In the end of the interactive process we will have a filtered seismogram with the attenuation of the noise and a high preservation of the interest signal. The steps of the MPD+SVD filter algorithm can be simplified as follows:

Algorithm 1 MPD+SVD filter algorithm

Input: Seismic trace \mathbf{d}

Choose a temporal window l_w

Gets de auto-correlation function R_d within l_w (Eq. (1))

Gets the filter coefficients \mathbf{g} solving Equation (2).

Gets the minimum phase wavelet \mathbf{w}_i solving Equation (3).

Put \mathbf{w}_i in a column j of the matrix \mathbf{W} (see Eq. (4)).

Move the window l_w to one sample and do it again.

Do it until fill all columns of the matrix \mathbf{W} .

SVD decomposition of the matrix \mathbf{W} .

We get: $\mathbf{W} = \tilde{\mathbf{W}}_1 + \tilde{\mathbf{W}}_2 + \dots + \tilde{\mathbf{W}}_L$

Now we have: $\mathbf{d} = \tilde{\mathbf{W}}_1 \mathbf{r} + \tilde{\mathbf{W}}_2 \mathbf{r} + \dots + \tilde{\mathbf{W}}_L \mathbf{r} = \sum_{i=1}^L \tilde{\mathbf{d}}_i$

Noise $\rightarrow \tilde{\mathbf{W}}_1 \mathbf{r} = \tilde{\mathbf{d}}_1$

Signal $\rightarrow \tilde{\mathbf{W}}_2 \mathbf{r} + \dots + \tilde{\mathbf{W}}_L \mathbf{r} = \sum_{i=2}^L \tilde{\mathbf{W}}_i \mathbf{r} = \sum_{i=2}^L \tilde{\mathbf{d}}_i$

Solve: $\mathbf{r}^* = (\sum_{i=2}^L \tilde{\mathbf{W}}_i)^{-1} (\sum_{i=2}^L \tilde{\mathbf{d}}_i)$

Output: Reflectivity function filtered \mathbf{r}^*

We write the code using the FORTRAN programming language. We parse the code using the paradigm MPI (Message Passing Interface). The MPI paralleling was done only with the

purpose of to send to each node a number of columns of the matrix that stores the seismic traces. After processing from within each node, the result was sent back to the master.

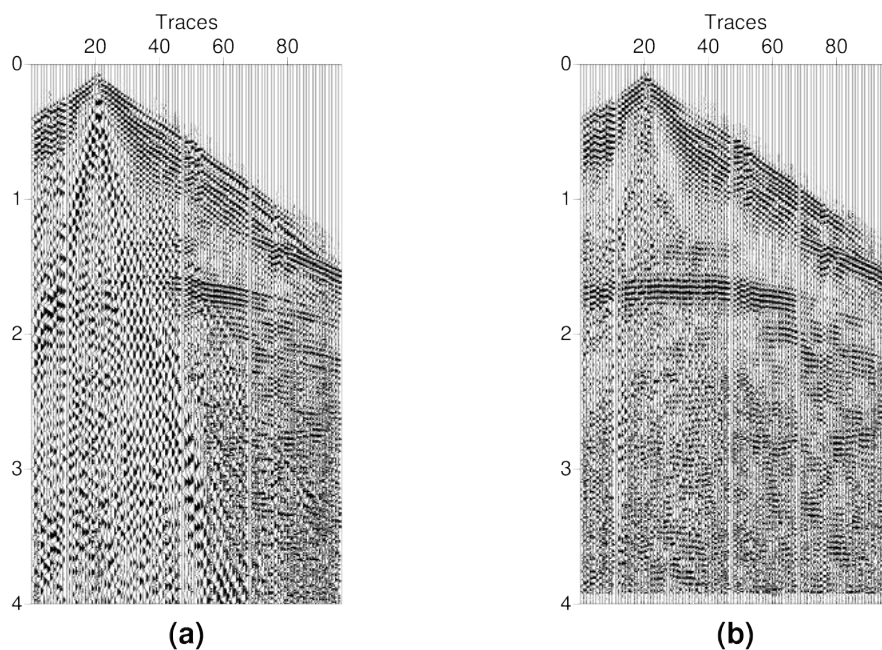


Figure 3 – Common-shot gather without filter application (a) and after MPD+SVD filter application (b).

2D seismic data processing from Tacutu Basin

The MPD+SVD filter separate the coherent noises in the first decomposition, because of that we test it in the groundroll attenuation. We use a 2D seismic data where this noise is predominant. The data is from the Tacutu Basin, an aborted Mesozoic rift located in the state of Roraima and the data about this seismic line are shown in Table 1.

Table 1 – Seismic acquisition parameters of the line 204-RL-247 from Tacutu Basin.

Seismic acquisition parameters	
Line	204-RL-247
Spread	1050-100-0-100-3850
t(s)	4
Δt (ms)	4
GC(%)	4800
Δs (m)	50
Δg (m)	50
Nc	96

We processed this 2D seismic data using the seismic processing package Seismic Unix (SU) with free distribution by CWP (Colorado School of Mines), shell scripts and a FORTRAN code was used to apply the filter MPD+SVD. We applied the processing flowchart described in Figure 2. First we converted the seismic data to SU format and then we done the seismic data geometry. After the mute and the edition of the seismic traces we applied the filter MPD+SVD. We performed the velocity analysis and then obtained the velocity field that was used to do the normal moveout correction and the migration of the seismic data. We applied the MPD+SVD filter with two interactions to groundroll attenuation in this paper.

RESULTS

In Figure 3(a) we can see the effect of groundroll noise on a common-shot gather. The groundroll appears in seismic record as a cone of high amplitudes and low frequencies, it masks the reflections and decreases the signal to noise ratio in the seismic section. The Figure 3(b) shows the same common-shot gather after MPD+SVD filter application. We can see that the MPD+SVD filter was efficient in attenuate the groundroll and reveal the reflections events that was masked by the noise. The continuity

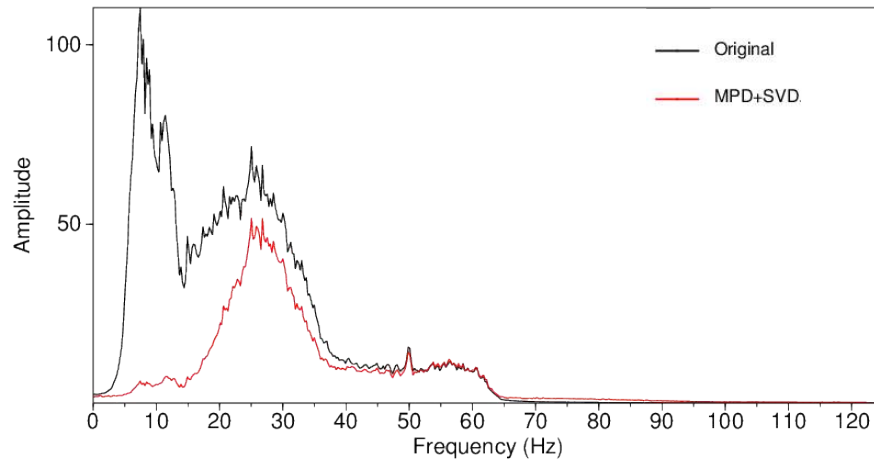


Figure 4 – Amplitude spectrum: common-shot gather without filter application (black) and after MPD+SVD filter application (red).

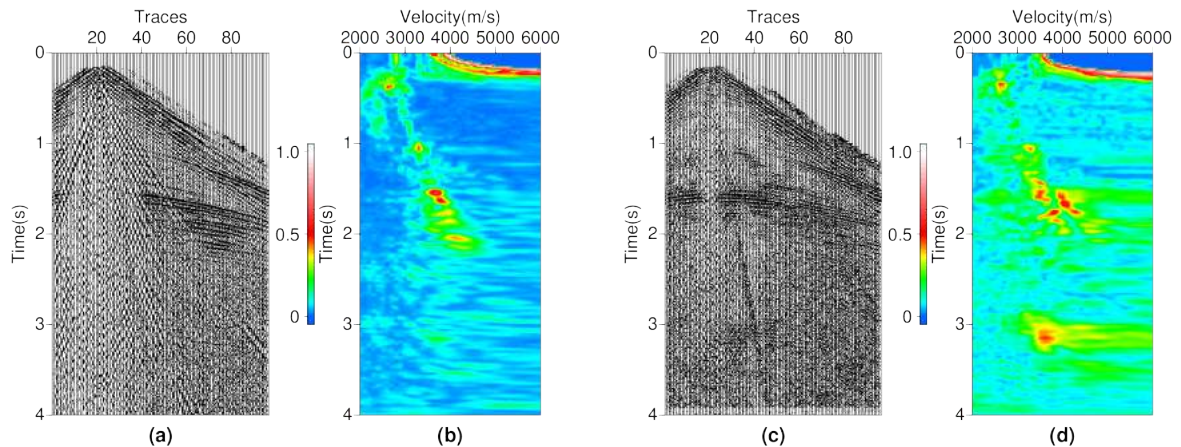


Figure 5 – Semblance panel: supergather original without filter application (a) and its semblance panel (b), supergather after MPD+SVD filter application (c) and its semblance panel (d).

of the events between 1.5 seconds and 2.0 seconds shows that this filter is very powerful to groundroll attenuation.

The Figure 4 shows the amplitude spectrum of the original data and the filtered data. If we observe the amplitude spectrum of the original common-shot gather, we notice the presence of the groundroll in the range of 5 Hz to 12 Hz characterized by high amplitudes in this low frequency zone (black curve), the amplitude spectrum of the filtered data after MPD+SVD filter (red curve) shows an attenuation in this band where the noise was located. The reflection events are much more highlighted after

AGC gain in comparison with a zone where was the low frequency noise. The method was efficient in attenuating the groundroll and preserving the interest events.

Furthermore we examined the effect of this filter in the velocity analysis step. For this we assembled a supergather from original data without filter application and a supergather after MPD+SVD filter application and we obtained the velocity spectrum (Fig. 5). Again, the presence of the noise in the form of a cone of low frequencies and high amplitudes is noted in Figure 5(a) and in Figure 5(b) its velocity spectrum.

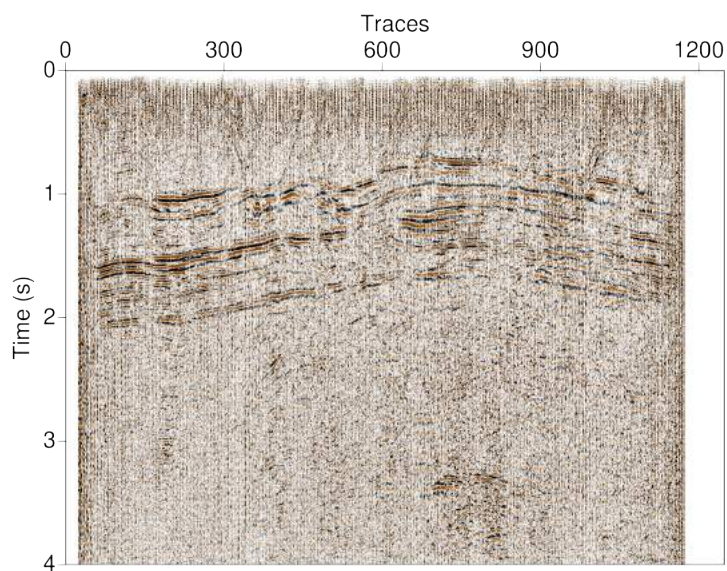


Figure 6 – Stacked seismic section without filter application.

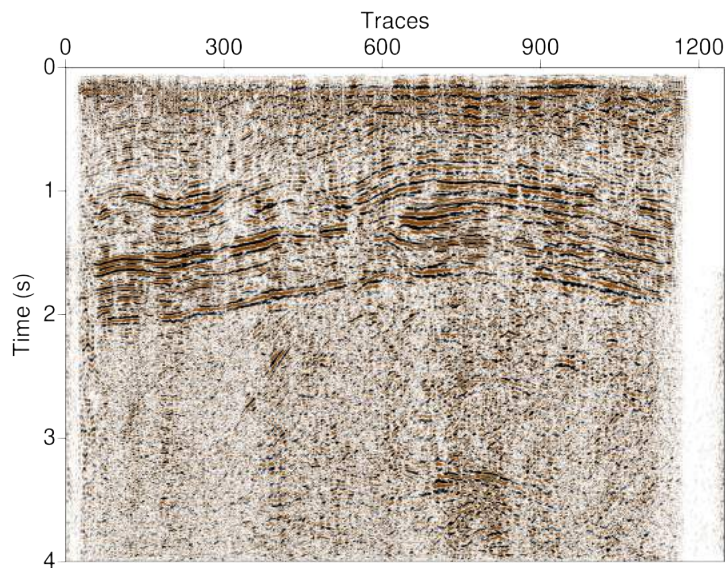


Figure 7 – Stacked seismic section after MPD+SVD filter application.

In Figure 5(c) there is a supergather that was built using CMPs after MPD+SVD filtering and in Figure 5(d) its velocity spectrum. We note that after filtering using the MPD+SVD filter there is an increase in the signal to noise ratio.

The Figure 6 is composed by original stacked seismic section. We note how the coherent noise groundroll makes

it difficult to see seismic reflections and their interpretation in the stacked seismic section. In the Figure 7 there is the stacked section after MPD+SVD filtering. We note the significant attenuation of the noise and a highlight of the reflectors, since without the influence of the noise the reflection events are much more evident. The Figure 8 shows the stacked section after the

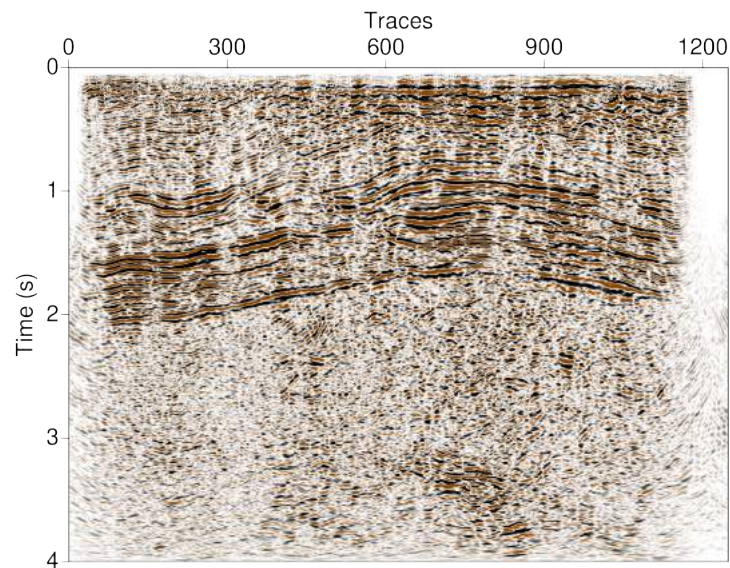


Figure 8 – Stacked seismic section after MPD+SVD filter and phase-shift migration.

migration in time using phase-shift method. It is possible to notice an increase in lateral resolution in the stacked seismic section.

CONCLUSION

The minimum phase decomposition method in conjunction with singular value decomposition proved to be a efficient tool for seismic signal analysis. The filtering using the MPD+SVD filter was effective in attenuating the coherent noise groundroll in addition to highlighting the events of interest in the stacked seismic section. The method was also effective in the attenuation of the undesired event without making large cuts in the frequency band of the signal, improved to stage of velocity analysis by increasing the signal to noise ratio in the seismogram and the result was a stacked seismic section with a good resolution.

ACKNOWLEDGEMENTS

This research was supported by FAPESB and INCT-GP/CNPq. The facility support from CPGG/UFBA is also acknowledged.

REFERENCES

ALVES FM. 2015. Aplicação do método de decomposição em modos empíricos e da filtragem SVD na atenuação de ruídos em dados sísmicos de reflexão. Master dissertation. Universidade Federal da

Bahia, Salvador, Brazil. Available on: <<http://www.pggeofisica.ufba.br/media/uploads/publicacoes/310.pdf>>. 69 pp.

ANDREWS HC & HUNT BR. 1977. Digital image restoration. Englewood Cliffs. Prentice-Hall. 238 pp.

FREIRE SLM. 1986. Aplicações do método de decomposição em valores singulares no processamento de dados sísmicos. Ph.D. thesis. Universidade Federal da Bahia, Salvador, Bahia, Brazil. 182 pp.

MELO P, PORSANI M & SILVA M. 2009. Ground-roll attenuation using a 2D time-derivative filter. *Geophysical Prospecting*, 57(3): 343–353.

PORSANI M, SILVA M, MELO P & URSIN B. 2009. Ground-roll attenuation based on SVD filtering. In: SEG Expanded Abstracts. Houston, Texas, United States of America. Volume 28(3381), 5 pp.

PORSANI MJ. 1986. Desenvolvimento de algoritmos tipo-Levinson para o processamento de dados sísmicos. PhD thesis, Universidade Federal da Bahia, Salvador, Brazil, 240 pp.

PORSANI MJ, SILVA MGS & URSIN B. 2013a. Dynamic estimation of reflectivity by minimum-delay seismic trace decomposition. *Geophysics*, 78(3): 109–117.

PORSANI MJ, URSIN B, SILVA MGS & MELO PEM. 2013b. Dip-adaptive singular-value decomposition filtering for seismic reflection enhancement. *Geophysical Prospecting*, 61(1): 42–52.

SANTOS AS. 2014. Atenuação do groundroll utilizando a filtragem direcional radial. Graduation course work, Universidade Federal da

Bahia, Salvador, Brazil. Available on: <<http://www.cpgg.ufba.br/gr-geof/geo213/trabalhos-graduacao/Anderson-Santos.pdf>>. 45 pp.

SILVA M. 2015. Empilhamento automático ao longo do mergulho local e novos métodos para processamento de dados sísmicos no domínio

do tempo. Ph.D. thesis. Universidade Federal da Bahia, Salvador, Bahia, Brazil. 111 pp.

SILVA MG. 2004. Processamento de Dados Sísmicos da Bacia do Tacutu. Master dissertation. Universidade Federal da Bahia, Salvador, Bahia, Brazil. 126 pp.

Recebido em 15 junho, 2018 / Aceito em 26 junho, 2019

Received on June 15, 2018 / Accepted on June 26, 2019

SIMULATING POROSITY AND PERMEABILITY OF THE NUCLEAR MAGNETIC RESONANCE (NMR) LOG IN CARBONATE RESERVOIRS OF CAMPOS BASIN, SOUTHEASTERN BRAZIL, USING CONVENTIONAL LOGS AND ARTIFICIAL INTELLIGENCE APPROACHES

Antonio Abel González Carrasquilla¹ and Victor Hugo Tapia Briones²

ABSTRACT. We examined, in this study, the artificial intelligence techniques ability in deriving parameters of the Nuclear Magnetic Resonance log, starting from conventional logs. To perform this, it was applied Fuzzy Logic and Artificial Neural Network techniques separately, forming independent schemes. On the other hand, Simple Average and Genetic Algorithm approaches were used to assign weighting factors to Fuzzy Logic and Artificial Neural Network estimates, with the objective to optimize the individual contributions of each one. To do this, the methodology used conventional well logs, that is, gamma ray, resistivity, neutron porosity, density and sonic logs. The wells are in an Albian carbonate reservoir in Campos Basin, Southeastern Brazil. The responses were compared with the Schlumberger free fluid porosity and the lateral permeability, both derived from Nuclear Magnetic Resonance log in the same wells. The results indicate that Artificial Neural Network performed better when compared with Fuzzy Logic, but this last was essential in the success of Simple Average and Genetic Algorithm estimates, which presented better results than these techniques individually. However, each approach showed a good fit with the parameters of the Nuclear Magnetic Resonance log, confirming the utility of the present methodology, in the case when there are only conventional logs, in the studied wells.

Keywords: geophysical well logging, Nuclear Magnetic Resonance, intelligent systems, Fuzzy Logic, Artificial Neural Network, Genetic Algorithm.

RESUMO. Examinamos, neste estudo, a habilidade das técnicas de inteligência artificial na determinação de parâmetros do perfil da Ressonância Magnética Nuclear, a partir de perfis convencionais. Para tanto, foram aplicadas, separadamente, as técnicas da Lógica Fuzzy e da Rede Neural Artificial formando esquemas independentes. Por outro lado, as abordagens da Média Simples e do Algoritmo Genético foram utilizadas para atribuir os fatores de ponderação às estimativas de Lógica Fuzzy e Rede Neural Artificial, com o objetivo de otimizar as contribuições individuais de cada uma. Com esse objetivo, a metodologia utilizou os perfis convencionais de dois poços, ou seja, raios gama, resistividade, porosidade neutrônica, densidade e sônico. Os poços pertencem a um reservatório carbonático Albian na Bacia de Campos, Sudeste do Brasil. As respostas foram comparadas com a porosidade do fluido livre e a permeabilidade lateral da Schlumberger, ambas derivadas do perfil da Ressonância Magnética Nuclear, nos mesmos poços. Os resultados indicam que a Rede Neural Artificial apresentou melhor desempenho, quando comparada com a Lógica Fuzzy, mas esta última foi essencial para o sucesso das estimativas da Média Simples e do Algoritmo Genético, os quais apresentaram melhores resultados do que estas técnicas individualmente. No entanto, cada abordagem apresentou um bom ajuste com os parâmetros do perfil da Ressonância Magnética Nuclear, confirmando a utilidade dessa metodologia, no caso em que existem apenas perfis convencionais nos poços estudados.

Palavras-chave: perfis geofísicos de poços, Ressonância Magnética Nuclear, sistemas inteligentes, Lógica Fuzzy, Rede Neural Artificial, Algoritmo Genético.

¹Universidade Estadual do Norte Fluminense Darcy Ribeiro (UENF), Laboratory of Engineering and Exploration of Petroleum (LENEP), Rodovia Amaral Peixoto, Km 163, Avenida Brennand, S/N, Imboacica, 27925-310, Macaé, RJ, Brazil – Phone: +55(22) 2765-6564. E-mail: abel@lenep.uenf.br

²Schlumberger Oil Services Ltd., Rua Internacional, 500, Granja dos Cavaleiros, 27930-075, Macaé, RJ, Brazil. Phone: +55(22) 2773-5151 – E-mail: hugotabri@gmail.com

INTRODUCTION

In the characterization of a reservoir, the Nuclear Magnetic Resonance (NMR) log predicts petrophysical parameters of geological formations more effectively than the conventional well logs, allowing a better evaluation and leading to more reliable results. This technique provides an important set of information, as total porosity, effective porosity, free fluid porosity, fluid type, saturations of the flushed zone, oil viscosity, permeability index, water adsorbed on clays, residual oil calculation, viscosity evaluation, anisotropy, heavy oil, tar sands, carbonate complex lithologies (pore distribution, pore types, pore connectivity and grain sizes), pseudo capillary – pressure curves, producibility, etc. However, NMR technique is costly and, therefore, is not performed on all the wells of an oilfield. Hence, it is important to develop advanced computational models to infer many parameters that it can provide us (Coates et al., 1999).

In the evolution of computational models, artificial intelligence techniques have shown good results in the synthesis of porosity and permeability curves using conventional logs as input (Nikravesh et al., 2003). In this sense, good applications of these techniques have been produced by Ogilvie et al. (2002), Lim & Kim (2004), Taghavi (2005), Abdulaheem et al. (2007), Ahrimankosh et al. (2010), Labani et al. (2010), Weldu et al. (2010) and Nashawi & Malallah (2010). Some works developed in our department, related to the Albian carbonates of the Campos Basin, were developed by Gomes (2017), Mureb (2018), Carvalho (2018), Al-Lahham (2018) and Tavares (2018), among others.

Thus, this work consists in combine different artificial intelligence techniques, such as Artificial Neural Network (ANN) and Fuzzy Logic (FL), couple with Simple Average (SA) and Genetic Algorithm (GA), through the softwares MATLAB (2019) and Interactive Petrophysics (LR Senery, 2019), to create a quantitative correlation between conventional logs and Schlumberger free fluid porosity (CMFF) and the lateral permeability (KSDR) curves derived from NMR log. From the learning acquired by intelligence systems in a test or training well, this correlation was extrapolated to a neighbor or blind test well to verify the reliability of the method.

GEOLOGICAL CONTEXT

The Campos Basin is one of the most productive oil basins along the Brazilian continental margin, accounting for more than 45% of national production based on data from 2018. The basin is in Southeastern Brazil, with the approximate position of Oilfield B discussed in this study, displayed in a red rectangle

with dashed line in Figure 1. The Albian carbonate reservoirs of Quissamã Formation are productive in this basin, having a typical porosity of 25% and, a permeability of 25 mD (Bruhn et al., 2003). The sedimentation of this carbonate started in the drift phase at the beginning of Albian with marine deposition (Fig. 2). The depositional model of this oilfield corresponds to a carbonate platform, and, according to Okubo et al. (2015), this depositional model characterizes the sedimentation in a high-energy environment (oolitic and oncolitic grainstones), a moderate-energy environment (oolitic peloidal grainstones and oncolitic bioclastic packstones) and a low-energy environment (peloidal bioclastic packstones and wackestones) (Fig. 3). In this oilfield, two wells, P1 and P2, were used to perform this study. The Well P1 is in the high-energy of the carbonate ramp and, the Well P2 is in the moderate-energy zone (Fig. 4). These reservoirs are heterogeneous and fractured, which results in a generally low recovery factor, complex rock properties and geophysical well data difficult to interpret. Carbonate reservoirs were characterized through a combination study of their geological characteristics, petrophysical properties and geophysical logs, data that provide a fundamental understanding of their geometry and dynamic properties.

MATERIALS AND METHODS

In the intelligent systems, discussed in this study, the conventional logs of each well were used as input, namely: gamma ray (GR), resistivity laterolog (RLA1), density (RHOZ), neutron porosity (NPOR) and sonic (DTCO) logs. As targets, it was employed Schlumberger-Doll Research (SDR) free fluid porosity (CMFF) and vertical permeability (KSDR), both derived from NMR log (Franco et al., 2011).

Two wells were selected to accomplish this study, a training well, called P1 and a neighbor blind test well, named P2, which cross a carbonate platform with great lithological variations. For Well P1, Figure 5 shows the description of Well P1 in Campos Basin, well logs, track 1: GR, track 10: RLA1, track 11: RHOZ and NPOR, track 14: NMR T2 distribution and geometrical mean cut-off, and track 15: resistivity image. Track 2: depth. Engineering information, track 3: jointer, and, track 7: oil occurrence. Geological information, track 4: cores, track 5: texture, track 6: grain size, and, track 8: facies. Track 9: petrophysical units. Laboratory measurements, track 12: porosity, and, track 13: permeability. The geological section and, the average porosity and permeability, for each section, are also shown. The logs of the Wells P1 and P2 are shown in the Figures

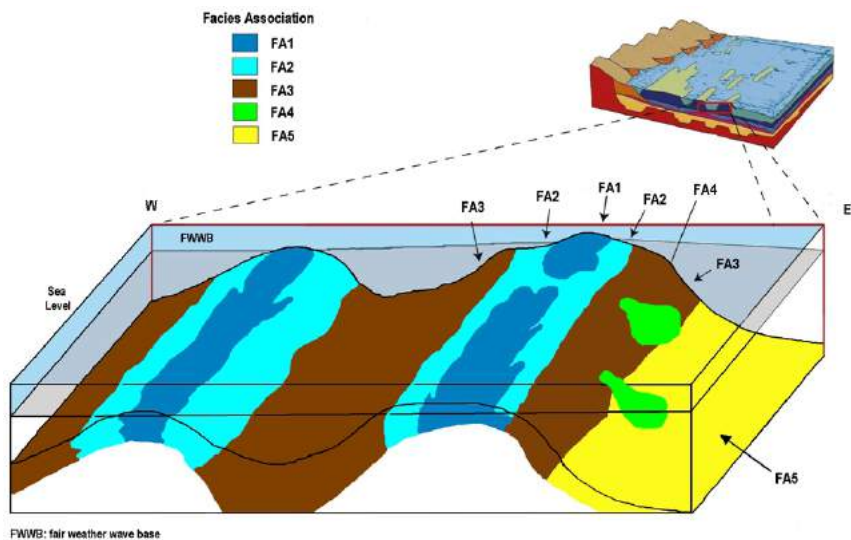


Figure 3 – Depositional model inferred for the carbonate platform in the Campos Basin during the Albian Age. Facies Association (FA): FA1=oncolitic and oolitic grainstones, FA2=oncolitic peloidal grainstones and oolitic bioclastic packstones, FA3=wackestones and peloidal bioclastic packstones, FA4=bioclastic packstones and oolitic wackestones/packstones and, FA5=pthonellid wackestones. FWWB=Fair Weather Wave Base. Note the physiographic position of this model compared to the scheme of Guardado et al. (1989) (modified from Okubo et al., 2015).

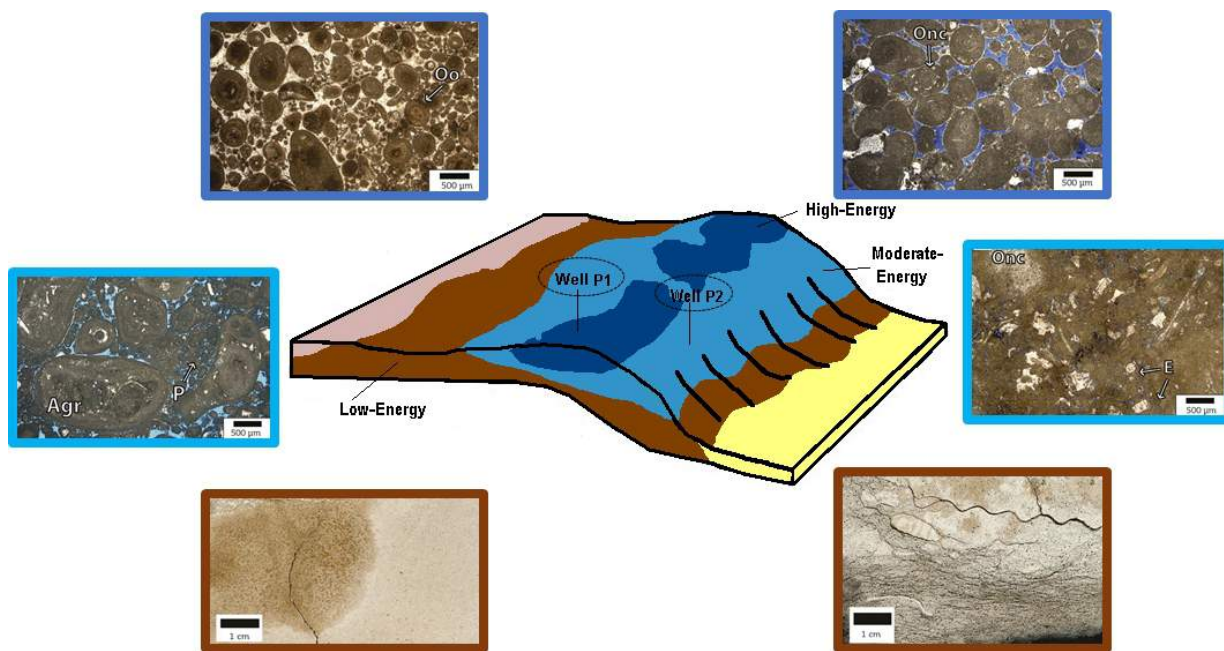


Figure 4 – The generalized location of the Wells P1 and P2 on the carbonate ramp depositional model with representative "depositional energy" designations based on characteristic lithofacies. The photomicrographs from plug samples of each lithofacies and their associated energy zone: oolitic and oncolitic grainstones of the high-energy zone (dark blue), oncolitic peloidal grainstones and oncolitic bioclastic packstones of the moderate-energy zone (light blue), and peloidal bioclastic packstones and wackestones of the low-energy zone (brown) (modified from Okubo et al., 2015).

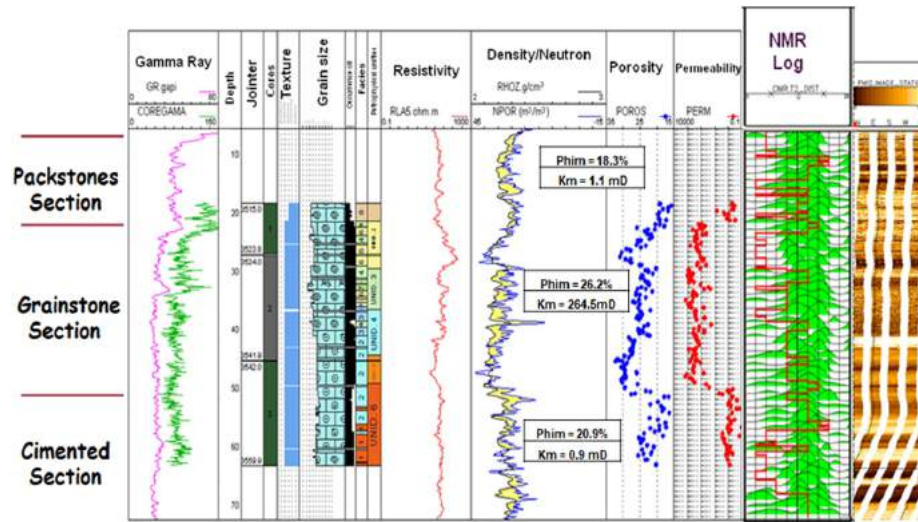


Figure 5 – Description of Well P1 in Campos Basin. Well logs, track 1: GR, track 10: RLA1, track 11: RHOZ and NPOR, track 14: NMR T2 distribution and geometrical mean cut-off, and track 15: resistivity image. Track 2: depth. Engineering information, track 3: jointer, and, track 7: oil occurrence. Geological information, track 4: cores, track 5: texture, track 6: grain size, and, track 8: facies. Track 9: petrophysical units. Laboratory measurements, track 12: porosity, and, track 13: permeability. The geological section and, the average porosity and permeability, for each section, are also shown.

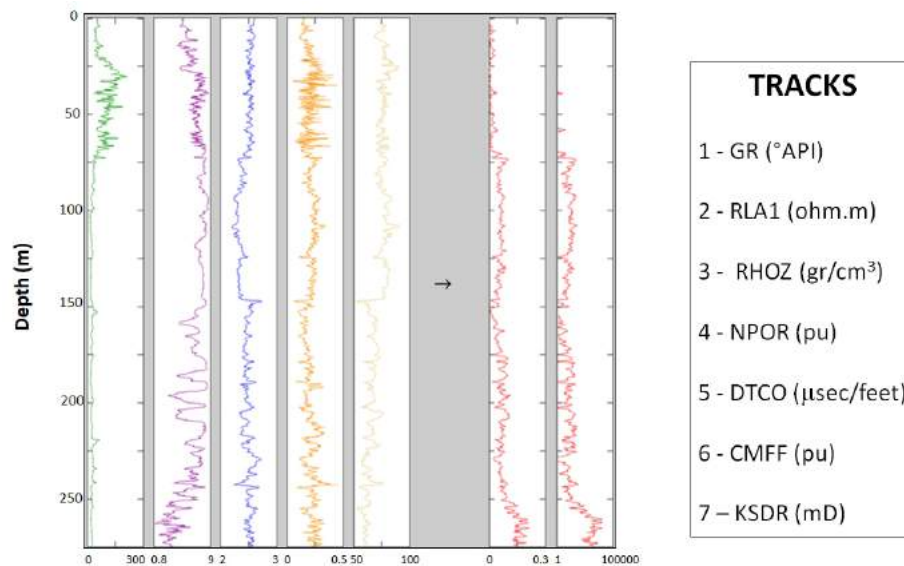


Figure 6 – Well P1 in Campos Basin. Tracks 1 to 5: gamma ray (GR), resistivity laterolog (RLA1), density (RHOZ), neutron porosity (NPOR) and sonic (DTCO) conventional logs; track 6: Schlumberger free fluid porosity (CMFF); track 7: Schlumberger vertical permeability (KSDR); both derived from NMR log.

6 and 7 show GR (track 1), RLA1 (track 2), RHOZ (track 3), NPOR (track 4) and DTCO (track 5) logs; the Schlumberger free fluid porosity (CMFF) in track 6; and, the Schlumberger vertical permeability (KSDR) in track 7.

This work combines different artificial intelligence techniques, such as Artificial Neural Network (ANN) and Fuzzy Logic (FL), coupled with a Simple Average (SA) and the Genetic Algorithm (GA) systems. The estimates of CMFF and KSDR

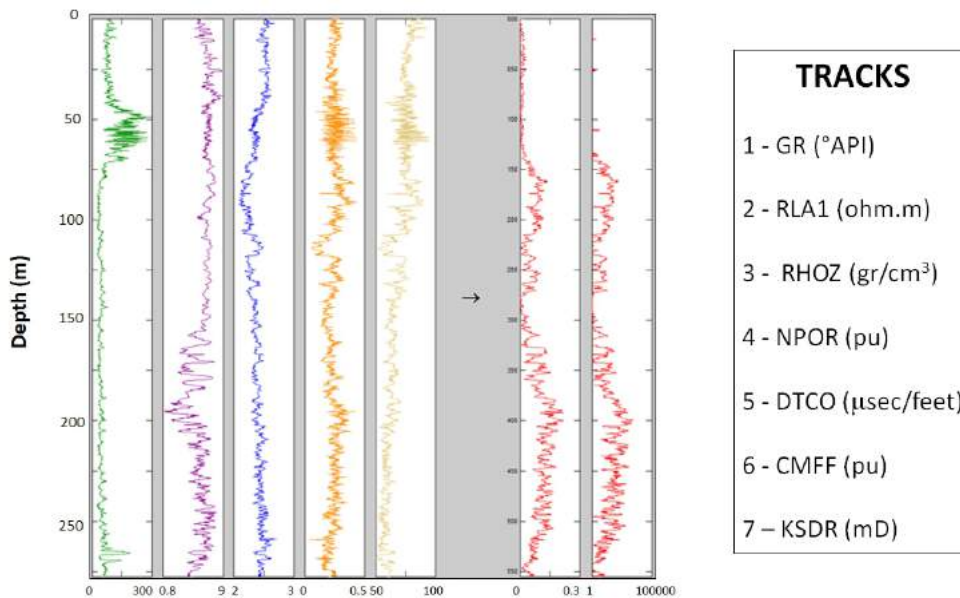


Figure 7 – Well P2 in Campos Basin. Tracks 1 to 5: gamma ray (GR), resistivity laterolog (RLA1), density (RHOZ), neutron porosity (NPOR) and sonic (DTCO) conventional logs; track 6: Schlumberger free fluid porosity (CMFF); track 7: Schlumberger vertical permeability (KSDR); both derived from NMR log.

were compared with the respective laboratory data to calibrate them (not shown in this article). In the end, the quality of the fit, between the Schlumberger and the intelligent systems estimates, is calculated through the Mean Squared Error (MSE). The basic principles of these approaches are shown below.

In the implementation of the FL system, five linguistic variables were used and considered enough to represent the large variation of the logs (Maximiano & Carrasquilla, 2011). Each variable was controlled by a triangular membership function and, using the FL toolbox of MATLAB (2019). The best results for this technique were obtained with the Mamdani scheme, which offered better control of membership functions and for carrying out inferences. Figure 7 illustrates the adjustment of the membership functions for RLA1 log input in the range [0.846 8.355].

Due to high variations shown on the logs, it was decided to create several rules that reflected more the combinations between the input logs and output logs. Thus, for CMFF, 288 fuzzy proposals were used, which resulted in an acceptable approximation in the validation process, with no adjustments of membership functions. In the case of KSDR, however, because its variation along the well, estimate was not satisfactory. So, it was decided to divide the log into 3 units of similar variations. For each of these sectors, a FL system was built, using each 77, 85 and 20 rules, respectively.

An ANN has three layers of neurons: an input layer, one hidden and one output (Russell & Norvig, 2010). To train CMFF was used a toolbox backpropagation neural network (MATLAB, 2019) with five neurons in the hidden layer and one neuron in the output layer. The stopping criterion used was the determination of a maximum value of 500 epochs, or iterations. On the other hand, to train KSDR, ten neurons were used in the hidden layer and one neuron in the output layer, with one thousand epochs as stopping criterion. Many trainings were conducted using more than one hidden layer, and, when this number was increasing, the accuracy of the estimate was better in the Well P1 validation process. However, the accuracy in the extrapolation in Well P2 was low and, for this reason, an ANN with only one layer was great. As neuron activation, the ANN models used, as transfer functions, a hyperbolic tangent function (Eq. 1), in the neurons of hidden layer and, a linear function (Eq. 2), in the neurons of output layer:

$$\tanh(s) = \frac{2}{(1 + e^{-2s})} - 1, \tag{1}$$

$$\text{lin}(s) = s, \tag{2}$$

where s represents the sum calculated for each neuron in each propagation. Figure 8 shows the ANN template used to estimate

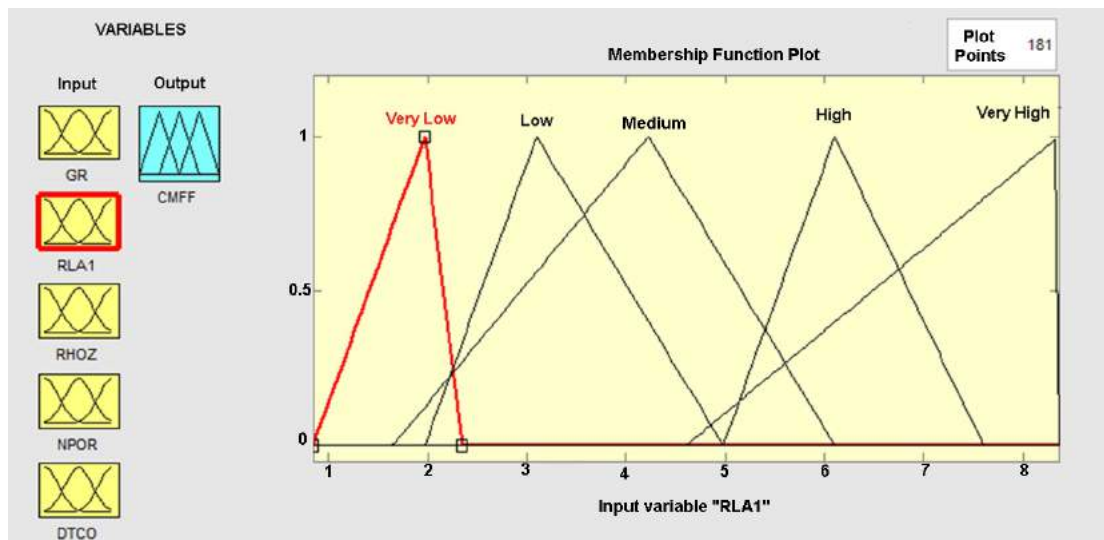


Figure 8 – Final adjustment of the Fuzzy Logic membership functions of the RLA1 resistivity log input to estimate porosity CMFF.

the porosity CMFF. The calculation of a neuron of the hidden layer can be represented by the following function:

$$net_i = w_{0i} + \sum_{j=1}^5 w_{ij}x_j, \tag{3}$$

where x_j are the input variables, w_{ij} are the weight factors for each input neurons of hidden layer and w_{0i} are the bias of each neuron of hidden layer. Considering the neuron of the output layer, the function of calculating the porosity and permeability of a propagation can be represented as follows, respectively:

$$\phi_{ANN} = f \left[v_0 + \sum_{i=1}^5 v_i f_i \left(\frac{2}{1 + e^{-2net_i}} \right) \right], \tag{4}$$

$$k_{ANN} = f \left[v_0 + \sum_{i=1}^{10} v_i f_i \left(\frac{2}{1 + e^{-2net_i}} \right) \right], \tag{5}$$

where v_i are the weight factors for each output neurons of the hidden layer and v_0 is the bias of the neuron of the output layer.

To build the GA approach, FL and ANN estimates were combined by assigning weights for the results of each one. The optimization was performed by minimizing the MSE, searching weights with the best contribution of each log and each scheme (Ogilvie et al., 2002), in the prediction of CMFF and KSDR for training Well P1. GA scheme is based on the summation of FL and ANN results, finding different weights for each approach, as shows in the following equations:

$$\phi_{GA} = P_1 \times \phi_{Fuzzy} + P_2 \times \phi_{ANN}, \tag{6}$$

$$k_{GA} = P_3 \times k_{Fuzzy} + P_4 \times k_{ANN}, \tag{7}$$

where P_1, P_2, P_3 and P_4 are the weight factors calculated by GA scheme. Figure 9 shows the GA scheme used to estimate the porosity CMFF.

The SA system is based on the elementary arithmetic average of FL and ANN systems described previously. With FL and ANN systems predicting CMFF and KSDR curves of the Well P1, whereby trained, it was proceeded to develop the SA structure which evaluate the result of FL and ANN prediction curves associated in the same ratio. The following equations show how were built the prediction logs of SA system:

$$\phi_{Mean} = 0.5 \times \phi_{Fuzzy} + 0.5 \times \phi_{ANN}, \tag{8}$$

$$k_{Mean} = 0.5 \times k_{Fuzzy} + 0.5 \times k_{ANN}, \tag{9}$$

in which the values $\phi_{Fuzzy}, k_{Fuzzy}, \phi_{ANN}$ and k_{ANN} correspond, respectively, to the porosity and permeability of FL and ANN estimates.

The validation process consisted in evaluating the intelligent model of learning, which was constructed and applied using conventional logs as input and CMFF and KSDR curves as output in the training or test Well P1. After this validation, an extrapolation process was executed to estimate CMFF and KSDR output curves of the neighbor Well P2, using as input its own conventional logs.

To evaluate the approximation of the curves generated by the intelligent systems with the target curves of Schlumberger

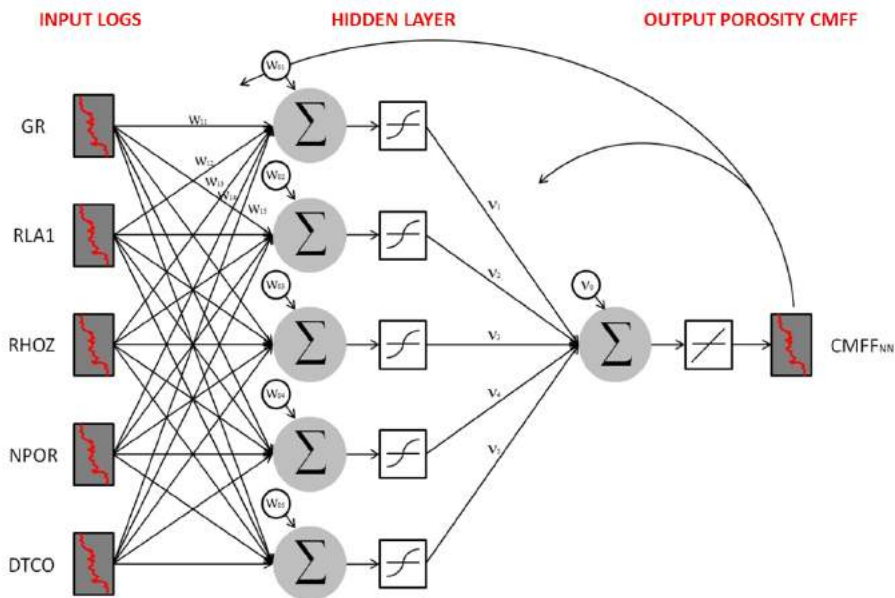


Figure 9 – The Artificial Neural Network scheme used to estimate porosity CMFF.

porosity and permeability, we used the MSE estimation, whose equations can be written as follows:

$$MSE_{\phi} = \frac{1}{n} \sum_{i=1}^n (\phi_{ANN_i} - \phi_i)^2, \quad (10)$$

$$MSE_k = \frac{1}{n} \sum_{i=1}^n (k_{ANN_i} - k_i)^2, \quad (11)$$

where n is the number of points of each log, ϕ_{ANN} and k_{ANN} correspond to the porosity and permeability logs of the ANN system and, ϕ_i and k_i are the CMFF and KSDR logs.

RESULTS AND DISCUSSIONS

Figures 10 and 11 show, respectively, the validation process for CMFF and KSDR in the training Well P1, where the tracks, from left to right, show the estimates for FL, ANN, SM and GA. In these figures, despite simulated curves (blue) do not fit the CMFF and KSDR (red) in the bottom of the well, they were able to identify a peak in the packstones zone, which may be related to the presence of vugs or an aquifer. This could be clarified with the resistive or acoustic well images, but we do not rely on them in the dataset. The GA gave the following weights to the FL and ANN curves for porosity:

$$\phi_{GA} = 0.18900 \times \phi_{Fuzzy} + 0.83224 \times \phi_{ANN}, \quad (12)$$

where the ϕ_{GA} value corresponds to the log calculated by GA. The weights were calculated by the Genetic Algorithm and are shown in the following equation for permeability:

$$k_{GA} = 0.11290 \times k_{Fuzzy} + 0.84600 \times k_{ANN}. \quad (13)$$

Comparing the different estimates, it was observed that ANN behaved better than FL one. On the other hand, SA approach, although used benefits of ANN estimate, was hampered by FL simulation. In the same sense, GA system identified the best combination of FL and ANN approaches, optimizing the fit between the curves. Even among comparisons, FL and ANN approaches obtained acceptable results for CMFF and KSDR curves.

Figures 12 and 13 show, respectively, the extrapolation processes for CMFF and KSDR curves for the neighbor Well P2. In the first 150 meters of these figures, it is possible to observe low CMFF and KSDR values, probably caused by an area rich in wackestone, where the estimates for all schemes present values above the real values for both parameters. Although some values are higher than NMR parameters, ANN simulation was able to identify this low CMFF zone. Still in these depths, some negative values for KSDR were estimated, which appear as "square form" in the estimated curves, where this kind of failures are acceptable to represent zones having very low KSDR values. Between 150 to 375 meters, comprising grainstones and half of the cemented grainstones zones, FL and ANN simulations estimate

- Genetic Algorithm (GA)
 - generates a random population,
 - assesses the suitability of ϕ_{GA} ,

$$\phi_{GA} = \text{MSE}(W_1 * \text{FL} + W_2 * \text{ANN} - \phi_{\text{CMFF}})$$
 - reproduces and selects the "parents",
 - crossing - a new generation,
 - mutation,
 - degree of aptitude.

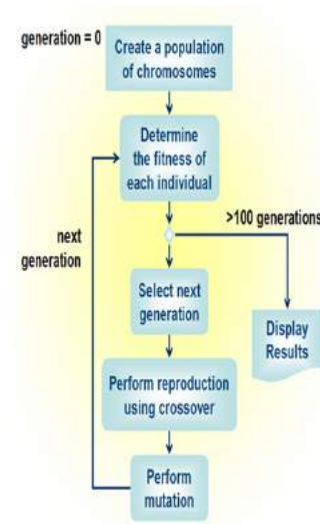


Figure 10 – The Genetic Algorithm scheme used to estimate the GA porosity (ϕ_{GA}). GA is Genetic Algorithm, MSE is Mean Squared Error, W_1 and W_2 are weights, FL is Fuzzy Logic, ANN is Artificial Neural Network, ϕ_{GA} is the GA estimated porosity and ϕ_{CMFF} is the Schlumberger free fluid estimated porosity.

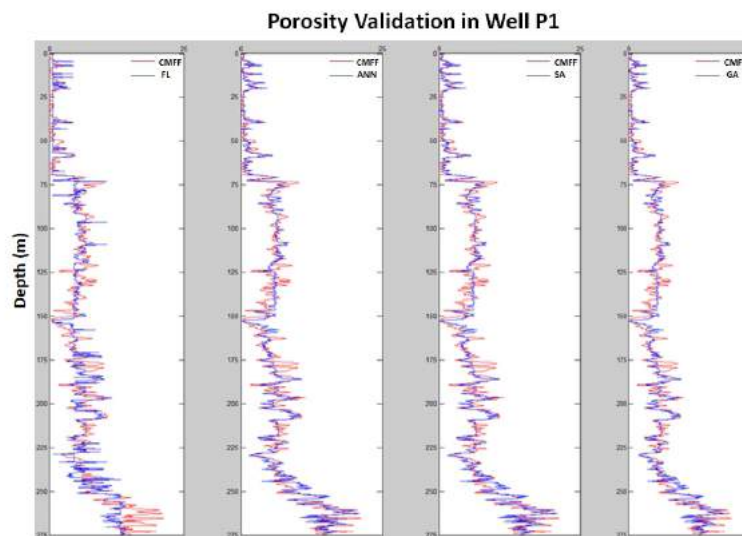


Figure 11 – Porosity validation in Well P1 of Oilfield A in Campos Basin.

the porosity variations in a reasonable manner. Above 375 meters, in packstones zone, ANN estimated CMFF curve with relative accuracy again, stood out over the others. However, FL scheme identified non-existent peaks of high CMFF above NMR values. In the rest of the log, FL estimate did not follow precisely the KSDR curve, but was able to identify the variation between the layers even with a "square form" curve. FL and ANN, as independent systems, identified the variations for both parameters in an acceptable form in neighbor Well P2, remembering always the

estimates in training well and the complexity characteristics of carbonate reservoirs. This proves that both systems achieved the same learning for a combination of conventional logs, that is, this region could have higher KSDR values, as recorded in Well P1. Anyway, as the Well P1, ANN estimates in Well P2 functioned better than the FL simulations. In the meantime, through the weights acquired by the GA scheme to estimate CMFF of the Well P1, the system sought to optimize GA estimates of FL and ANN approaches from the Well P2 in a single log. As the assigned

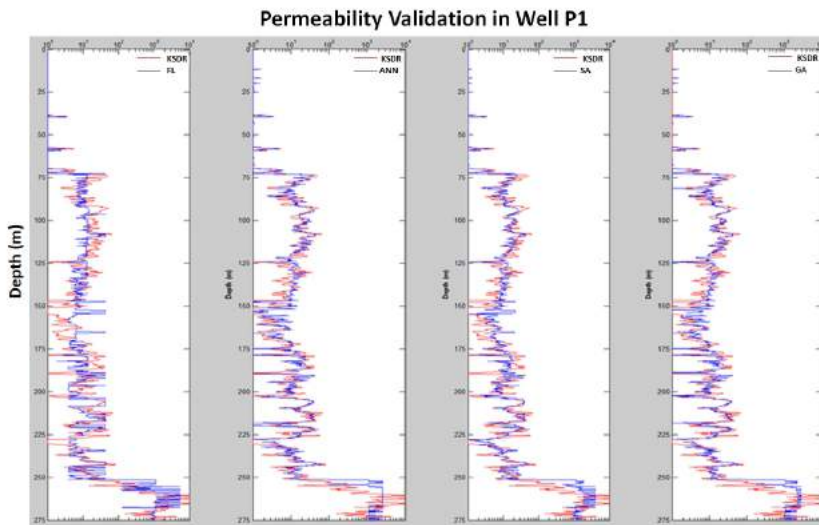


Figure 12 – Permeability validation in Well P1 of Oilfield A in Campos Basin.

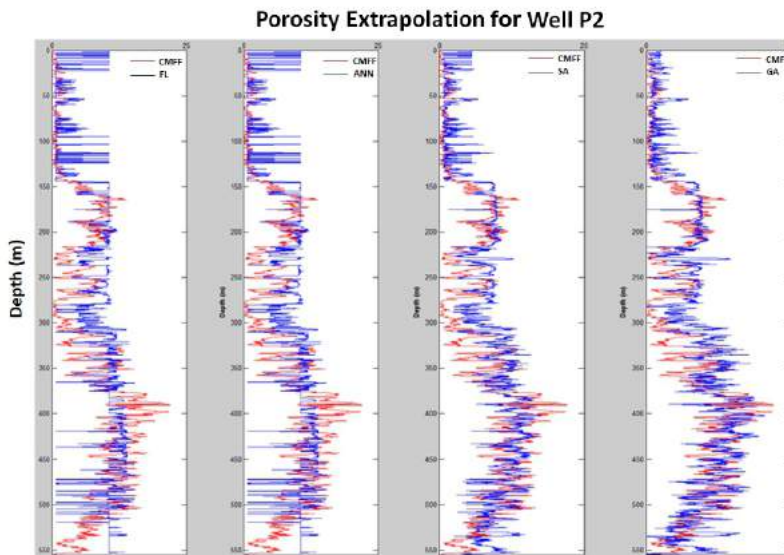


Figure 13 – Porosity extrapolation for Well P2 of Oilfield A in Campos Basin.

weight to ANN estimative is greater than the weight given to FL one, as soon as, GA simulation resembles ANN estimative. Something similar happened with SA scheme.

To compare the efficiency of each approach, it was calculated the MSE of each prediction, for both, the validation process in Well P1, as well as the extrapolation for Well P2. Table 1 shows the errors of the validations of CMFF and KSDR, as well as the classification of each method, according to their best approximation to the original NMR parameter curves. In the case of CMFF, ANN showed an error smaller than FL scheme, with an intermediate result for the SM approach. Although,

GA optimization obtained the best results, using weights to improve the ANN results and best part of FL estimate. In KSDR validation, the classification was equal to CMFF one, in other words, ANN overcame FL, SM approach remained between them and AG achieved again the best result. Despite the GA system have overcome the ANN validation, this improvement was not significant, because ANN obtained excellent results individually, which was reflected directly in GA estimate. On the other hand, Table 2 shows the errors of extrapolations of CMFF - KSDR and the classification of each intelligent system in accordance with the best results. In the case of CMFF, again, the ANN had better

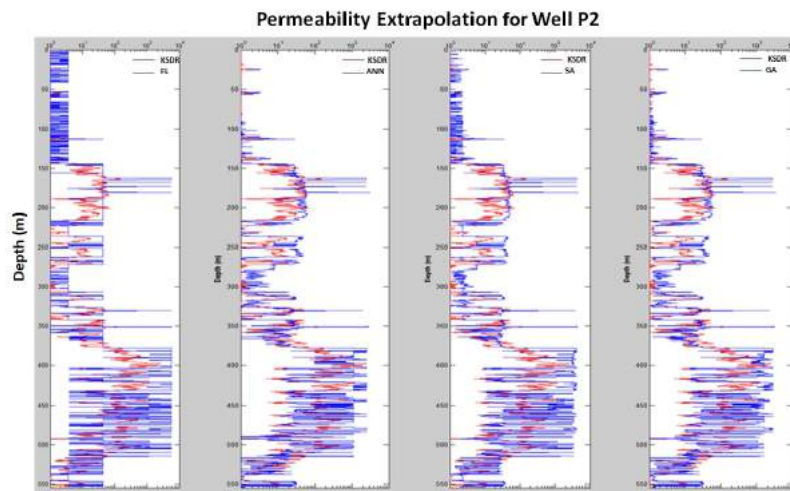


Figure 14 – Permeability extrapolation for Well P2 of Oilfield A in Campos Basin.

Table 1 – Comparison among the validation errors.

INTELLIGENT SYSTEM	POROSITY (μ)		PERMEABILITY (mD)	
	MSE (μ) ²	Rank	MSE (μ) ²	Rank
Fuzzy Logic (FL)	0.00035048	4	715520	4
Artificial Neural Network (ANN)	0.00017897	2	488170	2
Simple Average (SA)	0.00020668	3	528991	3
Genetic Algorithm (GA)	0.00017390	1	485011	1

Table 2 – Comparison among the extrapolation errors.

INTELLIGENT SYSTEM	POROSITY (μ)		PERMEABILITY (mD)	
	MSE (μ) ²	Rank	MSE (μ) ²	Rank
Fuzzy Logic (FL)	0.00182876	4	715520	4
Artificial Neural Network (ANN)	0.00126872	3	488170	1
Simple Average (SA)	0.00123483	1	528991	3
Genetic Algorithm (GA)	0.00124656	2	485011	2

performance than FL system. SM and GA schemes, through the average calculation and obtained weights, were able to reflect an optimization of FL and ANN estimates, even this improvement does not represent a significant error reduction compared with the other approaches. In the case of KSDR, ANN had the best accomplishment, followed by GA, SM and, as usual, FL in the last position.

CONCLUSIONS

In this work, artificial intelligence techniques were used to estimate the free fluid porosity and vertical permeability of the Nuclear Magnetic Resonance log, using as input gamma ray, resistivity, density, neutron porosity and sonic well logs. Four combinations were constructed, using, initially, Fuzzy Logic and Artificial Neural Network in independent schemes, while Simple

Average and Genetic Algorithm structures sought for optimized solutions. Due to high variation of the logs used, the construction of the Fuzzy Logic algorithm was troublesome in the creation of rules and adjusting the membership functions. These two stages are equivalent to the training phase of Artificial Neural Network. However, while Artificial Neural Network learns alone, Fuzzy Logic needs to be taught step by step. In general, both in the validation as extrapolation, the Artificial Neural Network system has achieved satisfactory results. The training of an artificial intelligence should not be precise in this type of study. After all, the two wells have similar geological standards, but different. The more you train an artificial intelligence for the solution of a given problem, the smaller its capacity for abstraction to solve different problems. In the case of Fuzzy Logic, the more the system is adjusted, the best results are obtained on extrapolation. After all, compared with an Artificial Neural Network, Fuzzy Logic would be a network with a very strong supervision, which would limit the learning of the intelligence only the necessary through greater freedom of the supervisor. The reductions in errors later acquired by Genetic Algorithm scheme and, on extrapolation, by the Simple Average system, do not represent significant improvement over the Artificial Neural Network rule. The Simple Average system is an elementary algorithm with fast simulation and requires no training but is dependent on other structures. As expected, the Genetic Algorithm scheme optimized results of Fuzzy Logic and Artificial Neural Network systems in the validation process of the Well P1. However, considering the estimates of the permeability of the Well P2, the difference of Fuzzy Logic system is so inferior to the Artificial Neural Network that harmed the Genetic Algorithm results. The results confirmed the efficacy in using these intelligent approaches, working well both individually and jointly, looking for the simulation of Nuclear Magnetic Resonance log parameters. Even though each of these intelligent techniques have achieved different estimates of the Schlumberger free fluid porosity and vertical permeability, the results were satisfactory, in both validation and extrapolation processes. However, the results show that to implement the process exposed in this work, Fuzzy Logic method would not be necessary to use it, because it always showed worse results than Artificial Neural Network, which proved more independent and easier to run the simulation, without the necessity choose membership functions. As the Simple Average and Genetic Algorithm schemes worked only as optimizers of Fuzzy Logic and Artificial Neural Network estimates, only the use of the Artificial Neural Network approach would be enough to make the simulations developed in this

article. Finally, it is recommended, for future work, to increase the number of correlation wells used to estimate porosity and permeability and thus distribute the weight of each parameter in Artificial Neural Network and Fuzzy Logic trainings. This is expected to reduce errors associated with profiling operations and well instability problems (enlargements) that may be mislabeled to geological issues.

ACKNOWLEDGEMENTS

The authors would like to thank ANP/Petrobras for the dataset, LR Senergy for assign to us an academic license of Interactive Petrophysics (IP) software, CAPES for the scholarship to Victor Briones and LENEP/UENF for the computing infrastructure.

REFERENCES

- ABDULRAHEEM A, SABAKHI E, AHMED M, VANTALA A, RAHARJA I & KORVIN G. 2007. Estimation of permeability from wireline logs in a Middle Eastern carbonate reservoir using Fuzzy Logic. In: SPE Middle East Oil and Gas Show and Conference. Manama, Bahrain, SPE. 1: p. 11–14.
- AHRIMANKOSH M, KASIRI N & MIRKALAEI S. 2010. Porosity and permeability prediction using Artificial Neural Network based on flow zone index in an Iranian heterogeneous carbonate reservoir. In: 14th International Oil, Gas & Petrochemical Congress. Narmak, Tehran, Research Institute of Petroleum Industry.
- AL-LAHHAM M. 2018. Permeability of carbonate reservoirs of the lower Albian determined with artificial intelligence techniques. Master Dissertation. UENF/CCT/LENEP, Macaé, RJ, Brazil. 144 pp.
- BRUHN C, GOMES J, LUCCHESI C & JOHANN P. 2003. Campos Basin: Reservoir characterization and management — Historical overview and future challenges. In: Offshore Technology Conference. Houston, Texas. OTC. paper OTC-15220, 14 pp.
- CARVALHO L. 2018. Simulation of the sonic logs in wells of the Campos and Santos Basins. Master Dissertation, UENF/CCT/LENEP, Macaé, RJ, Brazil. 70 pp. [In Portuguese].
- COATES G, XIAO L & PRAMMER M. 1999. NMR Logging: principles & applications. Houston: Halliburton Energy Services. 234 pp.
- FRANCO N, SCHUAB F & NOCCHI G. 2011. Study to determine T2 cut-offs by integrating the T2 distribution of the Nuclear Magnetic Resonance log with the pore throat distribution of the capillary pressure test by mercury injection. Report of the Project "Analysis of reservoir data". Petrobras/LENEP-UENF/BioRio Foundation Agreement, Macaé, RJ, Brazil. 213 pp. [In Portuguese].
- GOMES R. 2017. Comparative study of the permeability estimates of a Campos Basin carbonate reservoir obtained through machine learning

- methods. Master Dissertation, UENF/CCT/LENEP, Macaé, RJ, Brazil. 93 pp. [In Portuguese].
- LABANI M, KADKHODAIE-ILKHCHI A & SALAHSHOOR K. 2010. Estimation of NMR log parameters from conventional well log data using a committee machine with intelligent systems: a case study from the Iranian part of the South Pars gas field, Persian Gulf Basin. *Journal of Petroleum Science and Engineering*, 72: 175–185.
- LIM J & KIM J. 2004. Reservoir porosity and permeability estimation from well logs using Fuzzy Logic and Neural Network. In: SPE Asia Pacific Oil and Gas Conference. Perth, Australia, Society of Petroleum Engineers. n. 88476, 1: 18–20.
- LR SENERGY. 2019. Interactive Petrophysics v4.5, Online user's manual. Available on: <<http://www.lr.org>>. Access on: January 10, 2019.
- MATLAB. 2019. MATrix LABORatory. Online user's manual. Available on: <<https://www.mathworks.com/help/matlab>>. Access on: January 10, 2019.
- MUREB P. 2018. Use of multivariate statistics to estimate the permeability of a carbonate reservoir in the Campos Basin. Master Dissertation, UENF/CCT/LENEP, Macaé, RJ, Brazil. 68 pp. [In Portuguese].
- NASHAWI I & MALALLAH A. 2010. Permeability prediction from wireline well logs using fuzzy logic and discriminant analysis. In: SPE Asia Pacific Oil and Gas Conference and Exhibition. Brisbane, Australia, SPE. 1: 18-20.
- NIKRAVESH M, AMINZADEH F & ZADEH L. 2003. Soft computing and intelligent data analysis in oil exploration. Elsevier, Amsterdam. 754 pp.
- OGILVIE S, CUDDY S, LINDSAY C & HURST A. 2002. Novel methods of permeability prediction from NMR tool data. *DIALOG Magazine*, London Petrophysical Society. 1: 1-14.
- OKUBO J, LYKAWKA R, WARREN L, FAVORETO J & DIAS-BRITO D. 2015. Depositional, diagenetic and stratigraphic aspects of Macaé Group carbonates (Albian): example from an oilfield from Campos Basin. *Brazilian Journal of Geology*, 45(2): 243–258.
- RUSSELL S & NORVIG P. 2010. Artificial Intelligence. 3rd. ed., Prentice Hall, Upper Saddle River, New Jersey. 1151 pp.
- TAGHAVI A. 2005. Improved permeability estimation through use of Fuzzy Logic in a carbonate reservoir from Southwest Iran. In: SPE Middle East Oil and Gas Show and Conference. Kingdom of Bahrain, SPE. 1: 12–15.
- TAVARES M. 2018. Lithofacies, electrofacies and petrofacies in the characterization of an Albian carbonate reservoir using data mining and artificial intelligence. PhD Thesis, UENF/CCT/LENEP, Macaé, RJ, Brazil. 122 pp.
- WELDU T, GHEDAN S & AL-FARISI O. 2010. Hybrid AI and conventional empirical model for improved prediction of log-derived permeability of heterogeneous carbonate reservoir. In: SPE Production and Operations Conference and Exhibition. Tunis, Tunisia, SPE. 1: 8-10.

Recebido em 26 setembro, 2018 / Aceito em 25 junho, 2019

Received on September 26, 2018 / Accepted on June 25, 2019

